PART I

TWO-PHASE FLOW IN HIGH-HEAT-FLUX MICRO-CHANNEL HEAT SINK FOR REFRIGERATION COOLING APPLICATIONS

(Contract No. N00014-05-1-0408)

by

Prof. Issam Mudawar
Jaeseon Lee
Myungki Sung

Boiling and Two-Phase Flow Laboratory
School of Mechanical Engineering
Purdue University
West Lafayette, Indiana 47907
Tel. (765) 494-5705

September 2008

Final Report

Prepared for

Dr. Mark Spector
Office of Naval Research
Physical Science S&T Division, Code 331
800 N. Quincy St.
Arlington VA 22217-5660

REPORT DOCUMENTATION PAGE

Form Approved
OMB No. 0704-0188

PLEASE DO NOT RETURN YOUR FORM TO THE ABOVE ADDRESS.

1. REPORT DATE *(DD-MM-YYYY)*	2. REPORT TYPE	3. DATES COVERED *(From - To)*
09-11-2008	Final	04-01-20074 to 09-30-2008

4. TITLE AND SUBTITLE

Two-Phase Flow in High-Heat-Flux Micro-Channel Heat Sink for Refrigeration Cooling Applications

Part I

5a. CONTRACT NUMBER
NA

5b. GRANT NUMBER
N00014-04-1-0408

5c. PROGRAM ELEMENT NUMBER
NA

6. AUTHOR(S)

Mudawar, Issam
Lee, Jaeseon
Sung, Myung Ki

5d. PROJECT NUMBER
NA

5e. TASK NUMBER
NA

5f. WORK UNIT NUMBER
NA

7. PERFORMING ORGANIZATION NAME(S) AND ADDRESS(ES)

Purdue University
Boiling and Two-Phase Flow Laboratory
Mechanical Engineering Building, 585 Purdue Mall
West Lafayette, IN 47907

8. PERFORMING ORGANIZATION REPORT NUMBER
N00014-04-1-0408-FR

9. SPONSORING/MONITORING AGENCY NAME(S) AND ADDRESS(ES)

Office of Naval Research
ATTN: Mark Spector, ONR Code 331
One Liberty Center
875 N. Randolph Street
Arlington, VA 22203-1995

10. SPONSOR/MONITOR'S ACRONYM(S)
ONR

11. SPONSOR/MONITOR'S REPORT NUMBER(S)
NA

12. DISTRIBUTION/AVAILABILITY STATEMENT

Unlimited

13. SUPPLEMENTARY NOTES

NA

14. ABSTRACT

This report examines the pressure drop and heat transfer characteristics of two-phase micro-channel heat sinks. New models and correlations are proposed for both saturated and subcooled boiling conditions. These tools are shown to provide accurate predictions of presure drop, two-phase heat transfer coefficient and critical heat flux. Also discussed in this report is a new hybrid cooling system that combines the cooling attributes of micro-channel flow and jet impingement. It is shown this system is very effective at meeting the cooling demands of high-flux defense electronics, including the ability to dissipate in excess of 1000 W/cm2. Detailed predictive tools are provided to tackle the design of a hybrid cooling module.

15. SUBJECT TERMS

phase change, electronics cooling, micro-channel,jet impingement, hybrid cooling, refrigeration cooling

16. SECURITY CLASSIFICATION OF:			17. LIMITATION OF ABSTRACT	18. NUMBER OF PAGES	19a. NAME OF RESPONSIBLE PERSON
a. REPORT	b. ABSTRACT	c. THIS PAGE			Mudawar, Issam
U	U	U	UU	465	19b. TELEPHONE NUMBER *(Include area code)* 765-494-5705

TABLE OF CONTENTS

LIST OF TABLES

Table Page

Appendices Table

Table Page

Table Page

LIST OF FIGURES

Figure Page

Figure Page

Figure Page

NOMENCLATURE

Symbols

A	Cross-sectional area
A_1, A_2, A_3	Friedel's correlation constants
A_{base}	Total base area of micro-channel heat sink
A_{ch}	Cross-sectional area of micro-channel, H_{ch}/W_{ch}
AR	Aspect ratio of micro-channel
Bo	Boiling number
C	Two-phase multiplier parameter
C_1-C_5	Correlation constants
c_1, c_2, c_3	Correlation constants
C_c	Contraction coefficient
C_D	Drag coefficient
C_G	Dimensionless constant for rectangular micro-channels
C_{vt}	Two-phase parameter for laminar liquid-turbulent vapor flow
C_{vv}	Two-phase parameter based on laminar liquid-laminar vapor flow
CHF	Critical Heat Flux
Co	Convection number, Confinement number
c_p	Specific heat
D,d	Diameter
D_b	Bubble departure diameter
D_{eq}	Equivalent hydraulic diameter for uniformly heated channel
D_h,d_h	Hydraulic diameter
$D_{h,e}$	Hydraulic diameter of micro-channel based on heating perimeter
D_{tran}	Diameter corresponding to transition from macro- to micro-behavior

DNB	Departure from Nucleated Boiling
E	Correlation constant
f	Fanning friction factor
F_f	Constant in Eqs. (II.4.8) and (II.4.9)
Fr	Froude number
G	Mass velocity [kg/m^{2}s]
g	Gravitational acceleration
H_{ch}	Micro-channel height
H_{tc}	Distance from thermocouple to base of micro-channel
h	Local heat transfer coefficient [W/m^2 K]; enthalpy [J/kg]
$\bar{h}$	Mean heat transfer coefficient across base of heat sink
h_{fg}	Latent heat of vaporization
K	Friction constant for fully developed flow
K_i	Interfacial mass flux
k	Thermal conductivity [W/m K]
L	Length
L_{tc}	Axial location of copper block thermocouple
M_w	Molecular weight
m	Fin parameter
$\dot{m}$	Mass flow rate [g/s]
MAE	Mean absolute error
N	Correlation constant; number of experimental data; Number of micro-channels in test section
Nu	Nusselt number
n	Solid particle shape factor
ONB	Onset of nucleate boiling
P	Pressure [Pa]
ΔP	Pressure drop [Pa, bar]
P_r	Reduced pressure
Pr	Prandtl number

$PM\text{-}CHF$	Pre-mature critical heat flux
Pr	Prandtl number
q''	Heat flux through heat sink base area [W/m^2 or W/cm^2]
$q_c^{"}$	Critical heat flux for uniformly heated circular channel
$q_{eff}^{"}$	Heat flux based on total base area of micro-channel heat sink
$q_{eff,c}^{"}$	Critical heat flux based on total base area of micro-channel heat sink
$q_p^{"}$	Heat flux based on micro-channel's three-sided heated perimeter
$q_{p,c}^{"}$	Critical heat flux based on micro-channel's three-sided heated perimeter
Re	Reynolds number based on tube diameter
Re_{Dh}	Reynolds number based on channel hydraulic diameter
S	Correlation constant
T	Temperature
T^*	Dimensionless temperature
T_{tc}	Measured copper block temperature
T_w	Base wall temperature of micro-channel heat sink
$\overline{T_w}$	Mean base wall temperature of micro-channel heat sink
ΔT_{sub}	Subcooling
tc	Temperature measurement points inside heat sink block
TS	Test section
U	Mean layer velocity
u	Mean fluid velocity
v	Specific volume [m^3/kg]
W_{ch}	Micro-channel width
W_w	Half-width of copper sidewall
We	Weber number
X	Martinelli parameter
X_{vt}	Martinelli parameter for laminar liquid – turbulent vapor flow

X_{vv}	Martinelli parameter for laminar liquid – laminar vapor flow
x	Coordinate defines in Fig. II.2.4; Axial distance (Part III)
x'	Apparent quality
x_e	Thermodynamic equilibrium quality
$x^*_{e,in}$	Pseudo-inlet thermodynamic equilibrium quality with properties based on outlet pressure, $(h_{in} - h_{f,o})/h_{fg,o}$
x_o	Outlet thermodynamic equilibrium quality, $(h_o - h_{f,o})/h_{fg,o}$
y	Coordinate defined in Fig. II.2.4
Y^+	Dimensionless thickness of homogeneous two-phase layer
z	Stream-wise coordinate
Z^+	Dimensionless axial distance
z_{hy}^+	Dimensionless length

Greek Symbols

α	Void fraction
β	Ratio of channel depth to width
δ	Thickness of homogeneous two-phase layer
η	Fin efficiency
λ	Dimensionless number in Lee and Lee correlation
μ	Viscosity
ρ	Density
σ	Surface tension
σ_c	Contraction area ratio
σ_e	Expansion area ratio
τ	Shear stress
ϕ	Two-phase pressure drop multiplier
φ	Volumetric concentration of nanoparticles (Part III)
ψ	Dimensionless number in Lee and Lee correlation
ω	Volumetric quality

Superscript

–	Two-phase; Phase averaged property

Subscripts

3	Three-sided wall heating
4	Four-sided wall heating
A,a	Acceleration
ad	Adiabatic
b	Micro-channel base wall
bd	Bubble departure from wall
bf	Base fluid
c	Critical heat flux; contraction; Halfway location along micro-channel
ch	Channel
cor	Correlation
D	Diameter
e	Expansion; Thermodynamic equilibrium
exp	Experimental
F	Frictional pressure drop component
f	Saturated liquid; frictional
fg	Property difference between saturated vapor and saturated liquid
fo	Liquid only in entire channel
g	Saturated vapor
H	Homogeneous layer
HFE 7100	HFE 7100 base fluid
i	Interface between homogeneous two-phase layer and liquid
in	Channel inlet
L	Micro-channel length
lam	Laminar
m	Bulk fluid
nb	Nucleate boiling

nf	Nanofluid
ONB	Onset of nucleate boiling
out	Channel outlet
p	Solid particles
pred	Predicted
s	Solid (copper)
sat	Saturated
sc	Subcooled
sp	Single-phase
sub	Subcooling
tc	Thermocouple
tp	Two-phase
tot	Total
tran	Transition from macro- to micro-channel flow
tur	Turbulent
w	Channel wall condition
x	Local condition (Part III).

ABSTRACT

PART I. MICRO-CHANNEL HEAT SINK FOR DIRECT REFRIGERATION COOLING

While most recently electronic cooling studies have been focused on removing the heat from high-power-density devices, the present study also explores means of greatly decreasing the device operating temperature. This is achieved by incorporating a micro-channel heat sink as an evaporator in an R134a refrigeration loop. This system is capable of maintaining device temperatures below 55 °C while dissipating in excess of 100 W/cm^2.

The micro-channels were formed by machining 231 μm wide × 713 μm deep grooves into the surface of a copper block. Experiments were performed with refrigerant R134a that spanned the following conditions: inlet pressure of P_{in} = 1.44 - 6.60 bar, mass velocity of G = 127 - 654 kg/m^{2}s, inlet quality of $x_{e,in}$ = 0.001 - 0.25, outlet quality of $x_{e,out}$ = 0.49 - superheat, and heat flux of q'' = 31.6 - 93.8 W/cm^2.

Two-phase pressure drop was measured across a micro-channel heat sink that served as an evaporator in a refrigeration cycle. Predictions of the homogeneous equilibrium flow model and prior separated flow models and correlations yielded relatively poor predictions of pressure drop. A new correlation scheme is suggested that incorporates the effect of liquid viscosity and surface tension in the separated flow model's two-phase pressure drop multiplier. This scheme shows excellent agreement with the R134a data as well as previous micro-channel water data. An important practical finding from this study is that the throttling valve in a refrigeration cycle offers significant stiffening to the system, suppressing the large pressure oscillations common to micro-channel heat sinks.

Boiling heat transfer coefficients were measured by controlling heat flux (q'' = 15.9 - 93.8 W/cm^2) and vapor quality (x_e = 0.26 - 0.87) over a broad range of mass velocity. While prior studies point to either nucleate boiling or annular film evaporation

(convective flow boiling) as dominant heat transfer mechanisms in small channels, the present study shows heat transfer is associated with different mechanisms for low, medium and high qualities. Nucleate boiling occurs only at low qualities ($x_e < 0.05$) corresponding to very low heat fluxes, and high fluxes produce medium quality ($0.05 < x_e < 0.55$) or high quality ($x_e > 0.55$) flows dominated by annular film evaporation. Because of the large differences in heat transfer mechanism between the three quality regions, better predictions are possible by dividing the quality range into smaller ranges corresponding to these flow transitions. A new heat transfer coefficient correlation is recommended which shows excellent predictions for both R134a and water.

The systematic approach adopting the newly developed correlations reveals that while higher heat transfer coefficients are possible with greater mass velocities, those conditions are typically associated with wet compression corresponding to evaporator exit quality below unity and liquid entrainment at the compressor inlet. Wet compression compromises compressor performance and reliability as well as refrigeration cycle efficiency and therefore must be minimized by maintaining only slightly superheated conditions at the compressor inlet, or using a wet-compression-tolerant compressor. A parametric study of the effects of channel geometry on heat sink performance points to channels with small width and high aspect ratio as yielding superior thermal performance corresponding to only a modest penalty in pressure drop.

PART II. MICRO-CHANNEL HEAT SINK FOR INDIRECT REFRIGERATION COOLING

A new cooling scheme is proposed where the primary working fluid is pre-cooled to low temperature using an indirect refrigeration cooling system. The cooling performance was explored using HFE 7100 as working fluid and four different micro-channel sizes. High-speed video imaging was employed to help explain the complex interrelated influences of channel geometries and flow conditions on cooling performance. Unlike most prior two-phase flow studies, which involved annular film evaporation due

to high void fraction, the low coolant temperatures used in this study produced subcooled flow boiling conditions.

Increasing liquid subcooling decreased two-phase pressure drop because of decreased void fraction, caused by strong condensation at bubble interfaces, as well as decreased likelihood of bubble coalescence. It is shown macro-channel subcooled boiling pressure drop and heat transfer correlations are unsuitable for micro-channel flows.

A new model is proposed to predict the pressure drop characteristics of subcooled two-phase micro-channel heat sinks. This model depicts the subcooled flow as consisting of a homogeneous two-phase flow layer near the heated walls of the micro-channel and a second subcooled bulk liquid layer. Mass, momentum and energy control volume conservation equations are combined to predict flow characteristics for thermodynamic equilibrium qualities below zero. The model shows good predictions of pressure drop data for different mass velocities and subcoolings for four different micro-channel sizes.

The high subcooling greatly reduced both bubble departure diameter and void fraction, and precluded flow pattern transitions beyond the bubbly regime. CHF was triggered by vapor blanket formation along the micro-channel walls despite the presence of abundant core liquid. CHF increased with increasing mass velocity and/or subcooling and decreasing hydraulic diameter for a given total mass flow rate. A pre-mature type of CHF was caused by vapor backflow into the heat sink's inlet plenum at low mass velocities and small inlet subcoolings, and was associated with significant fluctuations in inlet and outlet pressure, as well as wall temperature. A systematic technique is developed to modify existing CHF correlations to more accurately account for features unique to micro-channel heat sinks, including rectangular cross-section, three-sided heating, and flow interaction between micro-channels.

PART III. ASSESSMENT OF THE EFFECTIVENESS OF NANOFLUIDS FOR SINGLE-PHASE AND TWO-PHASE HEAT TRANSFER IN MICRO-CHANNELS

Experiments were performed to explore the micro-channel cooling benefits of water-based nanofluids containing small concentrations of Al_2O_3. The high thermal conductivity of nanoparticles is shown to enhance the single-phase heat transfer coefficient, especially for laminar flow. Higher heat transfer coefficients were achieved mostly in the entrance region of micro-channels. However, the enhancement was weaker in the fully developed region, proving that nanoparticles have an appreciable effect on thermal boundary layer development. Higher concentrations also produced greater sensitivity to heat flux. Despite this enhancement, the overall cooling effectiveness of nanopartcles was quite miniscule because of the large axial temperature rise associated with the decreased specific heat for the nanofluid compared to the base fluid. For two-phase cooling, nanoparticles caused catastrophic failure by depositing into large clusters near the channel exit due to localized evaporation once boiling commenced. These and other practical disadvantages bring into question the overall merit of using nanofluids in micro-channel heat sinks.

PART I. MICRO-CHANNEL HEAT SINK FOR DIRECT REFRIGERATION COOLING

I.1 INTRODUCTION

I.1.1 Two-phase Pressure Drop in Micro-Channel

Two-phase pressure drop has been the subject of extensive research spanning many decades. Starting in the 1940s, researchers were concerned with developing predictive pressure drop models and correlations for mostly traditional industries such as steam and nuclear power generation, chemical and petroleum, desalination, refrigeration and air conditioning, etc.

With the recent emergence of new applications demanding high-heat-flux dissipation from small areas, the validity of popular pressure drop models and correlations became an open question. These new cooling demands were brought about mostly by the remarkable technological advances in the electronics industry. Since a key measure of improvement in device performance is the ability to integrate the largest number of electronic components in a given surface area, those advances have yielded unprecedented increases in device heat dissipation.

Cooling of electronic devices is fundamentally different from that of most conventional applications since not only does the heat need to be removed from the device surface, but the device must also be maintained at a relatively low temperature. Compounding this problem is the existence of an appreciable thermal resistance between the device and coolant, which is the result of various intermediate layers that are required for electronic packaging and interconnect. To compensate for the ever-increasing heat flux, maintaining an acceptable device temperature therefore requires simultaneously (1) enhancing the convective heat transfer coefficient and (2) reducing the coolant

temperature. Those concerns are key drivers behind the recent interest in using refrigerant-cooled micro-channel heat sinks.

A micro-channel heat sink possesses many unique attributes that are ideally suited for electronics cooling. Those include superior cooling characteristics, compactness, and minimal coolant usage, especially when the coolant changes phase inside the heat sink. Phase change capitalizes upon the coolant's latent heat of vaporization to absorb and ultimately dissipate a larger amount of heat than a single-phase coolant. Furthermore, the heat is removed at a fairly constant temperature that is dictated largely by the coolant's saturation temperature. Unlike single-phase heat sinks that compensate for the large heat removal by incurring an appreciable stream-wise temperature rise in both the coolant and heat sink, phase change maintains better temperature uniformity in the heat sink and aids in preventing local hot spots in the device surface.

However, two-phase micro-channel heat sinks are not without drawbacks. The small hydraulic diameter of a micro-channel can lead to appreciable pressure drop and corresponding increase in power consumption, which is undesirable in electronic systems. Therefore, a strong understanding of the relationship between pressure drop, flow rate and heat flux is of paramount importance to micro-channel heat sink design.

Many of the two-phase pressure drop models and correlations used in industry today stem from the pioneering Lockhart-Martinelli (1949) formulation, which has been modified by many investigators in pursuit of better predictions for macro-channels (e.g., Friedel [Collier and Thome (1994)], Chisholm (1973)). However, recent studies have shown this formulation produces poor predictions when attempted with small channels, suggesting different flow characteristic must be prevalent in the smaller channels.

Bowers and Mudawar (1994) were the first to provide a systematic assessment of the unique attributes of pressure drop across micro-channel heat sinks. To examine the influence of hydraulic diameter, they compared the pressure drop for refrigerant R113 in both mini-channel (d = 2.54 mm) and micro-channel (d = 510 μm) heat sinks. Using the homogeneous equilibrium model, they pointed out the serious drawbacks of a very small hydraulic diameter caused by the excessive pressure drop associated with acceleration of the two-phase mixture. Mishima and Hibiki (1996) modified the two-phase multiplier

in the Lockhart-Martinelli with a new parameter to improve pressure drop prediction for air-water flow in vertical capillary tubes with diameters of d = 1 - 4 mm. Triplett et al. (1999) investigated air-water flow in small circular tubes (d = 1.1, 1.45 mm) and triangular_channels (d_h = 1.09, 1.49 mm). The homogeneous equilibrium model showed good predictions for the bubbly and slug flow regimes but not the annular, and the Friedel's correlation (based on the separated flow model) was less accurate than the homogeneous model. Tran et al. (2000) investigated two-phase flow of refrigerants R134a, R12, and R113 in small circular channels (d = 2.46, 2.92 mm) and a rectangular channel (d_h = 2.40 mm). Most separated flow models predicted pressure drop values that were smaller than measured. Therefore, they developed a new correlation to better account for the effects of surface tension and channel diameter. Lee and Lee (2001) modified the Lockhart-Martinelli two-phase multiplier with a new parameter they correlated form their own data for air-water flow in rectangular channels (d_h = 0.784, 6.67 mm). Zhang and Webb (2001) investigated two-phase flow of refrigerants R134a, R22 and R404a in parallel circular channels (d = 2.13 mm) and recommended a new pressure drop correlation based on the separated flow model. Kawahara et al. (2002) investigated water-nitrogen flow in a 100 μm circular tube. They reported the homogeneous flow model generally overpredicted pressure drop data, while the separated flow model using a modified two-phase flow multiplier showed better agreement.

Recently, Qu and Mudawar (2002,2003) investigated the fundamental features of two-phase flow and heat transfer in a water-cooled micro-channel heat sink. Their work culminated in a comprehensive theoretical model which yielded good predictions of two-phase pressure drop and heat transfer.

The present study is an extension of recent efforts by Mudawar and co-workers to develop a comprehensive method for determining micro-channel heat sink pressure drop for coolants with drastically different thermophysical properties. New experiments were performed with R134a that were complimented by flow visualization. The heat sink was incorporated as an evaporator in a refrigeration cycle in an effort to achieve the aforementioned goals of high-flux removal while maintaining low surface temperatures. Using both the new R134a pressure drop data as well as Qu and Mudawar's earlier water

data, a new correlation scheme is recommended for two-phase pressure drop determination. This scheme is shown to yield far better accuracy than prior macro-channel and small channel correlations. Also discussed in this paper are various unique features of pressure drop in micro-channel evaporators and the suitability refrigerant-cooled heat sinks to electronic cooling applications.

I.1.2 Boiling Heat Transfer in Micro-Channel

The pioneering work by Tuckerman and Pease (1981) in the early 1980s spawned unprecedented interest in the use of micro-channel heat sinks as a means for dissipating large amount of heat from small, high-flux devices in a variety of computer and aerospace applications. While their work was focused entirely on single-phase heat sinks, recent research efforts have shifted to two-phase heat sinks, which offer significant advantages compared to their single-phase counterparts. A key drawback of single-phase heat sinks is the large (and often detrimental) temperature gradient in the device resulting from a steam-wise rise in the coolant temperature. Two-phase heat sinks capitalize upon latent heat exchange, which both increases the convective heat transfer coefficient inside the heat sink and helps maintain a more uniform device surface temperature, dictated mostly by the coolant's saturation temperature.

Despite these attributes, dissipating very large heat fluxes can lead to unacceptably high device temperatures. This is due to both the convective resistance of the coolant itself, as well as the heat diffusion resistance associated with the metallic structure of the heat sink, device and intermediate bonding agent. Avoiding high temperatures in high-flux temperature-sensitive devices can be achieved by greatly reducing the temperature of the coolant, i.e. by refrigeration. A simple means to accomplishing this goal is to incorporate the heat sink as an evaporator in a standard refrigeration cycle. This is precisely the system examined in the present study.

A key challenge to implementing this cooling scheme is the relatively poor understanding of two-phase flow and heat transfer phenomena in a micro-channel, let

alone refrigerant-cooled heat sinks. The present study aims to explore the heat transfer characteristics as well as the pressure drop characteristics of R134a in a two-phase heat sink.

The dominant heat transfer mechanism inside a small channel remains an open question. Dispute over this issue is evident in several recent studies concerning boiling heat transfer in mini- and micro-channels. Table 1.1 shows researchers are divided into two groups. The first shares the view that nucleate boiling is dominant and therefore dictates overall heat transfer inside the channel, citing the local heat transfer coefficient is dependent on heat flux, but not mass velocity or quality [Lazarek and Black (1982), Wambsganss et al. (1993), Tran et al. (1996), Bao et al. (2000), Mehendale and Jacobi (2000), Yu et al. (2002)]. The second group shares the observation that the local heat transfer coefficient is a function of quality and mass velocity in addition to wall heat flux [Kew and Cornwell (1997), Ravigururajan (1998), Yan and Lin (1998), Lee and Lee (2001), Lin et al (2001), Warrier et al. (2002), Wen et al. (2004), Huo et al. (2004)]. Experimental results by this second group generally show the local heat transfer coefficient decreases with increasing quality. This points to annual film evaporation (sometimes called convective boiling) as the dominant heat transfer mechanism.

Table I.1.1 Summary of prior relevant mini- and micro-channel studies.

Author(s)	Geometry	Fluid(s)	q'' [W/cm^2]	Flow Rate	x_e	h_{tp} [W/m^2 K]	Remarks
Lazarek & Black (1982) [3]	d = 3.1 mm L = 12.3, 24.6 cm semi-circular Single	R113	1.4 - 38.0	125 - 750 kg/m^2 s	< 0 - 0.60	2,000 – 10,000	$h_{tp} = f(q'')$ nucleate boiling dominant h_{tp} independent of x_e, G
Wambsganss et al. (1993) [4]	d = 2.92 mm L = 36.8 cm circular, single	R113	0.88 - 9.08	50 - 300 kg/m^2 s	0 - 0.90	1,500 – 7,000	$h_{tp} = f(q'')$ nucleate boiling dominant h_{tp} independent of x_e, G
Bower & Mudawar (1994) [5]	d = 2.54, 0.51 mm L = 2.86 cm circular parallel 17 micro, 3 mini	R113	3 - 256	45, 64 ml/min	< 0 - CHF		
Tran et al. (1996) [6]	d = 2.46 mm (circ.) d_h = 2.40 mm (rect.) L = 87.0 cm single	R12	3.6 - 12.9	44 - 832 kg/m^2 s	0 - 0.96	2,000 – 10,000	$h_{tp} = f(q'')$ nucleate boiling dominant h_{tp} independent of x_e, G

Table I.1.1 continued.

Author(s)	Geometry	Fluid(s)	q'' [W/cm^2]	Flow Rate	x_e	h_{tp} [W/m^2 K]	Remarks
Kew & Cornwell (1997) [7]	d = 1.39 - 3.69 mm L = 50.0 cm circular, single	R141b	0.97 - 9.0	188 - 1480 kg/m^2 s	< 0 - 0.95	1,000 – 7,000	$h_{tp} = f(q'', x_e)$ h_{tp} increases with x_e nucleate and convective boiling important
Ravigururajan (1998) [8]	d_h = 0.425 mm L = 2.052 cm rectangular 54 parallel	R124	8.0 - 65.0	75 - 250 ml/min	0 - 0.5	2,000 – 25,000	$h_{tp} = f(q'', x_e)$ h_{tp} decreases with x_e
Yan & Lin (1998) [9]	d = 2.0 mm L = 10.0 cm circular, 28 parallel	R134a	0.5 - 2.0	50 - 200 kg/m^2 s	0.1 - 0.90	2,000 – 6,000	$h_{tp} = f(q'', x_e, T_{sat})$
Bao et al. (2000) [10]	d = 1.95 mm L = 27.0 cm circular, single	R11, R123	0.5 - 20.0	50 - 1800 kg/m^2 s	< 0 - 0.90	3,000 – 17,000	$h_{tp} \propto q''^{0.735}$ nucleate boiling dominant h_{tp} independent of x_e, G

Table I.1.1 continued.

Author(s)	Geometry	Fluid(s)	q'' [W/cm^2]	Flow Rate	x_e	h_{tp} [W/m^2 K]	Remarks
Mehendale & Jacobi (2000) [11]	d_h = 0.8 mm L = 7.4 cm rectangular 52 parallel	R134a	0 - 0.34	0 - 0.5 g/s	0.07 – 0.25	0 – 9,000	h_{tp} = f(q'') nucleate boiling dominant h_{tp} independent of x_e, G
Lee & Lee (2001) [12]	d_h = 0.784,6.67 mm L = 30.0 cm rectangular single	R113	0.3 - 1.58	50 - 200 kg/m^2 s	0.15 - 0.75	1,000 – 5,000	h_{tp} = f(x_e) convective boiling dominant h_{tp} increases with x_e q'' effect minor
Lin, Kew & Cornwell (2001) [13]	d = 1.1 mm L = 50.0 cm circular, single	R141b	0.18 - 7.2	510 kg/m^2 s	< 0 – 1.0	1,000 – 6,000	h_{tp} = f(q'', x_e) nucleate and convective boiling important
Yu et al. (2002) [14]	d = 2.98 mm L = 91.0 cm circular, single	Water-ethylene glycol	10.0 - 30.0	50 - 200 kg/m^2 s	0 – 1.0	8,000 – 42,000	h_{tp} = f(q'') nucleate boiling dominant h_{tp} independent of x_e, G

Table I.1.1 continued.

Author(s)	Geometry	Fluid(s)	q'' [W/cm^2]	Flow Rate	x_t	h_{tp} [W/m^2 K]	Remarks
Warrier et al. (2002) [15]	d_h = 0.75 mm L = 30.74 cm rectangular 5 parallel	FC84	0 - 5.99	557 - 1600 kg/m^2 s	0.03 – 0.55		$h_{tp} = f(q'', x_t)$
Wen et al. (2004) [16]	d_h = 1.33 mm L = 28.0, 24.8 cm rectangular single	Water	2.6 - 16.0	57 - 211 kg/m^2 s	< 0 – 0.3	14,000 – 29,000	$h_{tp} \propto q''^{0.44}$ nucleate and convective boiling important
Huo et al. (2004) [17]	d = 2.01, 4.26 mm circular, single	R134a	1.3 - 15.0	100 - 500 kg/m^2 s	0 – 0.9	8,000 – 42,000	$h_{tp} = f(q'', x_t)$ nucleate and convective boiling important

Table I.1.2 Contrasting features of present study compared with prior small channel boiling studies.

	Present Study	Most Prior Studies
Application	Compact heat sink(cold plate)	Compact heat exchanger
Channel geometry	231 μm x 713 μm	d_h mostly > 1 mm
	L = 2.53 cm	L >> 10 cm
Heat flux	High	Low
Input heat flux	Uniform across flat surface	By external convection
Ratio of acceleration to total pressure drop	20 ~ 45%	Small to negligible
Working fluid	Environmentally-friendly refrigerant	Ozone-depleting refrigerants

The discrepancy between the two groups may be explained by the different coolants, operating conditions and channel sizes used by different investigators yielding different dominant mechanisms. This important issue will be discussed later in this paper.

As indicated earlier, the primary purpose of the present paper is to explore the two-phase heat transfer characteristics of a refrigerant-cooled micro-channel heat sink. Table 1.2 points out the unique focus of this study compared to prior small channel refrigerant studies. While much of the exiting refrigeration literature concerns long (L > 10 cm) mini-channels (d > 2 mm), the present study concerns a short heat sink (L = 25.27 mm) utilizing parallel micro-channels (231 μm x 713 μm). Furthermore, the heat sink examined in this study serves as a high-heat-flux evaporator (cold plate for electronic or power devices) subjected to a fairly uniform heat flux, while the vast majority of prior small-channel refrigeration research concerns mostly low heat flux evaporators that are heated by external convection. It is a primary goal of the present study to develop a fundamental understanding of dominant mechanisms, and recommend an accurate method for predicting the heat transfer performance of this unique cooling scheme.

I.1.3 System Implementation

While thermal management of high-heat-flux electronic devices has attracted significant attention in recent years, much of the published work concerns mainly the heat removal requirements. The heat is typically removed by a liquid coolant and ultimately rejected to ambient air. As heat flux levels continue to escalate, there is increasing concern over the ability to maintain acceptable device temperatures for an essentially fixed ambient air temperature. This is because of the appreciable thermal resistance comprised of not only the coolant's convection resistance, but the conduction resistance across the device itself and any intermediate bond/solder layers. This points to refrigeration cooling as an effective means for greatly reducing the coolant's temperature and therefore maintaining acceptable device temperatures when dissipating very high heat fluxes. The present study concerns the development of a liquid cooling scheme that capitalizes upon the merits of both high-performance micro-channel flow boiling and refrigeration cooling.

Many researchers have explored the merits of micro-channel heat sinks and demonstrated a notable enhancement in cooling performance compared to other liquid cooling schemes. This was quite evident from an early study by Tuckerman and Pease (1981) who used a single-phase liquid-cooled heat sink. But while their heat sink was quite effective at dissipating the heat, its reliance on sensible heating the coolant resulted in detrimental stream-wise temperature gradients along both coolant and heat sink. Reducing these gradients by increasing the coolant's flow rate was complicated by the appreciable pressure drop associated with micro-channel flow. Bowers and Mudawar (1994) showed how better temperature uniformity can be realized using two-phase micro-channel heat sinks, which remove the heat more isothermally by latent instead of sensible heat.

With its abundance, low cost and superior thermophysial properties, water has been the coolant of choice for many single-phase and two-phase micro-channel heat sink applications [Qu and Mudawar (2003)]. Its drawbacks, however, are (1) poor dielectric

properties, which can produce arcing/shorting in electronic devices, and (2) high saturation temperature. At one atmosphere, the saturation temperature of water (100 °C) precludes maintaining acceptable device temperatures. Lower saturation temperatures are possible at sub-atmospheric pressure, but the low pressures necessary to maintaining acceptable temperatures are known to initiate undesirable bubble nucleation effects [Mikic et al. (1970)], let alone the increased likelihood of air inclusion due to any system leaks.

Dielectric fluorochemical coolants such as FC-72, FC-87 and PF-5052 circumvent the aforementioned arcing/shorting problem. They also possess lower saturation temperatures at one atmosphere. Unfortunately their thermophysical properties are far inferior to those of water, and achieving acceptable device temperatures requires implementing effective surface augmentation techniques and/or supplying the coolant at a relatively high mass velocity [Mudawar (2001)].

Refrigeration cooling resolves the high device temperature concerns as well as provides the added benefits of faster switching time (due to increased electron mobility) and therefore better device performance, as well as reduced current leakage [Schmidt (2000)]. Those combined advantages lead to the introduction of several commercial refrigeration cooled computer systems in last decade [Schmidt (2000)].

With a refrigeration system, the coolant's saturation temperature is greatly decreased, sometimes far below sub-freezing temperatures. However, refrigeration requires increasing operation pressure, which contributes both added cost and complexity to a cooling system.

A primary focus of the present study is to incorporate a two-phase micro-channel heat sink as an evaporator in a vapor compression refrigeration system. This study will utilize the newly developed pressure drop and two-phase heat transfer coefficient correlations to explore several fundamental thermal aspects of the heat sink that were passed over in past commercial trial. Examined here is the effectiveness of the heat sink at removing high heat fluxes while maintaining low device temperatures, as well as the complex relationship between device heat flux, device temperature and coolant operating

conditions in the evaporator, and means of optimizing operating conditions in pursuit of better overall cooling performance and sound refrigeration system operation.

I.1.4 Research Objectives

The present research aims to explore the hydraulic and thermal characteristics of a two-phase micro-channel heat sink incorporated as an evaprator in a refrigeration cooling system. The objectives of this study are as follows:

- Evaluate the existing two-phase pressure drop estimation models for micro-channel heat sink in refrigeration cooling application.
- Develop the new reliable correlation schemes to predict the two-phase pressure drop in micro-channel heat sink.
- Investigate the pressure drop characteristics in micro-channel heat sink as an evaporator in refrigeration cycle.
- Evaluate the existing both macro and micro scale boiling heat transfer correlations with experimental data obtained from the refrigerant micro-channel heat sink.
- Demonstrate the two-phase flow patterns inside refrigerant micro-channel heat sink and investigate the related flow physics.
- Derive the physically reasonable boiling heat transfer correlation for two-phase micro-channel heat sink.
- Make sure the predictability of newly suggested correlations for two-phase pressure drop and boiling heat transfer with the fluid of different features.

I.2. EXPERIMENTAL METHODS

I.2.1 Apparatus and Measurement Techniques

Figure I.2.1 shows the test facility constructed for this study resembled a conventional refrigeration cycle save for using the micro-channel evaporator. The working fluid used in this study, R134a, is an environmentally friendly non-ozone-depleting HFC refrigerant with overwhelming popularity in most domestic refrigeration and air conditioning applications. Vapor compression was achieved with a DC rotary compressor whose power was determined from its measured current and voltage input. Heat was rejected from the loop via a conventional fin-tube condenser fitted with a cross-flow fan. The fan speed was controlled with a variable voltage transformer that helped modulate the subcooling of the two-phase mixture exiting the condenser. Throttling from high to low pressure was achieved by a manual metering valve situated upstream of the micro-channel evaporator test section.

Figure I.2.2 shows the primary components of the test section: a transparent polycarbonate cover plate, a G-10 fiberglass housing, an oxygen-free copper micro-channel heat sink, three cartridge heaters, and a G-10 support plate. The micro-channels were formed by cutting 53 of 231 μm wide and 713 μm deep micro-slots into the 25.3 mm × 25.3 mm top surface of the copper heat sink. The polycarbonate plastic (Lexan) cover formed the top surface for the micro-channels. The G-10 housing included upstream and downstream plenums to ensure uniform flow distribution between micro-channels and facilitate pressure and temperature measurement both upstream and downstream of the micro-channels. The copper heating block was encased in an insulating blanket to reduce heat loss to the ambient. Heat was supplied by the cartridge

heaters that were embedded beneath the micro-channels; these heaters were powered by a variable voltage transformer.

Two type-T thermocouples were inserted in the inlet and outlet plenums to measure fluid temperature at those locations. Another type-K thermocouple was inserted in the copper block halfway along the micro-channels. An absolute pressure transducer measured the inlet plenum pressure and a differential pressure transducer the pressure drop between the inlet and outlet plenums. Additional type-T thermocouples and absolute pressure transducers were located both downstream of the compressor and upstream of the throttling valve. A precision power meter connected to the cartridge heaters' variable voltage transformer was used to measure heat input to the coolant in the evaporator. All thermocouple and pressure transducer measurement signals were transferred to an NI-SCXI signal conditioner interfaced to data acquisition PC. The flow rate of R134a entering the micro-channel evaporator was measured by a glass rotameter situated downstream of the condenser, which also served as a visual indicator of liquid state at that location. Figure I.2.3 depicts photos of key components of the test facility.

The rotameter provided better than 2% accuracy in flow rate measurement. Errors in the pressure transducer and thermocouple measurements were less than 0.5% and ±0.3°C, respectively. Heat loss from the heat sink was estimated at less than 4% of the electrical power input.

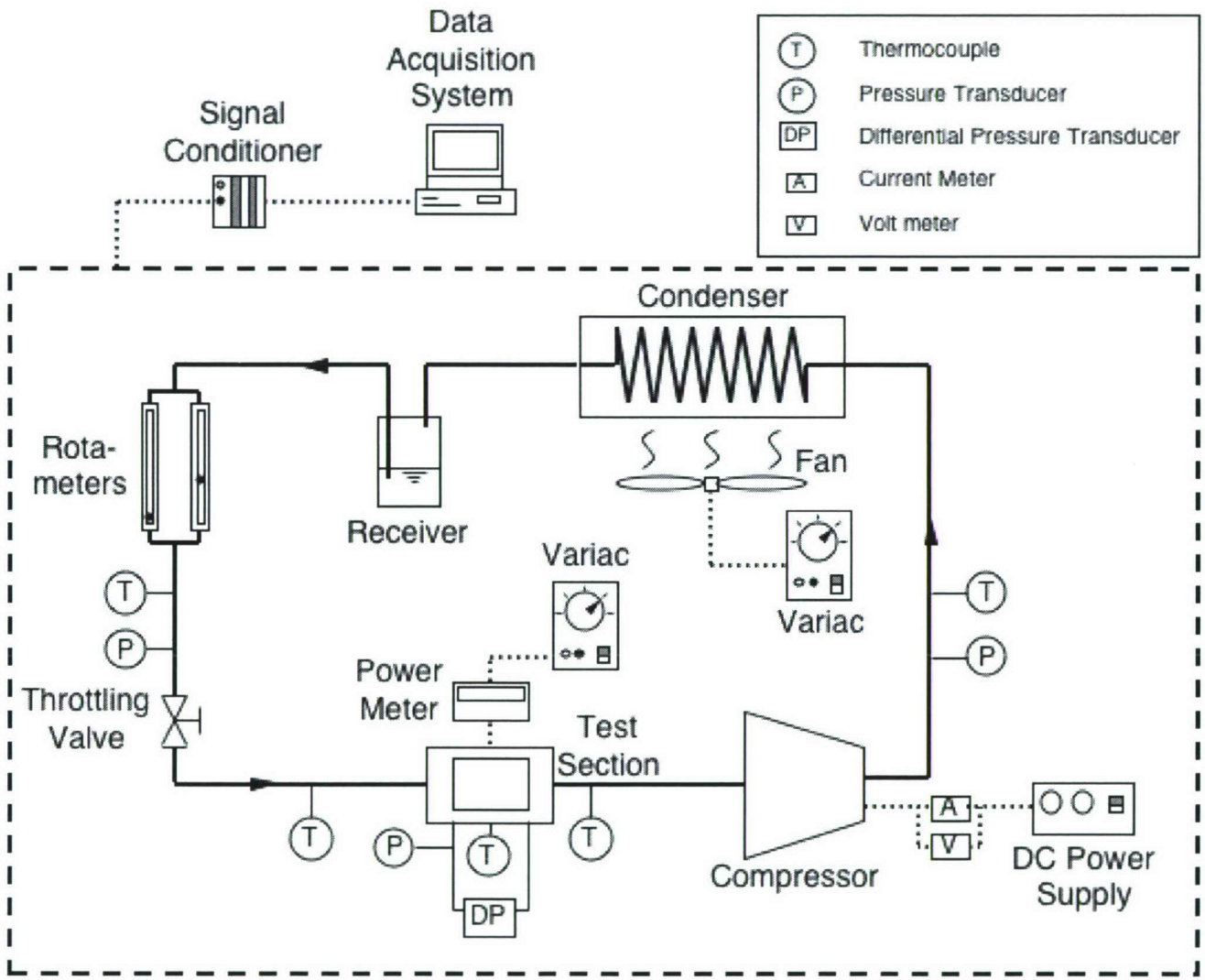

Figure I.2.1 Schematic of test loop.

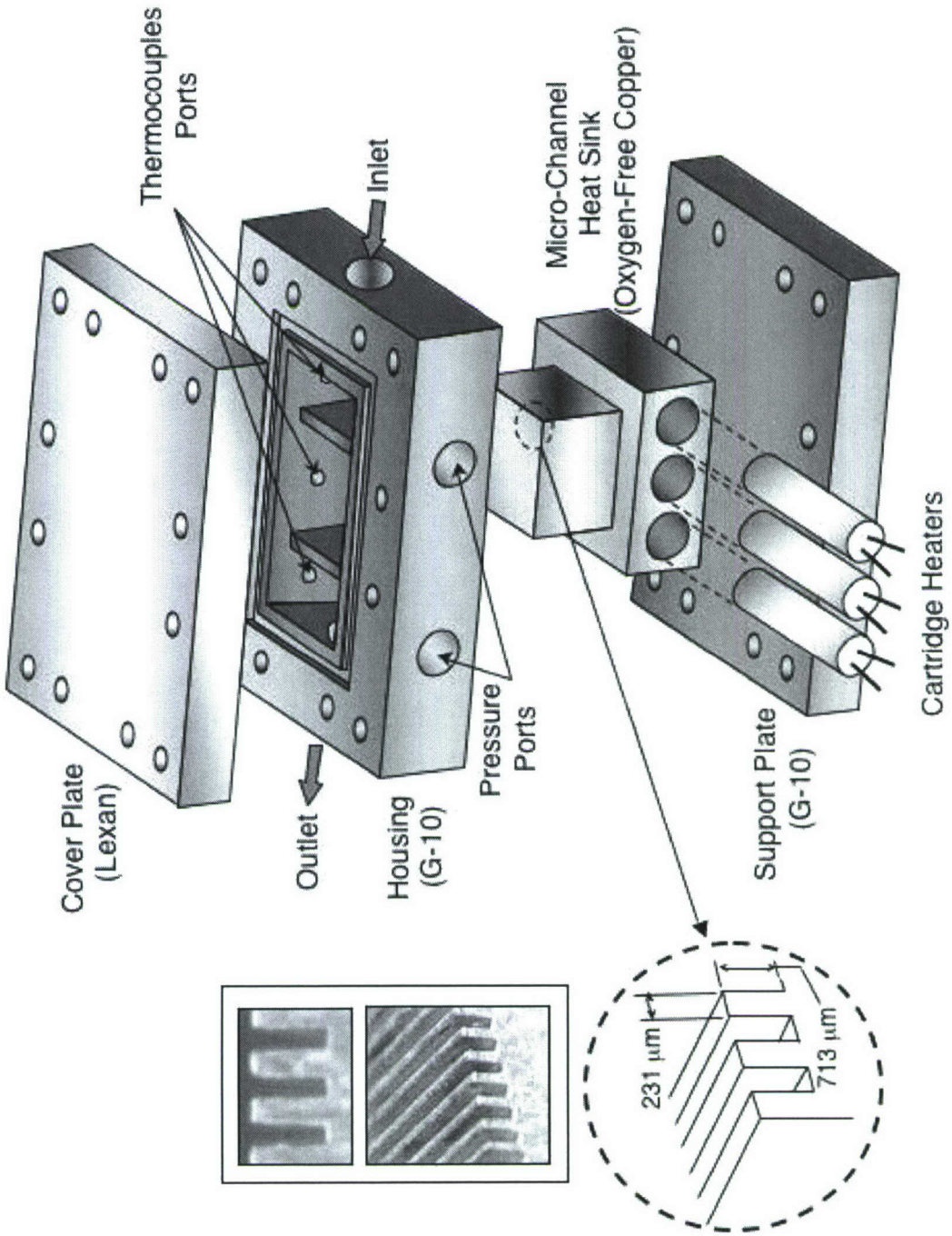

Figure I.2.2 Construction of micro-channel evaporator test section.

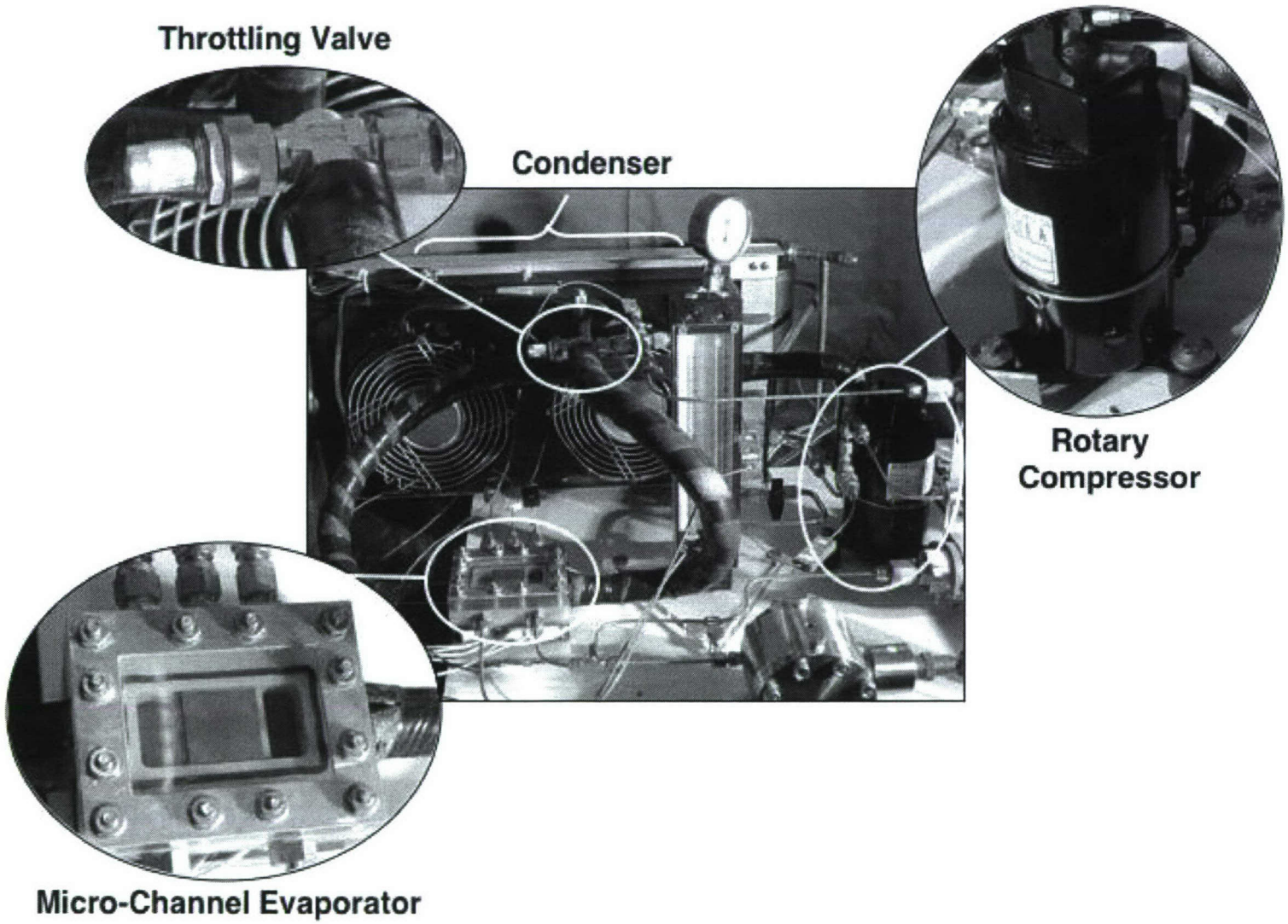

Figure I.2.3 Pictures of facility and key components.

I.2.2 Operatiing Conditions

The refrigerant left the compressor in superheated vapor state and was returned to subcooled liquid after passing through the condenser. Afterwards, the liquid was converted to a two-phase mixture by flashing across the throttling valve. The two-phase mixture entered the evaporator and was converted to superheated vapor before entering the compressor and repeating the cycle.

The mass flow rate of refrigerant entering the evaporator was calculated as the product of volumetric flow rate of liquid measured by the rotameter, and the density of liquid calculated from the temperature and pressure measurements. Since the throttling process is isenthalpic, the evaporator inlet enthalpy was determined from the liquid temperature and pressure measured downstream of the condenser. Using this enthalpy value and the evaporator measured inlet temperature or pressure provided accurate determination of the evaporator's inlet quality, $x_{e,in}$. The evaporator outlet quality was determined from the following energy balance:

$$x_{e,out} - x_{e,in} = \frac{4q'' L}{G d_h h_{fg}}. \tag{I.2.1}$$

Experimental operating conditions spanned the following ranges: inlet quality of $x_{e,in}$ = 0.001 - 0.25, outlet quality of $x_{e,out}$ = 0.49 - superheat, mass velocity of G = 127 - 654 kg/m^{2}s, heat flux of q'' = 159 - 938 kW/m^2 (15.9 - 93.8 W/cm^2), and inlet pressure of P_{in} = 1.44 - 6.60 bar.

I.3 TWO-PHASE PRESSURE DROP AND FEATURES

I.3.1 Determination of Pressure Drop

The evaporator pressure drop measured by the differential pressure transducer includes the sudden contraction loss at the micro-channel inlet and sudden expansion recovery at the outlet. Within the micro-channels, the two-phase pressure drop consists of frictional and accelerational components. Should the two-phase mixture undergo complete conversion to vapor within the micro-channel, a pressure drop corresponding to pure vapor flow would also be incurred in the downstream region of the micro-channels. In this case, the total pressure drop between the upstream and downstream plenums can be expressed as

$$\Delta P_{tot} = \Delta P_c + (\Delta P_f + \Delta P_a)_{tp} + \Delta P_{sp,g} - \Delta P_e. \tag{I.3.1}$$

The contraction pressure loss and expansion recovery were determined from the following relations [Collier and Thome (1994)]:

$$\Delta P_c = \frac{G^2 v_f}{2}\left[\left(\frac{1}{C_c}-1\right)^2 + \left(1-\frac{1}{\sigma_c^2}\right)\right]\left[1+\frac{v_{fg}x_{e,in}}{v_f}\right] \tag{I.3.2}$$

$$\text{and} \quad \Delta P_e = G^2\sigma_e(1-\sigma_e)v_f\left[1+\frac{v_{fg}x_{e,out}}{v_f}\right]. \tag{I.3.3}$$

The contraction coefficient C_c is a function of the contraction ratio σ_c. If the refrigerant exits the micro-channels as pure vapor, the exit quality $x_{e,out}$ in the pressure recovery term should be set equal to unity.

When the refrigerant is completely converted into vapor within the micro-channel, the pressure drop for the vapor flow region can be determined form the following relation [Shah and London (1978), Incropera and Dewitt (2002)]:

$$\Delta P_{sp,g} = \frac{2L_{sp}}{d_h} f_{sp,g} G^2 v_g, \tag{I.3.4}$$

where

$$f_{sp,g} Re_g = 24\left[1 - 1.3553\beta + 1.9467\beta^2 - 1.7012\beta^3 + 0.9564\beta^4 - 0.2537\beta^5\right]$$

$$\text{for } Re_g < 2{,}000, \tag{I.3.5a}$$

$$f_{sp,g} = 0.079 Re_g^{-0.25} \text{ for } 2{,}000 < Re_g < 20{,}000, \tag{I.3.5b}$$

and

$$f_{sp,g} = 0.046 Re_g^{-0.2} \text{ for } 20{,}000 < Re_g \ . \tag{I.3.5c}$$

The remaining contributions to the evaporator pressure drop are the two-phase frictional and accelerational components. These are discussed in the next section.

I.3.2 Two Phase Pressure Drop Model

I.3.2.1 Homogeneous Equilibrium Model (HEM)

The homogeneous equilibrium model is based on the assumption that the two-phase mixture behaves as a pseudo single-phase fluid with mean properties that are weighted relative to vapor and liquid content, and that only latent heat may be exchanged between the phases. Property variations resulting from pressure changes along the micro-channel result in complicating terms that account for kinetic energy changes, flashing, and compressibility [Bowers and Mudawar (1994)]. The resulting pressure gradient may be expressed as

$$-\left(\frac{dP}{dz}\right)_{tp} = \frac{\dfrac{2f_{tp}}{d_h} G^2 (v_f + x_e v_{fg}) + \dfrac{4q'' G v_{fg}}{d_h [h_{fg} + G^2 v_{fg}\{x_e v_g + (1 - x_e) v_f\}]}}{1 + G^2 \left\{ x_e \dfrac{dv_g}{dP} + (1 - x_e) \dfrac{dv_f}{dP} \right\} \left[1 - \dfrac{G^2 v_{fg}\{x_e v_g + (1 - x_e) v_f\}}{h_{fg} + G^2 v_{fg}\{x_e v_g + (1 - x_e) v_f\}} \right] - \left[\dfrac{G^2 v_{fg} \left\{ x_e \dfrac{dh_g}{dP} + (1 - x_e) \dfrac{dh_f}{dP} \right\}}{h_{fg} + G^2 v_{fg}\{x_e v_g + (1 - x_e) v_f\}} \right]}.$$

(I.3.6)

The first term in the numerator of Eq. (I.3.6) is the frictional gradient and the second the accelerational. The denominator includes kinetic energy, flashing and compressibility terms. The two-phase pressure drop can be determined by integrating Eq. (I.3.6) numerically along the stream-wise direction.

$$\Delta P_{tp} = \int_0^{L_{tp}} -\left(\frac{dP}{dz}\right)_{tp} dz \quad . \tag{I.3.7}$$

A key unknown in the two-phase pressure drop calculation using HEM is the two-phase friction factor, f_{tp}, which is a function of the two-phase Reynolds number

$$Re_{tp} = \frac{G\, d_h}{\mu_{tp}}. \tag{I.3.8}$$

Table I.3.1 shows the relations used to determine f_{tp} as well as several popular models of two-phase mixture viscosity, μ_{tp}.

Figure I.3.1 compares pressure drop predictions based on HEM (in addition to ΔP_c, $\Delta P_{sp,g}$ and ΔP_e) and each of the two-phase viscosity models with the experimental data. The Mean Absolute Error (MAE), defined as

$$MAE = \frac{1}{N}\sum\left[\frac{\left|\Delta P_{pred} - \Delta P_{exp}\right|}{\Delta P_{exp}} \times 100\right] , \tag{I.3.9}$$

was used to estimate the accuracy of model predictions. Figure I.3.1 shows the HEM models yield appreciable deviation from the data. The trend predicted by the Cicchitti two-phase viscosity model, Fig. I.3.1 (c), is somewhat different from that of the other

Table I.3.1 Two-phase mixture viscosity models adopted in the homogeneous equilibrium flow model.

	$f_{tp}Re_{tp} = 24\left[1 - 1.3553\beta + 1.9467\beta^2 - 1.7012\beta^3 + 0.9564\beta^4 - 0.2537\beta^5\right]$ for $Re_{tp} < 2{,}000$
	$f_{tp} = 0.079Re_{tp}^{-0.25}$ for $2{,}000 < Re_{tp} < 20{,}000$
	$f_{tp} = 0.046Re_{tp}^{-0.2}$ for $20{,}000 < Re_{tp}$
Author(s)	**Two-Phase Mixture Viscosity Model**
McAdams [Collier and Thome (1994)]	$\frac{1}{\mu_{tp}} = \frac{x_e}{\mu_g} + \frac{(1-x_e)}{\mu_f}$
Ackers [Yan and Lin (1998)]	$\mu_{tp} = \frac{\mu_f}{\left[(1-x_e) + x_e\left(\frac{\rho_f}{\rho_g}\right)^{0.5}\right]}$
Cicchitti et al. [Collier and Thome (1994)]	$\mu_{tp} = x_e\mu_g + (1-x_e)\mu_f$
Dukler [Collier and Thome (1994)]	$\mu_{tp} = \rho_{tp}\left[x_e v_g \mu_g + (1-x_e)v_f\mu_f\right]$
Beattie & Whalley (1982)	$\mu_{tp} = \omega\,\mu_g + (1-\omega)(1+2.5\omega)\mu_f$ $\omega = \frac{x_e v_g}{v_f + x v_{fg}}$
Lin et al. (1991)	$\mu_{tp} = \frac{\mu_f\mu_g}{\left[\mu_g + x_e^{1.4}\left(\mu_f - \mu_g\right)\right]}$

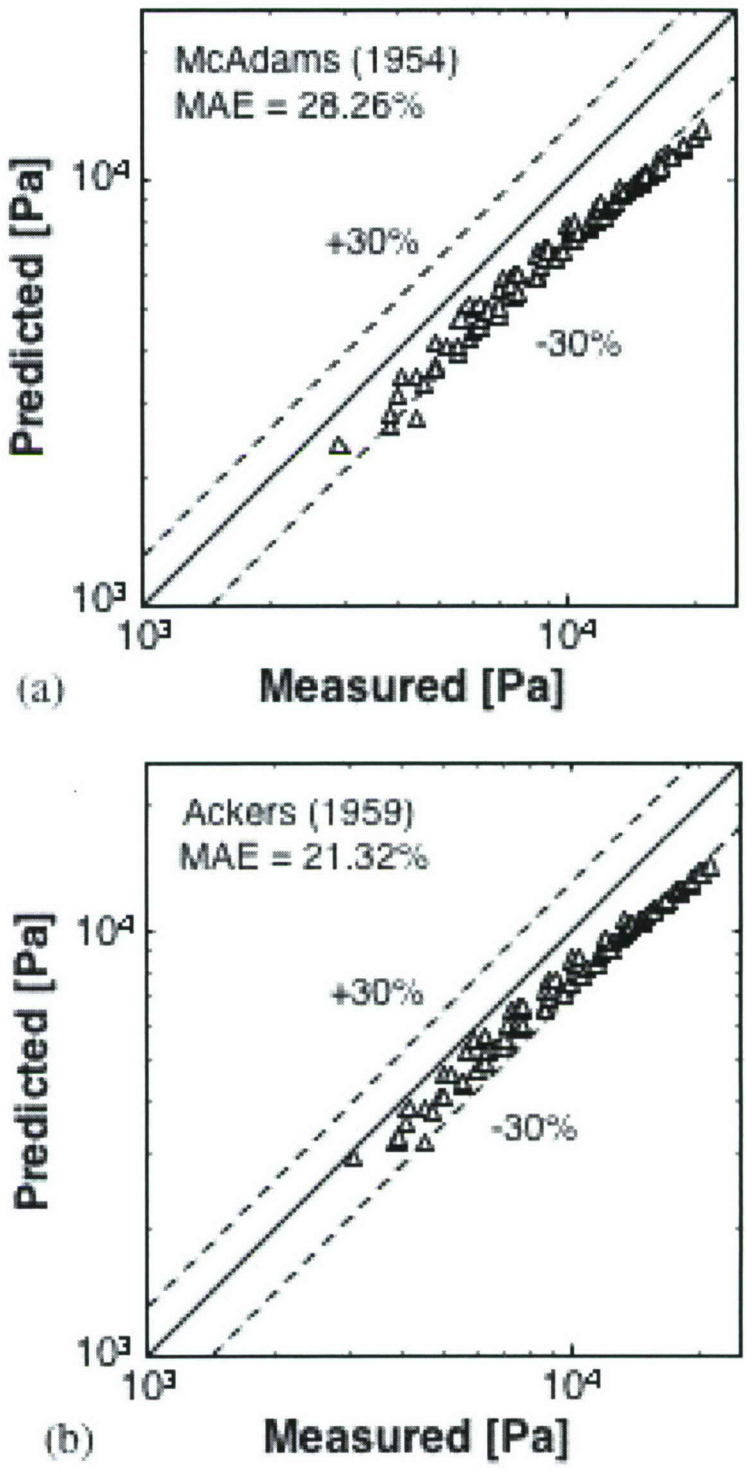

Figure I.3.1 Comparison of present R134a pressure drop data with homogeneous equilibrium model predictions based on two-phase viscosity models by (a) McAdams (1954), (b) ckers (1959), (c) Cicchitti et al. (1960), (d) Dukler (1964), (e) Beattie and Whalley (1982), and (f) Lin et al. (1991).

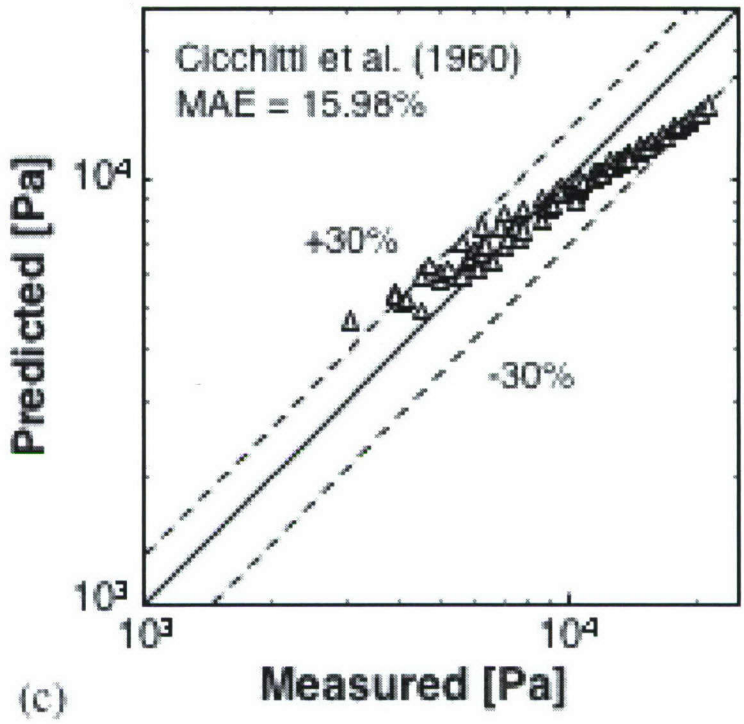

(c)

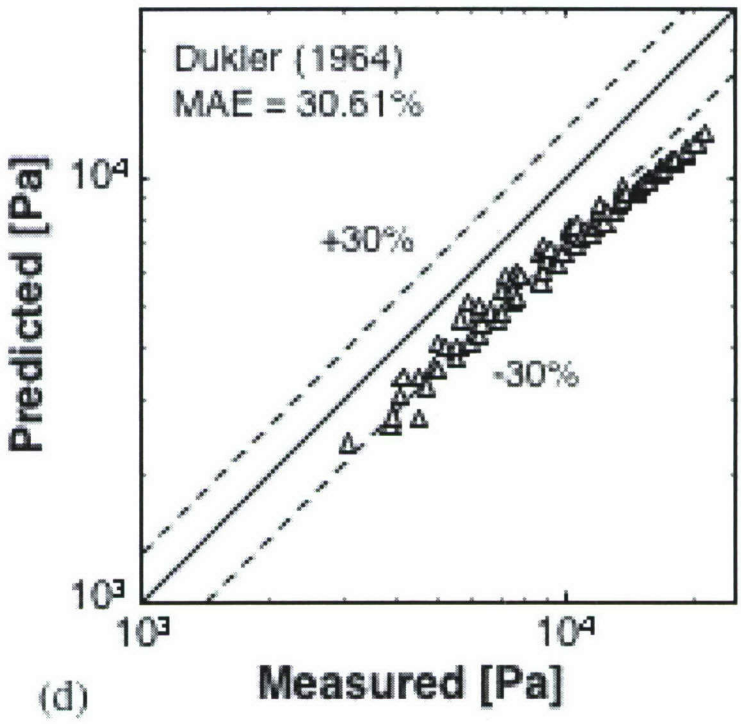

(d)

Figure I.3.1 continued.

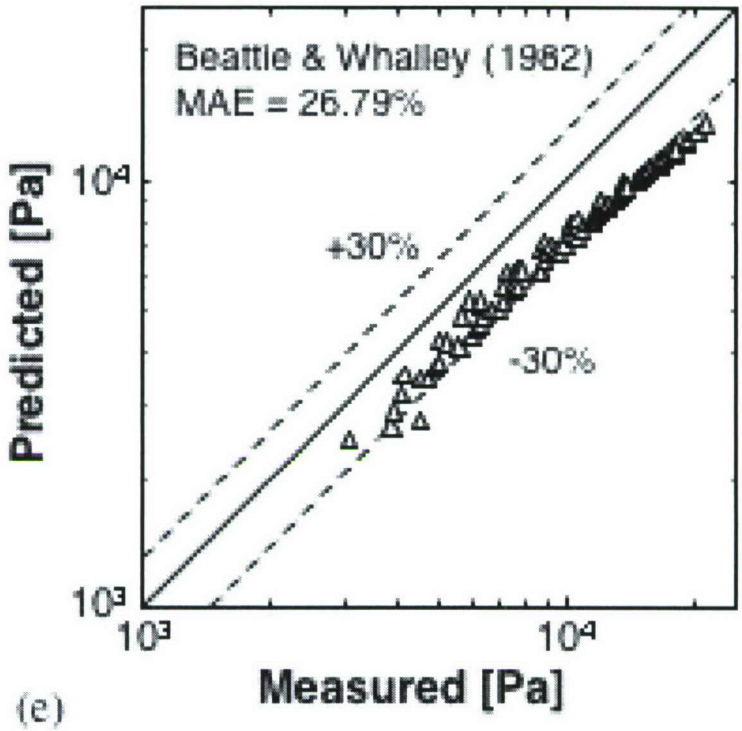

(e)

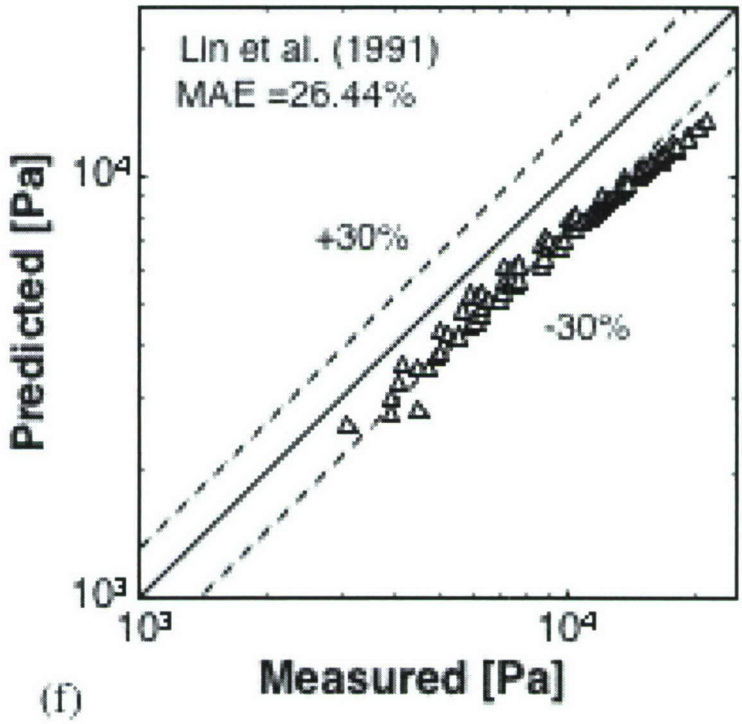

(f)

Figure I.3.1 continued.

models because this model is quality weighed and therefore provides significanty higher estimates of two-phase mixture viscosity at low quality than the other models. Since the low exit quality data are associated with smaller pressure drop, the Cicchitti model overpredicts these data but underpredicts the high exit quality data. The combination of overprediction at low quality and underprediction at high quality yields a relatively favorable MAE for the Ciccitti model. Nonetheless, Fig. I.3.1(c) shows this model does not capture the true pressure drop trend.

I.3.2.2 Separated Flow Model (SFM)

Table I.3.2 summarizes relations that were used to determine the two-phase frictional pressure drop based on the separated flow model, which include two popular macro-channel correlations (Lockhart-Martinelli and Friedel), and three recent small-channel correlations.

The accelerational two-phase pressure drop was expressed in terms of the evaporator's inlet and outlet conditions [Lockhart and Martinelli (1949)].

$$\Delta P_a = G^2 \left\{ \left[\frac{v_g x_{e,out}^2}{\alpha_{out}} + \frac{v_f (1 - x_{e,out})^2}{(1 - \alpha_{out})} \right] - \left[\frac{v_g x_{e,in}^2}{\alpha_{in}} + \frac{v_f (1 - x_{e,in})^2}{(1 - \alpha_{in})} \right] \right\}, \tag{I.3.10}$$

where the void fraction was determined from Zivi's (1964) popular relation

$$\alpha = \left[1 + \left(\frac{1 - x_e}{x_e} \right) \frac{v_f}{v_g} \right]^{-1}. \tag{I.3.11}$$

Figure I.3.2 compares pressure drop predictions of the different separated flow correlations with the experimental data. Interestingly, the predictions of the first two macro-channel correlations are not as poor as first thought. The small-channel correlations show appreciable deviation from the data.

Table I.3.2 Two-phase frictional pressure drop correlations based on separated flow model and corresponding MAE for R134a.

Author(s)	Remarks	Frictional Pressure Drop Correlation	MAE [%]
Lockhart & Martinelli (1949)	Fluids: Water, benzene, kerosene, Oil, etc. d_h = 1.49 - 25.83 mm	$\Delta P_f = \frac{2G^2 L_{tp}}{d_h x_{e,out}} \int_{x_{e,in}}^{x_{e,out}} f_f (1-x_e) v_f \phi_f^2 dx_e$ $\phi_f^2 = 1 + \frac{C}{X} + \frac{1}{X^2}, \quad X^2 = \left[(dp/dz)_f \Big/ (dp/dz)_g \right]$ $C = 5$ (laminar liquid – laminar vapor), $C = 10$ (turbulent liquid – laminar vapor), $C = 12$ (laminar liquid – turbulent vapor), $C = 20$ (turbulent liquid – turbulent vapor)	14.90
Friedel [Collier and Thome (1994)]	d_h = > 4 mm	$\Delta P_f = \frac{2 f_{fo} G^2 L_{tp} v_f}{d_h x_{e,out}} \int_{x_{e,in}}^{x_{e,out}} \phi_{fo}^2 dx_e$ $\phi_{fo}^2 = A_1 + \frac{3.24 A_2 A_3}{Fr_{tp}^{0.045} We_{tp}^{0.035}}$ $A_1 = (1-x)^2 + x^2 \left(\frac{\rho_f f_{go}}{\rho_g f_{fo}} \right), \quad A_2 = x^{0.78}(1-x)^{0.224}$, $A_3 = \left(\frac{\rho_f}{\rho_g} \right)^{0.91} \left(\frac{\mu_g}{\mu_f} \right)^{0.19} \left(1 - \frac{\mu_g}{\mu_f} \right)^{0.7}$ $Fr_{tp} = \frac{G^2}{g d_h \bar{\rho}^2}$, $We_{tp} = \frac{G^2 d_h}{\bar{\rho} \sigma}$, $\bar{\rho} = \frac{1}{x_e v_g + (1-x_e) v_f}$	24.00
Mishima & Hibiki (1996)	Fluid: Air-Water mixture d_h = 1 - 4 mm	$\Delta P_f = \frac{2G^2 L_{tp}}{d_h x_{e,out}} \int_{x_{e,in}}^{x_{e,out}} f_f (1-x_e) v_f \phi_f^2 dx_e$ $\phi_f^2 = 1 + \frac{C}{X} + \frac{1}{X^2}, \quad X^2 = \left[(dp/dz)_f \Big/ (dp/dz)_g \right]$ $C = 21\left[1 - \exp(-0.319 \cdot d_h)\right]; \quad d_h : [mm]$	34.37

Table I.3.2 continured.

Author(s)	Remarks	Frictional Pressure Drop Correlation	MAE [%]
Lee & Lee (2001)	Fluid: Air-Water mixture d_h= 0.78, 6.67 mm	$\Delta P_f = \frac{2G^2 L_{tp}}{d_h x_{e,out}} \int_{x_{e,in}}^{x_{e,out}} f_f (1-x_e) v_f \phi_f^2 dx_e$ $\phi_f^2 = 1 + \frac{C}{X} + \frac{1}{X^2}, X^2 = \left[(dp/dz)_f \Big/ (dp/dz)_g \right]$ $C = c_1 \lambda^{c_2} \psi^{c_3} Re_{fo}^{c_4}, \quad \lambda = \frac{\mu_f^2}{\rho_f \sigma d_h}, \quad \psi = \frac{\mu_f j_f}{\sigma},$ c_1, c_2, c_3, c_4 from Table 4 in Lee & Lee (2001)	16.04
Zhang & Webb (2001)	Fluids: R134a, R22, R404a d_h= 2.13 mm	$\Delta P_f = \frac{2 f_{fo} G^2 L_{tp} v_f}{d_h x_{e,out}} \int_{x_{e,in}}^{x_{e,out}} \phi_{fo}^2 dx_e$ $\phi_{fo}^2 =$ $(1-x_e)^2 + 2.87 x^2 \left(\frac{P}{P_c} \right)^{-1}$ $+1.68 x_e^{0.8} (1-x_e)^{0.25} \left(\frac{P}{P_c} \right)^{-1.64}$	50.07

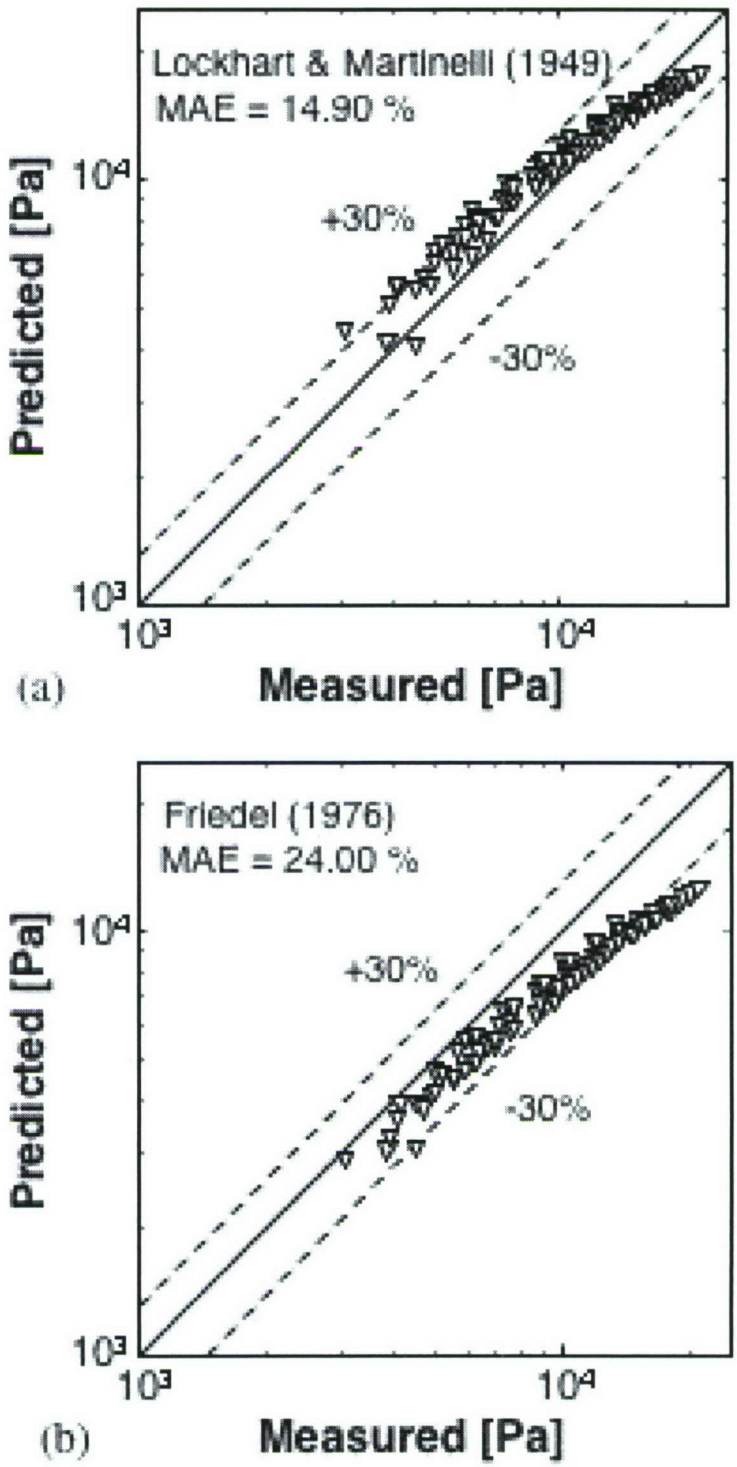

Figure I.3.2 Comparison of present R134a pressure drop data with separated flow model predictions based on correlations by (a) Lockhart and Martinelli (1949), (b) Friedel [Collier and Thome (1994)], (c) Mishima and Hibiki (1996), (d) Lee and Lee (2001), and (e) Zhang and Webb (2001).

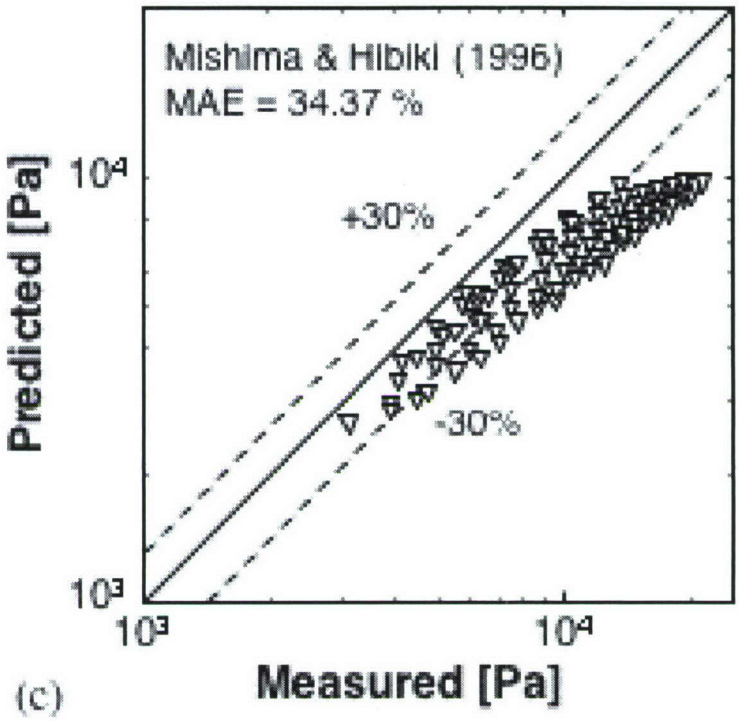

(c)

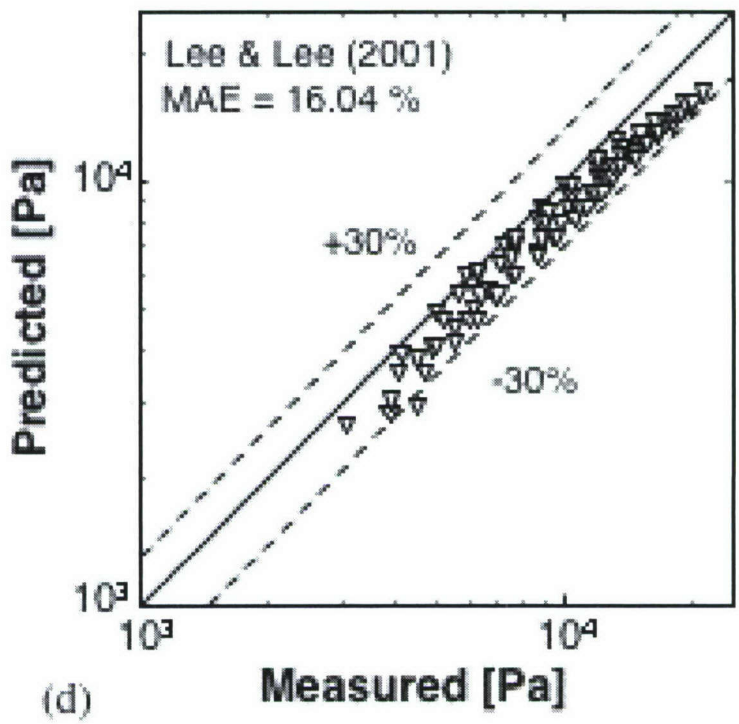

(d)

Figure I.3.2 continued.

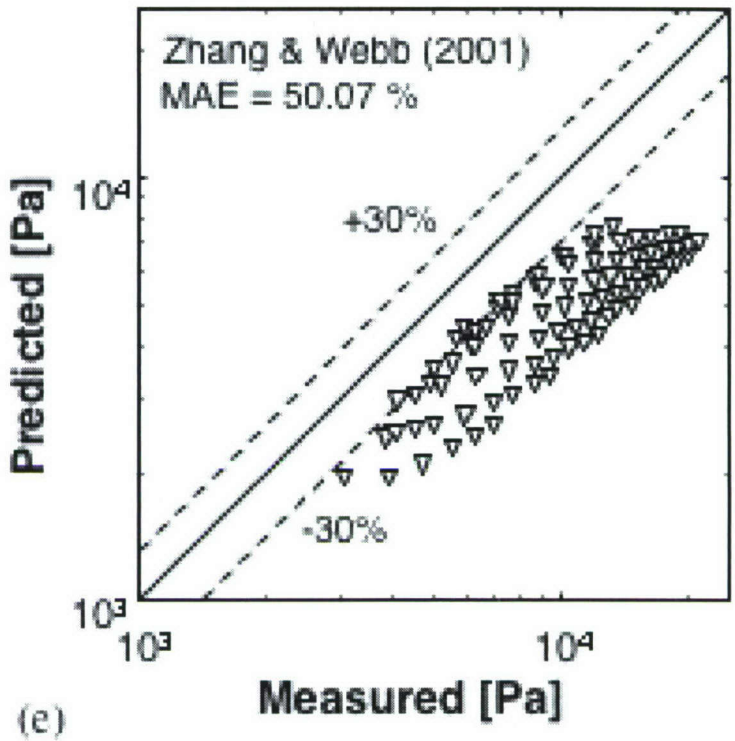

Figure I.3.2 continued.

I.3.3 New Correlation

A new approach was developed to improve the accuracy of pressure drop prediction in two-phase micro-channels. Since the bubbly and churn flow patterns are rarely detected in high-flux micro-channel flow [Kawahara et al. (2002), Qu and Mudawar (2003)], the separated flow model was deemed more appropriate than the homogeneous. This is especially the case with the present R134a experiments were the fluid entered the micro-channels as a two-phase mixture. Video imaging in the present study proved the flow was predominantly slug or annular, especially at high heat fluxes.

In both the slug and annular regimes, mass transfer by liquid breakup and deposition is highly influenced by surface tension. A new parameter is therefore sought to incorporate this effect in the separated flow model. Lee and Lee (2001) used the same rationale and suggested incorporating several dimensionless groups (see Table I.3.2) in the two-phase multiplier relation. As shown in Fig. I.3.2(d), their approach showed more favorable predictions of the present R134a data than the other two small-channel correlations.

A more mechanistic approach is adopted in the present study. It is assumed the added complexity of two-phase flow in a micro-channel is the net result of interactions between liquid inertia, liquid viscous force, and surface tension. Two key measures of these interactions are the Reynolds and Weber numbers based on liquid properties.

$$Re_{fo} = \frac{G d_h}{\mu_f} \tag{I.3.12a}$$

and

$$We_{fo} = \frac{v_f G^2 d_h}{\sigma} \quad . \tag{I.3.12b}$$

The two-phase pressure drop multiplier

$$\phi_f^2 = 1 + \frac{C}{X} + \frac{1}{X^2} \tag{I.3.13}$$

is modified with a new dimensionless parameter defined as

$$C = c_1 Re_{fo}^{c_2} We_{fo}^{c_3} . \tag{I.3.14}$$

To enhance the predictive capability of the new correlation, both the present R134a data and prior micro-channel water data of Qu and Mudawar (2003) were

examined. Large differences between the thermophysical properties of the two coolants were deemed highly effective at broadening the application range of the new correlation. Another key difference between the two data sets is both the liquid and vapor flows are laminar for the water data, while low viscosity rendered the vapor flow turbulent for R134a. Typical micro-channel operating conditions rarely produce turbulent liquid flow. Therefore, two separate correlations were derived for C based on the flow states of the liquid and vapor,

$$C_{vv} = 2.16\,Re_{fo}^{0.047}\,We_{fo}^{0.60} \quad \text{(laminar liquid-laminar vapor)} \qquad \text{(I.3.15a)}$$

$$C_{vt} = 1.45\,Re_{fo}^{0.25}\,We_{fo}^{0.23} \quad \text{(laminar liquid-turbulent vapor)} \qquad \text{(I.3.15b)}$$

Notice the stronger effect of surface tension where both liquid and vapor are laminar.

Figure I.3.3(a) shows excellent agreement of the pressure drop predictions based on the new correlation with the R134a data, both in terms of MAE and general trend. The largest deviation is concentrated in the low mass flux and low heat flux region where both the heat loss (which influences the accuracy of the heat flux used in the pressure drop model) and the flow rate measurement uncertainty are greatest.

Figure I.3.3(b) shows the present correlation is also very effective at predicting the micro-channel water data of Qu and Mudawar (2003).

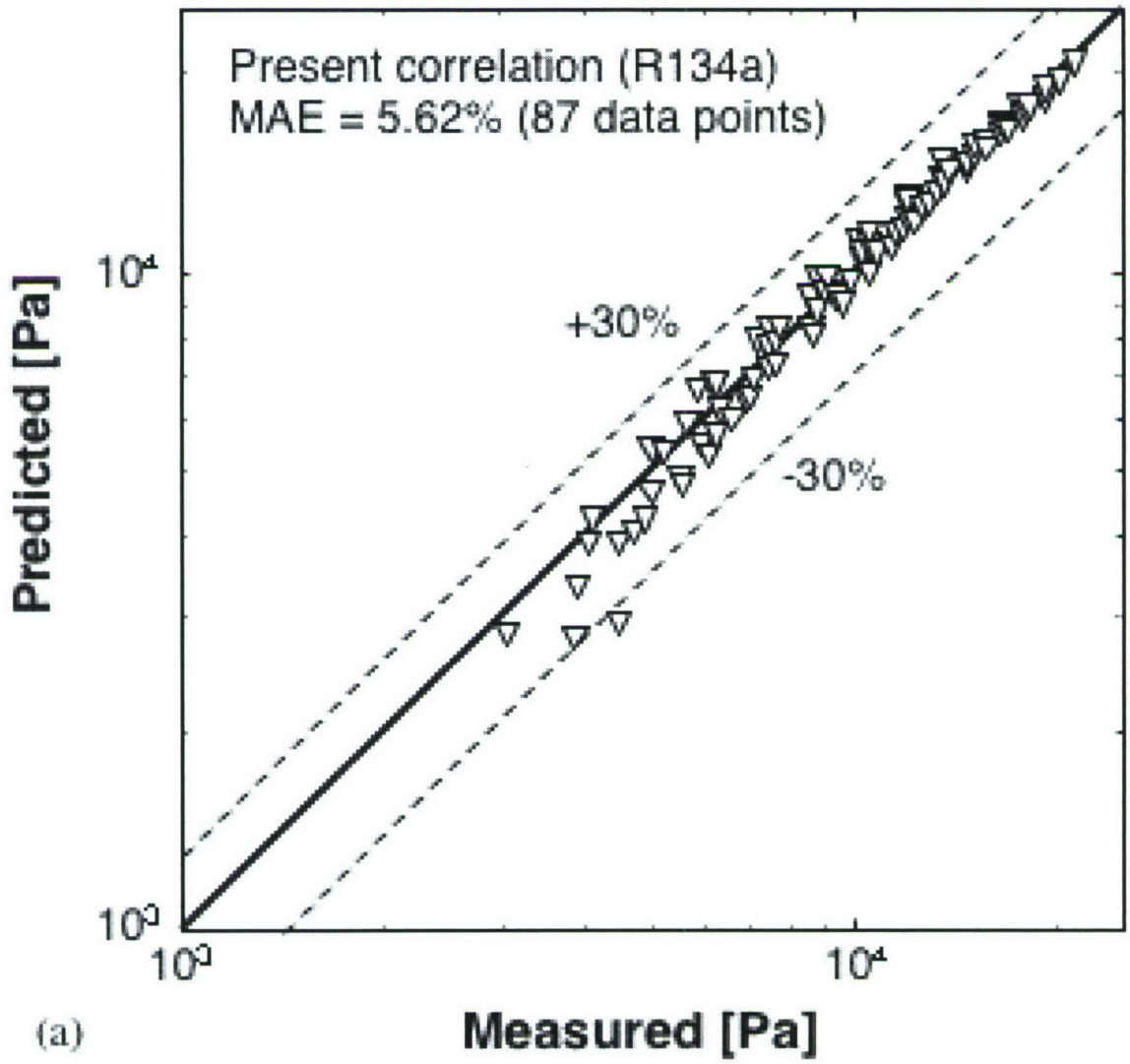

Figure I.3.3 Comparison of new correlation predictions with (a) present R134a data and (b) Qu and Mudawar's (2003) micro-channel water data.

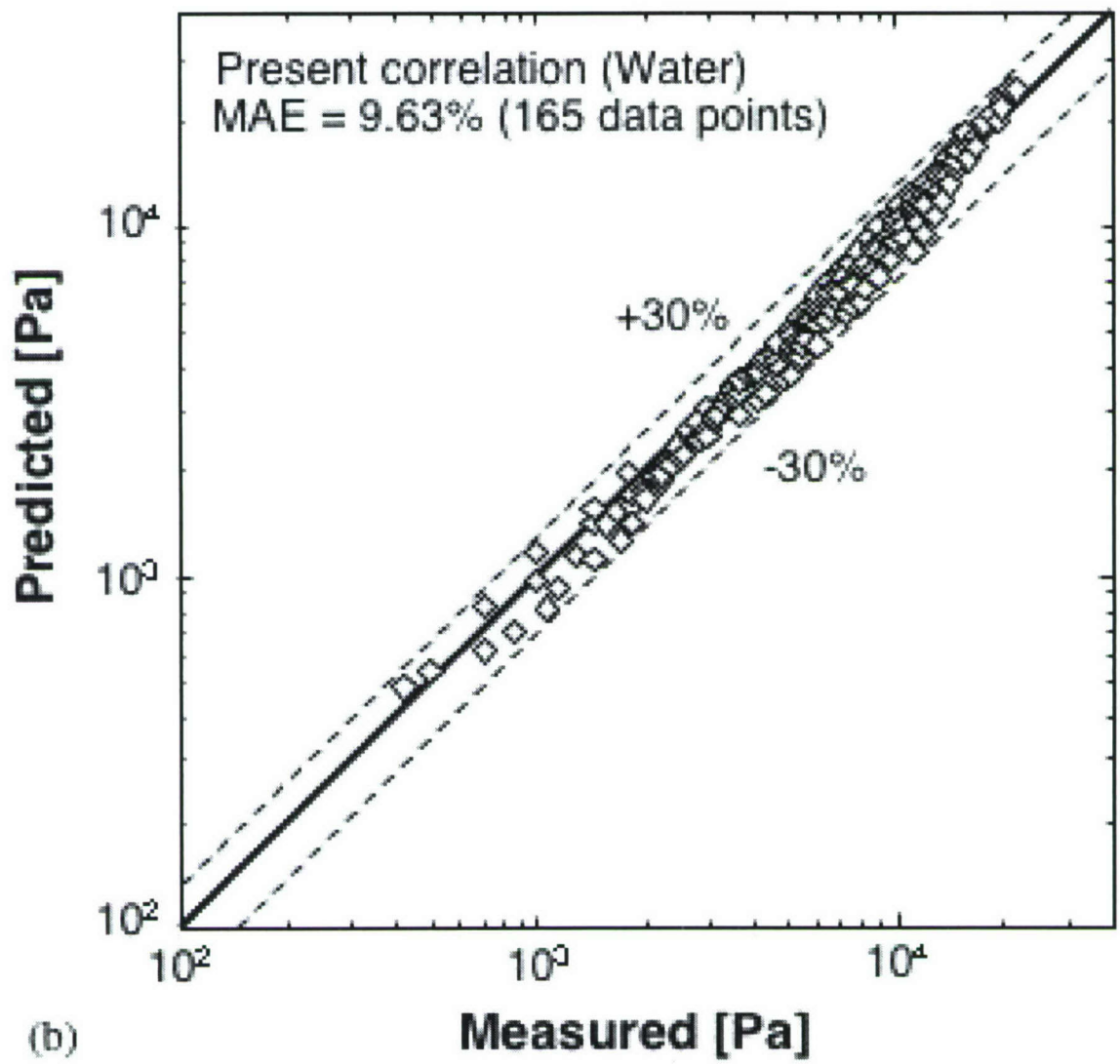

Figure I.3.3 continured.

I.3.4 Dominant Features of Two-Phase Pressure Drop

The newly developed correlation was used to explore several important trends concerning pressure drop in the present R134a study. Figure I.3.4(a) shows, for a constant heat flux, the two-phase pressure drop decreases with increasing outlet quality due mostly to decreasing mass velocity. This decrease appears to subside around an exit quality value of unity. Figure I.3.4(b) shows increasing heat flux for a constant mass velocity increases pressure drop up to a particular heat flux value beyond which pressure drop becomes constant or slightly decreases.

These trends can be explained by exploring the variations of individual components of pressure drop. Figure I.3.5 shows the contributions of these components to total pressure drop. For a constant mass velocity, the two-phase frictional and accelerational losses both increase with increasing heat flux up to a particular heat flux value corresponding to complete conversion into vapor. Beyond this point, the two-phase frictional loss decreases as the two-phase region begins to occupy a smaller portion of the channel length. However, the accelerational loss becomes constant beyond the same point as the flow is converted completely into vapor. Since the downstream portion of the channel is now occupied mostly by vapor, the decreased two-phase frictional loss is compensated for by a measurable increase in the single-phase vapor pressure loss. This explains why the total pressure drop becomes constant or decreases slightly with increasing heat flux beyond the point of full conversion into vapor.

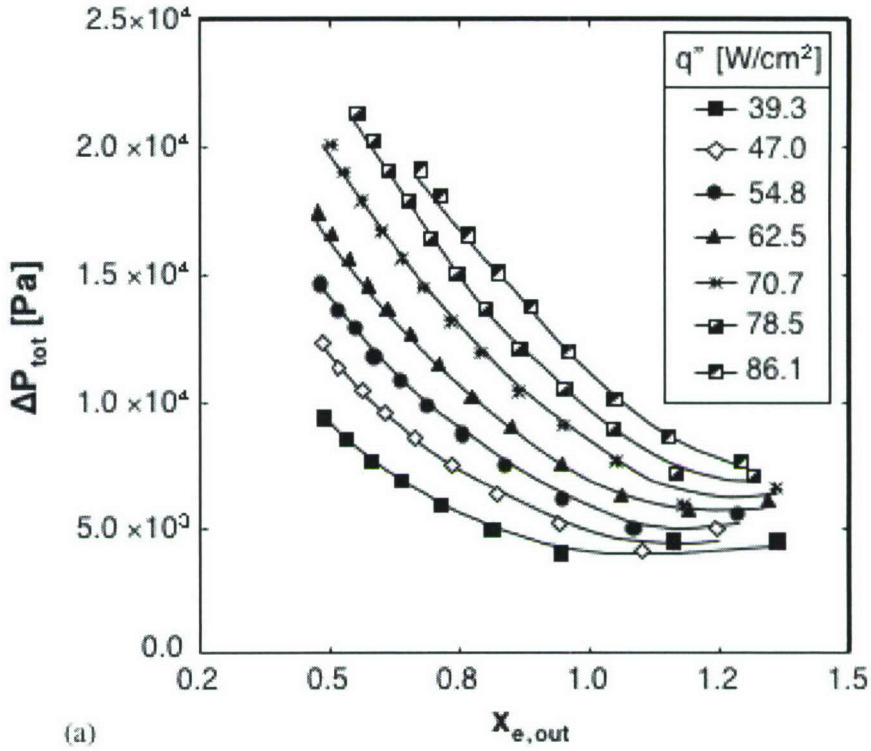

(a)

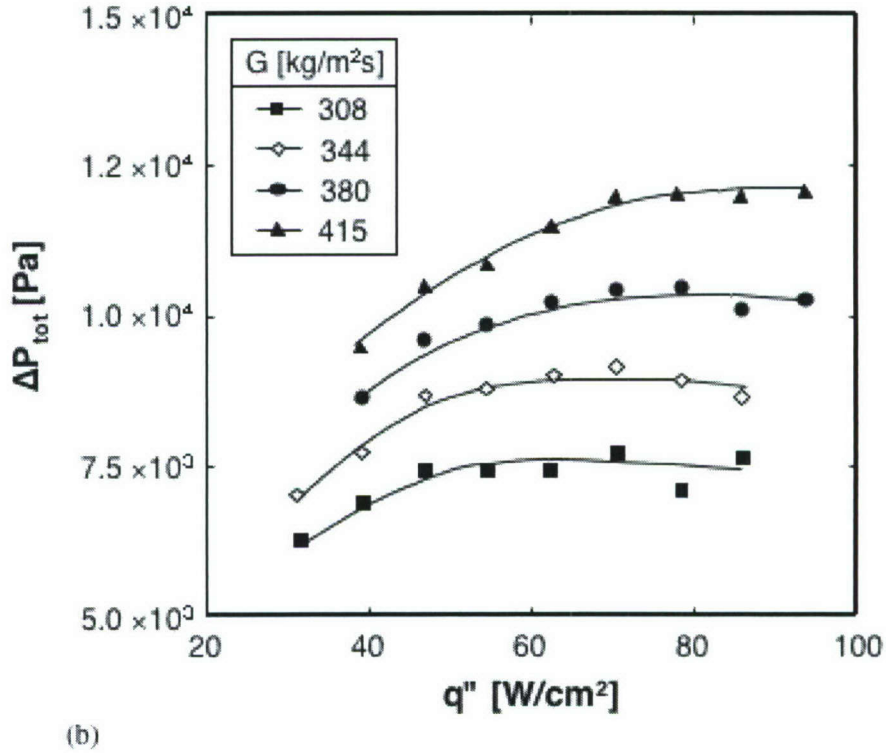

(b)

Figure I.3.4 Variation of measured R134a total pressure drop with (a) exit quality for different heat fluxes, and (b) heat flux for different mass velocities.

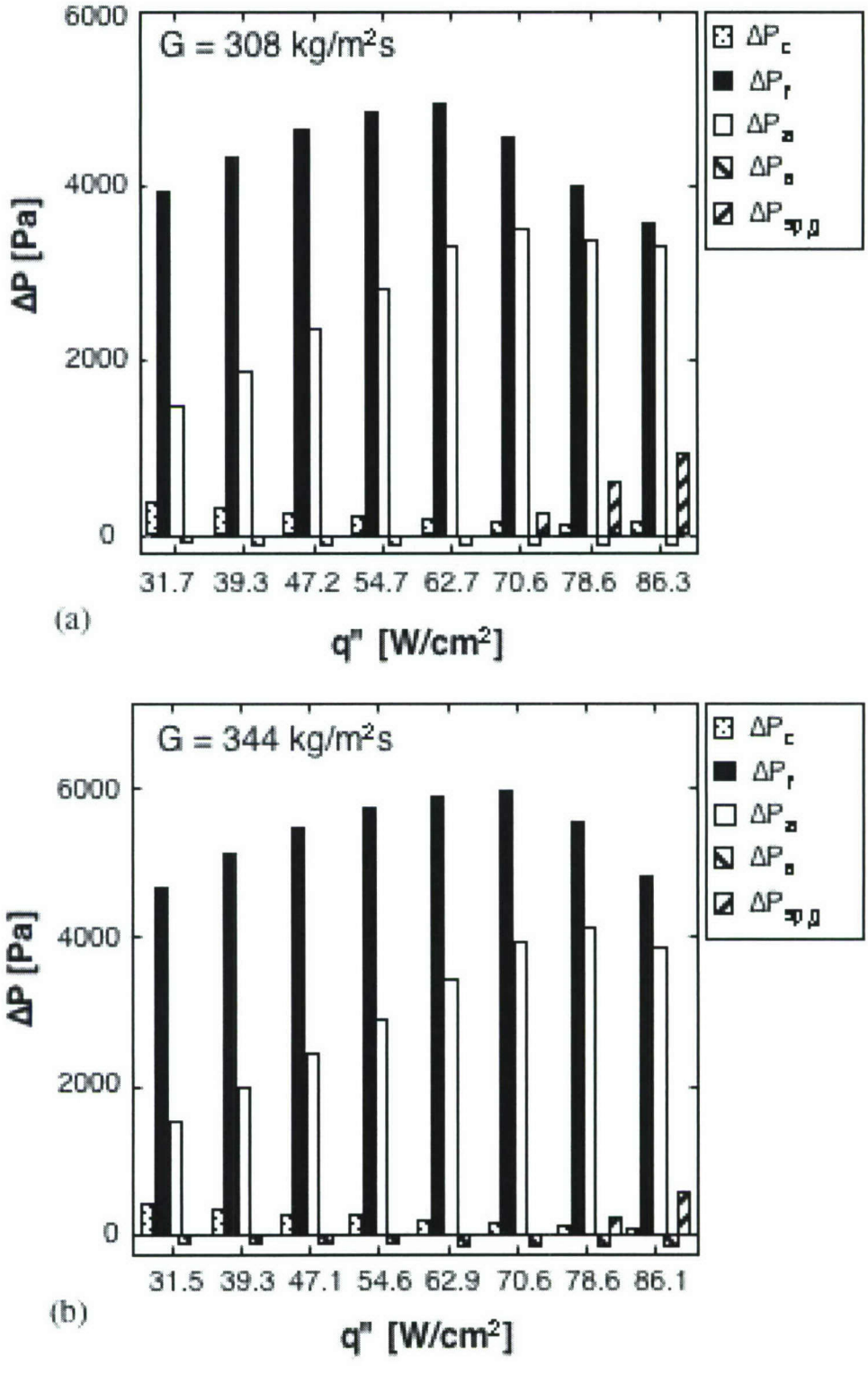

Figure I.3.5 Individual components of pressure drop for different heat fluxes and mass velocities of (a) 308, (b) 344, (c) 380, and (d) 415 kg/m^{2}s.

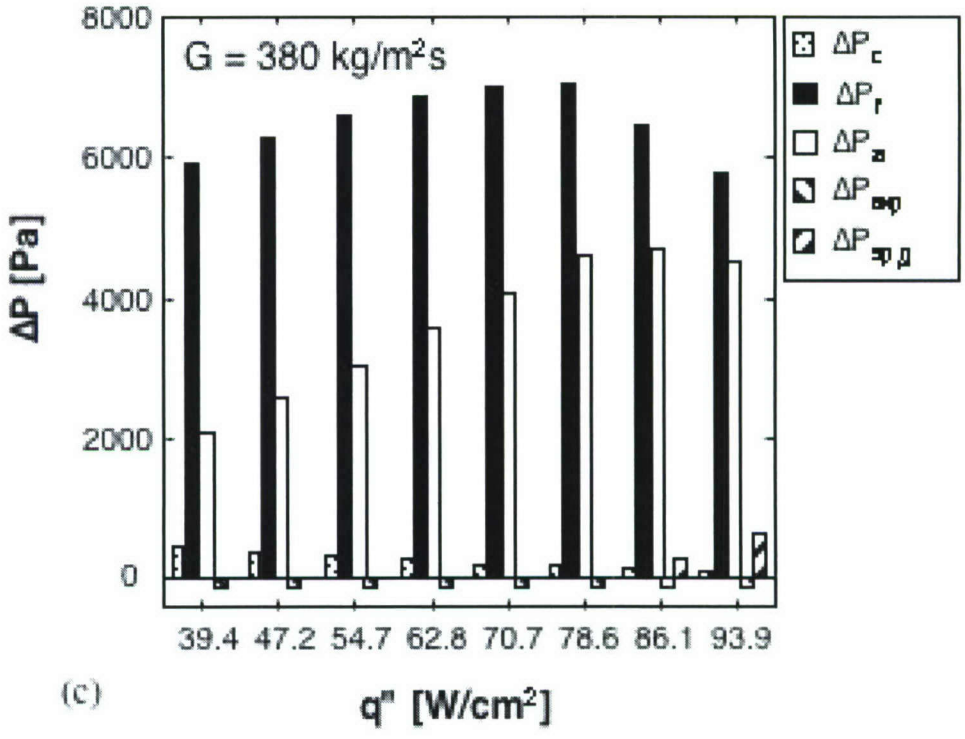

(c)

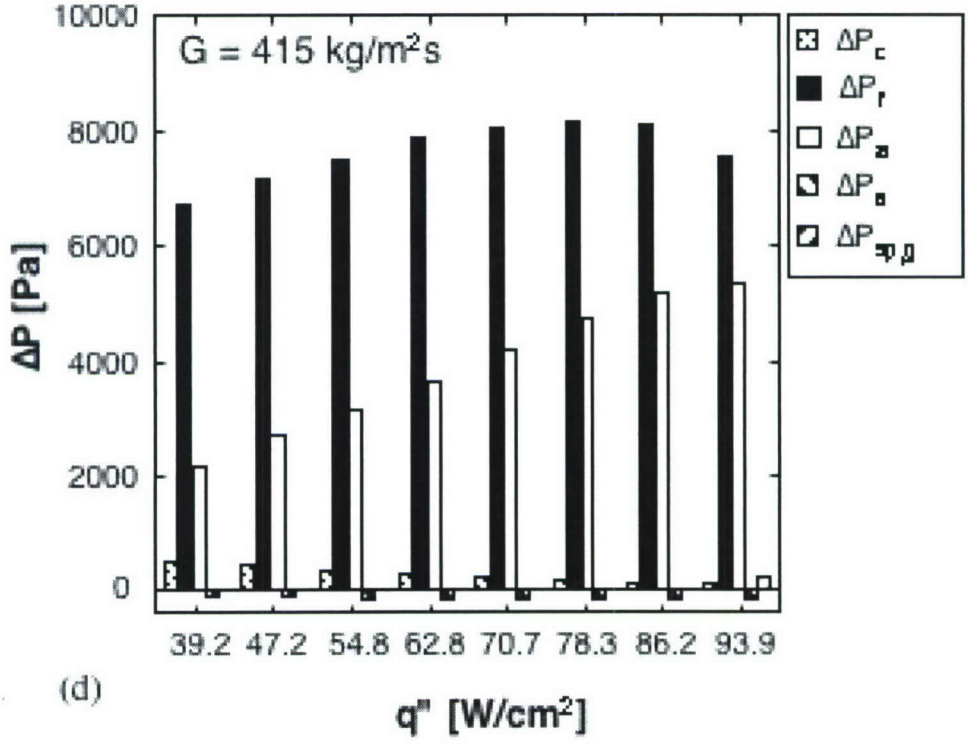

(d)

Figure I.3.5 continued.

I.3.5 Flow Instabilities

Intrinsic to any refrigeration cycle, the throttling valve located upstream of the evaporator offers important benefits to the operation of a micro-channel evaporator. Qu and Mudawar (2003) proved the interaction of the two-phase mixture with the upstream compressible volume in a flow loop can trigger 'severe pressure oscillation' which is also a precursor for premature critical heat flux (CHF). The throttling valve in the present system imparted greater stiffness to the system, precluding both this severe form of instability and the premature CHF.

Despite its effectiveness at suppressing the severe pressure oscillation, the micro-channel evaporator is still susceptible to a second 'parallel channel instability' [Qu and Mudawar (2003)] caused by interaction between micro-channels within the heat sink itself. This instability is quite random in nature and much milder than the aforementioned 'severe pressure oscillation.' This is demonstrated in Fig. I.3.6 in the form of temporal variations of pressure drop for different mass velocities at four representative heat fluxes. It is important to point out that mass velocity is strongly tied to the amount of throttling upstream of the evaporator. Reducing the throttling increases the mass velocity but increases the parallel channel instability as well. This trend is clearly evident in Figs. I.3.6(b) and (c). Despite the seemingly large increase in instability, the reader is cautioned that the amplitude of pressure fluctuation at the highest mass velocity of $G = 621$ kg/m^{2}s is only about 4000 Pa, which is hardly a reason for concern in a practical refrigeration system.

Figure I.3.6 provides valuable insight into the effect of heat flux on flow instability. Comparing Figs. I.3.6(c) and (d) shows increasing the heat flux for the same mass velocity aids in stabilizing the flow. This is apparently due to the higher heat flux increasing vapor production causing (1) a smaller portion of the micro-channel length being occupied by the two-phase mixture and (2) increasing pressure drop. Both effects increase the evaporator's stiffness for a given amount of upstream throttling.

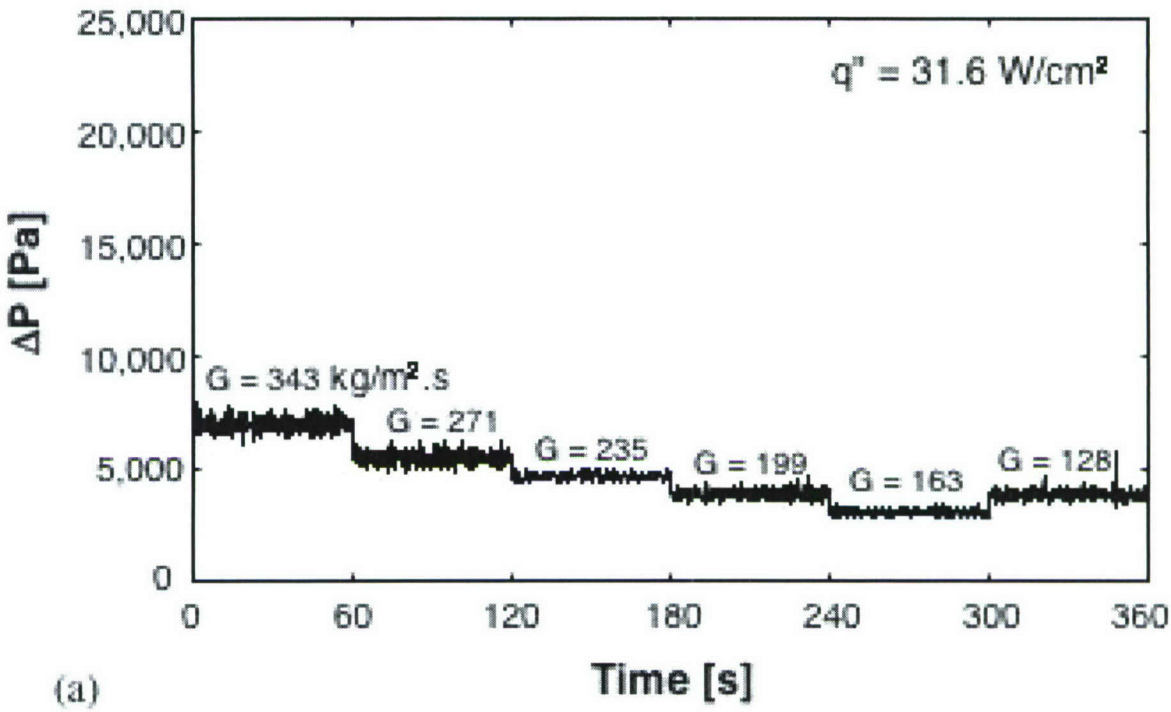

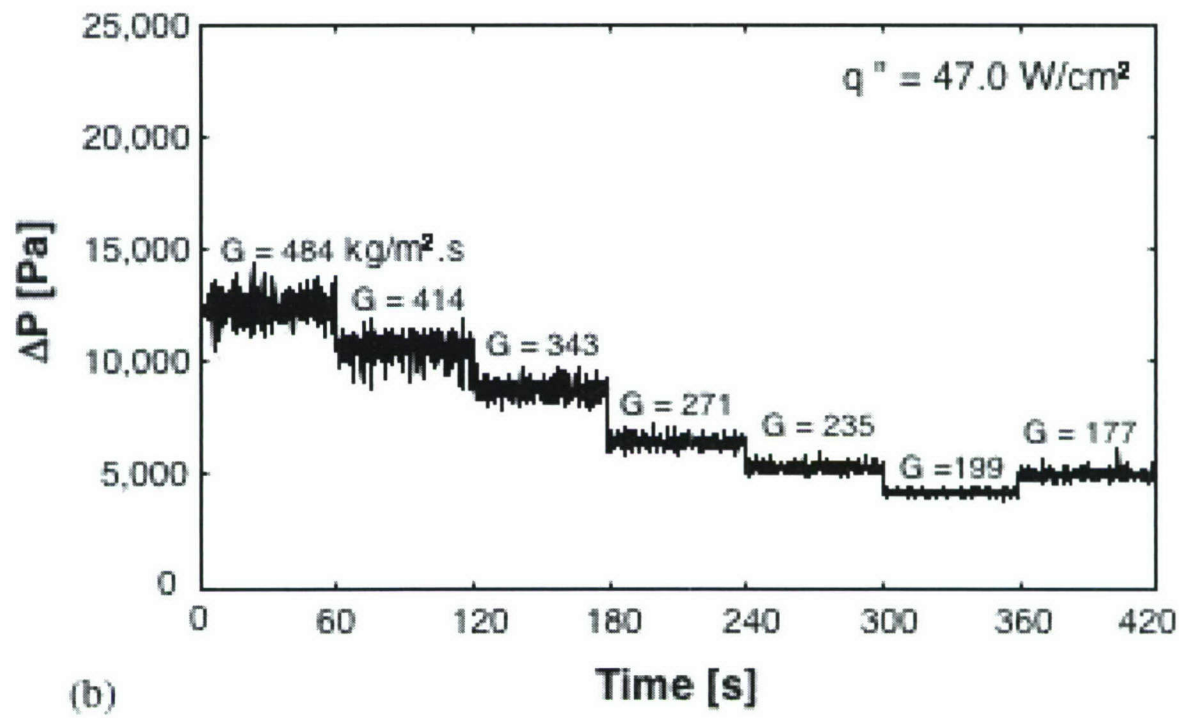

Figure I.3.6 Temporal variations of pressure drop for heat fluxes of (a) 31.6, (b) 47.0, (c) 62.6, and (d) 78.5 W/cm^2.

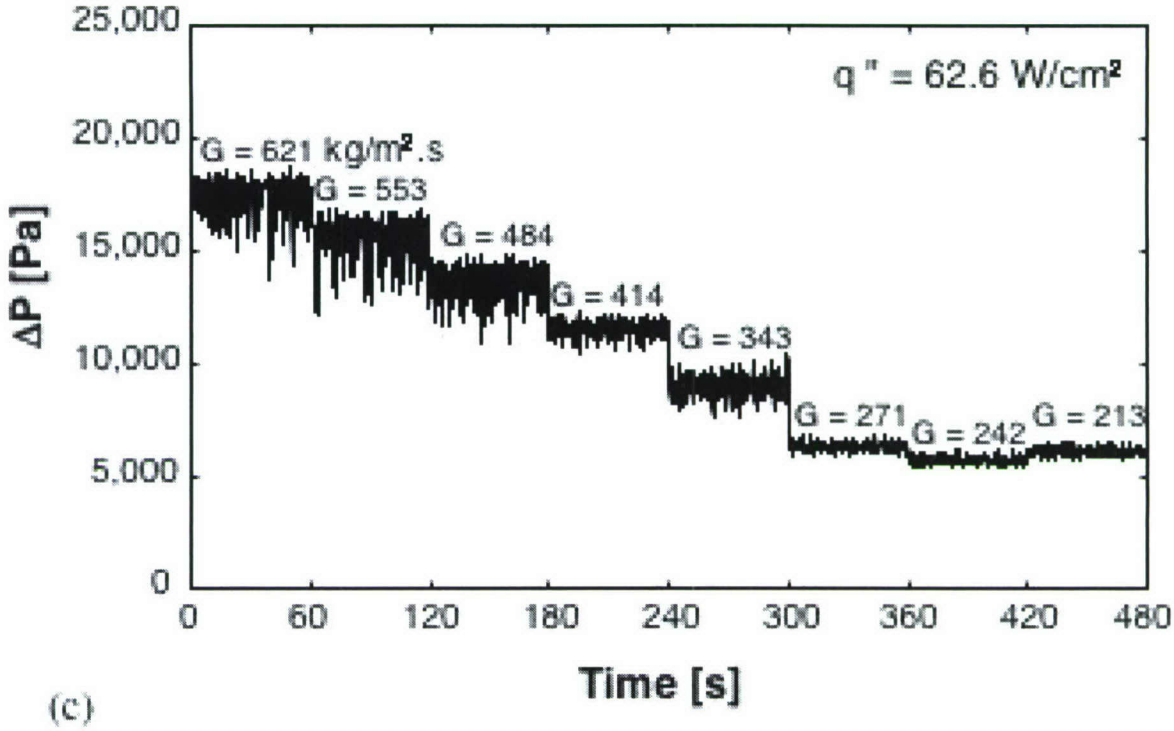

(c)

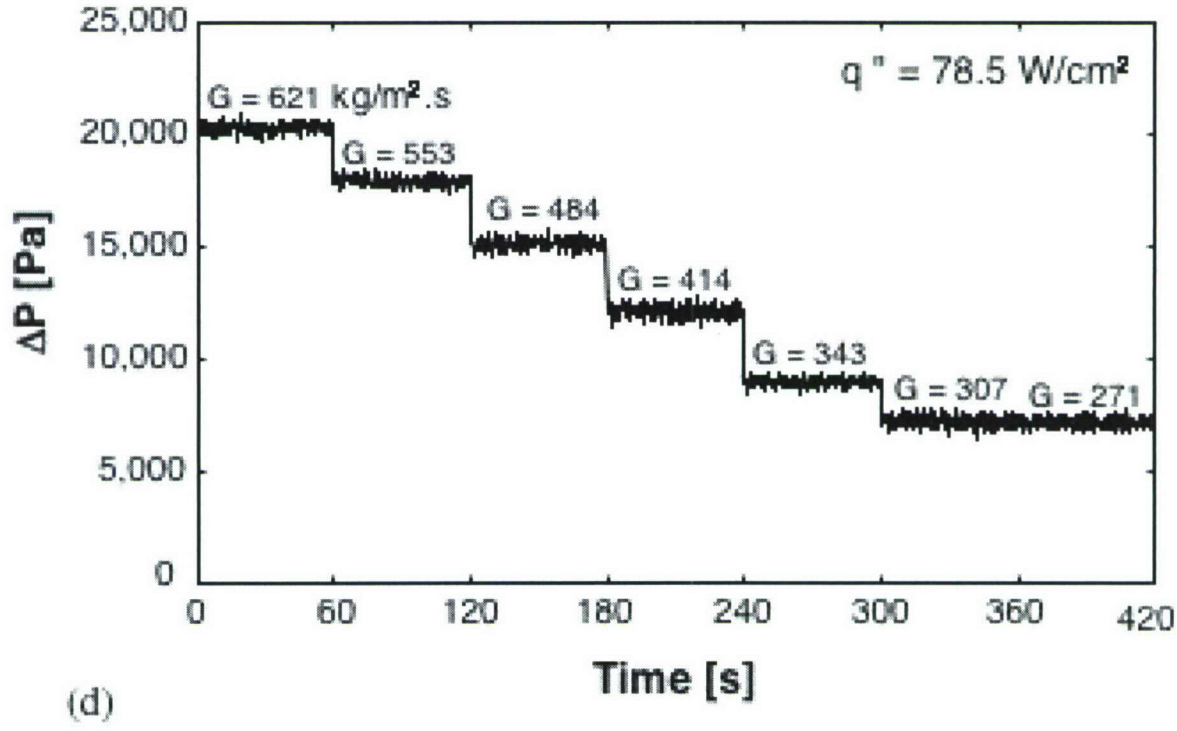

(d)

Figure I.3.6 continued.

I.4 BOILING HEAT TRANSFER IN MICRO-CHANNEL HEAT SINK

I.4.1 Determination of Heat Transfer Coefficient

Figure I.4.1 shows a unit control volume consisting of a single micro-channel and half of the surrounding copper walls. A simplified fin model of the copper walls is used to construct an energy balance for this control volume. Equating the heat influx to the unit cell through the bottom solid wall to the heat efflux by flow boiling along the micro-channel bottom and side walls (since the top wall is adiabatic) yields [Qu and Mudawar (2003)]

$$q''\left(W_{ch}+2W_{w}\right)=h_{tp}\left(T_{w,b}-T_{f,sat}\right)\left(W_{ch}+2\eta H_{ch}\right), \tag{I.4.1}$$

where η is the fin efficiency. Since the top wall is adiabatic, the fin efficiency is given by [Incropera and Dewitt (2002)]

$$\eta=\frac{\tanh\left(m H_{ch}\right)}{m H_{ch}}, \tag{I.4.2}$$

where m is the fin parameter defined as

$$m=\sqrt{\frac{h_{tp}}{k_{s}W_{w}}}. \tag{I.4.3}$$

The fin base temperature, $T_{w,b}$, was calculated using the assumption of one-dimensional heat diffusion between the plane of the thermocouple embedded in the copper block and the plane containing the fin base.

$$T_{w,b}=T_{tc}-\frac{q''H_{tc}}{k_{s}}. \tag{I.4.4}$$

The fluid temperature, $T_{f,sat}$, in Eq. (I.4.1) is the bulk temperature halfway along the micro-channel based on pressure at the same location determined from the measured inlet

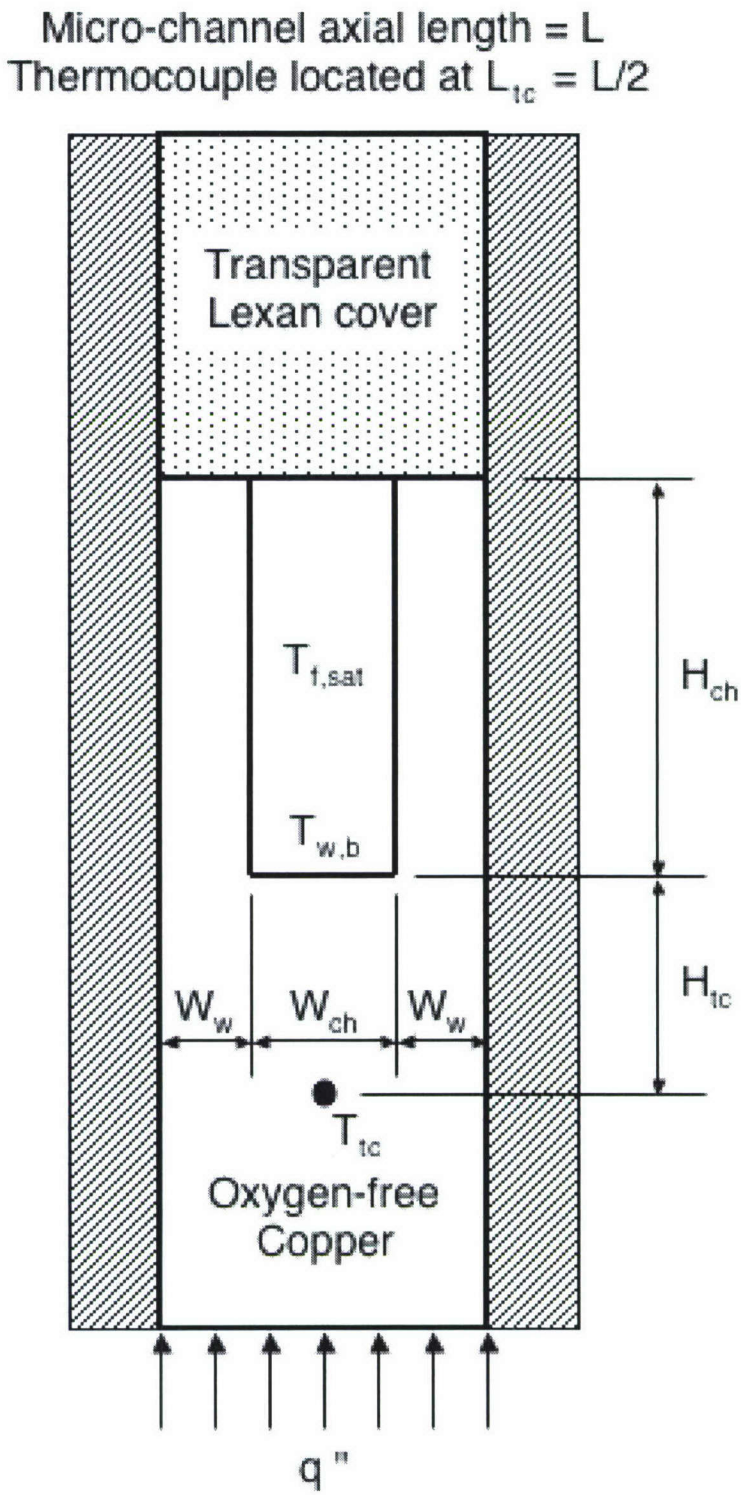

Figure I.4.1 Micro-channel unit cell .

pressure and the pressure drop correlation scheme presented in chpter I.3.3 of this report. Calculations revealed that, excepting superheated evaporator outlet conditions, $T_{f,sat}$, was close to the mean value of the measured inlet and outlet temperatures.

Equations (I.4.1) and (I.4.2) are therefore used to determine h_{tp} since all other parameters are easily measured or calculated. Figure I.4.2 shows the variation of the measured heat transfer coefficient h_{tp} at $z = L/2$ with quality at the same stream-wise location (obtained by substituting L in Eq. (I.2.1) by $L/2$) for different values of heat flux. This quality was varied experimentally by reducing mass flow rate (through increased throttling upstream of the evaporator) while maintaining a constant heat flux. To maintain reliable compressor operation, only values in excess of $x_{e,c} = 0.25$ could be tested. Figure I.4.2 shows h_{tp} decreases with increasing vapor quality, a basic feature of annular evaporative boiling, not nucleate boiling as was suggested in some of the earlier studies. Another noteworthy feature of the same data is the large magnitude of h_{tp} (2,000 – 50,000 W/m^{2}K), which is far superior to values typically attained with mini- and macro-channels.

Figure I.4.2 also shows the influence of heat flux on h_{tp} is very strong up to quality values around $x_{e,c} = 0.55$, beyond which there is a great diminution in the heat flux effect. For $x_{e,c} < 0.55$, the slope of h_{tp} versus $x_{e,c}$ is very steep for large heat fluxes but approaches zero at the lowest heat flux of $q'' = 15.9$ W/cm^2. This trend points to h_{tp} values becoming constant (independent of $x_{e,c}$) had even lower heat flux values been tested. As indicated earlier, the compressor precluded operating at such low heat fluxes.

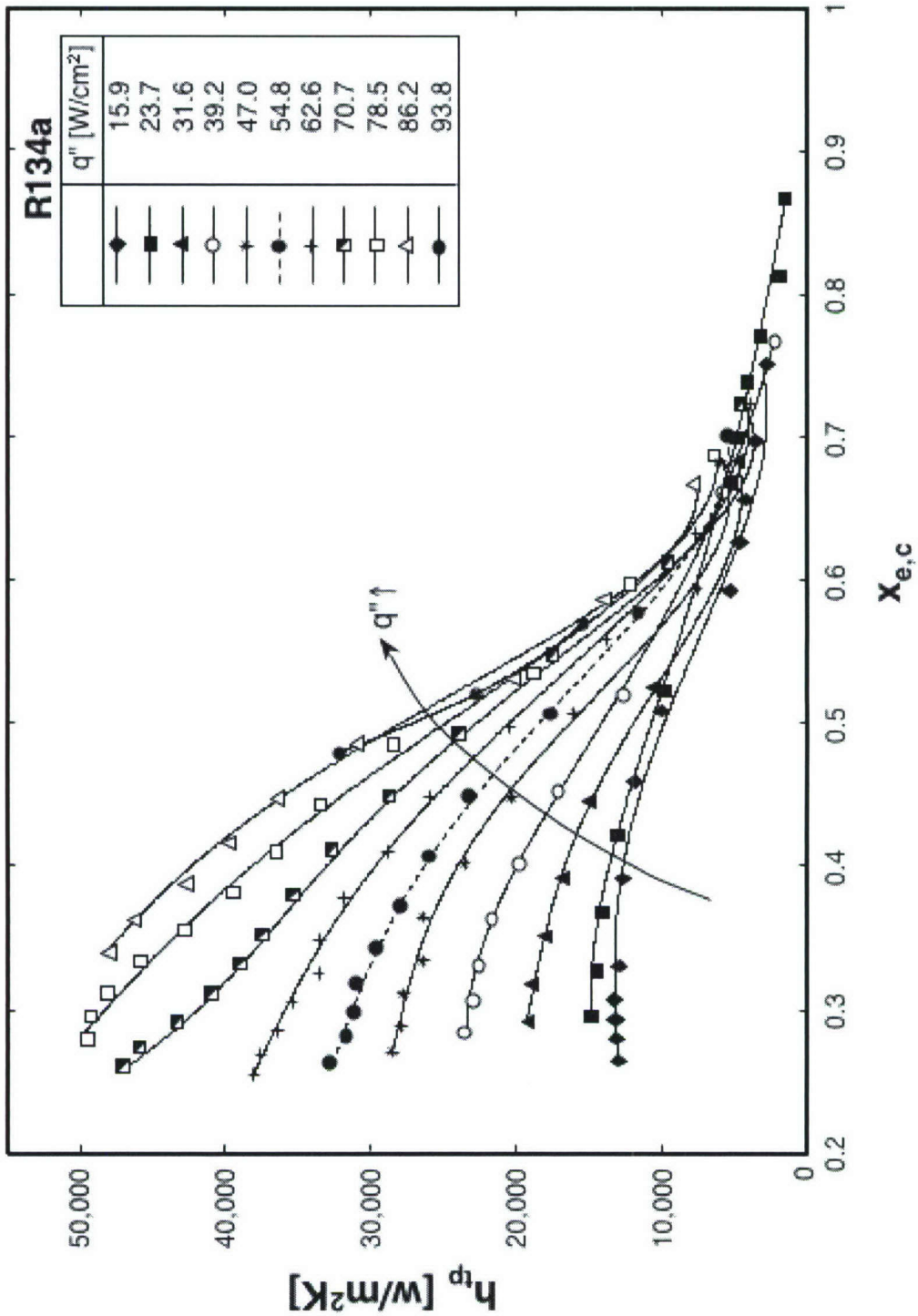

Figure I.4.2 Variation of local heat transfer coefficient for R134a with thermodynamic equilibrium quality for different heat fluxes.

I.4.2 Flow Visulalization

Flow visualization was used to better understand the aforementioned heat transfer coefficient trends. As indicated earlier, the transparent cover plate provided direct optical access to the boiling phenomena occurring within the micro-channel. The clarity of video and still images was limited by the small micro-channel size, lighting requirements, and internal reflection within the inner walls of the micro-channels. Figure I.4.3 shows an image of the flow in two adjacent micro-channels along with a schematic rendering of the same image at each of three values of quality halfway along the channel. Notice the slight differences in boiling pattern between the adjacent micro-channels. As explained in section I.3.5 concerning flow instabilities, these differences are the result of a mild parallel channel instability causing slight flow pattern variations among the micro-channels. This form of instability was more pronounced at lower quality values.

Figure I.4.3(a) shows a combination of slug flow and to a lesser extent bubbly flow for $x_{e,c}$ = 0.39. Small bubbles exhibited violent mixing in the liquid slugs between the elongated bubbles. There are two possible sources for these small bubbles. The first is entrance inclusion since the flow enters the evaporator as a two-phase mixture. The second is nucleation within the micro-channels, which can be easily detected for bubbles nucleating from the sidewalls. Previous studies with a water-cooled micro-channel heat sink showed bubbly flow could rarely be sustained [Qu and Mudawar (2003)]. In fact, annular flow was the dominant regime for most medium- and high-flux conditions. This drastic difference between two-phase flow patterns for R134a and water is explained by the low surface tension of R134a producing far smaller bubbles than in water [Mukherjee and Mudawar (2003)]. Very small bubbles are far more apt to travel discretely along a micro-channel before coalescing into long bubbles, thus enabling the bubbly and slug flow regimes to be more prevalent in refrigerant micro-channel flow.

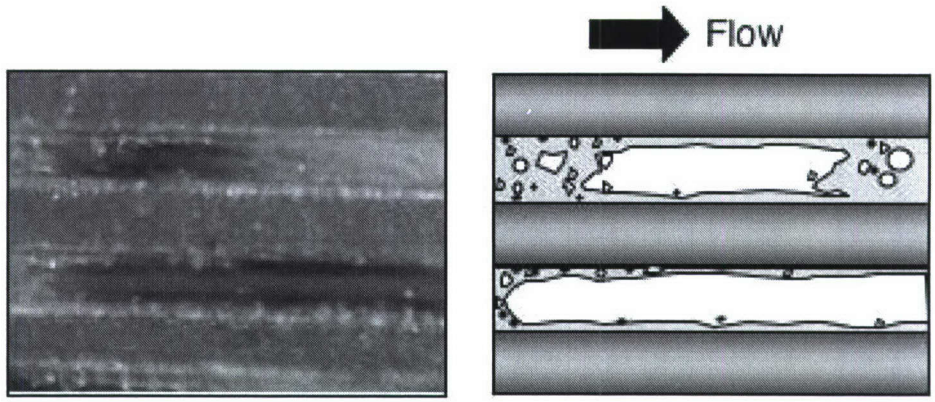

(a) $x_{e,c} = 0.39$, $q'' = 31.6$ W/cm^2, $G = 235.2$ kg/m^2 s

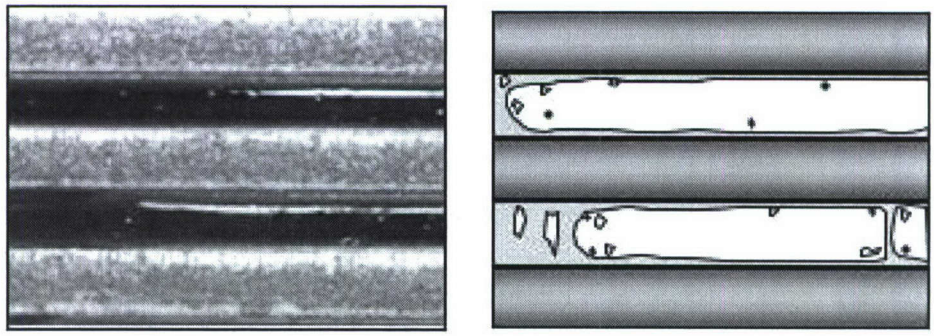

(b) $x_{e,c} = 0.53$, $q'' = 31.6$ W/cm^2, $G = 163.3$ kg/m^2 s

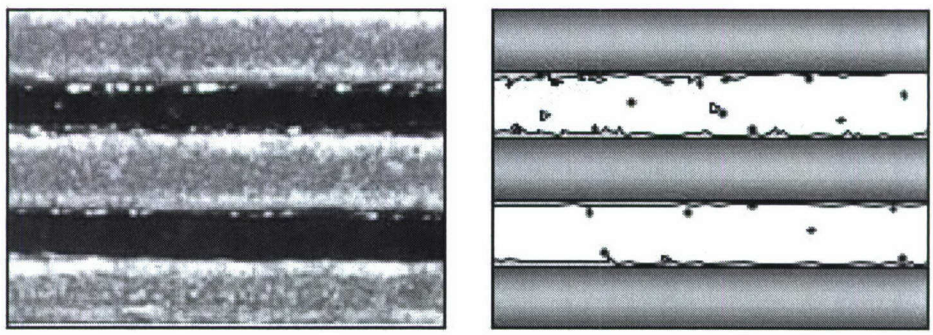

(c) $x_{e,c} = 0.68$, $q'' = 31.6$ W/cm^2, $G = 128.2$ kg/m^2 s

Figure I.4.3 Two-phase flow pattern and schematic renderings of R134a flow at (a) $x_{e,c} = 0.39$, $q'' = 31.6$ W/cm^2, $G = 235.2$ kg/m^{2}s; (b) $x_{e,c} = 0.53$, $q'' = 31.6$ W/cm^2, $G = 163.3$ kg/m^{2}s, and (c) $x_{e,c} = 0.68$, $q'' = 31.6$ W/cm^2, $G = 128.2$ kg/m^{2}s .

Figure I.4.3(b) shows the flow pattern at a quality value close to the transitional value discussed earlier in conjunction with the variation of h_{tp} with $x_{e,c}$, which was the upper quality boundary for a strong heat flux effect. This slug flow pattern consists mainly of elongated bubbles with very few small bubbles within the liquid slugs. Notice the two elongated bubbles in the lower micro-channel separated by a very thin liquid ridge, tending to coalesce into a single longer bubble or transition to annular flow.

Figure I.4.3(c) shows fully developed annular flow with a very thin liquid film covering the micro-channel walls at $x_{e,c} = 0.68$. The film appears too thin in certain locations to maintain adequate cooling. This is evident in the lower of the two micro-channels were dryout might be occurring locally, and where droplet deposition from the vapor core appears very sparse. These observations point to $x_e \approx 0.55$ as a lower boundary for local dryout, and perhaps critical heat flux (CHF) for refrigerant micro-channel flow.

Interestingly, Tran et al. (1996) detected transition from slug to annular flow around $x_e \approx 0.6$ - 0.7, compared to $x_e \approx 0.25$ - 0.35 for macro-channels. The present study points to transition values smaller than those of Tran et al. but greater than for macro-channels. Clearly, vapor quality is not the sole indicator for regime transition, and other parameters such surface tension and channel shape and dimensions must influence transition behavior.

I.4.3 Assessment of Prior Correlatins

Several popular macro-channel correlations and recently recommended small-channel correlations were examined for accuracy in predicting the present heat transfer data. These correlations are summarized in Table I.4.1. Since these correlations concern circular channels with uniform circumferential heating, predictions had to be adjusted for the three-sided wall heating and rectangular geometry of the present study using the following relation:

$$h_{tp} = h_{tp,cor} \frac{Nu_3}{Nu_4}, \tag{I.4.5}$$

where $h_{tp,cor}$ is the value predicted from a correlation, and Nu_3 and Nu_4 are the single-phase Nusselt numbers for laminar flow with three-sides and four-sides wall heating, respectively [Shah and London (1978)].

$$Nu_3 = 8.235\left(1 - 1.883\beta + 3.767\beta^2 - 5.814\beta^3 + 5.361\beta^4 - 2.0\beta^5\right) \tag{I.4.6}$$

and

$$Nu_4 = 8.235\left(1 - 2.042\beta + 3.085\beta^2 - 2.477\beta^3 + 1.058\beta^4 - 0.186\beta^5\right). \tag{I.4.7}$$

The first three correlations in Table I.4.1 are popular for determining the two-phase heat transfer coefficient for macro-channels. These correlations include a single-phase term, h_{sp}, based on turbulent liquid flow prevalent in large channels. The Dittus-Boelter relation used for h_{sp} is a key drawback to using these three correlations for micro-channel flow, where the liquid is almost invariably laminar. The laminar liquid flow is the reason behind using Eqs. (I.4.6) and (I.4.7) when evaluating h_{sp} in the three macro-channel correlations.

The five remaining correlations in Table I.4.1 were all developed for smaller channels. Notice that correlations 4, 5 and 7 assume heat transfer is dominated by nucleate boiling, while correlations 6 and 8 are based on a form similar to that of macro-channel correlations.

Figure I.4.4 compares the measured heat transfer coefficient to predictions based on each of the correlations from Table I.4.1. The predictive accuracy of a correlation was measured by the mean absolute error, defined as

$$MAE = \frac{1}{N} \sum \left[\frac{\left| h_{tp,pred} - h_{tp,\exp} \right|}{h_{tp,\exp}} \times 100 \right]. \tag{I.4.8}$$

Figure I.4.4 shows all eight correlations yield poor predictions of the present data. The macro-channel correlations generally overpredict the data in the high quality region (region of low h_{tp} values), and underpredict in the low quality region. The three small channel correlations based on nucleate boiling (correlations 4, 5 and 7) and two remaining small channel correlations (6 and 8) all show poor predictions, evidenced by their large MAE values.

Table I.4.1 Previous correlations for boiling in small channels.

No.	Author(s)	Correlation	Remarks
1	Chen (1966)	$h_{tp} = \left(\frac{Nu_3}{Nu_4}\right)\left(E\,h_{sp} + S\,h_{nb}\right)$ $h_{sp} = Nu\frac{k_f}{d_h}$, $Nu_{lam} = const$ [Refer to Eqs.(I.4.6) and (I.4.7)], $Nu_{tur} = 0.023\,Re_f^{0.8}\,Pr_f^{0.4}$ $h_{nb} = 0.00122\left(\frac{k_f^{0.79}\,c_{p,f}^{0.45}\,v_g^{0.24}}{\sigma^{0.5}\,\mu_f^{0.29}\,h_{fg}^{0.24}\,v_f^{0.49}}\right)\Delta T_{sat}^{0.24}\,\Delta P_{sat}^{0.75}$ $E = \left(1+\frac{1}{X^{0.5}}\right)^{1.78}$, $S = 0.9622 - 0.5822\tan^{-1}\left\{\frac{Re_f\,E^{1.25}}{6.18\times10^4}\right\}$ $X = \left[\left(dp/dz\right)_f \Big/ \left(dp/dz\right)_g\right]^{0.5}$, $Re_f = \frac{G(1-x_e)\,d_h}{\mu_f}$, $Pr_f = \frac{\mu_f\,c_{p,f}}{k_f}$	Macro-channel correlation
2	Shah (1982)	$h_{tp} = \left(\frac{Nu_3}{Nu_4}\right) Max(E,S)\,h_{sp}$ For $1.0 < N$, $S = 1.8/N^{0.8}$, $E = 230\,Bo^{0.5}$ *for* $Bo > 3\times10^{-5}$ or $E = 1 + 46\,Bo^{0.5}$ *for* $Bo < 3\times10^{-5}$ For $0.1 < N \le 1.0$, $S = 1.8/N^{0.8}$, $E = F\,Bo^{0.5}\exp(2.74\,N^{-0.1})$ For $N \le 0.1$, $S = 1.8/N^{0.8}$, $E = F\,Bo^{0.5}\exp(2.47\,N^{-0.15})$, $F = 14.7$ for $Bo \ge 11\times10^{-4}$ or $F = 15.43$ for $Bo < 11\times10^{-4}$ $N = Co$ for $Fr_f \ge 0.04$ or $N = 0.38\,Fr_f^{-0.3}\,Co$ *for* $Fr_f < 0.04$; $Co = \left(\frac{1-x_e}{x_e}\right)^{0.8}\left(\frac{v_f}{v_g}\right)^{0.5}$; $Fr_f = \frac{v_f^2\,G^2}{g\,d_h}$	Macro-channel correlation

Table I.4.1 continued.

No.	Author(s)	Correlation	Remarks
3	Liu & Winterton (1991)	$h_{tp} = \left(\frac{Nu_3}{Nu_4}\right)\left(\left(E\,h_{sp}\right)^2 + \left(S\,h_{nb}\right)^2\right)^{0.5}$ $h_{sp} = Nu\frac{k_f}{d_h}$, $Nu_{lam} = const$ [Eqs.(I.4.6) and (I.4.7)], $Nu_{Tur} = 0.023\,Re_f^{0.8}\,Pr_f^{0.4}$ $E = \left(1 + x_e\,Pr_f\left(\frac{v_g}{v_f} - 1\right)\right)^{0.35}$ $h_{nb} = 55\,P_r^{0.12}\left(-\log_{10}(P_r)\right)^{-0.55} M_w^{-0.5}\,q^{"0.67}$, $S = \left(1 + 0.055\,E^{0.1} Re_{fo}^{0.16}\right)^{-1}$ If $Fr_f \le 0.05$ replace E by $E\,Fr_f^{0.1-2Fr_f}$ and S by $S\,Fr_f^{0.5}$	Macro-channel correlation
4	Lazarek & Black (1982)	$h_{tp} = Nu_3\left[30\,Re_{fo}^{0.857}\,Bo^{0.714}\right]\left(\frac{k_f}{d_h}\right)$	Small channel correlation
5	Tran et al. (1996)	$h_{tp} = \left(\frac{Nu_3}{Nu_4}\right)\left[8.4\times10^5\left(Bo^2\,We_{fo}\right)^{0.3}\left(\frac{v_g}{v_f}\right)^{-0.4}\right]$; $We_{fo} = \frac{v_f\,G^2\,d_h}{\sigma}$	Small channel correlation
6	Lee & Lee (2001)	$h_{tp} = \left(\frac{Nu_3}{Nu_4}\right)\left(E\,h_{sp}\right)$ $E = 10.3\beta^{0.398}\,\phi_f^{0.598}$, $\phi_f^2 = 1 + \frac{C}{X} + \frac{1}{X^2}$, $C = 6.185\times10^{-2}\,Re_{fo}^{0.726}$ $X^2 = \left[\left(dp/dz\right)_f \Big/ \left(dp/dz\right)_g\right]$	Small channel correlation

Table I.4.1 continued.

No.	Author(s)	Correlation	Remarks
7	Yu et al. (2002)	$h_{tp} = \left(\frac{Nu_3}{Nu_4}\right)\left[6.4\times10^{6}\left(Bo^{2}\,We_{fo}\right)^{0.27}\left(\frac{v_g}{v_f}\right)^{-0.2}\right]$	Small channel correlation
8	Warrier et al. (2002)	$h_{tp} = \left(\frac{Nu_3}{Nu_4}\right)\left(E\,h_{sp}\right)$ $h_{sp} = Nu\frac{k_f}{d_h}$, $Nu_{lam} = const$ (Refer to Eqs. (I.4.6) and (I.4.7)), $Nu_{tur} = 0.023\,Re_f^{0.8}\,Pr_f^{0.4}$ $E = 1.0 + 6\,Bo^{1/16} + f(Bo)\,x_e^{0.65}$, $f(Bo) = -5.3\left(1 - 855\,Bo\right)$	Small channel correlation

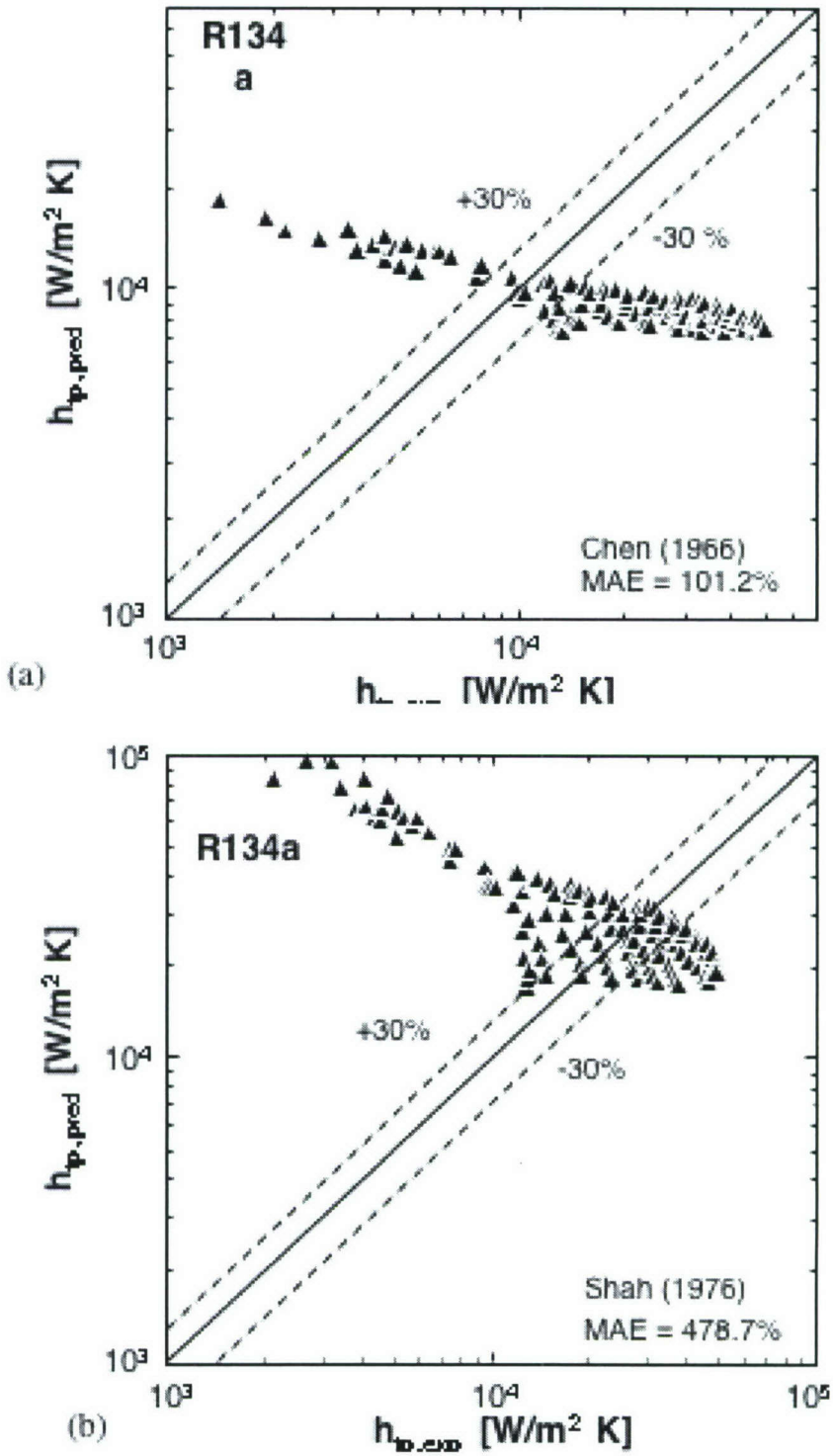

Figure I.4.4 Comparison of R134a heat transfer coefficient data with predictions based on (a) Chen (1966), (b) Shah (1976, 1982), (c) Lazarek and Black (1982), (d) Liu and Winterton (1991), (e) Tran et al. (1996), (f) Lee and Lee (2001), (g) Yu et al. (2002), and (h) Warrier et al. (2002).

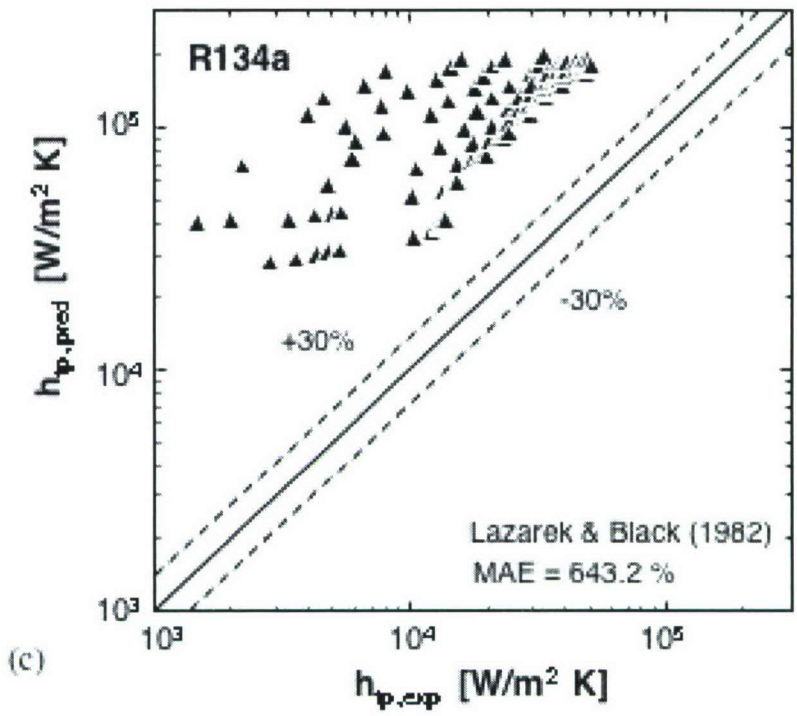

(c)

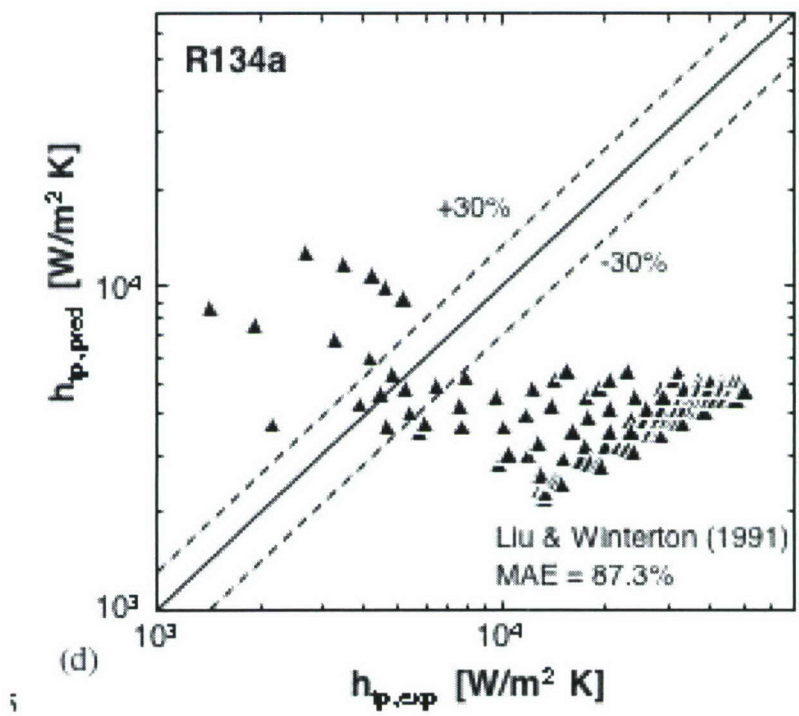

(d)

Figure I.4.4 continued.

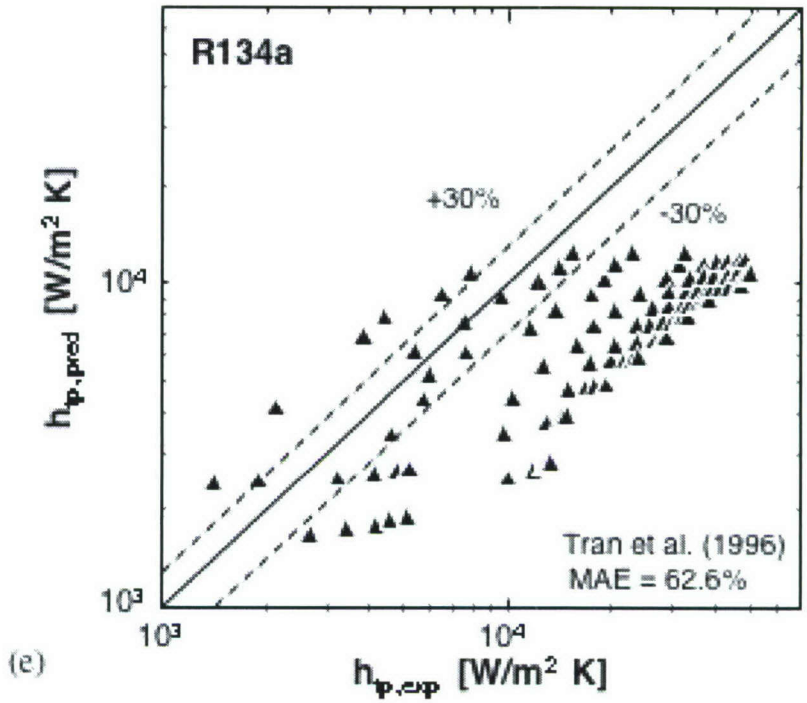

(e)

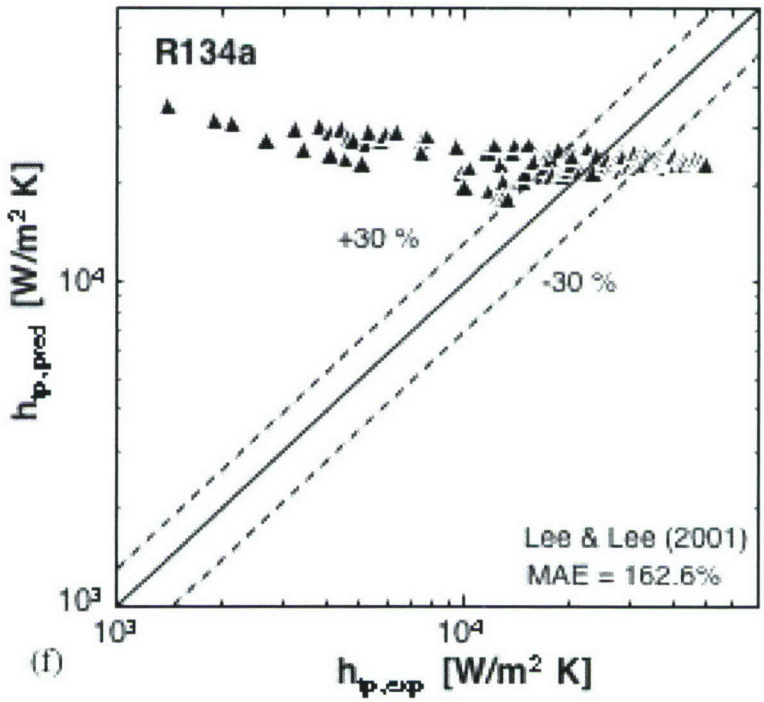

(f)

Figure I.4.4 continued.

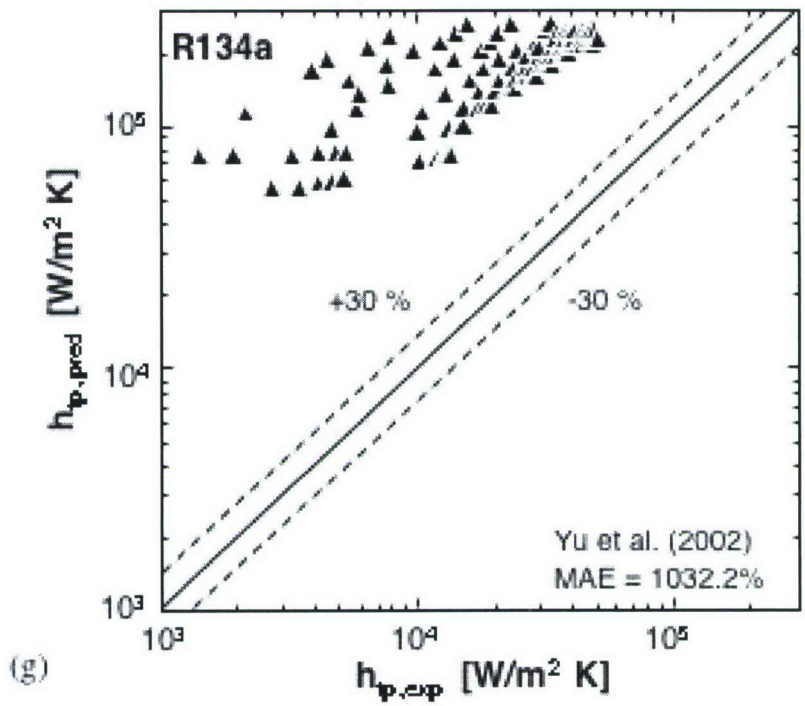

(g)

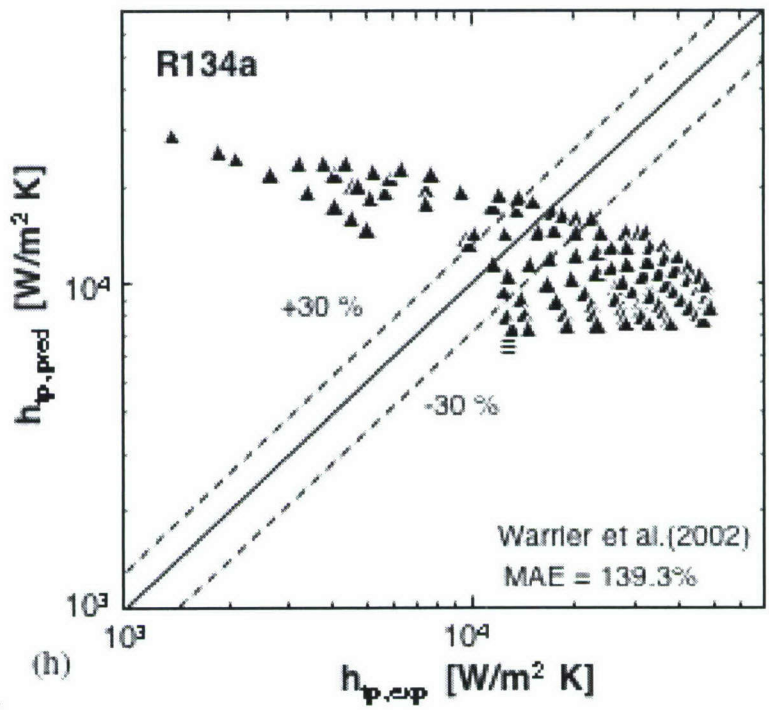

(h)

Figure I.4.4 continued.

I.4.4 New Correlation

The above assessment of prior correlations points a need for a new tool for accurate prediction of the heat transfer coefficient in refrigerant-cooled micro-channel heat sinks.

As indicated earlier, the compressor of the refrigeration system used in the present study precluded testing at low qualities. In order to both extend the quality range of the new correlation and demonstrate its validity for drastically different fluids, recent micro-channel water data by Qu and Mudawar (2003) were examined along with the new R134a data. Figure I.4.5 shows the variation of the two-phase heat transfer coefficient data with quality for the water data. Interestingly, the water data were obtained by modulating heat flux for a constant mass velocity, while the present R134a data were generated by regulating flow rate for a constant heat flux.

A new technique was sought that could correlate both the water and R134a data based on the Martinelli parameter, X, and account for micro-channel effects not represented in prior correlations. Exhaustive inspection of both the water and R134a databases showed two additional dimensionless parameters were required to adequately correlate all the data. They are the boiling number, Bo, and the liquid Weber number We_{fo}. Figures I.4.6 and I.4.7 show variations of X^2, Bo and We_{fo} with quality and heat flux for R134a and water, respectively, the latter being more concentrated in the low $x_{e,c}$ region. Overall, these three parameters show different trends for different quality ranges. Therefore, better predictions are possible by dividing the overall quality range into smaller ranges corresponding as closely as possible to the aforementioned flow transitions and data trends.

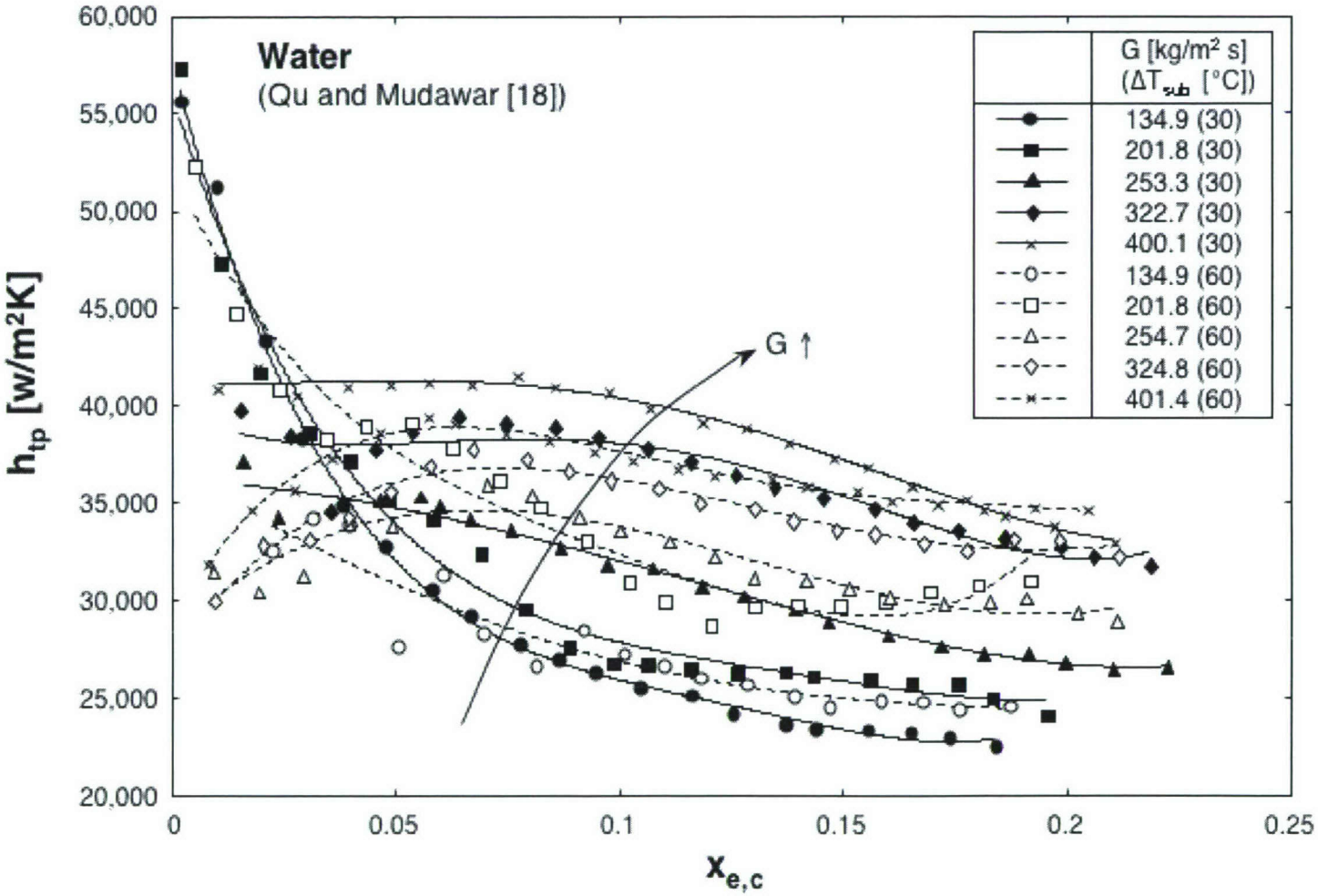

Figure I.4.5 Variation of local heat transfer coefficient for water [Qu and Mudawar (2003)] with thermodynamic equilibrium quality for different mass velocities.

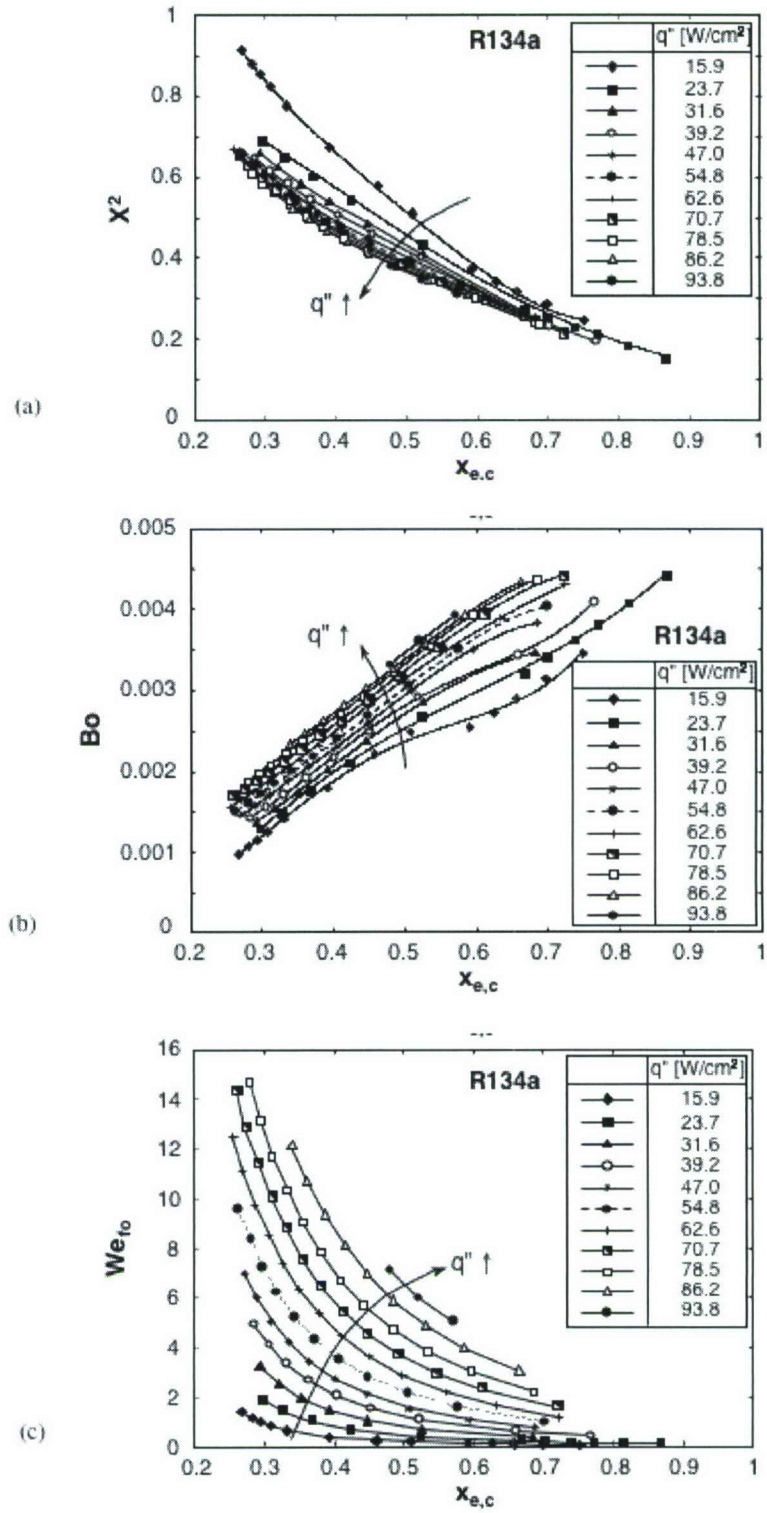

Figure I.4.6 Variations of (a) Martinelli parameter, (b) boiling number, and (c) Weber number with quality for R134a.

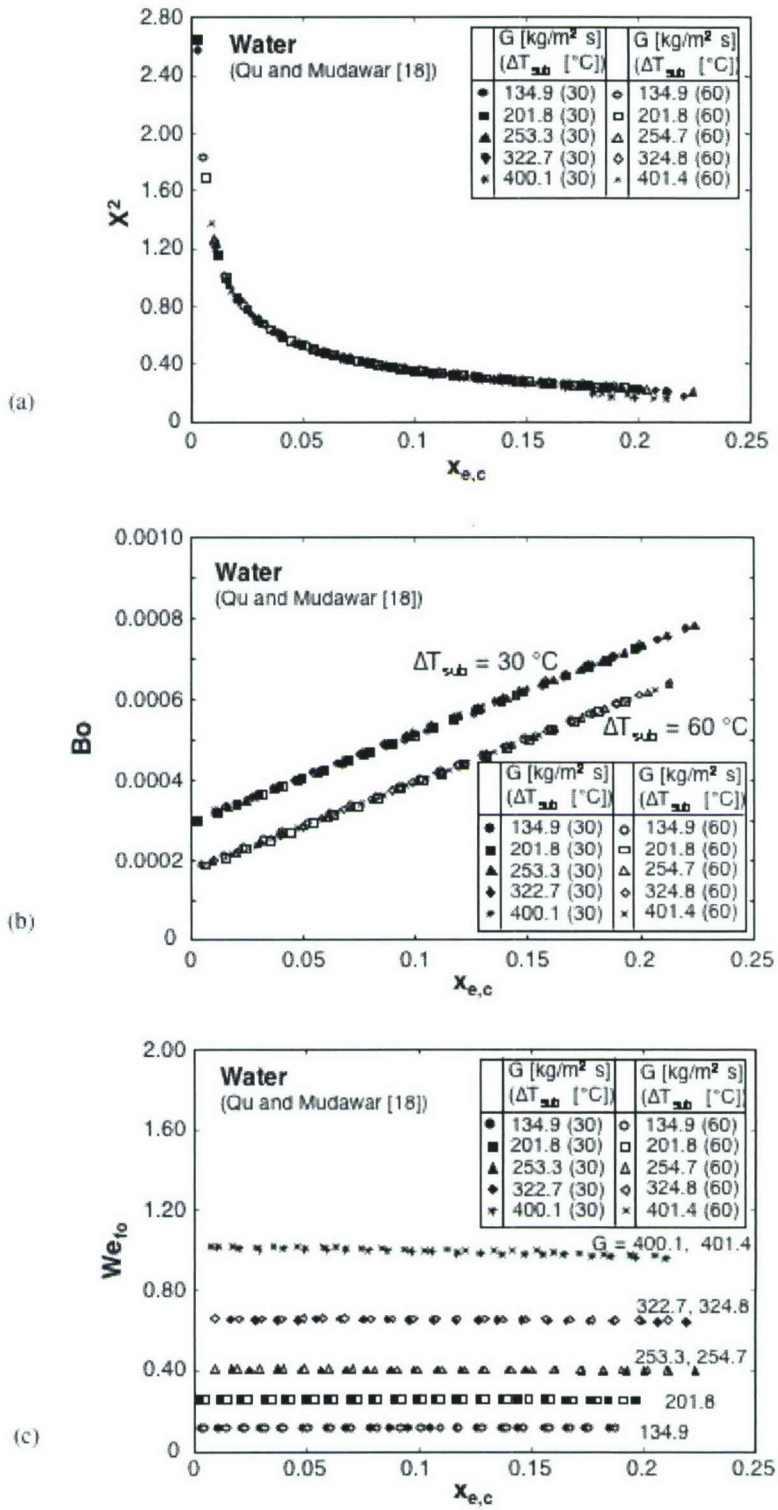

Figure I.4.7 Variations of (a) Martinelli parameter, (b) boiling number, and (c) Weber number with quality for water [Qu and Mudawar (2003)].

Three quality ranges provided adequate coverage of both the water and R134a databases. The first is a low quality range of x_e = 0 - 0.05. This low heat flux range is most closely associated with bubble nucleation and includes 50 water data points and none of the R134a data. These data show rapid and irregular variation of the heat transfer coefficient with quality as shown in Fig. I.4.5. Figure I.4.7(a) shows the Martinelli parameter in this range is uniquely determined by quality irrespective of flow rate or subcooling, and shows the sharpest decrease with increasing quality.

The second quality range is x_e = 0.05 - 0.55, which includes 83 R134a and 157 water data points. This range corresponds mostly to bubbly/slug flow, where the heat transfer data are no longer uniquely determined by the Martinelli parameter, but are sensitive to Bo and We_{fo} as well. The R134a and water data exhibit different trends with quality in this range. While the heat transfer coefficient decreases with increasing quality for both fluids, this decrease is far more pronounced for R134a, Fig. I.4.2, than for water, Fig. I.4.5. Those differences may be partially explained by the different values and trends of Bo and We_{fo} for the two fluids. Comparing Figs. I.4.6(b) and I.4.7(b) shows drastic differences in the magnitude of Bo, brought about mostly by a much smaller latent heat of vaporization for R134a compared to water. Figure I.4.6(c) shows far greater We_{fo} values for R134a compared to water, Fig. I.4.7(c), because of the much smaller surface tension of R134a. Furthermore, the large pressure changes in the R134a experiments produced appreciable property changes. Incorporating Bo and We_{fo} in the new correlation is anticipated to account for the drastic property variations that are far more accentuated in a micro-channel than in a macro-channel.

The last quality range is the liquid deficient region of x_e = 0.55 - 1.0, consisting of predominantly annular flow and local dryout. This includes 28 R134a data points but none of the water data. Figure I.4.6(a) shows a convergence of Martinelli number values for different heat fluxes. In this region, the thin annular film is gradually evaporated, sustained only by droplets entrained in the vapor core. Once the majority of droplets are depleted, evaporation results in monotonic thinning and eventual dryout of the liquid film. With this dryout, the heat transfer coefficient is greatly reduced as heat begins to be transferred directly to the vapor. Interestingly, the Martinelli parameter

approaches zero as quality goes to unity. Since dryout is followed by convection to vapor, a minimum value for the heat transfer coefficient correlation was set equal to that for convective heat transfer to pure vapor.

Table I.4.2 Present correlation scheme.

x_e	Correlation	Data	MAE
0 – 0.05	$h_{tp} = 3.856\, X^{0.267}\, h_{sp,f}$ $X^2 = \frac{(dp/dz)_f}{(dp/dz)_g}, \quad h_{sp,f} = \frac{Nu_3\, k_f}{d_h}$ $X_{vv} = \left(\frac{\mu_f}{\mu_g}\right)^{0.5}\left(\frac{1-x_e}{x_e}\right)^{0.5}\left(\frac{v_f}{v_g}\right)^{0.5}$ $X_{vt} = \left(\frac{f_f Re_g^{0.25}}{0.079}\right)^{0.5}\left(\frac{1-x_e}{x_e}\right)^{0.5}\left(\frac{v_f}{v_g}\right)^{0.5}$ $Re_g = \frac{G\, x_e\, d_h}{\mu_g}$	50 water data points	11.6%
0.05 – 0.55	$h_{tp} = 436.48\, Bo^{0.522}\, We_{fo}^{0.351}\, X^{0.665}\, h_{sp,f}$ $Bo = \frac{q''}{G\, h_{fg}}, \quad We_{fo} = \frac{v_f\, G^2\, d_h}{\sigma}$	83 R134a data points 157 water data points	11.9%
0.55 – 1.0	$h_{tp} = \max\left\{\left(108.6\, X^{1.665}\, h_{sp,g}\right), h_{sp,g}\right\}$ $h_{sp,g} = \frac{Nu_3\, k_g}{d_h}$ for laminar gas flow $h_{sp,g} = 0.023\, Re_g^{0.8}\, Pr_g^{0.4}$ for turbulent gas flow	28 R134a data points	16.1%

Table I.4.2 summarizes the new correlations for the three quality regions. The low and high quality regions are based solely on the Martinelli parameter while the mid range includes the effects of Bo and We_{fo} as well. Overall, convection to liquid is important for both the low and mid quality regions, while convection to vapor becomes important for the high quality region. For the latter, the low viscosity of R134a vapor yields vapor

Reynolds numbers corresponding to turbulent flow at high-heat-flux conditions despite the small hydraulic diameter of the micro-channel. Thus, the single-phase vapor term in the high quality correlation must allow for both laminar or turbulent vapor flow.

Table I.4.2 shows the effect of the Martinelli parameter is important for each of the three quality ranges. The present correlations show the heat transfer coefficient is proportional to the Martinelli parameter raised to a positive exponent, whereas prior macro-channel correlations employ a negative exponent for the same parameter.

Figure I.4.8 shows excellent agreement between predictions based on the new correlation scheme and both the R134a and water data. An overall MAE of 12.26% indicates excellent predictive capability, especially with most of the data falling within a ±30 % error range and capturing the correct data trend.

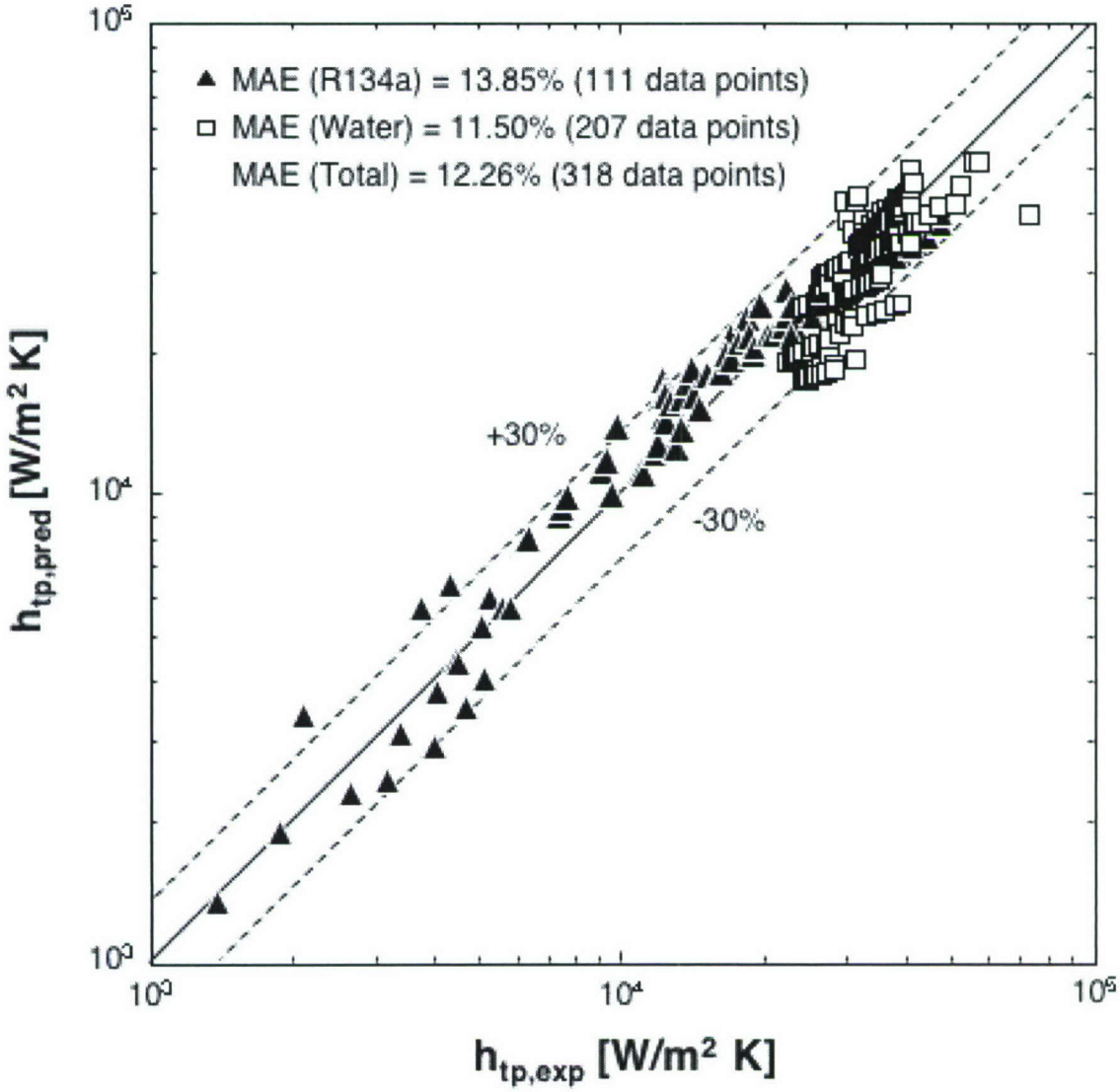

Figure I.4.8 Comparison of heat transfer coefficient data for R134 and water with predictions based on new correlation scheme.

I.5 IMPLEMENTATION OF MICRO-CHANNEL HEAT SINK

I.5.1 Experimental Results

A key parameter for assessment of the micro-channel heat sink's cooling performance is the measured heat sink temperature, T_{tc}. As illustrated in Fig. I.4.1, this temperature was measured by a type-K thermocouple situated a short distance beneath the base of the micro-channels halfway along the heat sink. The fluid at the same axial location is in saturated state for all operating conditions. Figure I.5.1 shows variations of the heat sink temperature and saturation temperature with mass velocity for four different values of evaporator heat load. The saturation temperature was determined from the measured evaporator inlet conditions using a two-phase pressure drop correlation developed at the section I.3. For a fixed evaporator thermal load, the mass velocity was modulated by the throttling valve. Increased throttling at low mass velocities produced appreciable pressure drop across the throttling valve. Both the copper and refrigerant temperatures show mild decreases with decreasing mass velocity, which is followed a big departure between the two temperatures at low mass velocities. When the compressor was operated within its normal capacity range, the copper block temperature curves indicate a minimum optimized cooling point. However, this optimal point is not evident outside the normal range (e.g. for Q_{evap} = 500 W).

This trend is closely associated with the transition from wet to dry compression. Figure I.5.2 shows a *P-h* diagram of the present refrigeration cycle for an evaporator thermal load of 200 W and two mass velocities. At the higher mass velocity of G = 343 kg/m^{2}s, the refrigerant exits the evaporator as a two-phase mixture corresponding to wet

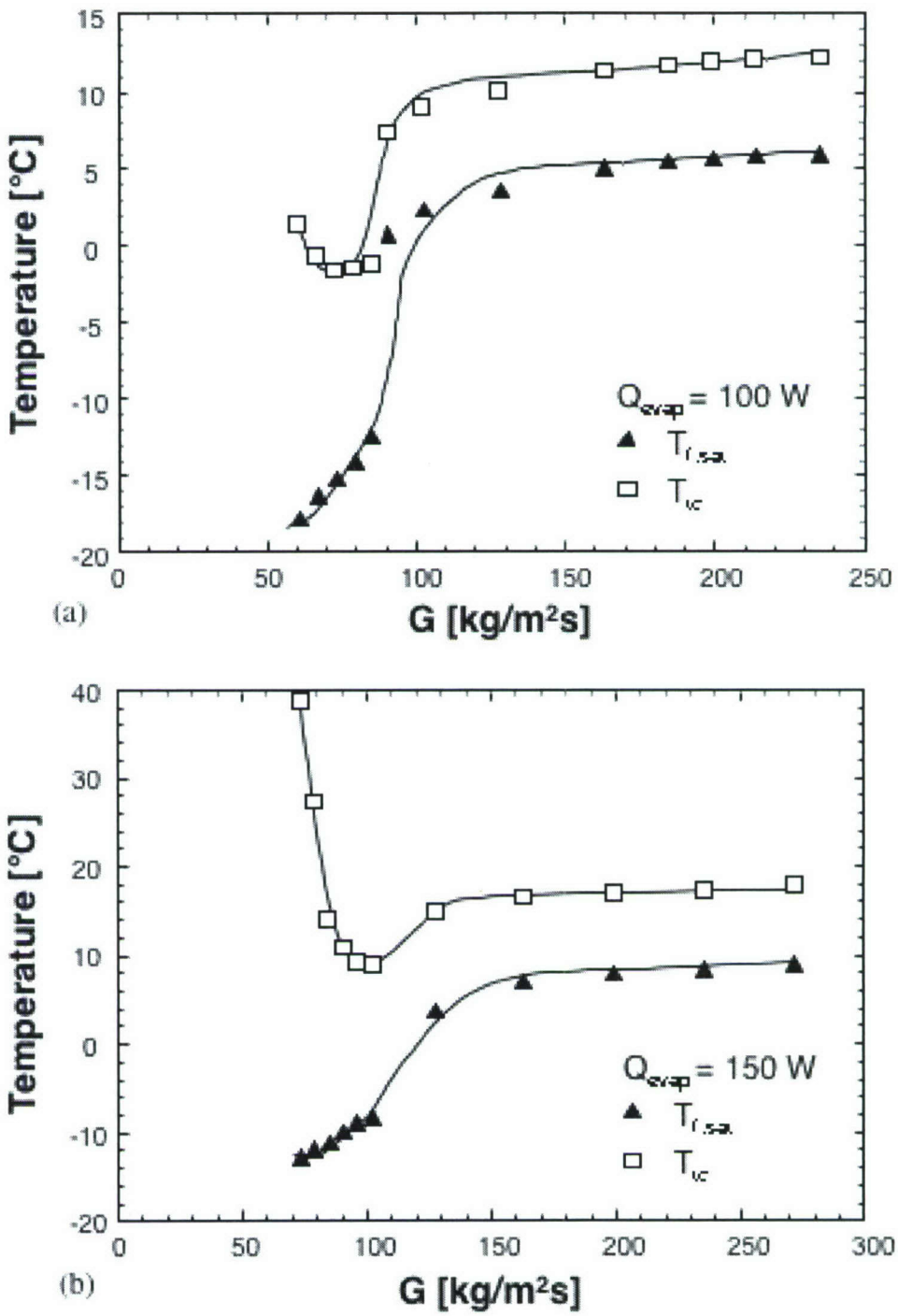

Figure I.5.1 Variation of measured copper and refrigerant temperature with mass velocity for evaporator heat loads of (a) 100, (b) 150, (c) 200, and (d) 500 W.

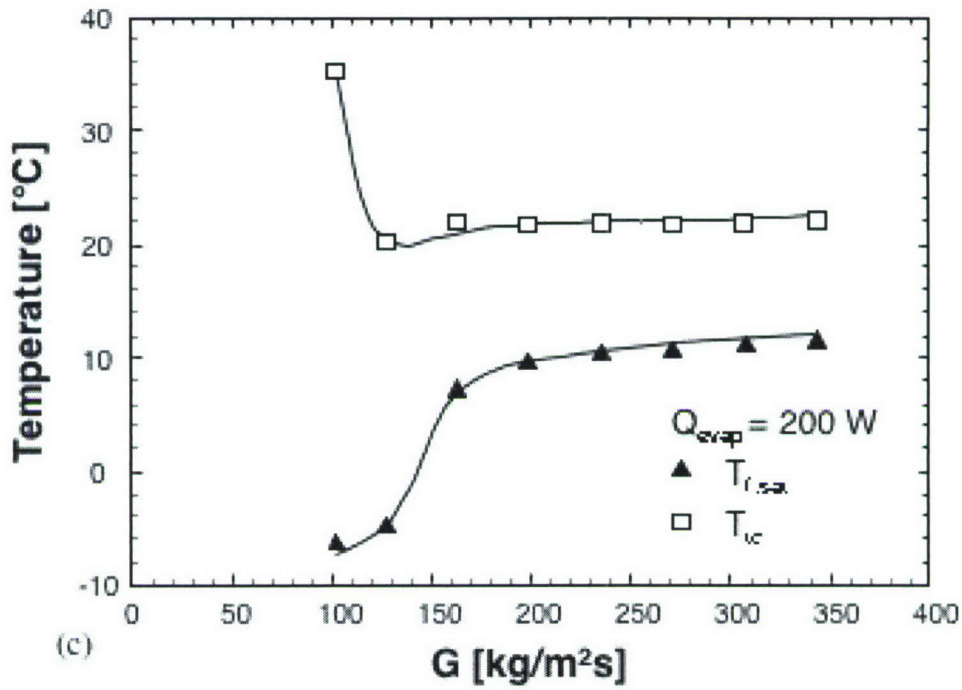

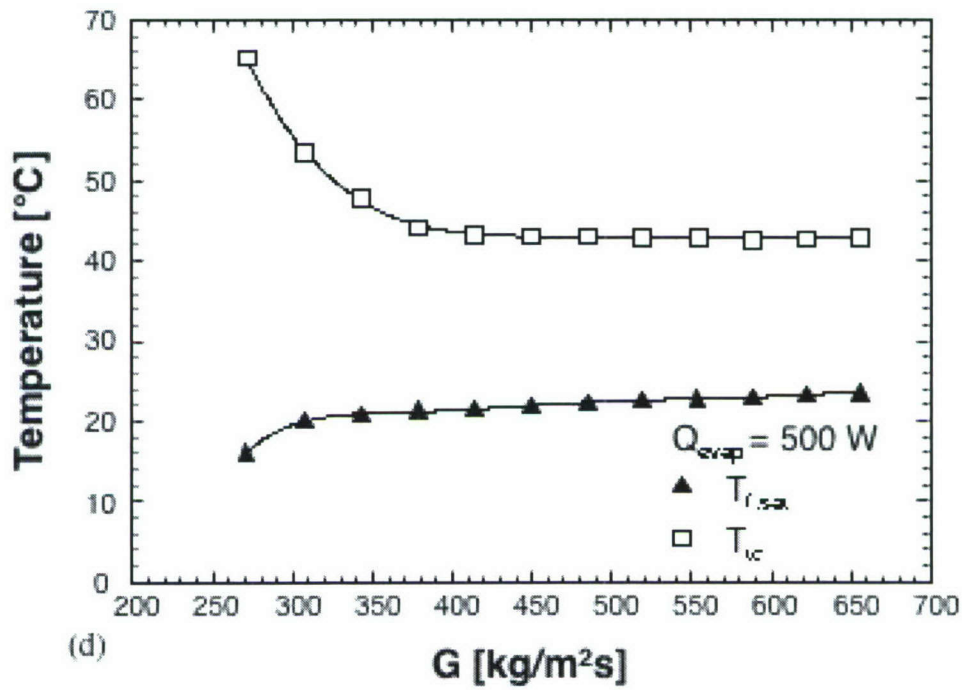

Figure I.5.1 continued.

compression (i.e. with liquid present at the compressor inlet). This condition is undesirable for most compressors. For example, reciprocating compressors are designed to shut down under such wet inlet conditions. On the other hand, rotary compressors can tolerate some wet compression, though their performance may be greatly degraded, let alone the potential damage to their mechanical components. Figure I.5.2 shows the lower mass velocity of G = 128 kg/m^{2}s producing superheated evaporator outlet conditions and dry compression. The compressor performance in this case is greatly enhanced, producing a far greater compression ratio that with wet compression. For a fixed condenser side temperature, dry compression also causes appreciable reduction in the evaporator side refrigerant temperature compared to wet compression.

Returning to Fig. I.5.1, the copper to fluid temperature difference (measure of thermal resistance of micro-channel heat sink) is fairly constant (less than 0.1 °C/W under most evaporator thermal load conditions) for wet compression conditions associated with high mass velocities. However, once dry compression commences as mass velocity is decreased, the thermal resistance begins to increase sharply.

Figure I.5.3 shows the variation of the refrigeration cycle's coefficient of performance (COP) with mass velocity for three evaporator thermal loads. These three cases are within the normal capacity range of the compressor. A far greater COP value is achieved for thermal loads that are higher than the normal range (e.g. Q_{evap} = 500 W). COP is defined here as the ratio of evaporator thermal load to compressor power consumption. COP is highly degraded for wet compression conditions associated with high mass velocities, and greatly enhanced with dry compression at low mass velocities. Notice, however, that further reduction in mass velocity causes a slight decline in COP, especially notable for Q_{evap} = 100 W. This can be explained by the greater superheat at the compressor inlet producing a larger specific volume of vapor, which requires greater compressor power for the same compression rate, i.e. yields a lower COP.

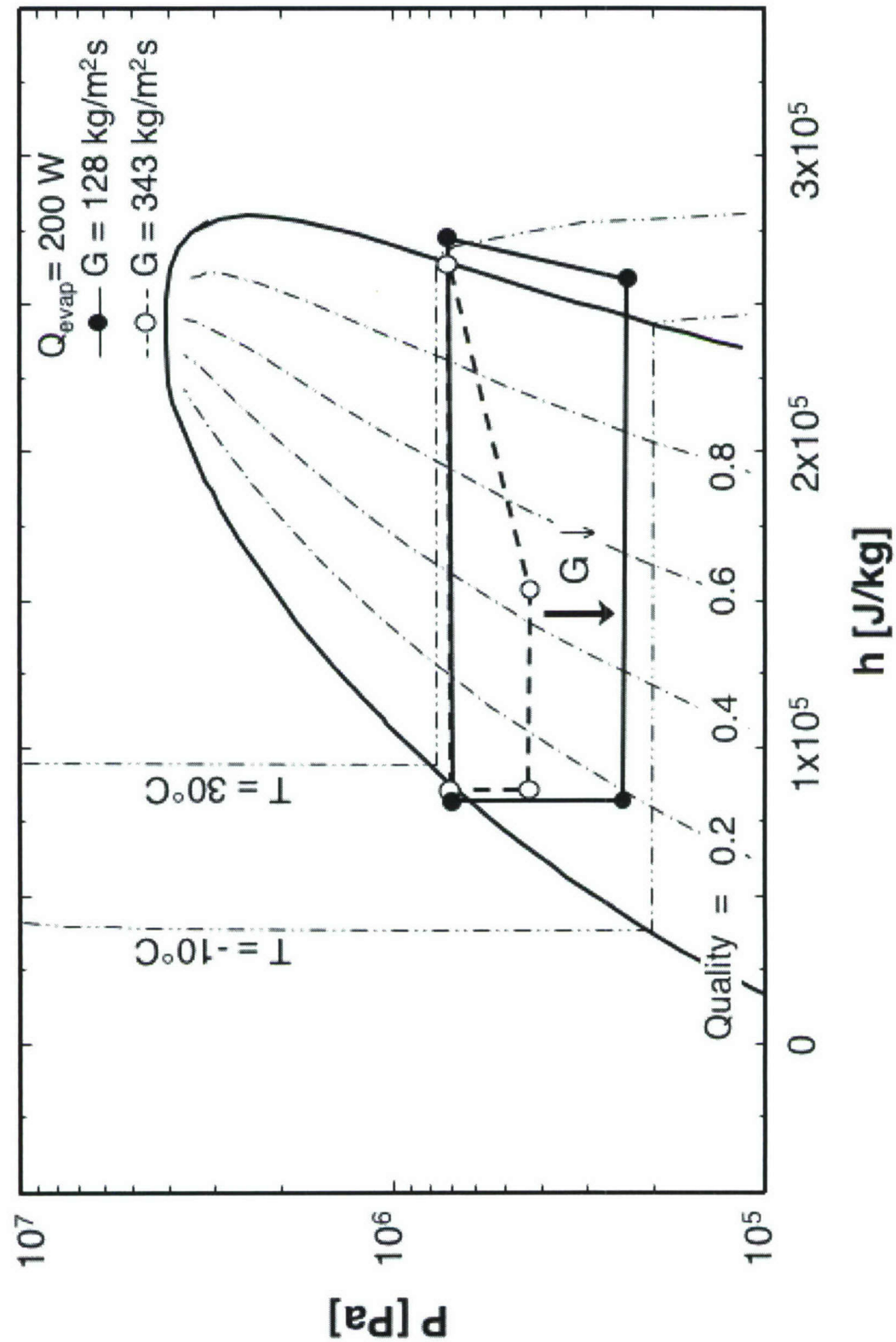

Figure I.5.2 Pressure-enthalpy (*P-h*) diagram for two evaporator mass velocities.

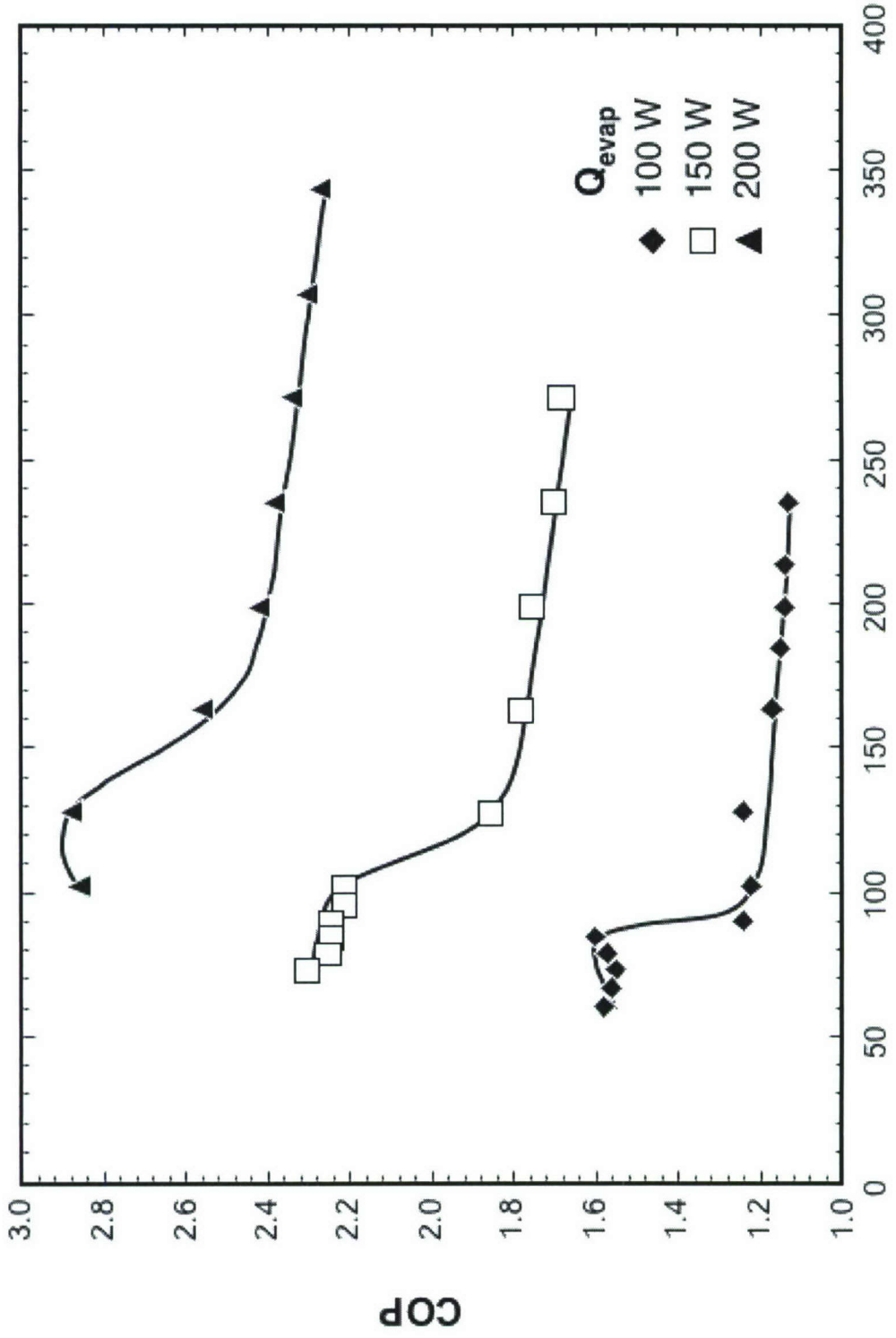

Figure I.5.3 Variation of cycle COP with mass velocity for three evaporator heat loads.

One may speculate a similar reduction in COP due to the increased specific volume caused by the relatively large pressure drop of a two-phase micro-channel evaporator. While the pressure drop per unit length is much greater for a micro-channel than for a conventional evaporator, it should be emphasized that the evaporator in this study is intended as a heat sink for a relatively short electronic device, so the evaporator pressure drop is fairly small even if the pressure gradient is large. This implies the effect of evaporator pressure drop on cycle performance is negligible. The *P-h* diagram in Fig. I.5.2 clearly demonstrates this point.

Overall, the compressor suction (inlet) condition poses a fundamental challenge to implementing micro-channel refrigeration cooling in electronic applications. On one hand, higher heat removal rates are possible with a lower evaporator exit quality, i.e. wet compression. On the other hand, optimum cycle performance and compressor reliability favor dry compression. Furthermore, heat dissipation from an electronic device is not constant during normal device operation. This points to the need to incorporate an adaptive control system (e.g. using a thermostatic expansion valve) to maintain minimal superheat at the compressor inlet.

I.5.2 Heat Sink Temperature Distribution

Aside from the need to remove the heat dissipated from an electronic device, the device temperature must be maintained as low and uniform as possible in order to minimize thermal stresses that can trigger mechanical failure. Since it is quite difficult to measure the temperature distribution along the heat sink, this distribution was inferred using correlations for two-phase pressure drop and heat transfer coefficient that were developed from previous chaptr I.3 and I.4. The thermodynamic equilibrium quality at any distance z along a micro-channel was calculated from equation (I.2.1) by replacing total lengthe L to locan length z. The local refrigerant saturation temperature was obtained from the saturated pressure determined from the pressure drop model.

Figure I.5.4 shows the calculated variations of quality, x_e, two-phase heat transfer coefficient, h_{tp}, and heat-sink base-wall temperature, $T_{w,b}$ (see Fig. I.2.4) along the flow direction for a total evaporator thermal load of Q_{evap} = 200 W and three different values of mass velocity. The local heat transfer coefficient decreases monotonically along the heat sink. Irregularities in this variation are due to the use of discrete correlations for h_{tp} corresponding to different quality regions. The heat transfer coefficient is highest at the inlet where liquid is abundant, and decreases sharply in the high quality region, corresponding to localized wall dryout and superheated flow ($x_e > 1$), where the heat is removed mostly by the vapor. Notice the appreciable increase in wall temperature in the high quality region, especially when the evaporator outlet is superheated (Fig. I.5.4 (c)). Considering heat sinks are relatively short and made from high conductivity material, the sharp increase in wall temperature depicted in Fig. I.5.4 (c) for a superheated outlet should be greatly dampened with an actual electronic device. As shown in Fig. I.5.4 (c), the area-averaged wall temperature, defined as

$$\overline{T}_{w,b} = \frac{\int_0^L T_{w,b}\, dz}{L}, \qquad \text{(I.5.1)}$$

is much smaller than the outlet temperature. Nonetheless, the localized temperature excursion towards the outlet must be minimized to avoid high thermal stresses. In other words, it is important to pursue acceptable outlet quality values while minimizing the temperature gradient along the heat sink.

(a)

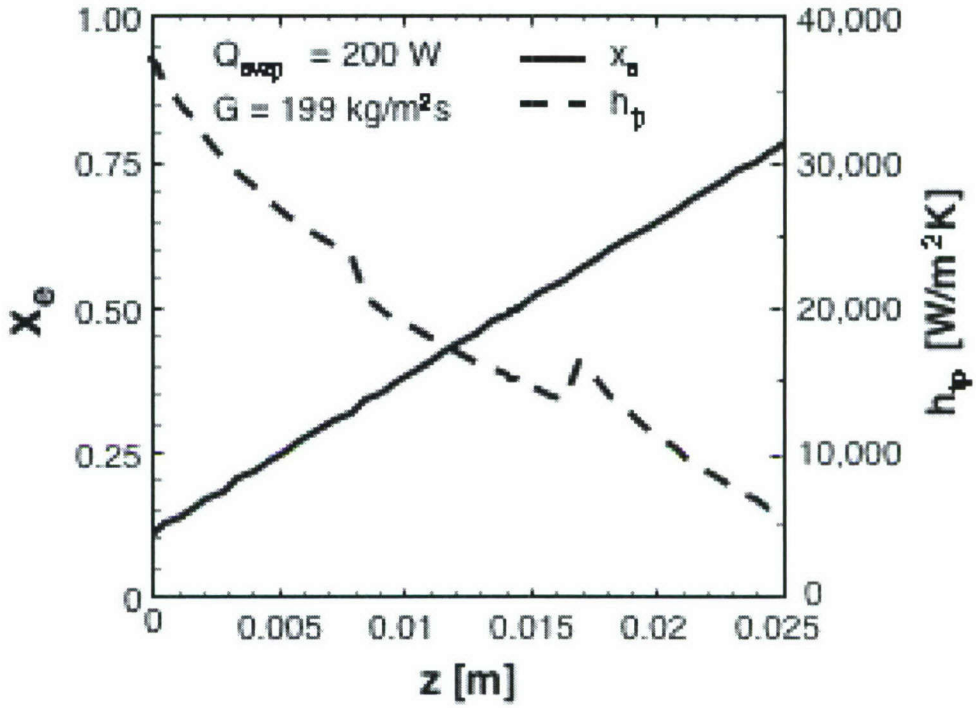

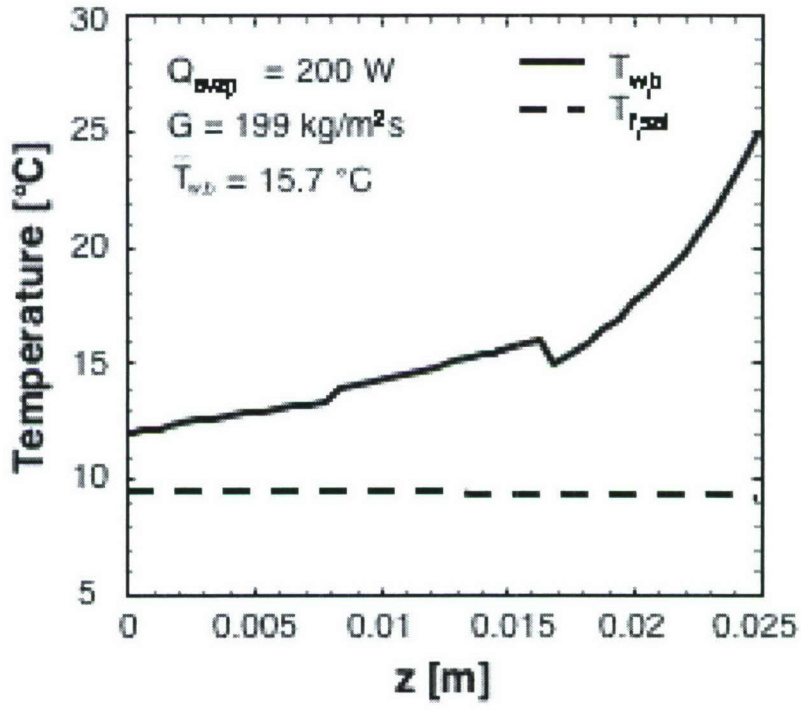

Figure I.5.4 Predicted variations of quality, two-phase heat transfer coefficient and channel base temperature along micro-channel for evaporator heat load of 200 W and mass velocities of (a) 199, (b) 163, and (c) 128 kg/m^2·s.

(b)

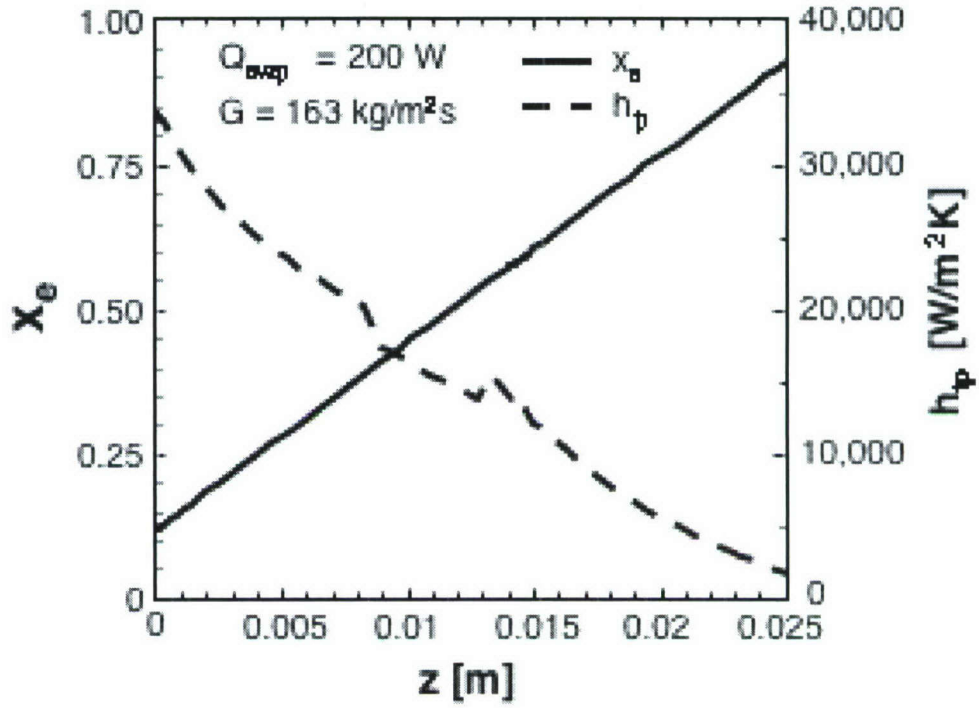

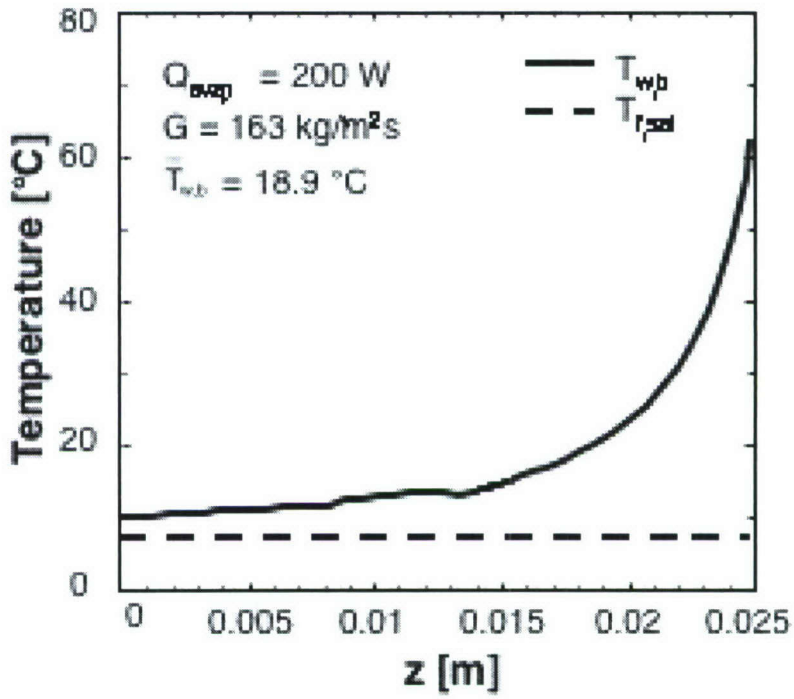

Figure I.5.4 continued.

(c)

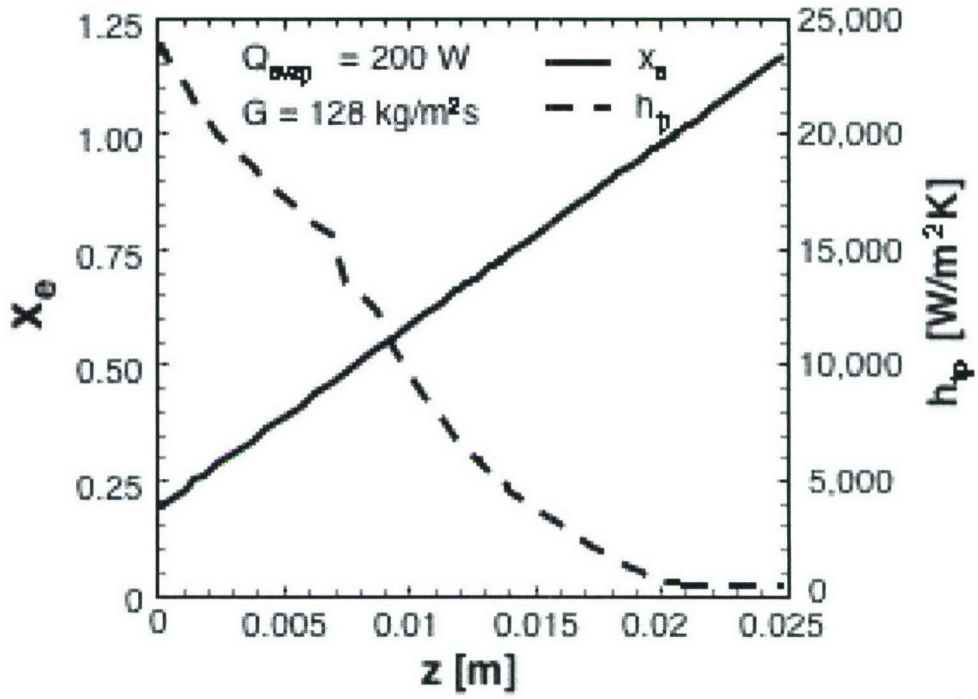

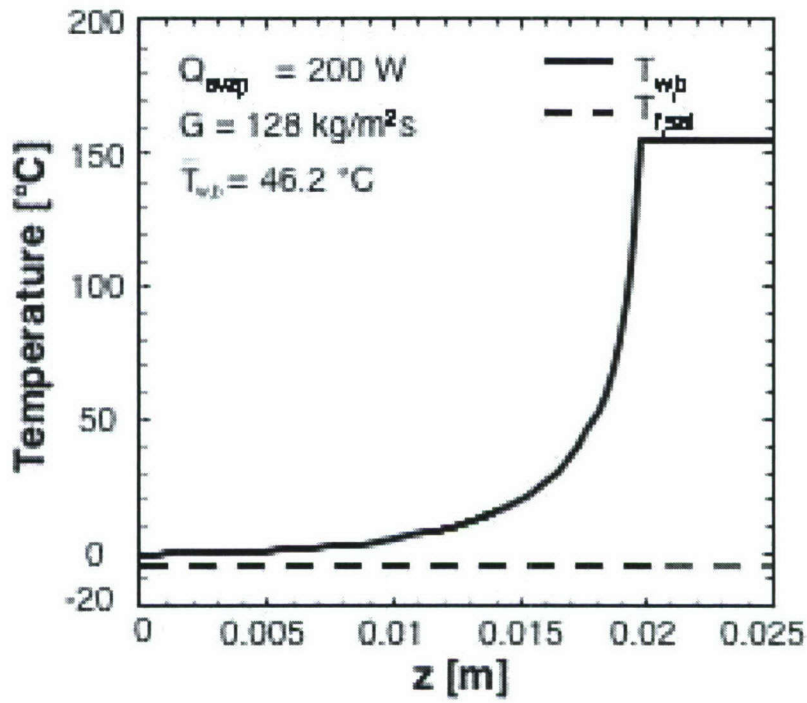

Figure I.5.4 continued.

I.5.3 Parametric Effects of Micro-Channel Geometry on Heat Sink Performance

To explore the effects of the heat sink's geometrical parameters on cooling effectiveness, several externally determined operating conditions were held constant. First, the heat sink was configured to cool a 2.53 x 2.53 cm^2 device surface dissipating a uniform heat flux of $q'' = 100$ W/cm^2 (total evaporator heat load of 640 W). Furthermore, refrigerant R134a was assumed to enter the evaporator at $P_{in} = 2.5 \times 10^5$ Pa as a two-phase mixture with a quality of $x_{e,in} = 0.05$. To ensure proper compressor operation (dry compression) and a good COP while precluding appreciable outlet wall temperature rise, the evaporator outlet quality was set at $x_{e,out} = 1.01$. Equation (I.2.1) was used to determine the mass velocity required to yield this outlet quality value. Finally, the parametric study employed a channel wall thickness equal to the channel width.

Figure I.5.5 (a) shows the effects of channel hydraulic diameter on heat sink performance for a fixed channel aspect ratio. Lower mean wall temperatures are achieved by decreasing the hydraulic diameter. However, this advantage is realized with a penalty of increased pressure drop. Figure I.5.5 (b) shows the effects of aspect ratio for a constant hydraulic diameter. Notice, the advantages of reducing both mean wall temperature and pressure drop are realized concurrently by increasing the aspect ratio.

Figure I.5.6 shows the effects of channel width for a fixed channel height. Figure I.5.6 (a) shows reducing the channel width for a fixed height decreases the hydraulic diameter while increasing the aspect ratio. Figure I.5.6 (b) shows decreasing channel width produces the desired decrease in mean wall temperature, brought about mainly by reducing the hydraulic diameter. By maintaining a high aspect ratio, the same decrease in channel width is shown yielding only a modest increase in pressure drop. These findings point to a very important tactic in designing micro-channel evaporators: using narrow micro-channels with a high aspect ratio.

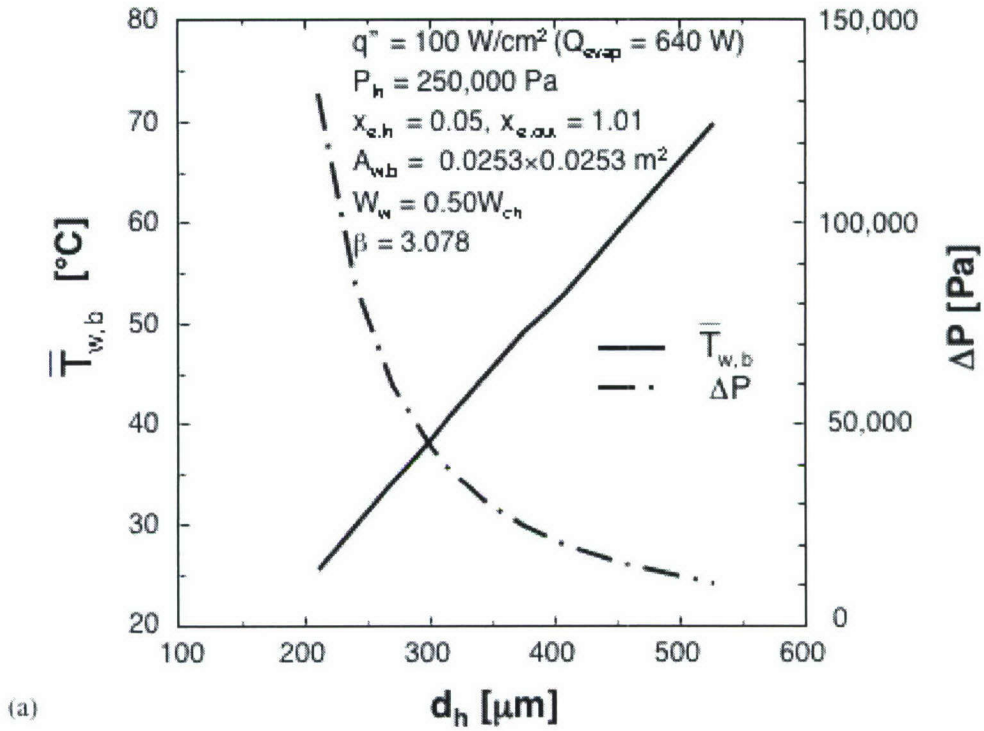

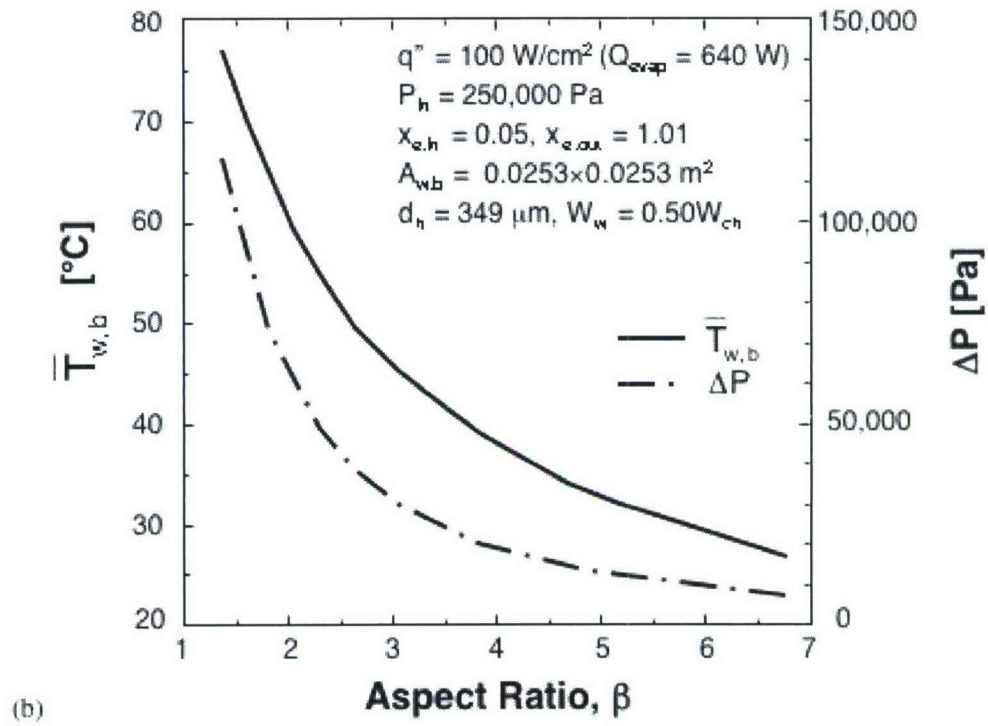

Figure I.5.5 Variations of mean micro-channel base temperature and pressure drop with (a) hydraulic diameter and (b) channel aspect ratio.

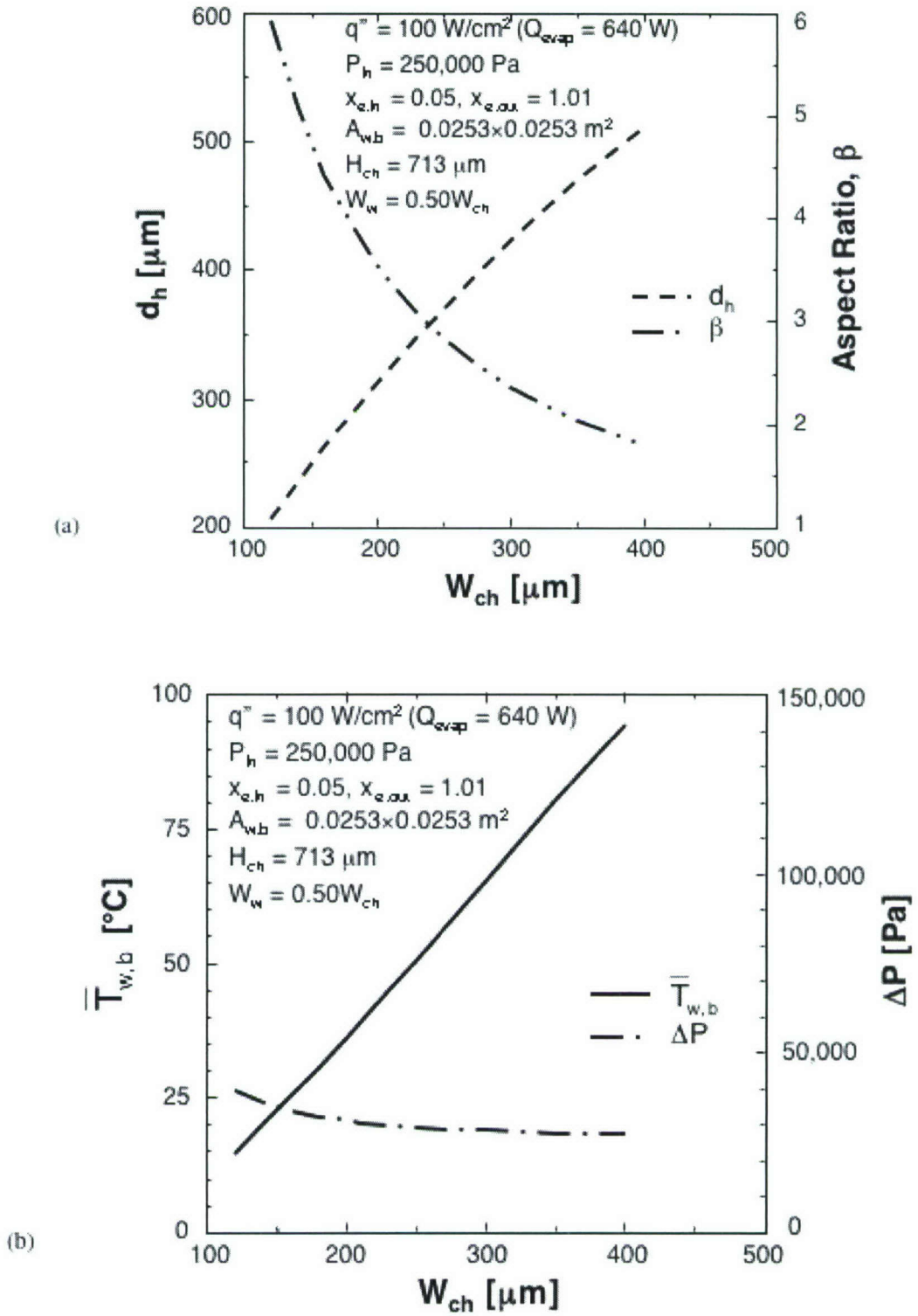

Figure I.5.6 (a) Variations of hydraulic diameter and aspect ratio with channel width for constant channel height. (b) Variations of mean channel base temperature and pressure drop with channel width for constant channel height.

I.6 CONCLUSIONS

I.6.1 Two-phase Pressure Drop in Micro-Channel

The pressure drop characteristics were investigated experimentally for a heat sink with parallel rectangular micro-channels that served as an evaporator in an R134a refrigeration cycle. Both homogeneous equilibrium and separated flow models were assessed for accuracy in predicting the new data, and a new correlation was developed to improve the overall predictive capability of the latter. Key findings from the study are as follows:

(1) Using several popular two-phase viscosity models, the homogenous equilibrium model generally underpredicted the present R134a data.

(2) Popular macro-channel separated flow model correlations generally yielded better predictions of pressure drop than some recent small-channel correlations.

(3) Since two-phase flow in high-flux micro-channel heat sinks is predominantly slug or annular, a new correlation was developed that was based on the separated flow model. The new correlation incorporates the effects of liquid inertia, viscous force and surface tension on the two-phase pressure drop multiplier. Excellent agreement is achieved between pressure drop predictions based on the new correlation and both present R134a data and prior micro-channel water data.

(4) The total pressure drop generally increases with increasing mass velocity and/or heat flux. However, there is appreciable diminution in this increase where complete conversion to vapor takes place inside the micro-channels.

(5) The throttling valve in a refrigeration cycle offers important benefits to the operation of a micro-channel evaporator. By stiffening the system against interactions between the two-phase flow in the evaporator and the upstream compressible volume, the

throttling valve serves to suppress any large pressure oscillations, allowing only mild parallel channel instability to take place.

I.6.2 Boiling Heat Transfer in Micro-Channel

Experiments were performed to explore the heat transfer characteristics of a micro-channel heat sink incorporated as an evaporator in a refrigeration cycle. Flow visualization studies at different quality values were used along with heat transfer coefficient data to develop a new correlation scheme for micro-channel flow that was validated for both R134a and water. Key findings from the study are as follows:

(1) Two-phase heat transfer in micro-channel heat sinks is associated with different mechanisms for low, medium and high quality flows. Bubbly flow and nucleate boiling occur only at low qualities ($x_e < 0.05$) corresponding to very low heat fluxes. High fluxes produce medium quality ($0.05 < x_e < 0.55$) or high quality ($0.55 < x_e < 1.0$) flows (depending on flow rate), where the heat transfer is dominated by annular film evaporation. Because of the large differences in heat transfer mechanism between the three quality regions, better predictions are possible by dividing the quality range into smaller ranges corresponding to these flow transitions.

(2) While the Martinelli parameter commonly used in macro-channel correlations is important to each of the three quality ranges, accurate correlation of data for different coolants requires incorporating the effects of boiling number and Weber number for the medium quality range.

(3) A new three-range two-phase heat transfer coefficient correlation is recommended which shows excellent predictive capability for both R134a and water.

I.6.3 System Implementation

This study was performed to explore optimum conditions for incorporating a micro-channel heat sink as an evaporator in a refrigeration loop. Experimental measurements and numerical results were used to assess the thermal performance of the heat sink in relation to the performance of the refrigeration cycle. Key conclusions from the study are as follows:

(1) Utilizing a micro-channel heat sink as an evaporator in refrigeration loop provides several important thermal benefits such as high-flux dissipation, low surface-to-coolant resistance, and most importantly low device temperature.

(2) Higher heat transfer coefficients are possible with greater mass velocities. However, greater mass velocities are typically associated with wet compression conditions corresponding to evaporator exit quality below unity and liquid entrainment at the compressor inlet. Wet compression compromises compressor performance and reliability as well as refrigeration cycle efficiency. Wet compression must therefore be minimized by maintaining only slightly superheated conditions at the compressor inlet, or using a wet-compression-tolerant compressor.

(3) Another thermal disadvantage of a superheated evaporator outlet is the likelihood of a localized increase in the solid wall temperature towards the outlet, which can cause large thermal stresses at the same location. Practical solutions are therefore needed to develop systems which are both wet compression tolerant and that include adaptive flow control to maintain the desired evaporator outlet quality.

(4) A parametric study of the effects of channel geometry on heat sink performance points to channels with small width and high aspect ratio as yielding superior thermal performance corresponding to only a modest penalty in pressure drop.

PART II. MICRO-CHANNEL HEAT SINK FOR INDIRECT REFRIGERATION COOLING

II.1 INTRODUCTION

II.1.1 System and Flow Visualization

Aggressive pursuit of faster signal speed and superior performance of electronic devices has precipitated unprecedented increases in heat dissipation at all levels of electronics packaging, device, module and system. New innovative cooling methods are therefore required to remove the dissipated heat. Today, localized heat dissipation from advanced microprocessors has already exceeded 100 W/cm^2, while high-end defense applications such as lasers, microwave devices, and radars are beginning to exceed 1000 W/cm^2 (Mudawar, 2001). Another primary function of an electronics cooling system is to maintain device temperature below a limit that is set by both material and reliability concerns. This limit varies with application, from 85 °C for commercial microprocessors to about 125 °C for defense electronics (Mudawar, 2001).

Any high-flux liquid-cooled electronic module can be characterized by an overall thermal resistance between device and ambient (typically room air). This resistance is the sum of all conductive resistances of materials comprising the electronic package as well as the convective resistances of coolant internal to the package as well as the ultimate ambient cooling fluid. Advances in both material and packaging have greatly reduced the overall thermal resistance of the package. Similar aggressive efforts are underway to reduce the internal convective resistance using such powerful cooling schemes as micro-channel flow and jet impingement, especially where the coolant undergoes phase change.

The difficulty implementing even the most aggressive and powerful cooling schemes is that, for fixed overall resistance and ambient temperature, device temperature increases fairly linearly with increasing heat dissipation rate. This relationship is especially problematic for defense electronics, where dissipating say 1000 W/cm^2 would bring the device well above its maximum temperature limit. To circumvent this problem, direct or indirect low temperature cooling systems could facilitate appreciable reduction in the temperature of coolant inside the electronic package, and, hence, in the temperature of the device itself.

During the past few years, there has been a noticeable increase in the number of commercial systems that capitalize on low temperature cooling (Peeples, *et al.*, 2000, Schmidt and Notohardjono, 2002). The most popular of those is the vapor compression refrigeration system, which features high mechanical reliability and good ratio of temperature drop to thermal capacity. Even lower temperatures are possible with cryogenic cooling systems such as Joule-Thomson, Stirling cycle, pulse tube, thermo-acoustic, Gifford McMahon and submerged liquid cryogen. Aside from their cooling merits, cryogenic temperatures provide the benefits of better reliability and enhanced performance (Kirschman, 1985). In fact, much faster switching time has been clocked with devices at 100 K compared to those at above ambient temperature. However, a key drawback to cryogenic cooling systems is very low thermal capacity, let alone high cost. These drawbacks render vapor compression systems the most feasible choice for applications demanding low temperature cooling. These systems possess good thermal capacity and can yield cooling temperatures from 0 to -100 °C.

Two types of refrigeration cooling systems are possible. The first involves incorporating the cooling module as an evaporator in the vapor compression cycle. In other words, the refrigerant serves as primary coolant for the electronic device. This configuration can be classified as *direct refrigeration cooling*. The second involves rejecting the heat from the primary coolant via a heat exchanger to refrigerant flowing in a separate vapor compression cycle. This configuration can be classified as *indirect refrigeration cooling*, and is the focus of the present study.

Recently, the author of the present study proposed a new direct refrigeration cooling system incorporating a micro-channel evaporator inside which the electronic device is cooled by the refrigerant (Lee and Mudawar, 2005a, 2005b, 2006). Using R-134a as working fluid, their study yielded convective heat transfer coefficients comparable to those for water, which has far better thermal transport properties than R-134a (Lee and Mudawar, 2005b). However, compromises had to be made between enhancing the evaporator's performance and the performance of the cycle as a whole. On one hand, enhancing the evaporator's thermal performance while avoiding dryout favors reducing the evaporator's exit quality. However, this may compromise the performance of the compressor, which favors dry superheated evaporator exit conditions (Lee and Mudawar, 2006). A practical solution was recommended that involved the use of a thermal load control device (*e.g.,* thermostatic expansion valve) to ensure only slightly superheated vapor conditions at the compressor inlet.

The present study concerns the second, indirect refrigeration cooling configuration. A key advantage of this configuration over the direct refrigeration configuration is that it decouples the quality requirements of the micro-channel heat sink from those of the compressor in the vapor compression cycle. Two advantages are readily realized with this decoupling. First, the aforementioned compressor problems are completely eliminated. Second, by sizing the vapor compression cycle separately, the cooling system can be designed to simultaneously handle both the required heat rejection capacity and heat rejection temperature. The present study centers on the performance of the micro-channel heat sink using a properly sized indirect refrigeration cooling system.

Using indirect refrigeration cooling, there is greater control over two-phase behavior inside the micro-channel. While two-phase flow inside a direct-refrigeration-cooled micro-channel evaporator is predominantly annular, indirect cooling can maintain even highly subcooled flow boiling conditions, which can greatly enhance convective heat transfer coefficient and delay critical heat flux (CHF).

The earlier part of present study describes the indirect refrigeration cooling system and experimental methods used. Also discussed in this part is flow boiling behavior that is captured with the aid of high-speed video imaging and photomicrography. Using four differently sized micro-channel heat sinks and broad ranges of operating conditions, the captured two-phase behavior is used to identify dominant mechanisms at heat fluxes up to an including CHF. This behavior is also used in the consecutive part of the study for assessment of existing pressure drop and heat transfer coefficient correlations and model development.

II.1.2 Subcooled Boiling Pressure Drop and Heat Transfer

II.1.2.1 Application of Subcooled Flow Boiling for Hig-Flux Cooling

Flow boiling is known for its ability to produce very high convective heat transfer coefficients, which is why it is widely used in many applications demanding high-flux heat removal. Two main regimes are possible with flow boiling, subcooled and saturated; each is also made up of sub-regimes. Subcooled and saturated boiling can occur concurrently in a long heated channel if the incoming fluid is supplied below saturation temperature corresponding to the inlet pressure. With an inlet thermodynamic equilibrium quality below zero, subcooled boiling prevails in the inlet region and as the quality rises along the channel, a point is ultimately reached where transition to saturated boiling takes effect. Because of large differences in void fraction, the heat transfer mechanism for subcooled boiling is categorically different from that for saturated boiling. In the subcooled region, liquid flow is more abundant and phase-change occurs mostly by bubble formation at the wall. High void fractions in saturated boiling are associated with churn, slug and annular flows in which bubble nucleation is gradually replaced by evaporation of a residual liquid film at the heated wall.

In general, higher average heat transfer coefficients are possible with subcooled flow boiling than with saturated. Critical heat flux (CHF) is also greater for subcooled boiling. Furthermore, there are drastic differences in CHF mechanism between the two

regimes. Subcooled CHF (commonly referred to as "departure from nucleate boiling" or DNB for short) is often the result of localized vapor blanket formation along the heated wall even while liquid is abundant in the core. On the other hand, CHF in saturated boiling occurs in a predominantly liquid deficient region, and is usually the result of dryout of the annular liquid film.

Clearly, subcooled boiling is quite advantageous for high-flux applications. This regime can be achieved in a variety of ways, the two most common are increasing mass velocity and increasing liquid subcooling at the inlet. Channel geometry can also have a strong effect on the extent of the subcooled boiling region. For example, channels with small length-to-diameter ratio are more likely to maintain subcooled boiling.

As discussed in the previous chapter, the recent advances in microelectronics have triggered unprecedented increases in heat dissipation. This trend has spurred the development of many types of phase-change cooling schemes that are aimed at both removing the heat and maintaining low surface temperatures. Micro-channel heat sinks have emerged as one of the most effective thermal solutions, given their compactness and ability to produce very high heat transfer coefficients while demanding low coolant flow rates and small coolant inventory.

Early micro-channel studies were focused mainly on single-phase flow. An often-cited study by Tuckerman and Pease (1981) proved such devices could dissipate up to 790 W/cm^2 from a simulated electronic heat source using water as working fluid. Interestingly, flow boiling in micro-channels has been the subject of intense study since the mid-1970s at the Massachusetts Institute of Technology Energy Laboratory for cooling of electrodes in magnetohydrodynamic energy converters and turbine blades (Mudawar, *et al.*, 1985). A fairly large number of studies of flow boiling in micro-channels have been published since the mid-1990s (*e.g.,* Bowers and Mudawar, 1994a, 1994b, 1994c, Mudawar and Bowers, 1999, Lee and Lee, 2001a, 2001b, Yu, *et al.*, 2002, Qu and Mudawar, 2002, 2003a, 2003b, 2003c, Lee and Mudawar, 2005a, 2005b). Mudawar and Bowers (1999) showed highly subcooled and high mass velocity flow

boiling of water in small diameter tubes could safely dissipate heat fluxes as high as 27,000 W/cm^2.

The present study suggestes an indirect refrigeration cooling scheme where the primary coolant inside the micro-channel heat sink is brought to very low temperature at the micro-channel inlet in order to maintain highly subcooled conditions. Despite the small hydraulic diameter of the micro-channels, the low coolant temperature was shown to preserve subcooled boiling along much of the micro-channel length, especially at high mass velocities.

The primary objectives of this part of the study are to:

(1) Explore the parametric trends of subcooled boiling pressure drop and heat transfer.

(2) Evaluate the effectiveness of previous correlations in predicting the new data.

(3) Develop more accurate correlations for both pressure drop and heat transfer.

(4) Develop mechanistic models for both pressure drop and heat transfer.

II.1.2.2 Thermodynamic Considerations in Subcooled Flow Boiling

As indicated in the previous section, subcooled flow boiling occurs when liquid is supplied into a heated channel is subcooled state. Single-phase heat transfer to liquid occurs over a finite length of the channel until bubbles begin to form along the wall, indicating transition to subcooled boiling. As core liquid temperature continues to rise along the channel, transition to saturated boiling ultimately ensues. Because of strong departure from thermodynamic equilibrium, predicting subcooled boiling is a very challenging endeavor, especially in the ability to develop reliable models for pressure drop and heat transfer.

Figure II.1.1 shows a simplified schematic of the transitions from single-phase cooling to saturated boiling. Following a classification by Collier and Thome (1994), the subcooled boiling region is comprised of two zones. The first is a *highly subcooled*

zone whose upstream edge corresponds to the onset of boiling, z_{ONB}. Within this zone, bubbles are able to form but show minor growth while still attached to the wall. Suppressed bubble growth in this zone is the result of a thermal balance between superheat effects at the wall and condensation along the bubble interface. A second *developed subcooled zone* begins at z_{bd} at which bubbles begin to detach into the liquid flow where they condense slightly but are able to endure and even coalesce with one another. The second zone extends downstream to the location where thermodynamic equilibrium quality, defined as

$$x_e = \frac{h_f - h_{f,sat}}{h_{fg}}, \tag{II.1.1}$$

reaches zero. This location marks the upstream edge of the saturated boiling region. A key distinction between the highly subcooled zone and developed subcooled zone is that void fraction is a wall effect for the first and a bulk flow effect for the second.

The existence of the two subcooled zones will be verified in the flow visualization experiments. In these experiments, bubbles upstream of the departure point showed mild thermal growth while sliding along the wall. Downstream of the departure point, bubbles grew in size and were able to detach and coalesce with one another.

II.1.2.3 General Trends of Subcooled Boiling Pressure Drop

As subcooled liquid heat ups along the wall of a heated channel, its viscosity decreases. Increasing the wall heat flux causes further reduction in liquid viscosity. Therefore, pressure drop associated with pure liquid flow decreases with increasing wall heat flux. The trend changes significantly when vapor begins to form. Here, increasing wall heat flux increases both the two-phase frictional and accelerational gradients of pressure drop. Pressure drop therefore begins to increase with increasing heat flux. These trends are illustrated in Fig. II.1.2 in the form of a normalized plot of

pressure drop versus wall heat flux. The pressure drop, ΔP, for a given wall heat flux is normalized with respect to pressure drop corresponding to adiabatic flow, ΔP_{ad} ($q'' = 0$). Wall heat flux is normalized with respect to the value q''_{sat} of heat flux required to bring thermodynamic equilibrium quality of the flow to zero at the channel exit, where

$$q''_{sat} = \frac{\dot{m}\, c_{p,f} \left(T_{sat} - T_{in}\right)}{A_{base}} \,. \tag{II.1.2}$$

Tong *et al.* (1997) indicated the onset of nucleate boiling (ONB) does not coincide exactly with the point of minimum pressure drop in Fig. II.1.2, and ONB generally occurs at a lower heat flux. One possible explanation for this offset is the existence of the highly subcooled zone. Because void fraction is quite small in this zone, any increases in two-phase frictional and accelerational pressure gradient are dwarfed by the pressure gradient of liquid, which covers a large fraction of wall area in the highly subcooled zone. The situation is quite different after the point of vapor departure, where the two-phase frictional and accelerational pressure gradients begin to increase substantially because of a large increase in void fraction.

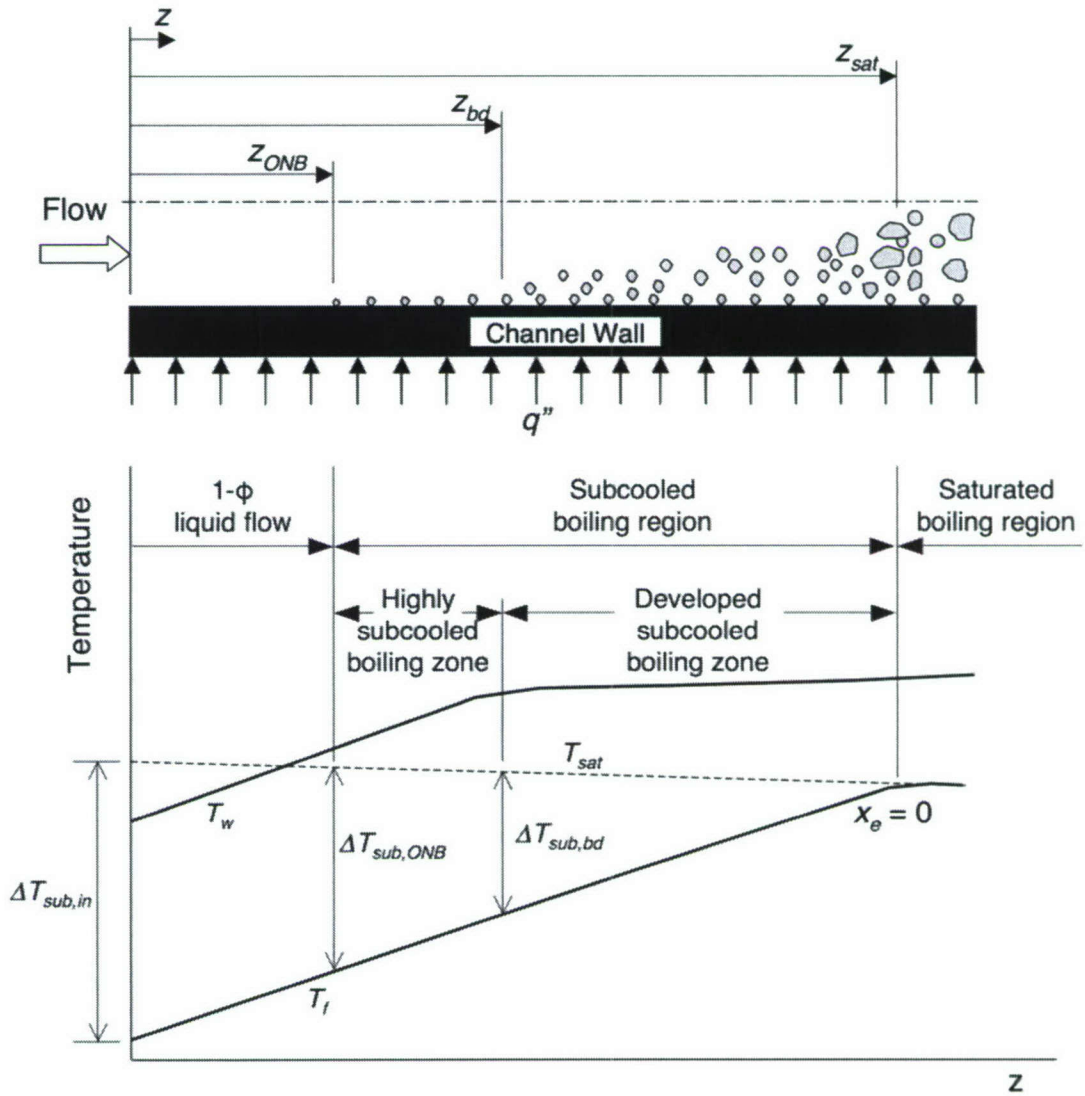

Fig. II.1.1 Schematic representation of subcooled boiling zones.

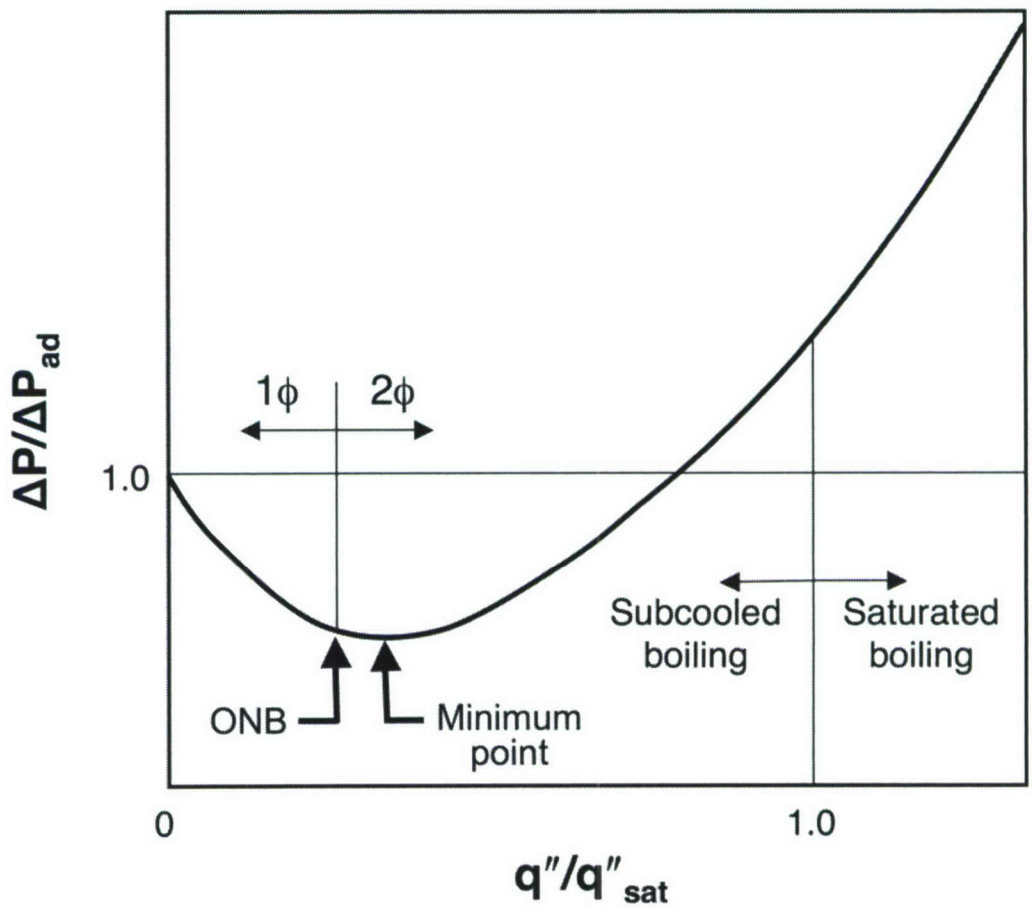

Fig. II.1.2 Normalized plot of pressure drop versus wall heat flux for subcooled boiling.

II.1.3 Two-phase Flow Model for Subcooled Boiling Pressure Drop

The present study concerns highly subcooled flow boiling, where sub-zero quality is preserved even as the fluid exits the micro-channels. Here, vapor is formed by nucleation at the wall with a highly subcooled liquid core flow. Severe departure from thermodynamic equilibrium renders modeling of two-phase flow in this case highly elusive.

Pressure drop is a key parameter in the design of a two-phase cooling system. Pressure drop in subcooled flow boiling consists of frictional and accelerational components, and the magnitude of each is highly dependent on void fraction. Departure from thermodynamic equilibrium greatly complicates the task of relating void fraction to flow quality, which is the primary reason behind the difficulty predicting pressure drop in subcooled flow boiling.

While a few models have been proposed for void fraction in subcooled flow boiling (*e.g.,* Rouhani, 1968, Levi, 1967, Saha and Zuber, 1974, Kroeger and Zuber, 1968), use of these models have yielded poor predictions of pressure drop, as suggested by Hoffman and Wong (1992). Dormer and Bergles (1969) and Tong *et al.* (1997) developed an alternative approach to predicting pressure drop for macro-channel flows using empirical formulation. However, correlation evaluations in this study yielded poor predictions for micro-channel flows.

The present study is the first attempt at developing a theoretical control-volume-based model for subcooled flow boiling pressure drop. Control-volume-based models have been quite effective at predicting both pressure drop and heat transfer in saturated flow boiling in micro-channel heat sinks (Qu and Mudawar, 2003a, 2003c) as well as flow boiling critical heat flux (Sturgis and Mudawar, 1999). The model proposed in this study is particularly suited for situations involving severe non-equilibrium between the vapor and liquid phases.

II.1.4 Critical Heat Flux in Subcooled versus saturated Flow Boiling

Critical heat flux (CHF) is arguably the most important design limit for systems involving heat dissipation from heat-flux controlled surfaces. The occurrence of CHF is associated with a sudden, large reduction in the heat transfer coefficient, which is caused by the loss of liquid contact with the solid surface upon which evaporation or flow boiling is occurring. Depending on heat flux magnitude, thermophysical properties, and operating conditions, the loss of coolant contact can result in surface overheating, burnout, or some other form of catastrophic system failure; hence the importance designers place on accurately determining the CHF limit.

Electronics cooling is a rather recent application where CHF determination is crucial to the safe design and operation of high performance microprocessors. The transition from air-cooling to single-phase liquid cooling and, ultimately, two-phase cooling has been spurred by an unprecedented rise in chip heat flux, brought about by aggressive integration of an increasing number of electronic components in a single chip. Nowhere is this rise more alarming than in defense electronics, such as those found in directed energy laser and microwave weapons, and in radars. Current developments in these applications point to the need to dissipate as high as 1000 W/cm^2 at the device level as commented before. This task is complicated by the fact that only dielectric coolants are permitted in these applications. Despite their many attractive attributes, such as high dielectric strength and compatibility with most materials comprising an electronic package, these coolants possess relatively poor thermal transport properties. Therefore, every effort must be made to enhance their cooling potential in order to safely dissipate the anticipated high heat fluxes.

Present study suggests a thermal management solution for high-flux defense electronics in which the dielectric coolant HFE 7100 is pre-cooled by a secondary refrigeration cooling system before entering a micro-channel heat sink to which the electronic device is attached. The refrigeration system provides two key benefits. First, it reduces the temperature of the HFE 7100, which helps maintain relatively low

device temperatures when dissipating very high heat fluxes. Second, the low temperature of HFE 7100 helps maintain subcooled flow boiling conditions inside the heat sink, which greatly increases CHF for a given flow rate. This system was capable of dissipating in excess of 700 W/cm^2.

The present study concerns the determination of CHF for this indirect-refrigeration-cooled micro-channel configuration. Unlike most published two-phase micro-channel studies, which involve saturated boiling, the present cooling configuration involves highly subcooled flow boiling. The key difference between subcooled boiling and saturated boiling is that subcooled boiling occurs at the surface with a bulk liquid temperature below the saturated temperature. With high subcooling, boiling commences when the applied heat flux is capable of superheating liquid adjacent to the surface. Because subcooling is highest in the inlet region of the micro-channel, bubbles near the inlet quickly re-condense at the wall. As the bulk liquid temperature increases along the micro-channel, bubbles are able to grow larger and detach from the surface, mixing into the bulk flow where they undergo partial or full condensation. Condensation greatly reduces the magnitude of void fraction in subcooled compared to saturated boiling. Unlike the drastic flow pattern transitions in saturated flow (bubbly, churn, slug, annular), subcooled flow boiling is dominated by bubbly flow alone. Those differences in flow pattern have a strong bearing on both the mechanism and magnitude of CHF for subcooled versus saturated boiling.

Figure II.1.3 illustrates these differences in CHF mechanism. For saturated flow boiling, large increases in void fraction trigger a succession of flow regimes. The flow eventually culminates in the high void fraction annular flow pattern, where cooling is sustained by evaporation of a thin liquid film along the surface. CHF results from dryout of the liquid film as the surface is exposed directly to the vapor. While the ensuing downstream mist flow provides some cooling by droplet impact with surface, the heat transfer coefficient is drastically smaller than upstream of the dryout point. Dryout typically occurs with low inlet subcoolings, low mass velocities, and large length-to-diameter ratios, and CHF magnitude with dryout is relatively small.

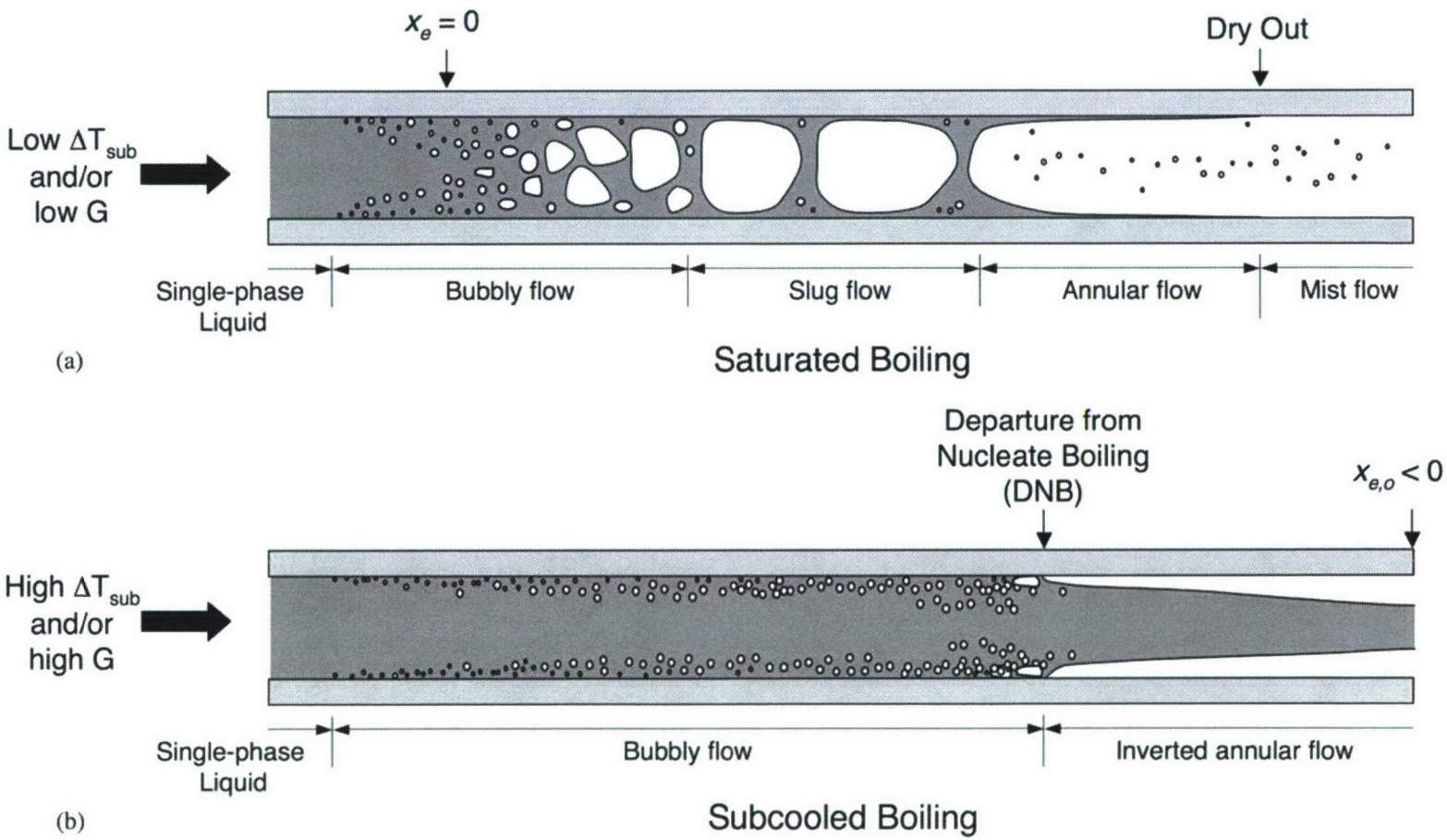

Figure II.1.3 CHF mechanisms for flow boiling in uniformly heated channel: (a) dryout in saturated flow boiling and (b) DNB in subcooled flow boiling.

With highly subcooled flow boiling, bubbly flow persists over much of the channel length, and CHF ensues when bubbles near the wall coalesce into a localized vapor blanket that causes a sharp reduction in the local heat transfer coefficient. This form of CHF is termed Departure from Nucleate Boiling (DNB) and occurs with high inlet subcoolings, high mass velocities, and small length-to-diameter ratios. The magnitude of CHF is much higher than with dryout, and the ensuing surface temperature rise is far more catastrophic.

A significant body of literature has been published that addresses subcooled flow-boiling CHF. The majority of these studies are devoted to the development of correlations from large CHF database or limited experimental data (Mudawar and Bowers, 1999, Hall and Mudawar, 1999, 2000a, 200b, Katto, 1978, 1981, Katto and Ohno, 1984, Kureta and Akimoto, 2002); most of these studies are focused on water data and nuclear reactor cooling. Theoretical treatments of DNB are far more limited (*e.g.* Lee and Mudawar, 1988, Weisman and Pei, 1983, Kwon and Chang, 1999).

Because most prior subcooled boiling studies concern nuclear reactor cooling, available correlations typically address high-pressure water conditions. No effort has yet been made to assess the suitability of these correlations to electronic cooling applications and dielectric coolants.

II.1.5 Micro-Channle versus Macro-Channel Flow Boiling

Another limitation of prior flow boiling CHF correlations is that they are derived from data for macro-channel. Despite the intense recent interest in micro-channel heat sinks for electronic cooling applications, very few studies have been published that address CHF determination (Qu and Mudawar, 2004, Wojatan *et al.*, 2006); alas, these studies concern only saturated flow boiling CHF.

Different recommendations have been made concerning the channel size below which the channel begins to behave as a micro-channel. For the most part,

recommendations have been based on hydraulic diameter. For example, Thome (2004) suggested diameters of 100 – 600 μm be classified as micro-channels.

Distinguishing between macro- and micro-channel flows cannot be based on channel size alone. As will be shown below, a channel may behave as a micro-channel for certain fluids and operating conditions and as a macro-channel for others. Clearly a more rigorous treatment is necessary to define a mechanistically based boundary between the two flow extremes.

For two-phase flow, this boundary is closely related to the ratio of bubble size to channel diameter, the larger the ratio, the more likely that the flow will behave as a micro-channel flow. Kew and Cornwell (1997) used this rationale to determine the boundary between micro-channel and macro-channel flows based on a Confinement number defined as

$$Co = \left[\frac{\sigma}{g\left(\rho_f - \rho_g\right) D_h^2} \right]^{1/2}. \qquad \text{(II.1.3)}$$

They showed that channels become too confining when $Co > 0.5$, which is where macro-channel assumptions begin to fall apart. Table II.1.1 summarizes hydraulic diameter values corresponding to $Co = 0.5$ for several fluids. Notice that low surface tension fluids, such the dielectric coolants FC-72 and HFE 7100, and refrigerant R134a, have lower hydraulic diameters corresponding to the transition from macro- to micro-channel flow, whereas water, with its higher surface tension, produces micro-channel flow in larger channels. However, the boundary values listed in Table II.1.1 are quite larger than those deemed typical of micro-channel flows.

A key weakness of Eq. (II.1.3) is that it is based on the ratio of surface tension force to buoyancy, evidenced by the appearance of gravitational acceleration in the definition of the Confinement number. While this criterion is a good representation for pool boiling in, say, a confined vertical channel, it is not able to account for bubble size in a flow-boiling situation. Aside from surface tension, bubble size in flow boiling is dominated by liquid drag rather than buoyancy. In the present study, an alternative

measure of the boundary between macro- and micro-channel flows is developed which incorporates the influence of liquid drag on bubble size. Equating the drag force on the bubble to the surface tension force that holds the bubble to the wall gives

$$C_D\left(\frac{\pi D_b^2}{4}\right)\frac{1}{2}\rho_f U^2 \sim \pi D_b \sigma. \tag{II.1.4}$$

A channel tends to confine the flow when the diameter determined from Eq. (II.1.4) approaches the diameter of the channel. Therefore, the channel diameter corresponding to the transition from macro- to micro-channel flow can be determined from the relation

$$D_{tran} \leq D_b. \tag{II.1.5}$$

For circular channels, D_{tran} is simply the diameter of the channel.

Two-phase micro-channel flow applications of practical interest are characterized by modest laminar Reynolds numbers, generally greater than 50. Under these conditions, the drag coefficient can be determined from Liao (2002)

$$C_D = \frac{24}{Re_{tran}}\left(1+\frac{3}{160}Re_{tran}\right). \tag{II.1.6}$$

Combining Eqs. (II.1.4) to (II.1.6) and substituting $G = \rho_f U$, yield the following criterion for the transitional channel dimension,

$$D_{tran} = \frac{160}{9}\frac{\left(\sigma\rho_f - 3\mu_f G\right)}{G^2}. \tag{II.1.7}$$

Table II.1.2 shows calculated values of D_{tran} for water and HFE 7100 based on Eq. (II.1.7). Notice how these values are significantly smaller than those given in Table II.1.1, and more representative of values deemed typical of micro-channel flow in recent experimental studies. Table II.1.2 also shows decreasing surface tension and/or increasing mass velocity enables smaller channels to behave as macro-channels.

In is interesting to note that Eq. (II.1.7) can also be expressed as a Weber number criterion for confinement

$$We_{tran} = \frac{160}{9} \frac{1}{\left(1 + \frac{160}{3Re_{tran}}\right)}, \tag{II.1.8}$$

which can be approximated as

$$We_{tran} = \frac{160}{9} \tag{II.1.9}$$

for high mass velocities. Equation (II.1.9) shows Weber number plays an important role in micro-channel flows, and its effect must therefore be incorporated in any micro-channel CHF correlation. This important issue will be discussed later in this study.

Table II.1.1. Fluid properties and hydraulic diameters corresponding to transition from macro- to micro-channel flow for different coolants at one bar based on Eq. (II.1.3).

Fluids	T_{sat} [°C]	h_{fg} [kJ/kg]	ρ_f [kg/m^3]	ρ_g [kg/m^3]	σ [mN/m]	Co (D_h=1.0 mm)	D_{tran} (Co = 0.5) [mm]
Water	99.6	2258	959	0.59	59.0	2.50	5.0
FC-72	55.9	83.54	1603	13.1	12.0	0.88	1.75
R134a	-26.4	217.2	1378	5.19	15.5	1.07	2.14
HFE 7100	59.6	111.7	1373	9.58	15.7	1.08	2.17

Table II.1.2. Fluid properties and hydraulic diameters corresponding to transition from macro- to micro-channel flow for water and HFE 7100 at one bar based on Eq. (II.1.7).

Fluids	T_{sat} [°C]	ρ_f [kg/m^3]	μ_f [kg/m.s]	σ [mN/m]	G [kg/m^{2}s]	D_{tran} [mm]
Water	99.6	959	2.83×10^{-4}	59.0	500	3.99
					1000	0.990
					2000	0.243
HFE 7100	59.6	1373	3.57×10^{-4}	15.7	500	1.49
					1000	0.364
					2000	0.0863

II.2. EXPERIMENTAL METHODS

II.2.1 Indirect Refrigeration Cooling System

Figure II.2.1 shows the diagram of flow loop for this newly proposed indirect refrigeration cooling scheme. As indicated earlier, the vapor compression system is completely isolated from the primary cooling loop containing the micro-channel module. The working fluid in the primary cooling loop is HFE 7100. This 3M Novec fluid has very low freezing point below -100 °C and a relatively moderate boiling point of 60 °C at atmospheric pressure. Like other phase change electronic cooling fluids (e.g., FC-72 and FC-87), HFE 7100 has excellent dielectric properties, is very inert, and its surface tension is much smaller than that of water. But while its shares the zero ozone depletion potential of recent dielectric coolant, HFE 7100 as well as the entire Novec family of coolants also have unusually low global worming potential. Table II.2.1 provides representative values for the thermophysical properties of HFE 7100.

As shown in Fig. II.2.1, HFE 7100 is circulated from a reservoir through the primary loop with the aid of a centrifugal pump. The primary coolant then enters a heat exchanger where its temperature is greatly reduced by rejecting heat to the secondary refrigeration loop. Exiting this heat exchanger, the primary coolant passes through a filter followed by a Coriolis mass flow meter before entering the micro-channel test section. Throttling valves are situated both upstream and downstream of the test section to control both flow rate and pressure drop. Exiting the downstream valve, the primary coolant is returned to reservoir. Figure II.2.1 highlights another practical advantage of an indirect refrigeration cooling system. Because the primary and refrigeration loops are completely isolated, the micro-channel test section maintains only a mild operating pressure, which is advantageous for electronics cooling applications.

To achieve high cooling capacity at low temperatures, a cascade cycle is used in the refrigeration system. This two-stage compression system employs two different refrigerants, R507 for the high compression stage and R508b for the lower stage. With the cascade feature, this system is capable of rejecting 550 W at -80 °C and its capacity increases with increasing temperature. Another feature of this system is its ability to control the temperature of HFE 7100 in the primary loop at the heat exchanger outlet to within ± 0.5 °C.

Table II.2.1 Summary of thermophysical properties of HFE 7100.

	k_f [W/m.K]	μ_f [kg/m.s]	$c_{p,f}$ [kJ/kg.K]	σ [mN/m]
T = - 30 °C	0.0796	14.741×10^{-4}	1073.0	18.214
T = 0 °C	0.0737	8.265×10^{-4}	1133.0	15.683

	T_{sat} [°C]	h_f [kJ/kg]	h_{fg} [kJ/kg]	ρ_f [kg/m^3]	ρ_g [kg/m^3]
P = 1.0 bar	59.63	92.76	111.7	1372.7	9.575
P = 3.5 bar	104.41	145.5	97.61	1238.9	32.143

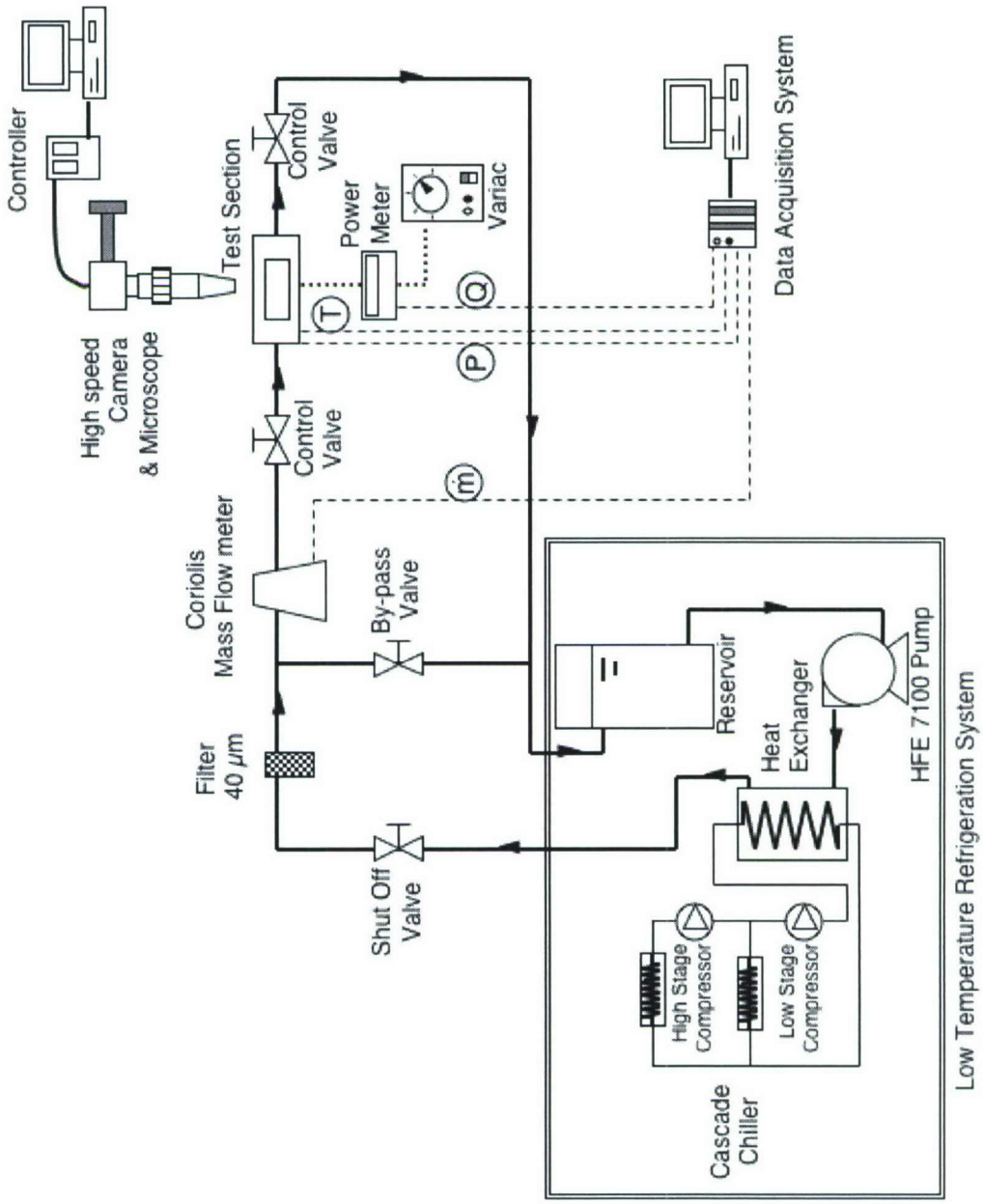

Figure II.2.1 Flow diagram for indirect refrigeration cooling system.

II.2.2 Micro-Channel Test Section

Figure II.2.2 illustrates the construction of the micro-channel test section. Micro-channels with rectangular cross-section were formed by micro-slotting the top surface of an oxygen-free copper block with the aid of a series of thin carbide blades. The enlarged underside of the copper block has four bores to accommodate high-power-density cartridge heaters. The top portion of the copper block is inserted into a rectangular housing made from G-11 fiberglass plastic which is compatible with both low and high temperature operation. This housing features coolant inlet and outlet ports, micro-channel inlet and outlet plenums, and both pressure and temperature instrumentation ports. The micro-channels were formed by clamping a polycarbonate plastic cover plate atop the housing and the copper block. This transparent cover plate provided top viewing access to the flow inside the micro-channels. All other surfaces of the copper block were carefully insulated to minimize heat loss to the ambient.

To examine the effects of micro-channel hydraulic diameter and aspect ratio, four different copper blocks were machined, each containing different micro-channel features. All four copper blocks had the same top 0.5 cm wide by 1.0 cm long heat transfer area. Dimensions of the four test sections are given in Table II.2.2. Figure II.2.3 shows microscope images of the micro-channels in each test section.

Table II.2.2 Test section dimensions.

	W_{ch} [μm]	W_w [μm]	H_{ch} [μm]	AR	D_h [μm]	L [cm]	N
TS #1	123.4	84.2	304.9	2.47	175.7	1.0	24
TS #2	123.4	84.6	526.9	4.27	200.0	1.0	24
TS #3	235.2	230.3	576.8	2.45	334.1	1.0	11
TS #4	259.9	205.0	1041.3	4.01	415.9	1.0	11

II.2.3 Operating Condtions and Measurements

As indicated earlier, the indirect refrigeration cooling system ensured the delivery of primary coolant (HFE 7100) to micro-channel test section at precise temperature using automated feedback contol. Tests were performed at two test module HFE 7100 inlet temperatures, - 30 and 0 °C. Lower temperatures were possible but avoided because frost on the test section's transparent cover plate prohibited optical access.

Aside from inlet temperature, the test matrix for the present study included variations of flow rate of the primary coolant and heat flux; a constant test section's outlet pressure of 1.138 bar was maintained throughout the study. Table II.2.3 provides ranges of key parameters of the study for each of the four test sections.

The test section's instrumentation included pressure transducers and thermocouples for both the inlet and outlet plenums. Three type-T thermocouples were also inserted in the copper block beneath the micro-channels as illustrated in Fig. II.2.4. The three thermocouple measurements ($T_{tc,1}$, $T_{tc,2}$, $T_{tc,3}$) enabled the calculation of heat transfer coefficients and wall temperatures at the base of the micro-channel ($T_{w,1}$, $T_{w,2}$, $T_{w,3}$) immediately above using a fin analysis method and the assumption of 1-D vertical conduction as discussed in Part I and Qu and Mudawar (2003a, b). Other measurements included electrical power input to the test section's four cartridge heaters using a Wattmeter, and mass flow rate using the Coriolis flow meter. All measurements were made simultaneously and processed by an HP3852 data acquisition system.

Table II.2.3 Experimental operating conditions.

	T_{in} [°C]	$\dot{m}$ [g/s]	P_{out} [bar]	G [kg/m^2.s]	Re_{Dh}	q'' [W/cm^2]
TS #1	-30, 0	2.0 - 5.0	1.138	2200 - 5550	265 - 1170	0 - 560
TS #2	-30, 0	2.0 - 5.0	1.138	1280 - 3210	175 - 780	0 - 580
TS #3	-30, 0	2.0 - 5.0	1.138	1330 - 3350	304 - 1360	0 - 640
TS #4	-30, 0	2.0 - 20.0	1.138	670 - 6730	189 - 3370	0 - 750

II.2.4 Measurement Uncertainty

One primary concern in the present study was to accurately determine the uncertainty in heat flux measurement. Despite the large convective heat transfer coefficient inside the micro-channels, the relatively small wetted area compared to overall surface area of the copper block was a reason for concern over potentially large heat loss. For single-phase flows, this heat loss can be easily determined by comparing the fluid's sensible heat rise to the electrical power input. Unfortunately, this method cannot be applied in two-phase situations. Therefore a new method was devised to determine the heat loss.

An iterative calculation technique was used. In the first iteration, zero heat loss was assumed and both the convective heat transfer coefficients and wall temperatures inside the micro-channel were calculated at the axial locations of the thermocouples using the aforementioned fin analysis method and the assumption of 1-D vertical conduction. A finite element model was constructed for the entire test section, including housing, cover plate and insulation, which accounted for external natural convection. Boundary conditions for the micro-channel in the finite element model were determined by averaging the three heat transfer coefficient values from the first iteration and using a fluid temperature equal to the average of the measured inlet and outlet temperatures. Heat loss was the estimated using the finite element model. In the second iteration, a new heat flux value was used after deducting heat loss from total electrical power input. New values the convective heat transfer coefficients were determined for the three axial locations of thermocouples inside the micro-channels using the fin analysis method and assumption of 1-D vertical conduction. Using a new average of the three heat transfer coefficient values, the finite element model was used once more to provide an updated estimate of heat loss. Further iteration was attempted until the three heat transfer coefficient values converged. This required about 7 to 13 iterations depending on test section and operating conditions. With this approach, heat loss was estimated at 14 to 20% of electrical power input for single-phase conditions, and 6 to 14% for two-phase

conditions. The experimental data presented in this study have all been corrected for this heat loss.

Uncertainties in the temperature measurements were ± 0.5 °C for inlet fluid temperature control and ± 0.3 °C for thermocouple readings. Accuracies of other measurement instruments were as follows: ± 0.5% for the pressure transducers, ± 0.1% for the Coriolis flow meter, and ± 0.1% for the Wattmeter.

II.2.5 Photographic Method

Flow visualization played a major role in capturing two-phase flow behavior in the micro-channels. A high-speed digital video imaging system was used for this purpose. Two key requirements for capturing the complex interfacial features in a micro-channel with high resolution are high shutter speed and high magnification. The Photron FASTCAM-Ultima camera system used in the present study is capable of shutter speeds up to 1/120,000 s. However, the maximum shutter speed used was dictated by lighting limitations. Lighting was provided by a PerkinElmer Xenon source fitted with an Olympus fiber optic cable that focused the light on the photographed region of the micro-channel. The present study employed a shutter speed of 1/8000 s for relatively slow isolated bubbles and 1/15000 s for fast and/or coalescing bubbles.

To achieve high magnification, two different Infinity K-2 lenses were used. The first provides 4 to 5.8 times magnification and a 1.1 to 1.6 mm field of view. This lens was quite effective for test sections TS #3 and TS #4, capturing 3 to 4 micro-channels in each test section. The other lens provides 8 to 10.7 times magnification and a 0.6 to 0.8 mm field of view. This lens was used with test sections TS #1 and TS #2, which had about half the micro-channel width of TS #3 and TS #4. This second lens captured 7 to 9 micro-channels in TS #1 and TS #2.

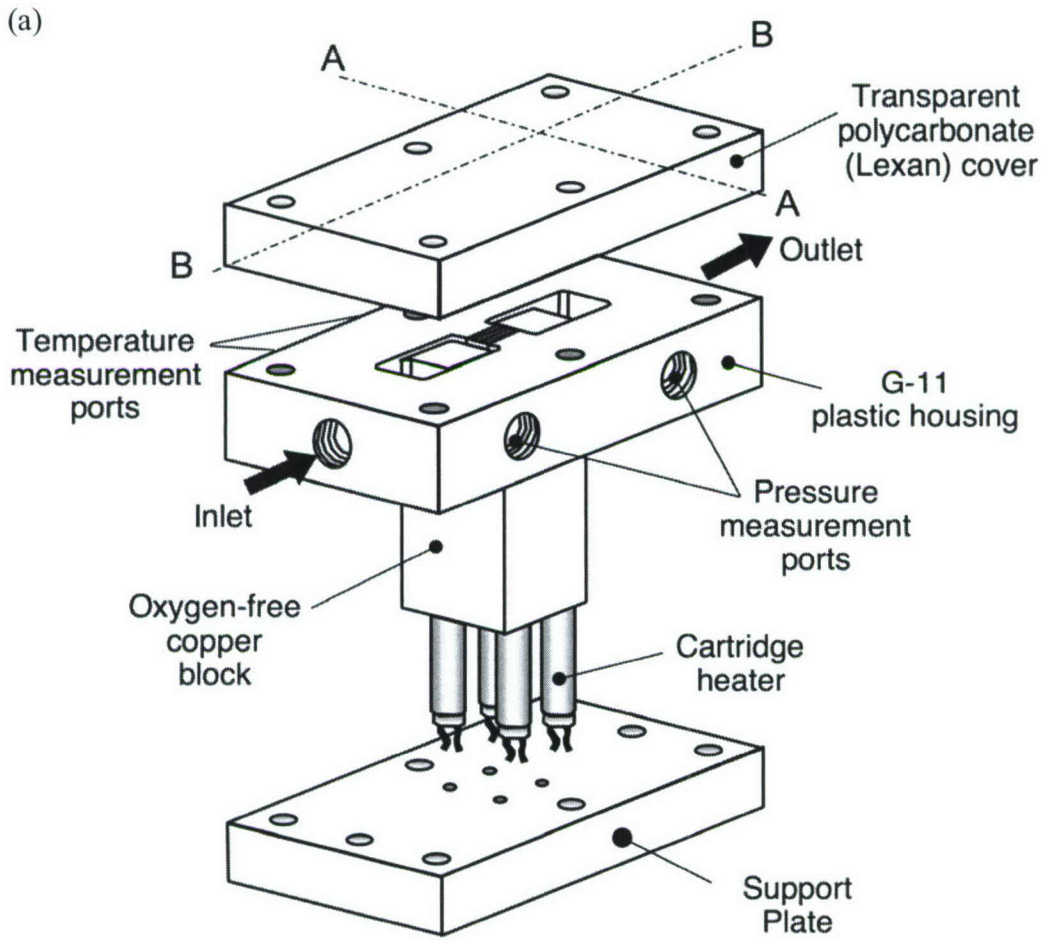

Fig. II.2.2 (a) Isometric view of micro-channel test section.
(b) Cross-sectional view (A-A). (c) Side sectional view (B-B).

(b)

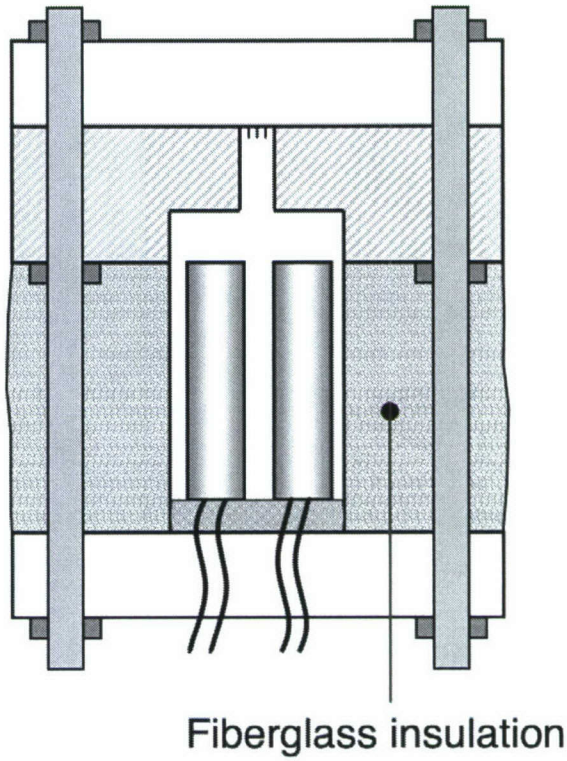

(c)

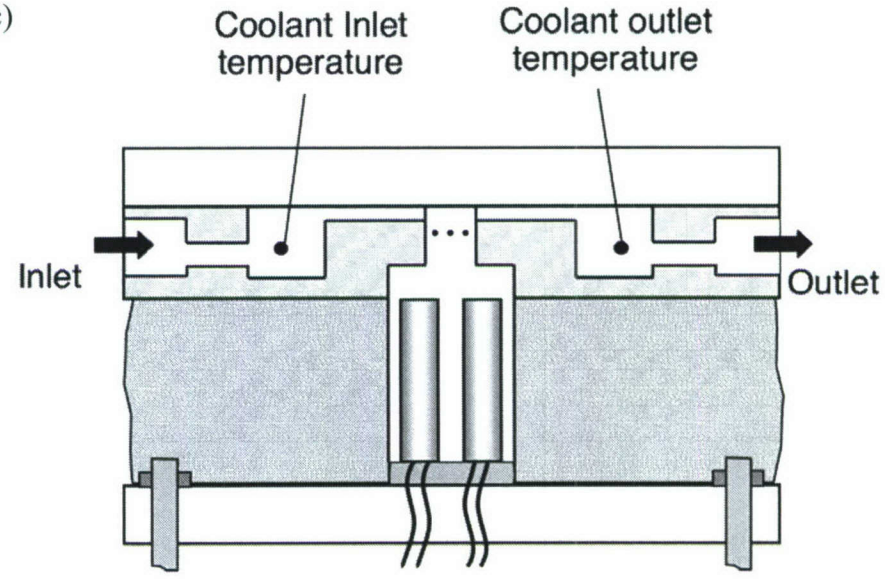

Fig. II.2.2 continued.

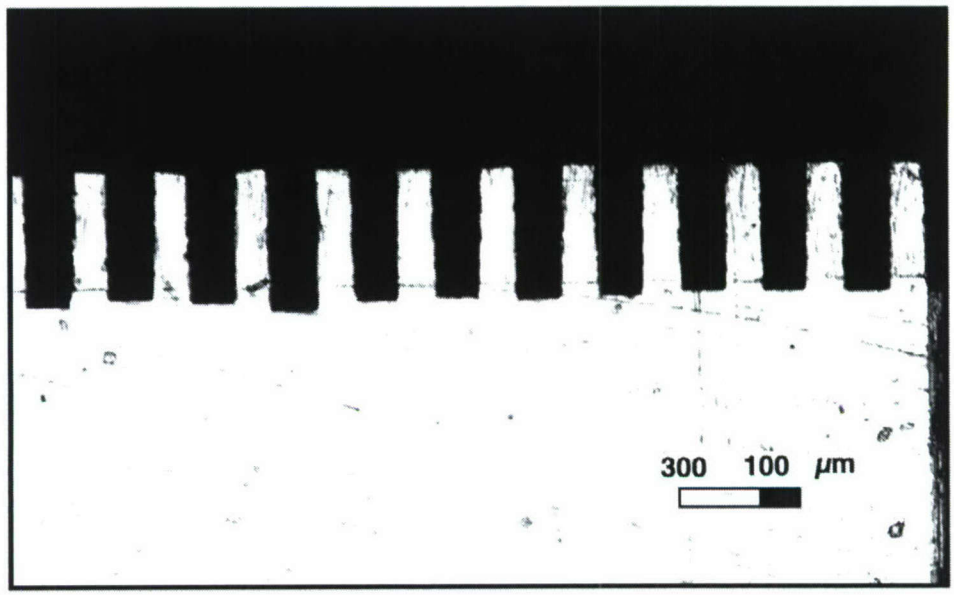

(a)

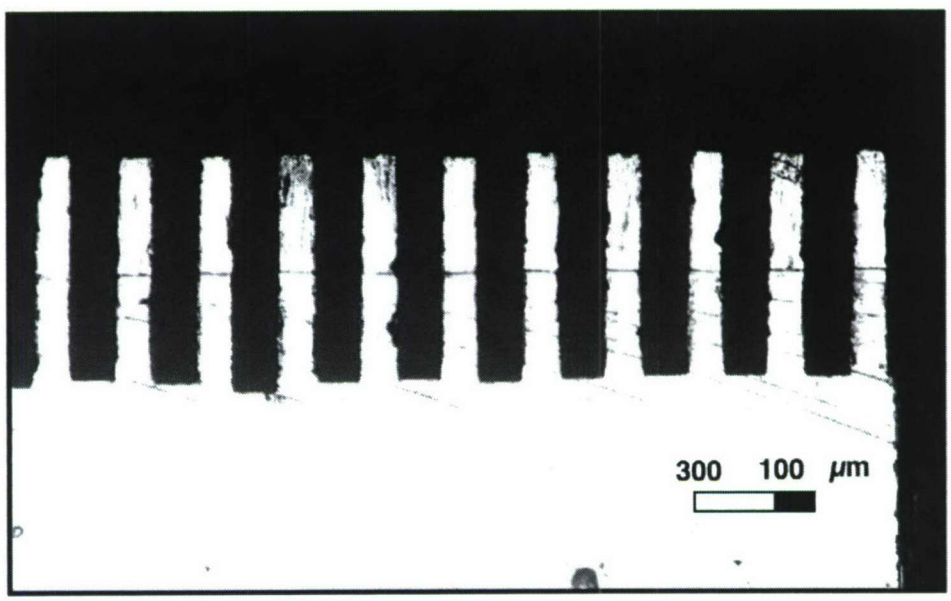

(b)

Figure II.2.3 Microscope images of micro-channels: (a) TS #1 (D_h = 175.7 μm), (b) TS #2 (D_h = 200.0 μm), (c) TS #3 (D_h = 334.1 μm), and (d) TS #4 (D_h = 415.9 μm).

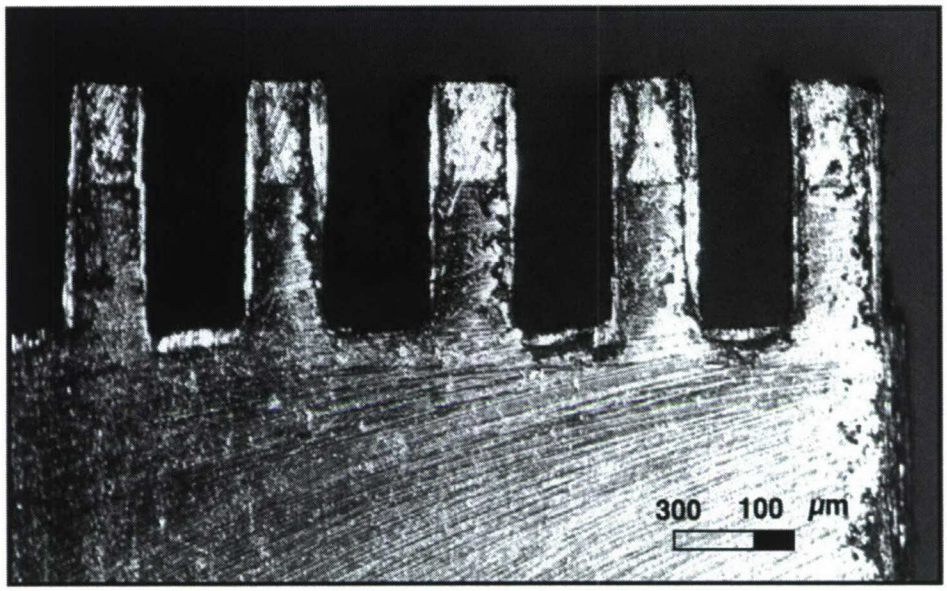

(c)

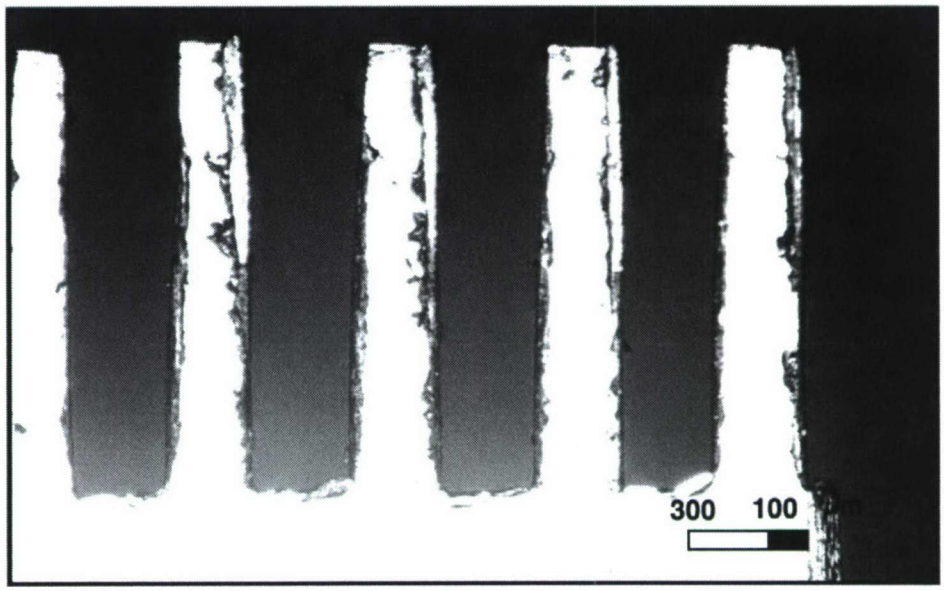

(d)

Figure II.2.3 continued.

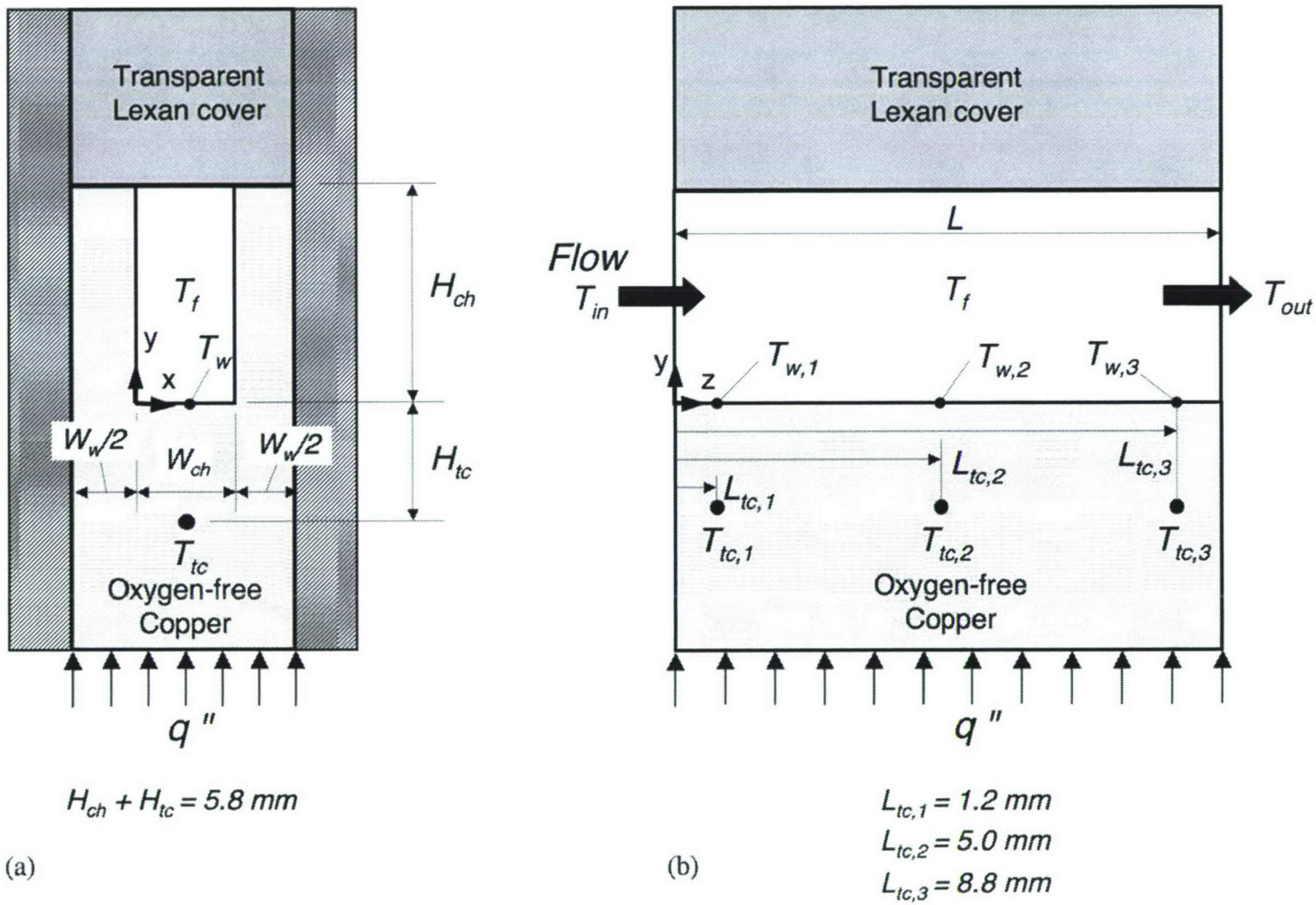

Figure II.2.4 Micro-channel unit cell and locations of thermocouples in (a) *x-y* plane and (b) *y-z* plane.

II.3 FLOW VISUALIZATION

II.3.1 Heat Transfer Results

II.3.1.1 Subcooled Flow Boiling Regime

Figure II.3.1 shows for TS #1 variations of the measured fluid outlet temperature and mean temperature of the micro-channel bottom wall with heat flux for two mass flow rates. Notice how wall temperature is below ambient temperature for fluxes as high as 120 W/cm^2 depending on flow rate; these conditions typically fall into the single-phase region. Figure II.3.1(b) shows single-phase cooling sustained well above 200 W/cm^2 for $\dot{m}$ = 5 g/s. However, fluid temperature for both flow rates never reached saturation. This is especially the case for the higher of the two flow rates. This indicates subcooled boiling conditions prevail inside the test section for both flow rates. The outlet temperature data suggest even highly subcooled boiling conditions for the higher flow rate. This shows that with the high degree of subcooling achieved with indirect refrigeration cooling, subcooled boiling can be achieved even at very high fluxes. This is especially the case at high flow rates.

In fact, subcooled boiling prevailed for almost all operating conditions of the present study, regardless of test section. What was different among the different operating conditions was the degree of subcooling inside the micro-channels. This issue will become more apparent from the video images discussed below.

From a modeling standpoint, subcooled boiling poses major challenges, particularly in terms of predictions of void fraction and pressure drop. Interestingly, most the published literature on two-phase micro-channel heat sinks concerns saturated boiling, where annual flow is dominant. The complexity of the present situation

warrants careful assessment of interfacial interactions inside the micro-channel heat sink. In fact, this is the primary goal of the present study.

II.3.1.2 Representative Boiling Curve

Figure II.3.2 shows subcooled boiling curves for TS#3 for inlet temperatures of -30 and 0 °C. Despite the similarity in boiling curve shape, appreciable differences in subcooled boiling behavior were observed between the two cases.

Indicated in Fig. II.3.2 are several data points ('A' to 'F') for T_{in} = 0 °C, spanning conditions between the onset of boiling and CHF. Point 'G' for the same inlet temperature corresponds to conditions during the transient that followed CHF. For the comparison purposes, point 'H' corresponds to subcooled boiling conditions for T_{in} = -30 °C. Because of the highly subcooled state at this lower temperature, boiling behavior showed far less variation with heat flux than at 0 °C. Representative video images that were captured at these points are presented and discussed in the following sections.

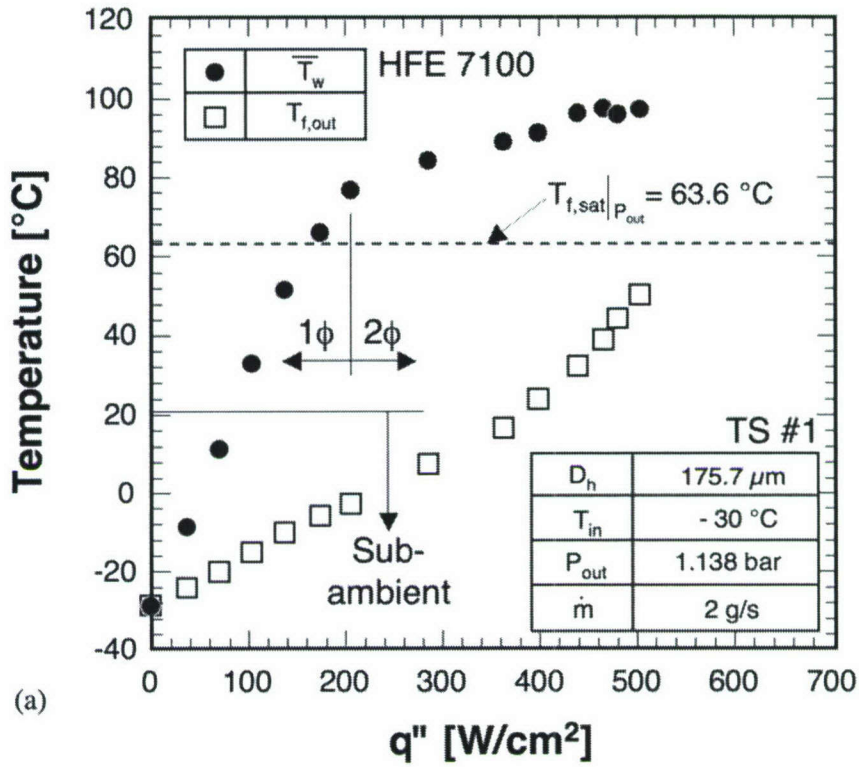

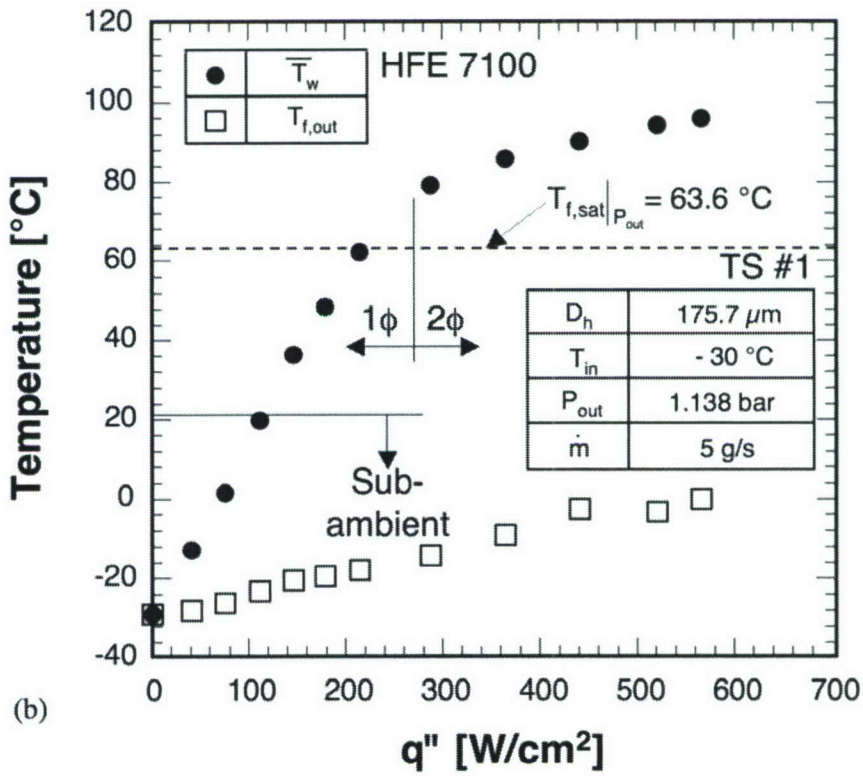

Figure II.3.1 Variations of measured fluid outlet temperature and mean micro-channel bottom wall temperature with heat flux for TS #1 at (a) $\dot{m}$ = 2 g/s and (b) $\dot{m}$ = 5 g/s.

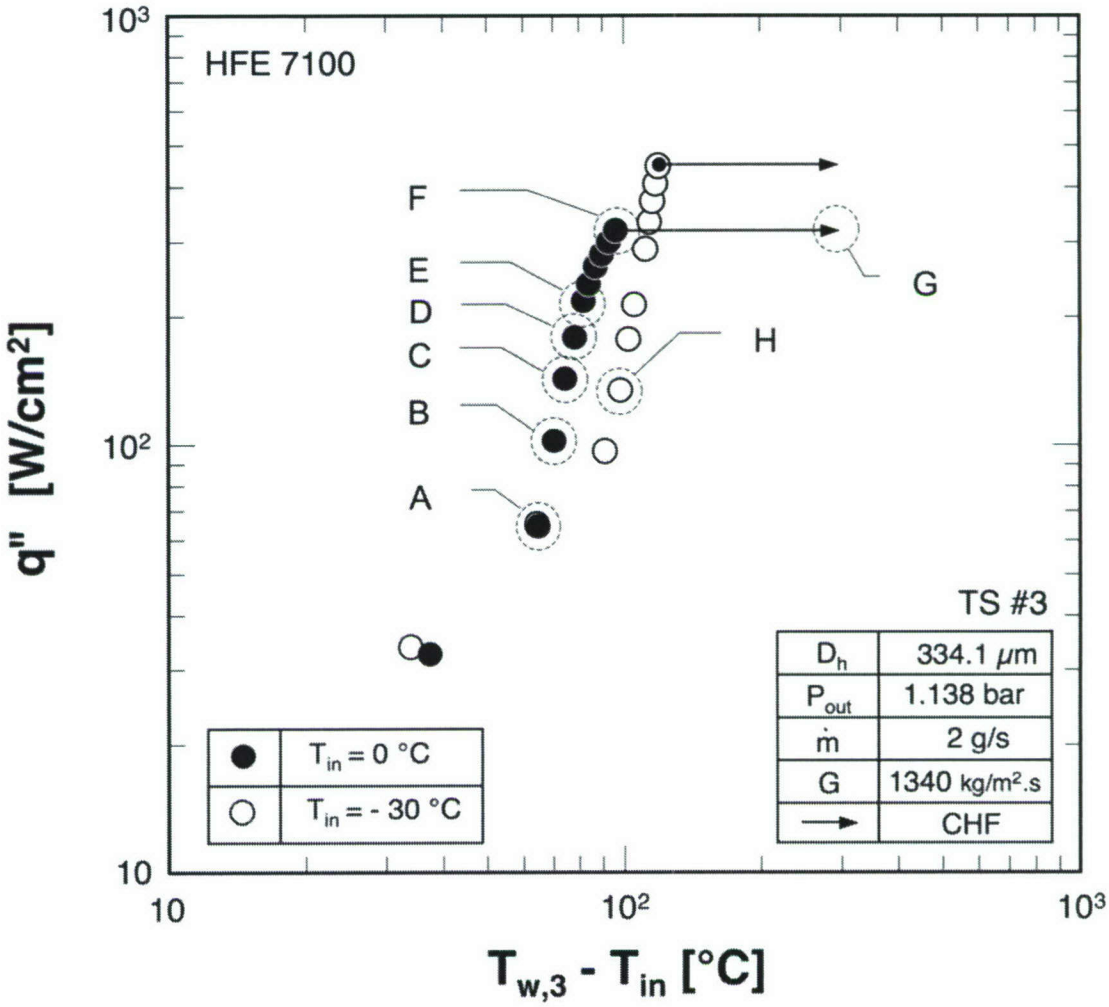

Figure II.3.2 Subcooled boiling curves for TS #3 for two inlet temperatures. Specific data points are indicated where video images of subsequent figures were captured.

II.3.2 Nucleate Boiling Region

Figure II.3.3(a) shows initial bubble formation corresponding to point 'A' in Fig. II.3.2. This is the point where the slope of the boiling curve undergoes rises sharply due to transition from the single-phase to nucleate boiling regions. Because of limitations in focal range of the microscope lens used with the video camera, the channel length is shown divided into three regions, inlet, middle and outlet. There is slight overlap of the captured length of the middle region with both the inlet and outlet regions. Figure II.3.3 (a) shows early nucleation does not occur uniformly in all micro-channels. Some channels show an abundance of bubbles while others show virtually no bubbles at all. However, even in the more populated micro-channels, bubbles appear to maintain fairly large separation distances, precluding any coalescence that may lead to axial growth in the void fraction. It should be emphasized that the bubbles depicted in Fig. II.3.3(a) do not necessarily correspond to the sites from which they nucleated or location in the micro-channel's cross-section. A lateral force associated with the velocity profile across the liquid tends to keep bubbles in the vicinity of the micro-channel walls [Lee and Mudawar (1989)]. Furthermore, while the video images do not depict the location of bubbles relative to the channel depth, it is expected bubble growth favors the bottom wall of the micro-channel, where liquid is warmest.

Figure II.3.3(b) shows flow boiling images corresponding to point 'B' in Fig. II.3.2. Here, with a higher heat flux, increased liquid superheat near the wall increases the number of nucleating sites, resulting in more bubbles along the micro-channels. The increased superheat also allows the bubbles to reach a large diameter than at point 'A'. Notice that the ratio of bubble separation distance to bubble diameter decreases appreciably from point 'A', increasing the likelihood of bubble coalescence in the outlet region. It should also be noted that with the increased wall superheat, bubble nucleation is evident in all the micro-channels.

Figure II.3.3(c) shows images corresponding to point 'C' in Fig. II.3.2. With this yet higher heat flux, increased wall superheat precipitates an increase in the number of active nucleating sites and therefore number of bubbles along the micro-channel. The

ratio of separation distance to bubble diameter is also greater, meaning bubbles can more easily coalesce into larger ones. The outlet region in particular shows signs of appreciable coalescence, an early indicator of transition to slug flow. Nonetheless, bubbly flow appears to dominate all three heat flux conditions corresponding to points 'A', 'B' and 'C'.

Figure II.3.4 depicts flow blow images corresponding to further increase in heat flux. Here, further increases in wall superheat facilitate large increases in the number of bubble nucleating upstream, as well as significant increase in void fraction spurred by coalescence of bubbles along the micro-channel. Figure II.3.4(a) shows oblong bubbles forming in the outlet region for point 'D'. Notice in the outlet regions both oblong slug flow bubbles and smaller discrete bubbles appear to form at the same axial location. This can be explained by differences in bubble behavior across the depth of the micro-channel. Because of the temperature gradient between the base and top of the micro-channel's cross-section, bubbles near the base are more likely to coalesce into large oblong bubbles, while the smaller discrete bubbles near the top have less superheat to grow and coalesce. This shows the complexity of assigning a boiling regime for a given heat flux and axial location.

Figure II.3.4(b) shows the departure from bubbly to slug flow moves upstream to the middle region for point 'E'. There is also now appreciable increase in the length of slug flow bubbles in the outlet region, as well as a diminution in the number of small discrete bubbles in the same region.

Figure II.3.3 Flow boiling images of inlet, middle and outlet regions for TS #3 (D_h = 334.1 μm) at T_{in} = 0 °C: (a) point 'A', (q'' = 64.9 W/cm^2), (b) point 'B', (q'' = 102.3 W/cm^2), and (c) point 'C' (q'' = 142.8 W/cm^2).

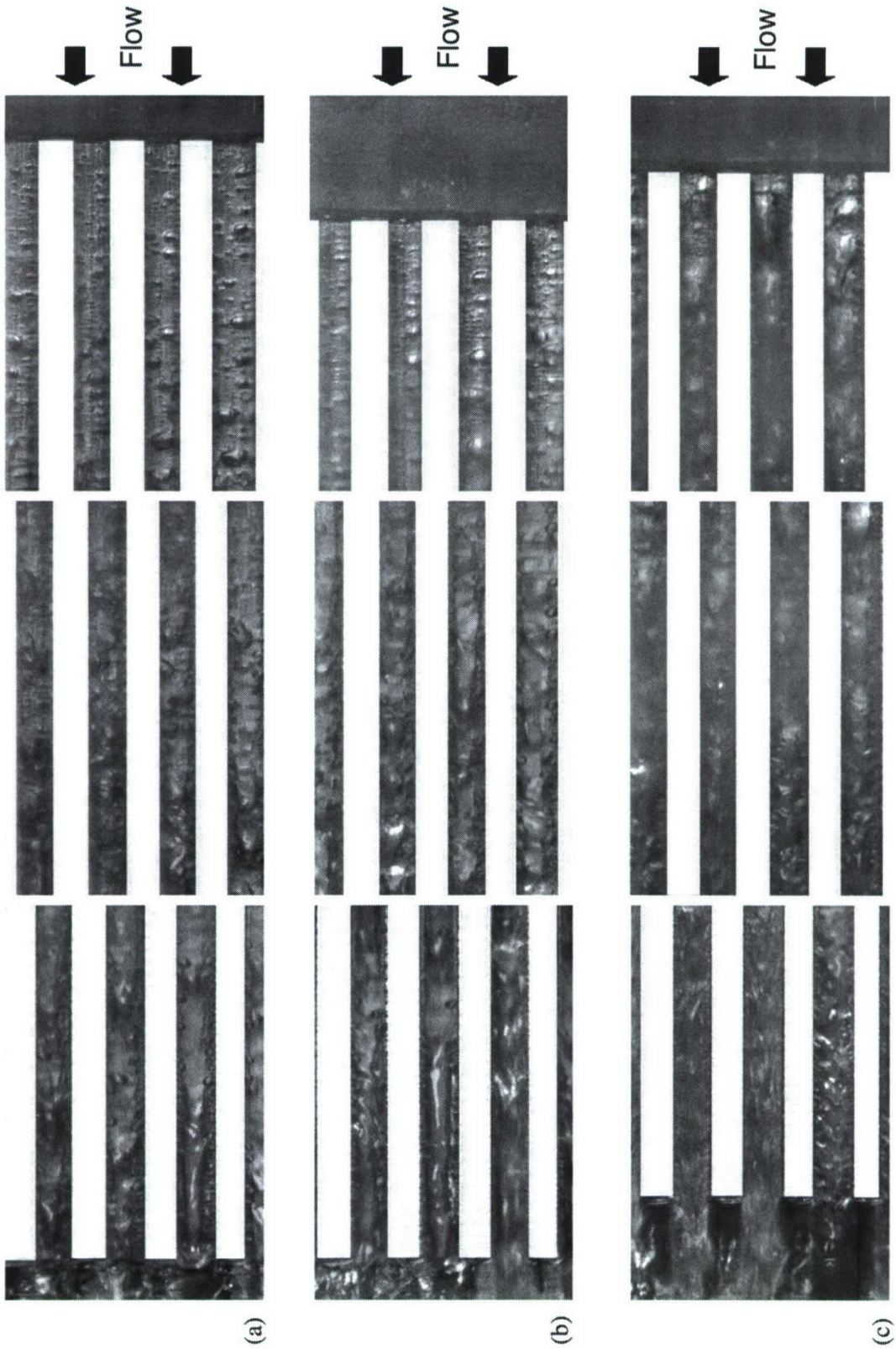

Figure II.3.4 Flow boiling images of inlet, middle and outlet regions for TS #3 (D_h = 334.1 μm) at T_{in} = 0 °C: (a) point 'D' (q'' = 178.2 W/cm^2), (b) point 'E' (q'' = 218.3 W/cm^2), and (c) point 'F' (q'' = 318.3 W/cm^2).

II.3.3 Critical Heat Flux

For point 'F', Fig. II.3.4(c) shows a further shift in the slug flow regime upstream to the inlet region. This point corresponds to the last steady-state condition in the nucleate boiling region before the onset of CHF. High stream-wise flow acceleration associated with the sharply increased void fraction caused coherent vapor jets to be ejected from the channel outlet. Unfortunately, limitations on frame rate of the video camera precluded detailed resolution of interfacial activity in these jets.

CHF occurred when heat flux was increased slightly from point 'F'. Figure II.3.5(a) shows an image of the upstream region of the micro-channels that was captured while the heat sink temperature was escalating unsteadily. A thin layer of vapor is shown covering the micro-channel walls from the very inlet. As illustrated in Fig. II.3.5(b), abundant subcooled liquid is still visible in the core region fully separated from the micro-channel walls by the vapor layer. It should be noted that capturing the video segment from which this image was obtained involved significant risk to the test section parts, especially the transparent polycarbonate cover plate. This is why it was quite difficult to obtain prolonged segments of this event.

II.3.4 Effects of Subcooling

As discussed in the previous section, inlet temperature and, more importantly, inlet subcooling plays a very important role in all aspects of bubble nucleation, growth and coalescence along the micro-channels. A reduced inlet temperature increases the superheat in the vicinity of the micro-channel walls. As shown in Fig. II.3.2, the increased subcooling delays the onset of boiling to a higher heat flux. The effects of subcooling become readily apparent when comparing images in Fig. II.3.6 that were captured at T_{in} = -30 °C to those at T_{in} = 0 °C, Fig. II.3.3(c), for about the same heat flux. Strong condensation effects at -30 °C suppresses bubble growth and coalescence,

prolonging the bubble growth regime and delaying transition to slug flow to much higher heat fluxes compared to 0°C inlet temperature.

Another important effect of the increased subcooling is the appreciable increase in CHF. Figure II.3.2 shows a CHF of 446.9 W/cm^2 for T_{in} = -30 °C compared to 318.3 W/cm^2 for T_{in} = 0 °C.

II.3.5 Effects of Micro-Channel Geometry

The effects of channel geometry are more complicated than those of subcooling. Figure II.3.7 depicts images obtained with TS #2, whose hydraulic diameter is D_h = 200 μm and width of W_{ch} = 123.4 μm, compared to D_h = 334.1 μm and W_{ch} = 235.2 μm for TS #3 depicted in Fig. II.3.6. It should also be noted that Fig. II.3.7 corresponds to the same inlet temperature and heat flux, T_{in} = -30 °C and q'' = 134 W/cm^2, respectively as Fig. II.3.6, and about same mass velocity (G = 1281 kg/m^2.s for Fig. II.3.7 comparing to 1340 kg/m^2.s for Fig. II.3.6). Note that micro-channel width appears to be the same in Figs. II.3.6 and II.3.7 because of the higher magnification lens used to capture the images in Fig. II.3.7; only the middle region of the micro-channels was captured with this lens.

Figure II.3.7 shows far less bubble nucleation and coalescence than in Fig. II.3.6. This may be explained by the 1.85 times greater wetted area for TS #2 compared to TS #3. The increased area both decreases the local wall heat flux and wall for TS #2, delaying the entire nucleation process. Another noticeable feature of boiling in TS #2 is increased ratio of bubble size to micro-channel width despite the decreased wall superheat. Clearly visible in the middle micro-channel in Fig. II.3.7 is a bubble whose size is two-third the micro-channel width. A smaller micro-channel width might promote the growth of bubbles that span the entire width of the micro-channel.

Figures II.3.6 and II.3.7 illustrate the complex combined influence of micro-channel geometry in subcooled boiling. Such influences can have drastic influence on the heat transfer performance of a micro-channel heat sink. The complexity of

parametric influences highlights the need for mechanistic modeling of subcooled boiling in micro-channels.

II.3.6 Instabilities and Premature CHF

The interfacial behavior discussed earlier in conjunction with Fig. II.3.5 can be described as 'normal CHF' since it follows the depiction of subcooled boiling CHF in large channels. However, a second drastically different type of CHF was encountered in the present study, which is best described as 'pre-mature CHF'. This type of CHF was associated with significant instability and flow oscillation.

Figure II.3.8 depicts a series of images separated by very short time intervals. Schematic of the same interfacial patterns are also shown to better explain the depicted behavior. A key difference between this cases and those depicted in earlier figures is its much lower mass velocity, $G = 670$ kg/m^2.s. With this lower mass velocity, a much larger volume of vapor is produced inside the micro-channels for the same inlet temperature and heat flux. This causes vapor coalescence into slug and even annular flow as far upstream as the inlet region. With the lower mass velocity, the momentum of incoming liquid in the upstream plenum becomes too weak to overcome the relatively large pressure exerted by the coalescent vapor. This caused vapor in the micro-channel to flow backwards towards the inlet plenum. Vapor from adjacent micro-channels merges into one large vapor mass inside the inlet plenum, momentarily blocking any incoming liquid from entering the micro-channels and causing temporary dryout and temperature rise in the micro-channels. With this blockage, the upstream pressure gradually increases and a point reach when this pressure becomes high enough to push all vapor mass downstream through the micro-channels, providing momentary wetting of the micro-channel walls and reducing wall temperatures. This was followed by vapor coalescence inside the micro-channels and a repeat of the same build-up/purge cycle. This cycle occurred with very high frequency and was associated with large fluctuations in both pressure and temperature. Conditions worsened with time as mean temperature

kept increasing with each new cycle. In fact, the peak temperature recorded by thermocouples in the copper heating block was about 200 °C when the images depicted in Fig. II.3.8 were captured.

Fortunately, premature CHF can be prevented in two different ways. The first involves increasing the momentum of incoming liquid by increasing mass velocity. With sufficiently high liquid momentum, vapor backflow is prevented before it can even begins to form the large vapor mass in the upstream plenum. The second method is to lower the inlet temperature to take advantage of condensation and reduced bubble growth and coalescence. Both methods were proven to prevent the occurrence of premature CHF in the present study.

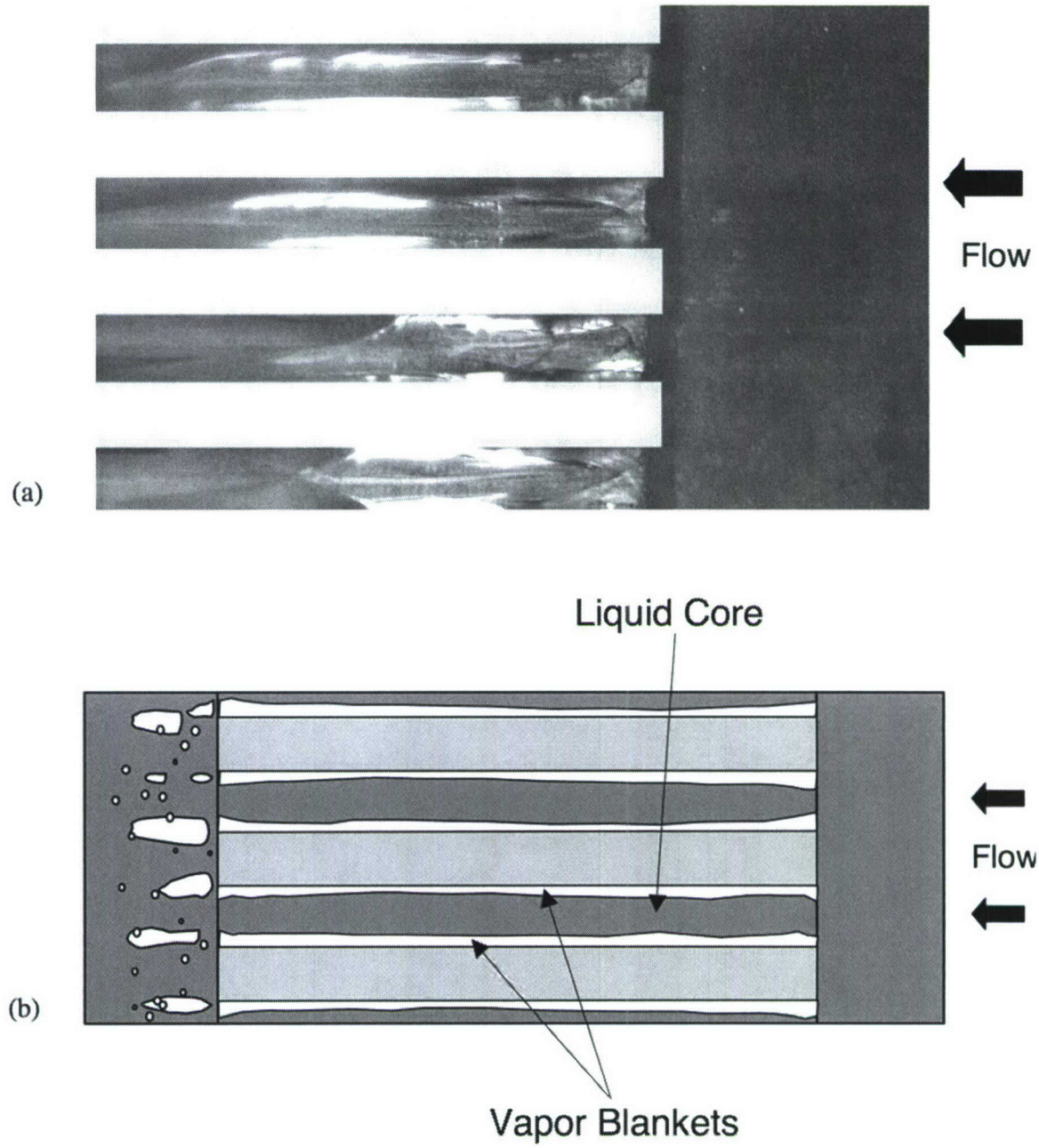

Figure II.3.5 (a) Flow image of inlet region for TS #3 (D_h = 334.1 μm) at T_{in} = 0 °C captured at point 'G' during transient following CHF. (b) Schematic representation of interfacial conditions at point 'G'.

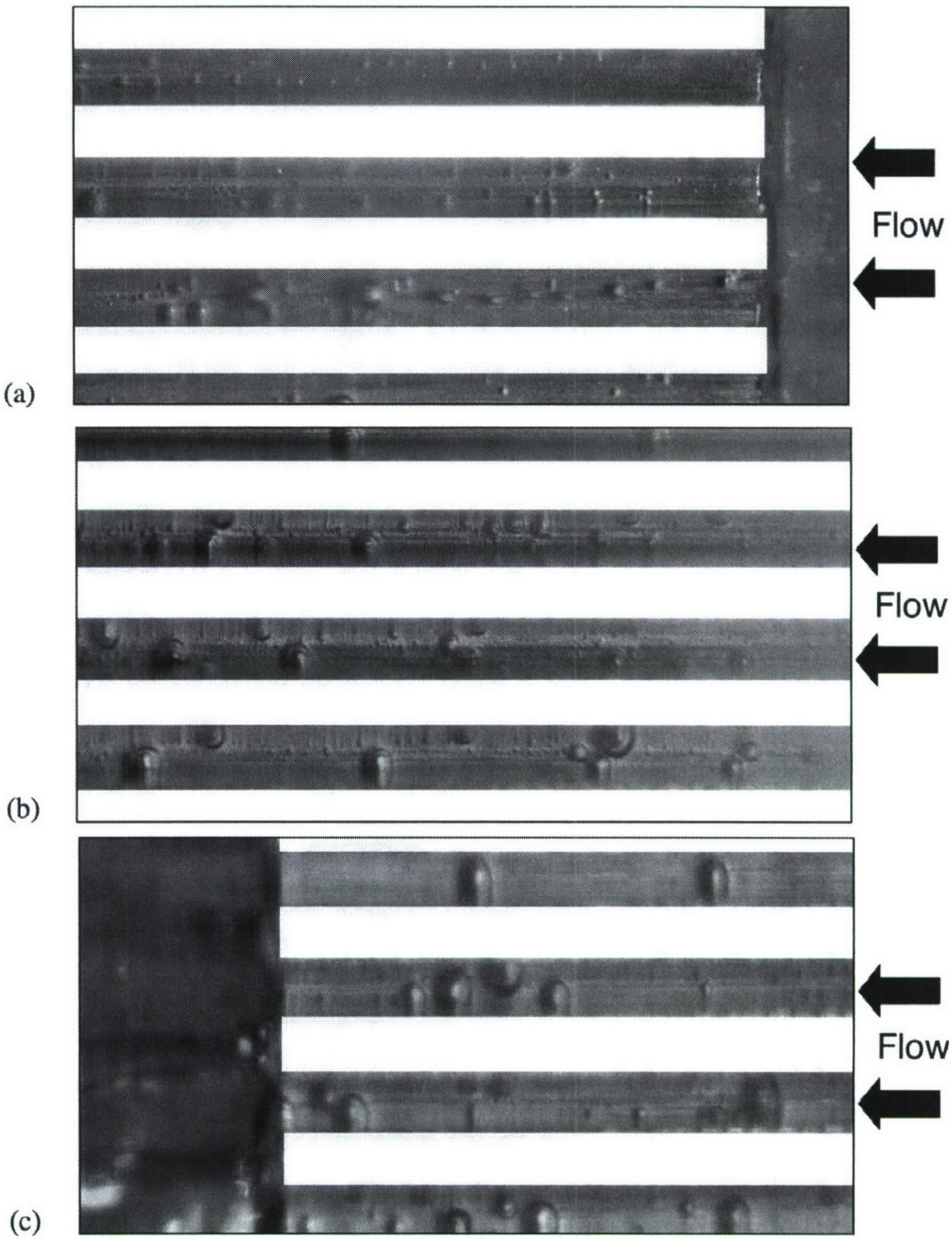

Figure II.3.6 Flow boiling images for TS #3 (D_h = 334.1 μm) at low temperature of T_{in} = -30 °C and q'' = 134.0 W/cm^2 corresponding to point 'H'. (a) Inlet region, (b) middle region, and (c) outlet region.

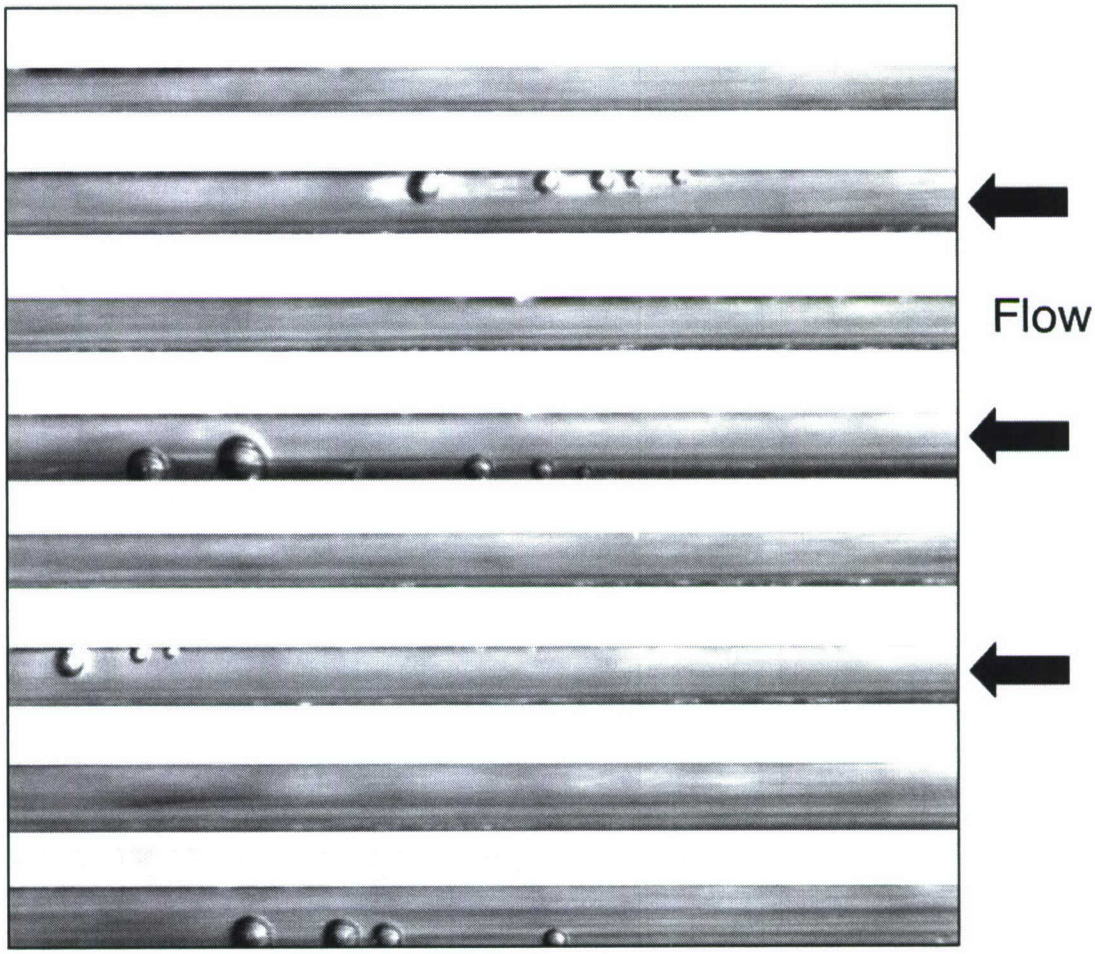

Figure II.3.7 Flow boiling image of middle region of micro-channel with smaller width and hydraulic diameter (TS #2, D_h = 200 μm) for T_{in} = -30 °C, G = 1281 kg/m^2.s, and q'' = 134.0 W/cm^2.

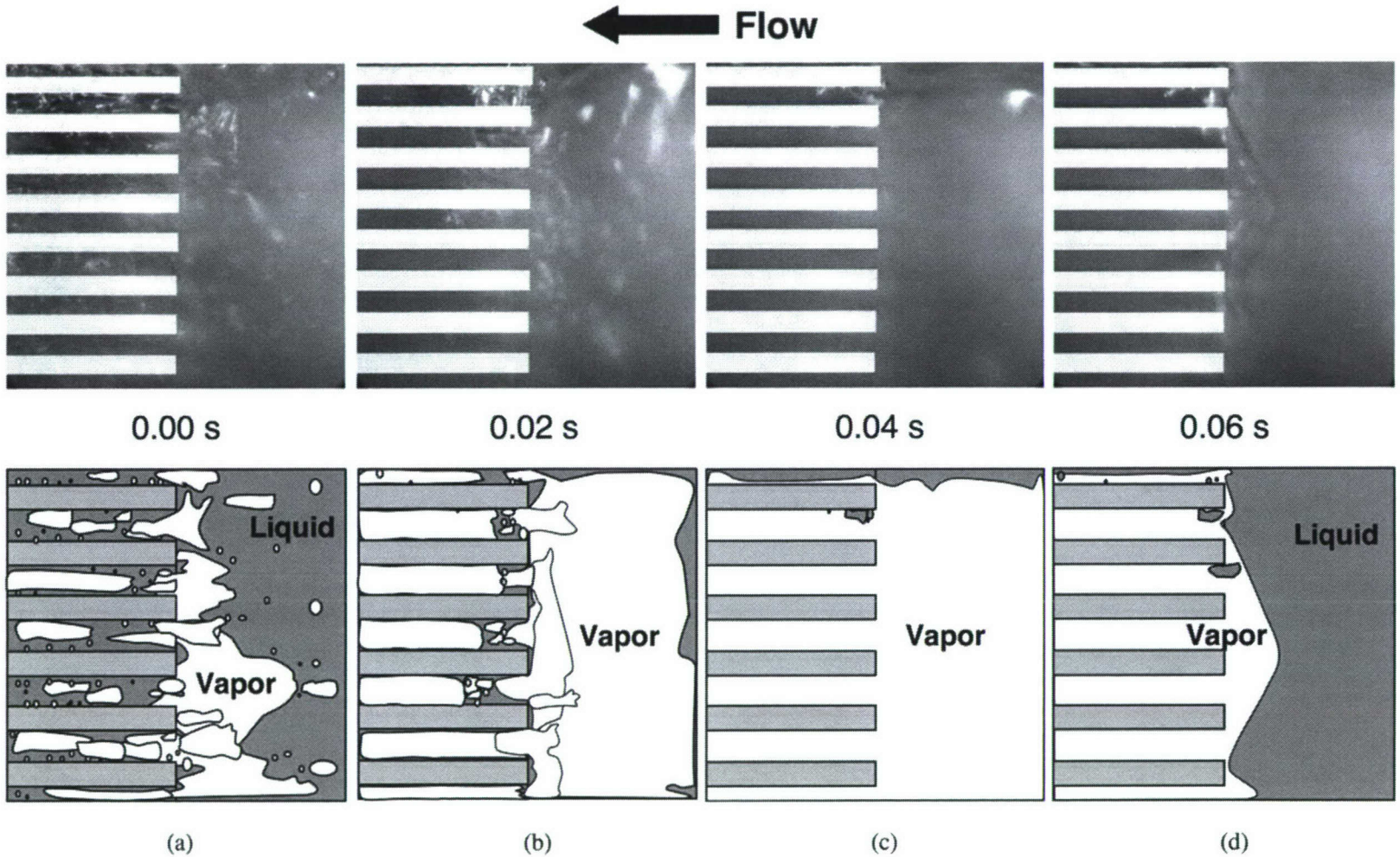

Figure II.3.8 Premature CHF and flow oscillations in TS #4 (D_h = 415.9 μm) for T_{in} = 0 °C, G = 670 kg/m^2.s, and q'' > 250.0 W/cm^2: (a) initial vapor pocket buildup in upstream plenum, (b) growth of vapor mass, (c) complete blockage of inlet plenum by vapor mass, and (d) purging of vapor mass along micro-channels.

II.4 EXPERIMENTAL RESULTS AND CORRELATIONS

II.4.1 Pressure Drop Results

II.4.1.1 Experimental Pressure Drop Results

Figure II.4.1 shows variations of measured pressure drop for test section TS #2 with heat flux for different flow rates and two inlet temperatures. Raw pressure drop data are presented in Fig. II.4.1(a) and shown in normalized form in Fig. II.4.1(b). Details of the geometry and operating conditions for this and the other three tests sections are given in the chapter II.2. Arrows in Fig. II.4.1 indicate the observed ONB, which marks the onset of subcooled boiling. As suggested in the chapter II.1.2, ONB occurs before the point of minimum pressure drop. In virtually all of the present data, an increase in the slope of pressure drop characteristics from the minimum point occurred with the first heat flux increment following ONB. This makes identifying any differences between ONB and point of vapor departure quite elusive. High heat fluxes and corresponding relatively large heat flux increments may have contributed to the difficulty capturing the differences between the two conditions.

Figure II.4.1 also demonstrates a monotonic shift to higher pressure drop with increasing coolant flow rate as well as a corresponding delay in ONB to higher heat fluxes. However, the effect of subcooling is a bit more complex. As indicated in the previous section, pressure drop in the single-phase liquid region (before ONB) is highest for adiabatic flow and decreases with increasing heat flux due to decreasing liquid viscosity. Figure II.4.1(a) shows decreasing inlet liquid temperature causes a shift to higher pressure drop for a given flow rate because of increased liquid viscosity. However, decreasing the inlet temperature *decreases* the normalized pressure drop (see

Fig. II.4.1(b)) because of a stronger viscosity dependence on liquid temperature at lower temperatures. Figure II.4.1 also shows lower inlet temperatures delay ONB to higher heat fluxes, a trend that was captured in the flow visualization experiments discussed in the previous chapter II.3 of this study.

Figure II.4.1 shows the effect of decreasing inlet temperature is reversed in the subcooled boiling region. Here, lower inlet temperatures produce a relatively mild increase in pressure drop following ONB at -30 °C compared to 0 °C. This trend can be explained by the strong condensation effects at low inlet temperatures greatly reducing both void fraction and the overall influence of phase change on pressure drop.

Figure II.4.2 shows the variation of pressure drop with heat flux for the four different test sections. Indicated in this figure are mass velocity values for each test section corresponding to the same mass flow rate of 5 g/s. Pressure drop for the single-phase and two-phase regions can be represented, respectively, by

$$\left(\frac{dp}{dz}\right)_{sp,f} = \frac{2f_{sp}}{D_h} G^2 v_f \tag{II.4.1}$$

and

$$\left(\frac{dp}{dz}\right)_{tp} = \left(\frac{dp}{dz}\right)_{tp,F} + \left(\frac{dp}{dz}\right)_{tp,A} = \frac{2f_{tp}}{D_h} G^2 \bar{v} + G^2 \frac{d\bar{v}}{dz} \quad , \tag{II.4.2}$$

where f_{sp} and f_{tp} are the single-phase and two-phase friction factors, respectively. Figure II.4.2 displays the strong dependence of pressure drop on mass velocity evident in both of the above equations. Equations (II.4.1) and (II.4.2) also show pressure drop for both single-phase flow and two-phase flow increases with decreasing hydraulic diameter. This is also manifest in Fig. II.4.2, where the highest pressure drop is associated with the smallest hydraulic diameter (TS #1, D_h = 175.7 μm) and largest mass velocity (G = 5546 kg/m^2.s).

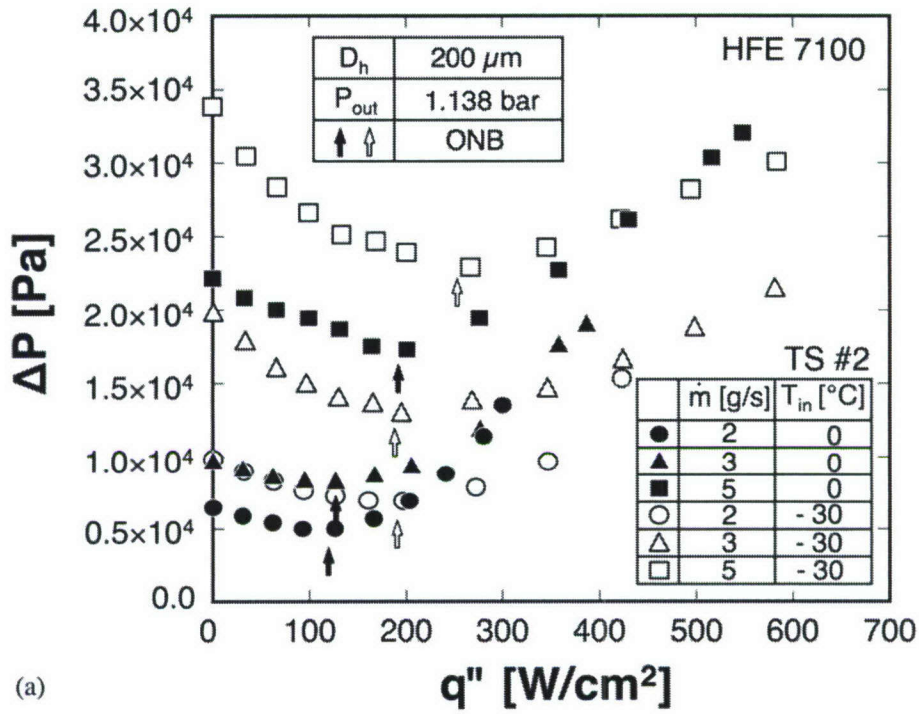

(a)

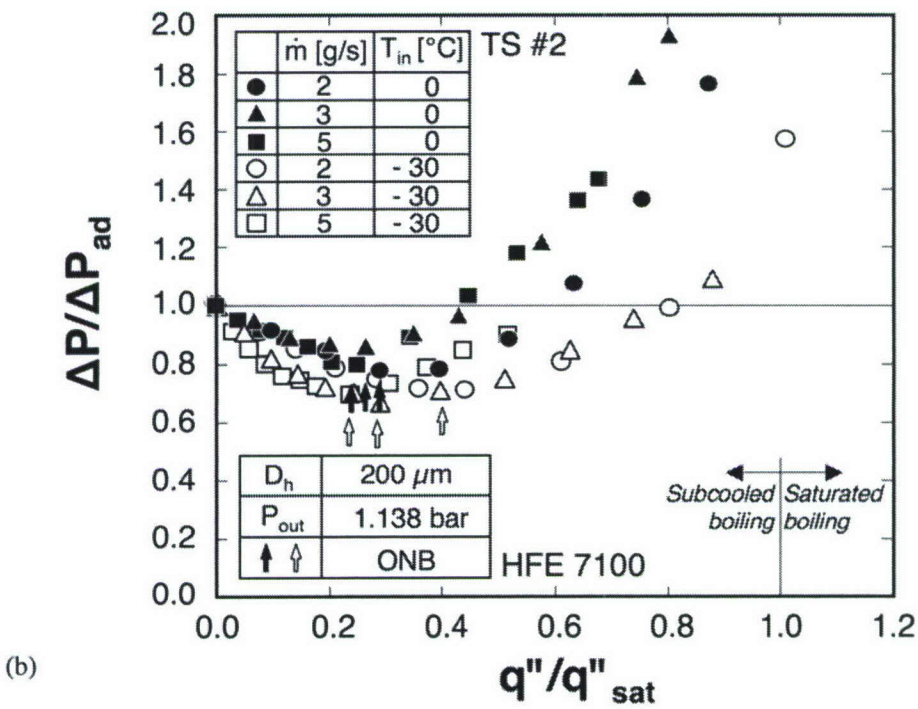

(b)

Figure II.4.1 (a) Variation of pressure drop for test section TS #2 (D_h = 200 μm) with heat flux for different flow rates and inlet temperatures, and (b) corresponding normalized pressure drop plot.

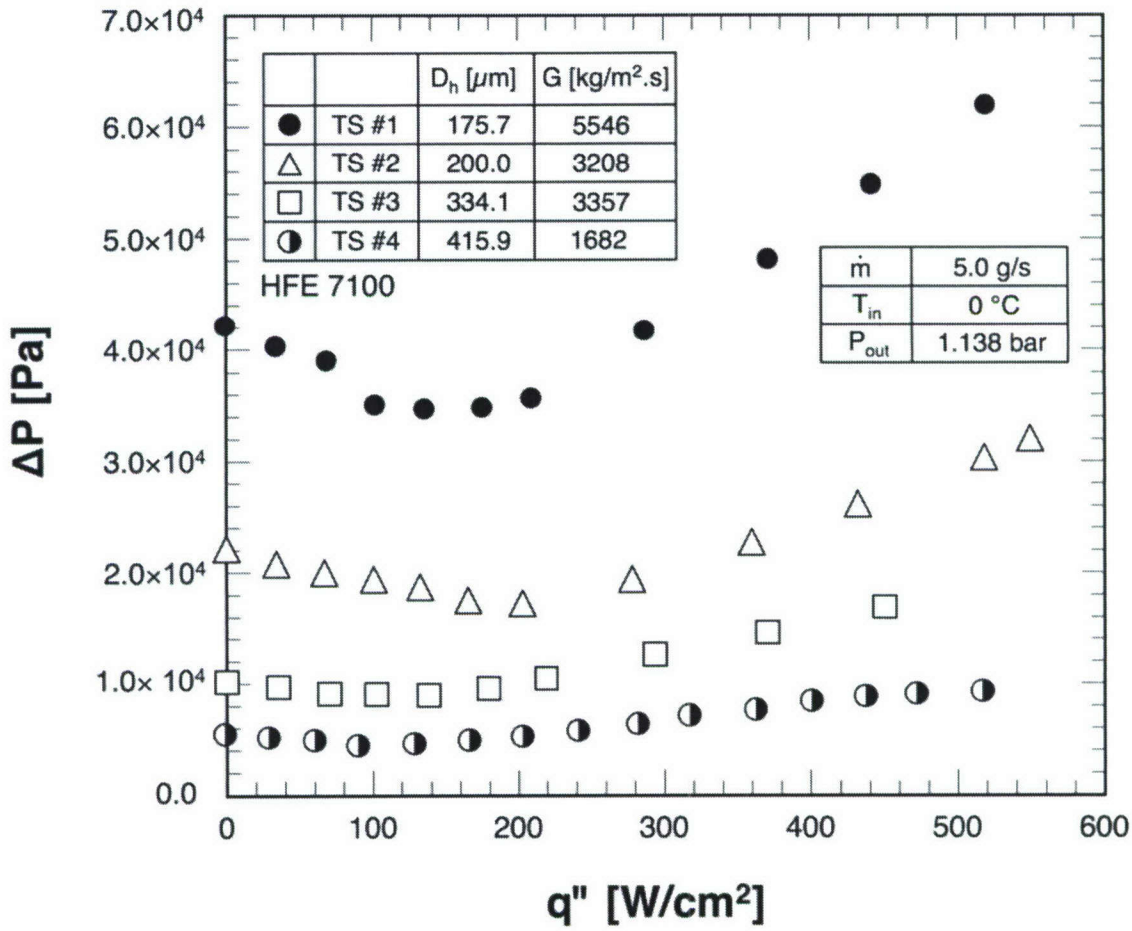

Figure II.4.2 Variation of pressure drop with heat flux for different micro-channel geometries and mass velocities.

II.4.1.2 Evaluation of Prior Correlations

Past studies have followed two general approaches to evaluating and correlating subcooled boiling pressure drop data. The first consists of evaluating the individual components of pressure drop, namely friction and acceleration (also gravity for inclined flows) as suggested by Eq. (II.4.2). An appropriate two-phase flow model is adopted in evaluating each component, and approximations are used to estimate friction factor as well as the relationship between quality and void fraction. In a recent publication (Lee and Mudawar, 2005a), the author of the present study summarized homogeneous and separated flow models for predicting pressure drop for two-phase micro-channel heat sinks. These models were intended for saturated flow boiling situations only.

One difficulty in utilizing this method is the inability to determine the extent of the subcooled boiling region. Some authors suggested using the bubble departure point for this purpose (e.g., Bowring's analysis in Coller and Thome, 1994, Saha and Zuber, 1974), but, as discussed earlier, there is no definitive assessment of the validity of this approach. Other difficulties stem from the inability to predict quality and void fraction in the subcooled region with a reasonable degree of certainty. Since thermodynamic equilibrium quality is negative in this region, an apparent non-equilibrium quality must be used instead. Hoffman *et al.* (Hoffman and Kline, 1985, Hoffman and Wong, 1992) examined available correlations for quality and void fraction to evaluate subcooled boiling pressure drop. Different correlations produced drastically different predictions, and some yielded very unrealistic values.

The second approach to evaluating subcooled boiling pressure drop, which is adopted in the present study, is to normalize pressure drop data relative to adiabatic flow as discussed earlier in conjunction with Figs. II.1.2 and II.4.1. For the single-phase region, the present pressure drop data were compared to the following relation (Kays and Crawford, 1980):

$$\frac{\Delta P}{\Delta P_{ad}} = \frac{f_{sp}}{f_{sp,ad}} = \left(\frac{\mu_f}{\mu_{f,ad}}\right)^N, \tag{II.4.3}$$

where $N = 0.58$ for laminar heating. Figure II.4.3 shows Eq. (II.4.3) is quite successful at predicting pressure drop data for all four test sections corresponding to laminar flow with $Re_{Dh} < 1500$.

To determine ΔP using Eq. (II.4.3), the adiabatic pressure drop must first be determined by integrating Eq. (II.4.1) across the heat sink, taking into account the variation of friction factor along this predominantly developing flow. A detailed procedure for determining single-phase pressure drop for developing flow in rectangular micro-channels is provided in Qu and Mudawar (2003a).

Bergles and Dormer (1969) performed extensive subcooled boiling pressure drop measurements for a single tube diameter of 5.08 mm. They segregated their data according to pressure, subcooling and mass flux, and developed chart type correlation plots for pressured drop estimation. Later, Tong, *et al.* (1997) combined their own data for D_h = 1.05 - 2.44 mm diameter tubes with the Bergles and Dormer charts, and recommended replacing the earlier charts with the following correlation:

$$\frac{\Delta P}{\Delta P_{ad}} = \left(\frac{L_{sc}}{L_{sat}}\right)^{1.3} exp\left\{\left(\frac{L_{sc}}{L_{sat}}\right) + 1.35\right\} \quad \text{for} \quad L/D_h = 25 \tag{II.4.4a}$$

and

$$\frac{\Delta P}{\Delta P_{ad}} = \left(\frac{L_{sc}}{L_{sat}}\right)^{1.3} exp\left\{\left(\frac{L_{sc}}{L_{sat}}\right) + 0.4\right\} \quad \text{for} \quad L/D_h = 50, \tag{II.4.4b}$$

where L_{sc} and L_{sat} are, respectively, the length of the subcooled boiling region (from the end of the single-phase region) and the length measured from the inlet that is required to bring the fluid to saturated state. For a rectangular micro-channel, the latter length is given by

$$L_{sat} = \frac{GW_{ch}H_{ch}}{q''(W_{ch} + W_w)} c_{p,f}(T_{sat} - T_{in}), \tag{II.4.5}$$

The L/D_h values for the test sections used in the present study are close to those given in Eqs. (II.4.4a) and (II.4.4b) (L/D_h = 56.8, 50.0, 29.9 and 24.0 for TS #1, TS #2, TS #3 and TS #4, respectively). However, estimating L_{sc} for the present data is quite

difficult because of both the small length of the micro-channels and the difficulty detecting ONB. To resolve this problem, only data corresponding to conditions where subcooled boiling was observed over the entire length (*i.e.*, $L_{sc} = L$) are examined. Figure II.4.4 shows significant departure of predictions based on Eqs. (II.4.4a) and (II.4.4b) from those specific data in terms of both slope and magnitude. This departure can be attributed to several factors. First, the two correlations contain five key parameters: mass velocity, inlet subcooling, outlet pressure, and two geometrical parameters (D_h and L/D_h ratio). There are appreciable differences between the parameters of the database from which the correlations were derived and those of the present study. For example, hydraulic diameter is 2.5 - 14 times smaller, mass velocity 5 - 60 times smaller, and pressure 6 - 9 times lower than the earlier database. Another key difference is working fluid. Past correlations, which were intended mainly for nuclear applications, used water as working fluid. The fluid used in the present study, HFE 7100, has far smaller latent heat of vaporization and surface tension than water; it is also far more wetting.

The weak predictions displayed in Fig. II.4.4 highlight the need for new models and/or correlations that are specifically suited for micro-channel flows and can tackle different types of fluids. Those are key objectives of ongoing research efforts by the author.

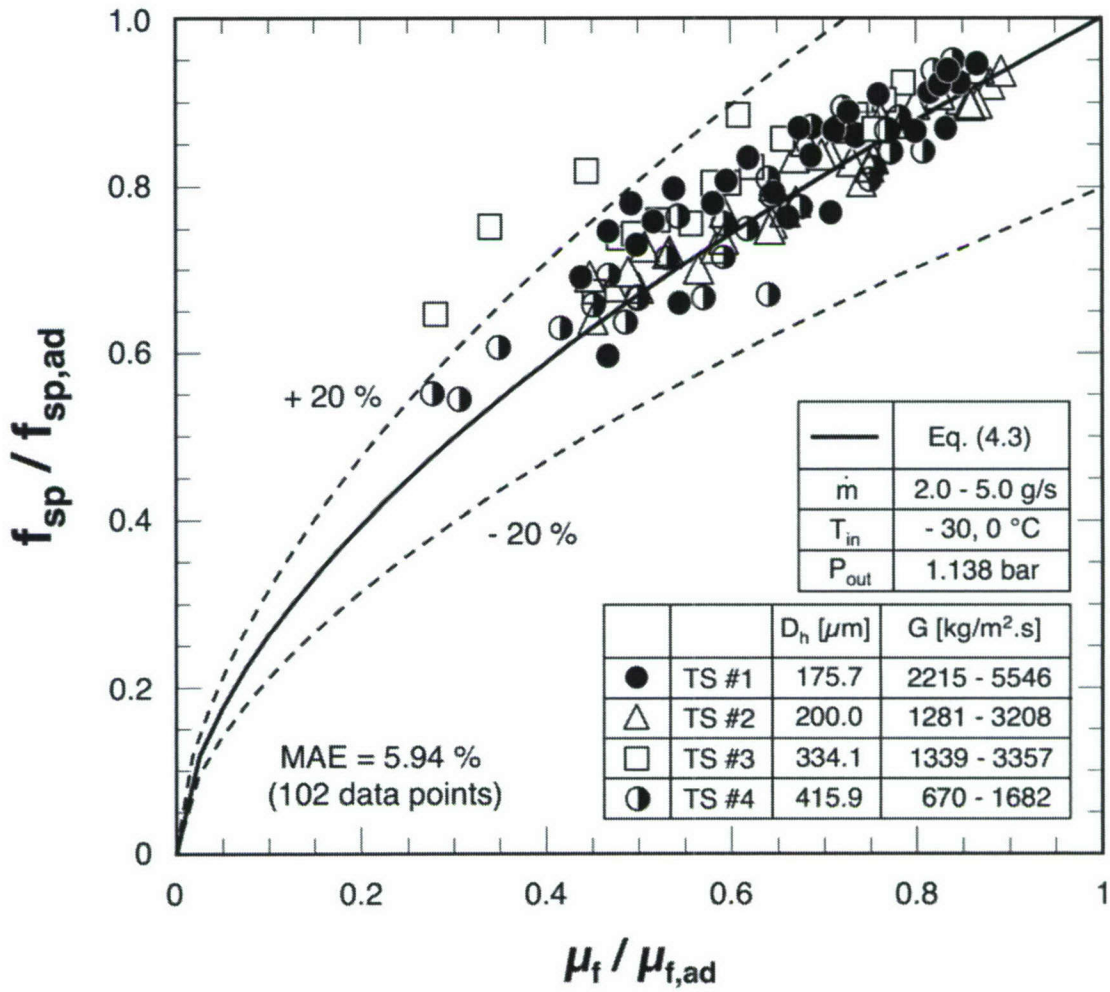

Figure II.4.3 Comparison of single-phase pressure drop data with predictions based on Eq. (II.4.3).

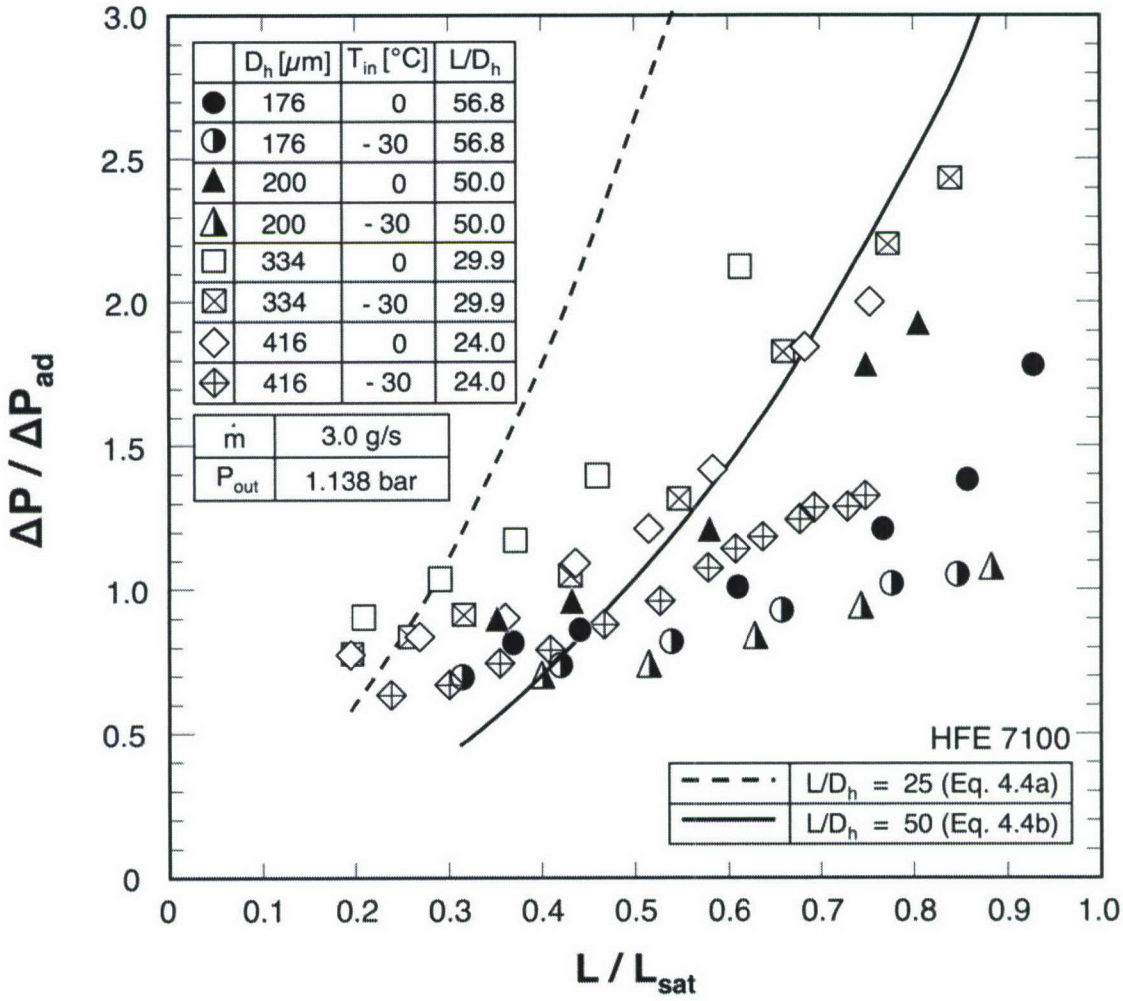

Figure II.4.4 Comparison of subcooled pressure drop data with predictions based on Eqs. (II.4.4a) and (II.4.4b).

II.4.2 Heat Transfer Results

II.4.2.1 Boiling Curves

Figure II.4.5 shows boiling curves for TS #4, which has the largest hydraulic diameter of D_h = 416 μm. These tests produced remarkable performance, exceeding 700 W/cm^2 for the highest mass velocity case. Interestingly, the relatively large hydraulic diameter for this particular test section produced the lowest mass velocity for a given flow rate compared to the other three test sections. This resulted in poorer cooling performance for TS #4 than the other test sections. This implies cooling performance well above 700 W/cm^2 is possible with the smaller hydraulic diameters. Those cases were not attempted because their pressure drop at high mass velocities exceeded the capability of the pump used in the present study. Efforts are underway to modify the loop in preparation for future experiments involving high flow rates with the three smaller hydraulic diameters.

Figure II.4.5(a) shows the effects of mass flow rate on boiling performance for TS #4. With the inlet temperature held constant, there is very little effect of flow rate on the nucleate boiling region. This means the heat transfer coefficient in this region is independent of mass velocity. The effects of flow rate are evident mostly in the single-phase region and at CHF. Higher flow rates are shown shifting the single-phase data upwards and delaying ONB to higher heat fluxes and higher surface temperatures. Higher CHF values are also achieved by increasing the flow rate. Notice that CHF conditions were reached with only the lower flow rates. Since the nucleate boiling region for the higher flow rates exceeded 700 W/cm^2, temperatures in the test module were quite elevated for both the cartridge heaters and fiberglass plastic parts, prompting the operator to halt the testing even before CHF was reached. Efforts are underway to improve the test module's design to enable future testing at yet higher heat fluxes.

Figure II.4.5(b) shows the effects of inlet temperature on boiling performance. Prominently captured in this plot are the two distinct nucleate boiling regions, each is associated with a different inlet temperature. This departure is the result of representing

the temperature axis as the difference between wall and inlet rather than saturation temperature. Increasing subcooling is shown delaying ONB and increasing CHF.

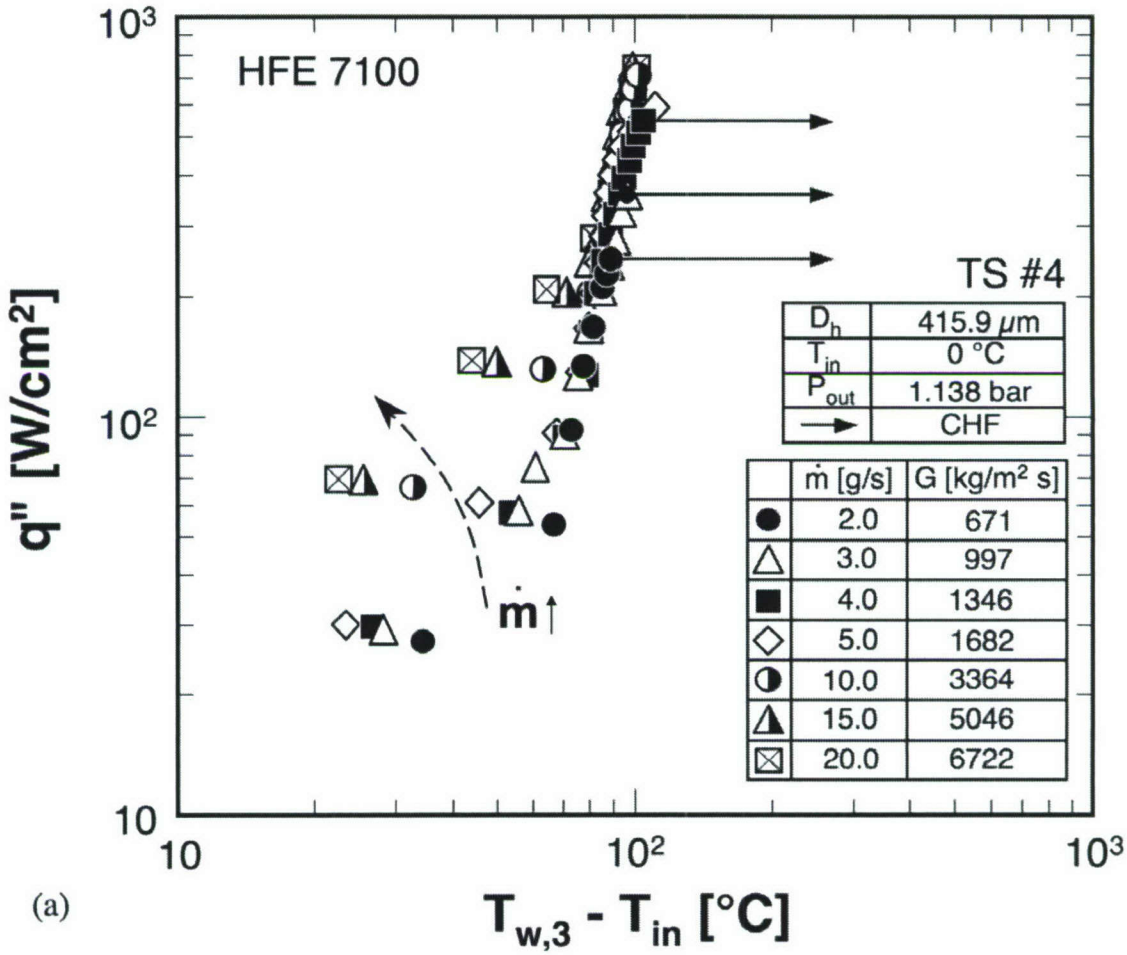

Figure II.4.5 Subcooled boiling curves for TS #4 (D_h = 415.9 μm) for (a) different flow rates and (b) different inlet temperatures.

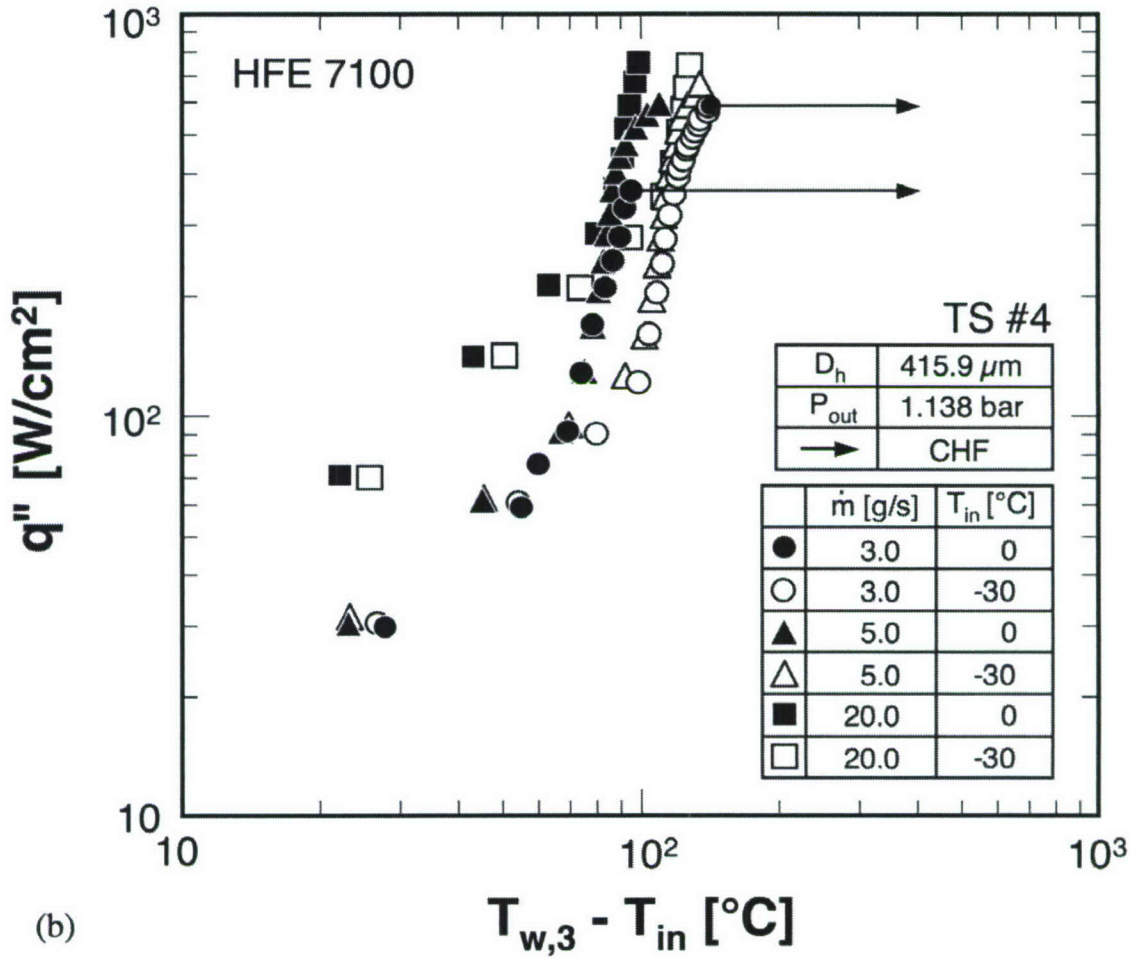

(b)

Figure II.4.5 continued.

II.4.2.2 Heat Transfer Coefficient Data

Figure II.4.6 shows for TS #4 the variation of mean heat transfer coefficient, which is average of local heat transfer coefficients for three micro-channel base locations above the thermocouples, with the mean of the three base temperatures at the same locations. Values of the local heat transfer coefficient and channel bottom wall temperature were determined using an iterative technique described in the chapter II.2.4. With a saturation temperature for HFE 7100 of 63 °C (based on outlet pressure), Fig. II.4.6 shows phase change occurs 5 to 14 °C above saturation temperature, depending on flow rate and inlet temperature. Before this point, cooling is the result of single-phase heat transfer to liquid. The transition to nucleate boiling is marked by a sharp increase in the magnitude of the heat transfer coefficient.

For fully developed laminar internal flow, single-phase heat transfer is associated with a constant Nusselt number, regardless of mass flow rate. However, Fig. II.4.6 shows mild changes in the heat transfer coefficient with flow rate because most of the micro-channel length in the present study consisted of developing entrance flow. Within this region, increasing mass flow rate (and therefore Reynolds number) increases the extent of the entrance region, resulting in a higher average single-phase heat transfer coefficient. Inlet temperature has a relatively minor effect, mostly in the form of mild variations in liquid properties. Figure II.4.6 shows nucleate boiling data follow a well-defined trend, fairly independent of flow rate or inlet subcooling except for near-CHF data.

Figure II.4.7(a) shows the variation of average heat transfer coefficient with mean wall temperature for the four test sections at the same inlet temperature and same flow rate. For fully developed laminar flow, the heat transfer coefficient is inversely proportional to hydraulic diameter. However, as discussed above, heat transfer coefficient in the present study is strongly influenced by entrance effects. Figure II.4.7(a) shows TS #1, which has the smallest hydraulic diameter of D_h = 176 μm, yields the highest single-phase heat transfer coefficient. However, TS #2 (200 μm) and TS #3 (334 μm) yield fairly equal $\overline{h}$ values despite the large difference in their hydraulic

diameters. This trend can be explained by the increased $\bar{h}$ for TS #3 resulting from a higher Reynolds number. There are also secondary effects for all tests sections resulting from micro-channel aspect ratio.

The nucleate boiling data in Fig. II.4.7(a) show a more complicated trend. Here, TS #4, which has the largest hydraulic diameter and therefore smallest mass velocity, shows the poorest two-phase performance. However, the highest heat transfer coefficients are achieved with TS #3 followed by TS #2 and then TS #1. Therefore, decreasing hydraulic diameter does not yield a monotonic increase in two-phase heat transfer coefficient. Secondary effects, such as channel width, sidewall thickness and aspect ratio, must play additional role.

This complex trend may be explained by the flow visualization results discussed in the chapter II.3. Aside from its larger D_h and lower G compared to both TS #1 and TS #2, TS #3 also has larger micro-channel width, W_{ch}. As discussed in the chapter II.3, narrow width facilitates earlier transition from bubbly to slug flow, which suppresses nucleate boiling activity and reduces the two-phase heat transfer coefficient. This is clearly manifest in Fig. II.4.7(a) in the form of superior two-phase performance for TS #3 compared to both TS #1 and TS #2. This may also be the reason why TS #2 provides better two-phase heat transfer performance compared to TS #1. While both have the same micro-channel width and wall thickness, TS #2 has deeper micro-channels (*i.e.,* larger H_{ch}), allowing more room for bubbles to move along the micro-channel with reduced interaction with other bubbles compared to TS #1.

The effects of hydraulic diameter and subcooling on the two-phase heat transfer coefficient are also shown in Fig. II.4.7(b). For a given heat flux, smaller micro-channels delay the commencement of subcooled boiling because of both their high mass velocity and increased wetted area, as was discussed in the chapter II.3. Higher subcooling produces a similar trend.

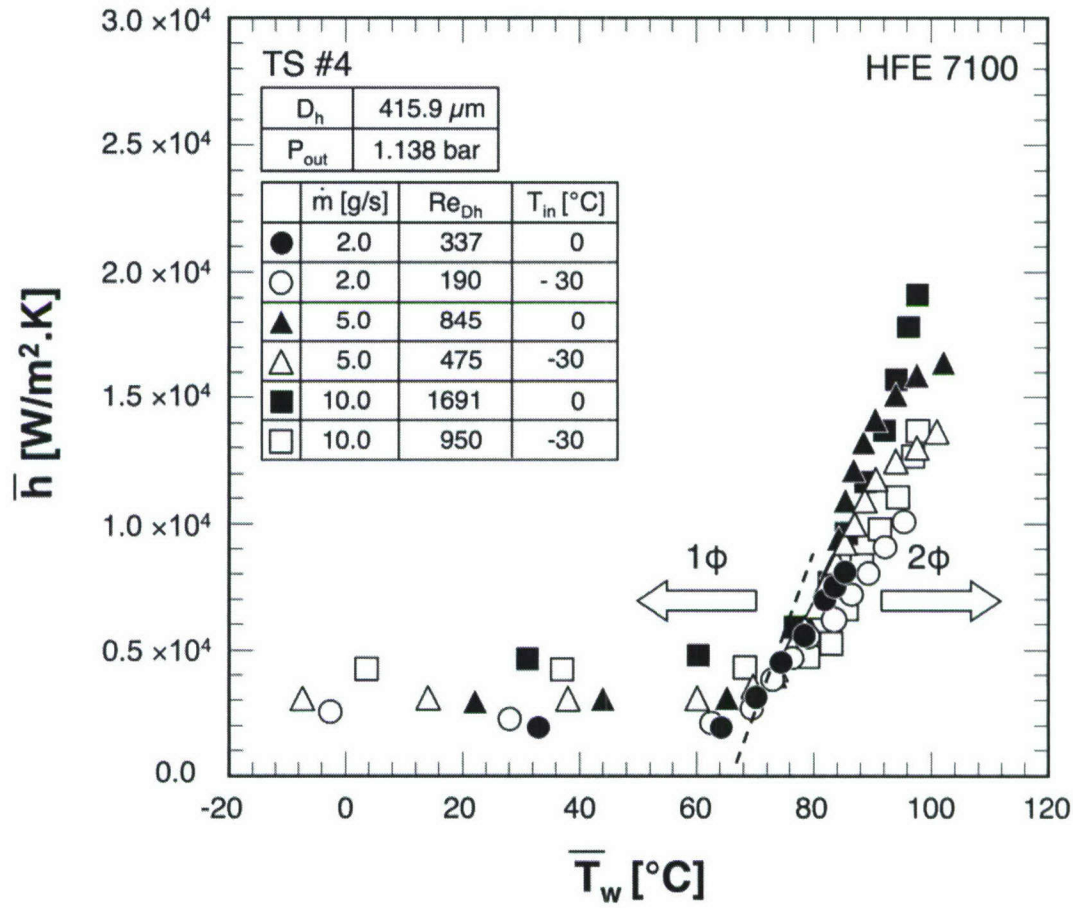

Figure II.4.6 Variation of mean heat transfer coefficient with mean wall temperature for test section TS #4 for different flow rates and two inlet temperatures.

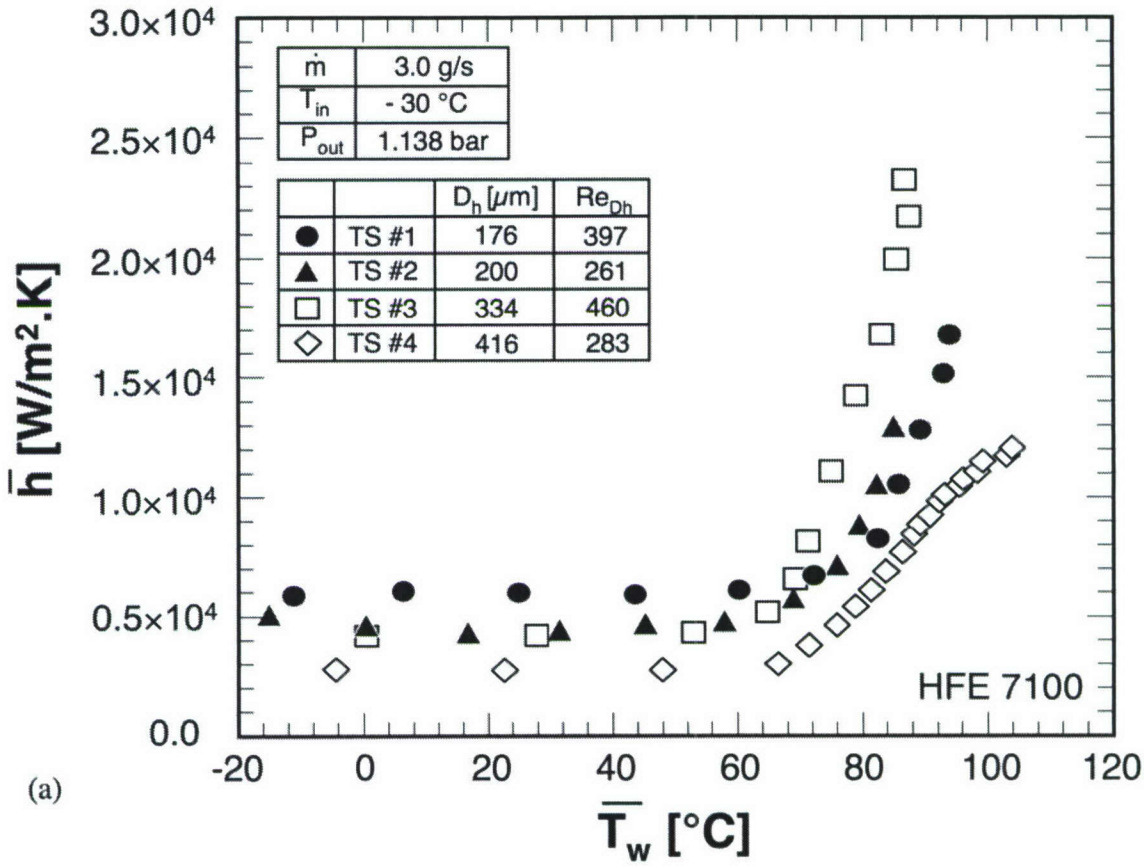

(a)

Figure II.4.7 (a) Variation of average heat transfer coefficient with average wall temperature for different hydraulic diameters. (b) Variation of average heat transfer coefficient with heat flux for different hydraulic diameters and two inlet temperatures.

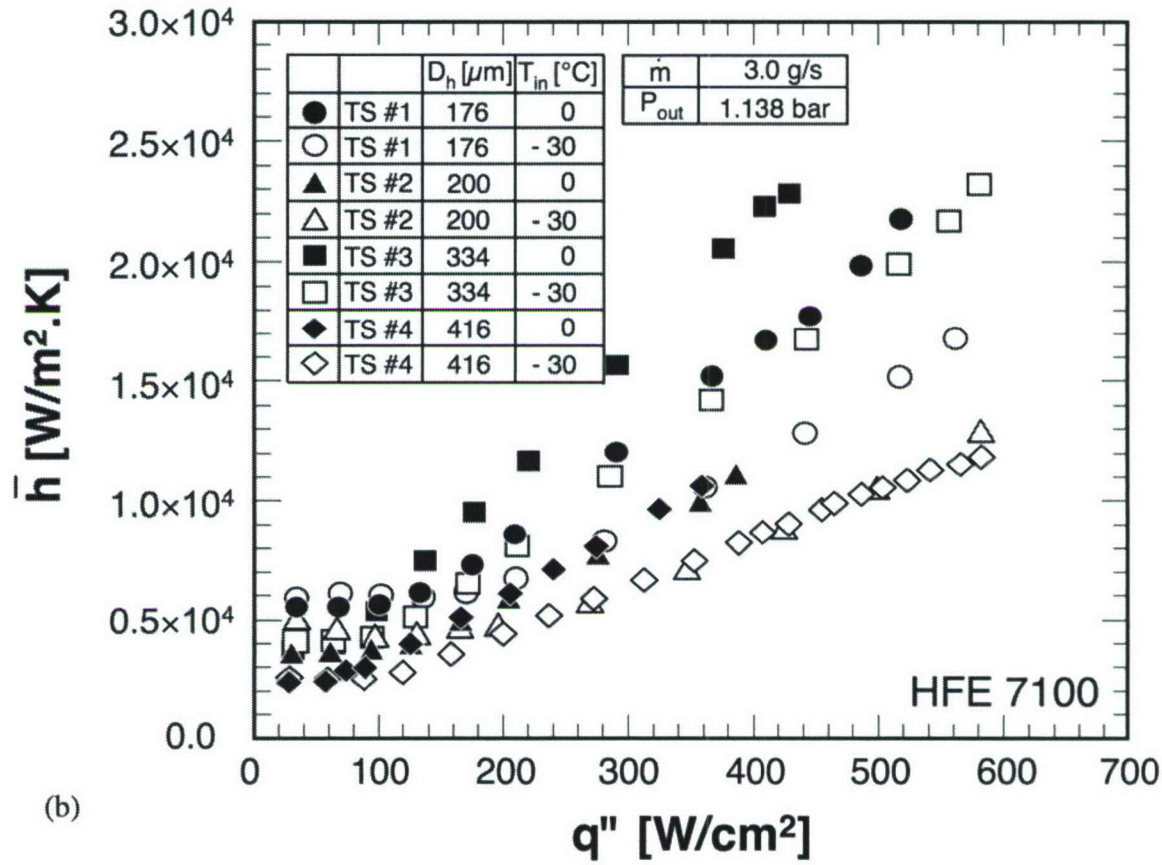

(b)

Figure II.4.7 continued.

II.4.2.3 Evaluation of Prior Correlations

Very few correlations are available in the literature for the prediction of subcooled boiling heat transfer. Table II.4.1 provides a select summary of correlations whose predictions are compared to the present data. The Shah correlation for saturated boiling has shown favorable predictive capability for macro circular tubes (Shah, 1976). He later modified his original correlation to tackle subcooled boiling as well (Shah, 1977). Kandlikar also developed a correlation for saturated boiling (Kandlikar, 1990), which he later modified to fit subcooled boiling data for various types of fluids, water and refrigerants (Kandlikar, 1998). The correlations of both Shah and Kandlikar require knowledge of the single-phase heat transfer coefficient, h_{sp}. Since the primary goal here is to assess the capability of correlations at predicting two-phase heat transfer, h_{sp} in these correlations was replaced by mean values measured in the present study.

Figure II.4.8 compares predictions based on the Shah saturated and subcooled boiling correlations, as well as Kandlikar's subcooled boiling correlations, to present data for the four tests sections corresponding to T_{in} = 0 °C. Kandlikar's saturated boiling correlation is excluded because it yielded unusually poor predictions. In the initial stages of the subcooled boiling region, Fig. II.4.8 shows Shah's subcooled boiling correlation overpredicts the present data, while his saturated boiling correlation underpredicts; the data fall midway between the two. However, Shah's two correlations and the present data do converge at the end of the subcooled boiling region. Kandlikar correlations on the other hand show poor overall predictions. Figure II.4.9 shows fairly similar predictive trends for T_{in} = - 30 °C.

Another type of subcooled boiling correlation consists of presenting the ratio of subcooled boiling Nusselt number to single-phase Nusselt number as a function of boiling number, Jacob number, and density ratio. Such are the correlations by Papell (1963) and Moles and Shaw (1972). Figure II.4.10 shows the Papell correlation predicts the present data with a mean absolute error of 69.8%. Interestingly, better predictions are achieved with lower aspect ratio test sections (TS #1 and TS #3) than those with

higher aspect ratio (TS #2 and TS #4). However, it is difficult to draw definitive conclusions about this trend in the absence of any geometrical parameters in the correlation itself. Table II.4.1 shows predictions of the Moles and Shaw correlation are far worse than those of Papell's.

II.4.2.4 New Correlation

While none of the prior correlations provided accurate predictions, Shah's saturated and subcooled correlations showed some promise. Since the present data fell about halfway between the two correlations, the following new correlation was derived that yields values close to the mean of these correlations.

$$q'' = 230 Bo^{0.5} h_{sp} \left[0.828 \Delta T_{sat} + 0.463 \Delta T_{sat}^{-0.04} \Delta T_{sub}^{0.81} \right]. \qquad \text{(II.4.12)}$$

In this equation, the boiling number dependence of the original correlations was preserved, but the dependence on wall superheat and subcooling was adjusted to yield least mean absolute error from the data. Figure 4.11 shows this new correlation predicts 260 heat transfer data points for all four test sections with a mean absolute error of 9.1%, with almost all the data falling within ± 30% of predicted values.

A key drawback in using Eq. (II.4.12) is the difficulty directly inferring the magnitude of the heat transfer coefficient. A second correlation is therefore suggested for direct estimation of the subcooled boiling heat transfer coefficient. Like the second group of correlations in Table II.4.1, the normalized two-phase Nusselt number is correlated according to the form

$$\frac{Nu_{tp}}{Nu_{sp}} = 90.0\, Bo^{0.9}\, Ja^{*-0.98}\, We^{*0.15}\, \beta^{-0.42}, \qquad \text{(II.4.13)}$$

where
$$Ja^* = \frac{c_{p,f}\, \Delta T_{sub,in}}{h_{fg}}, \quad We^* = \frac{G^2 D_h}{\left(\rho_f - \rho_g\right)\sigma}, \text{ and } \beta = \frac{H_{ch}}{W_{ch}}. \qquad \text{(II.4.14)}$$

Unlike earlier correlations, Eq. (II.4.13) accounts for all relevant physical parameters of subcooled flow boiling in micro-channels. The effects of heat flux, inlet subcooling, surface tension and geometry are accounted for in four respective dimensionless groups: boiling number, Jacob number, Weber number and channel aspect ratio. Figure II.4.12 compares the predictions of this new correlation with experimental data for the four test sections. Although the mean absolute error for this correlation is greater than for Eq. (II.4.12), Eq. (II.4.13) enables direct calculation of the two-phase heat transfer coefficient as well as accounts for all the parameters that were shown in previous discussion of this study to influence cooling performance.

Table II.4.1 Subcooled boiling heat transfer correlations.

Author(s)	Correlations		MAE	Remarks
Shah (1976)	$q'' = 230\,Bo^{0.5}\,h_{sp}\,\Delta T_{sat}$, $Bo = \dfrac{q''}{G\,h_{fg}}$	(4.6)	35.1 %	Saturated boiling (various Newtonian fluids except liquid metals)
Shah (1977)	$q'' = 0.54\left\{230\,Bo^{0.5}\,h_{sp}\right\}\left(\Delta T_{sub}\right)^{7.83/8.33}\left(\Delta T_{sat}\right)^{1/8.33}$, where $\Delta T_{sat} = T_w - T_{sat}$ and $\Delta T_{sub} = T_{sat} - T_f$	(4.7)	44.3 %	Subcooled boiling (water, ammonia, refrigerants, alcohols, CCl_4, K_2CO_3, etc)
Kandlikar (1998)	$q'' = \left[1058\left(G\,h_{fg}\right)^{-0.7} F_f\,h_{sp}\,\Delta T_{sat}\right]^{1/0.3}$, $F_f = 1.0$ for water	(4.8)	313 %	Water subcooled boiling
	$q'' = \left[1058\left(G\,h_{fg}\right)^{-0.7} F_f\,h_{sp}\,\Delta T_{sat}\right]^{1/0.3}$, $F_f = 1.5$ for R - 12	(4.9)	1381 %	Refrigerant subcooled boiling (other F_f values recommended for different refrigerants)
Papell (1963)	$\dfrac{Nu_{tp}}{Nu_{sp}} = 90.0\,Bo^{0.7}\left(\dfrac{h_{fg}}{c_{p,f}\,\Delta T_{sub}}\right)^{0.84}\left(\dfrac{\rho_g}{\rho_f}\right)^{0.756}$	(4.10)	69.8 %	Water, ammonia
Moles and Shaw (1972)	$\dfrac{Nu_{tp}}{Nu_{sp}} = 78.5\,Bo^{0.67}\left(\dfrac{h_{fg}}{c_{p,f}\,\Delta T_{sub}}\right)^{0.50}\left(\dfrac{\rho_g}{\rho_f}\right)^{-0.03} Pr_f^{0.45}$	(4.11)	658 %	Water, acetone, isopropyl alcohol

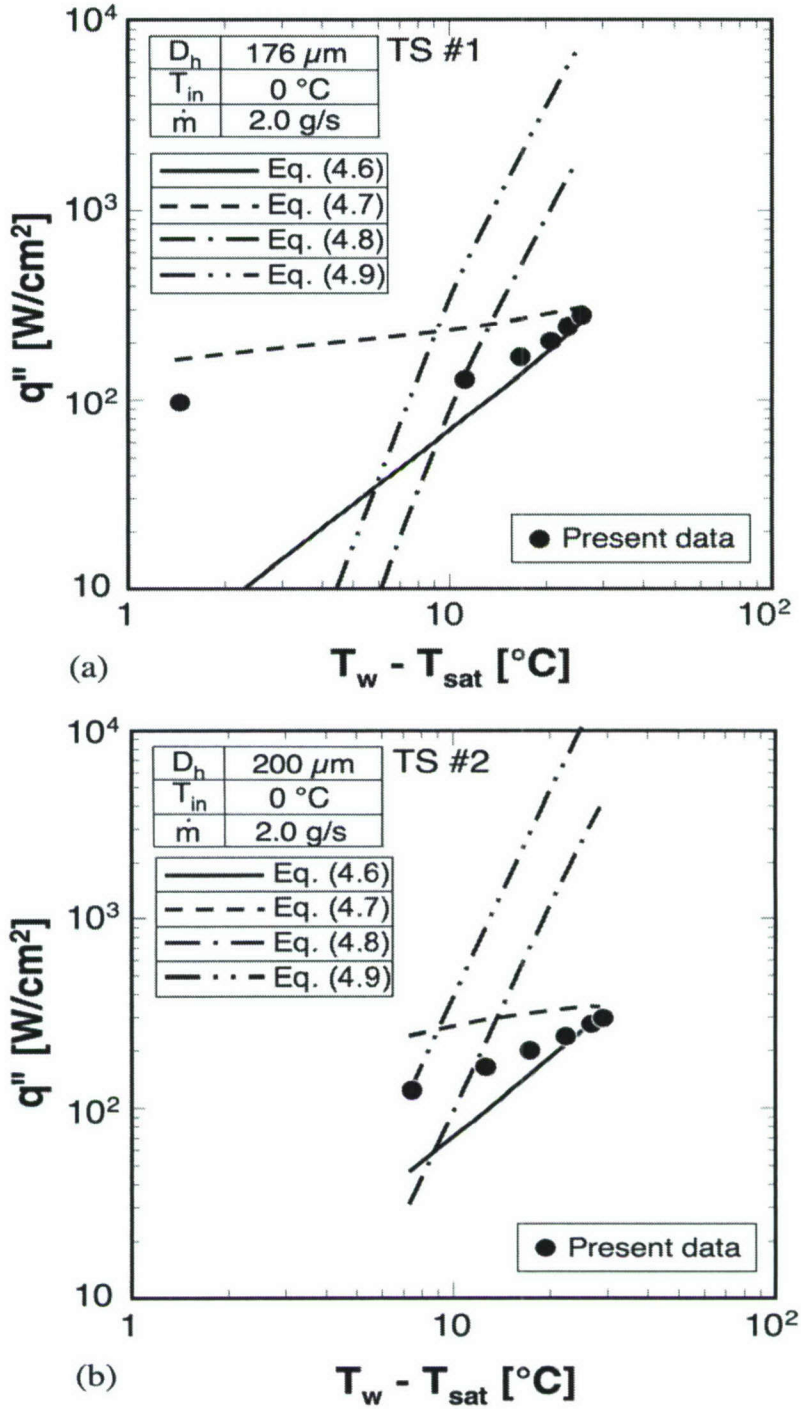

Figure II.4.8 Comparison of predictions of prior two-phase heat transfer correlations and present subcooled boiling data corresponding to T_{in} = 0 °C for (a) TS #1, (b) TS #2, (c) TS #3, and (d) TS #4.

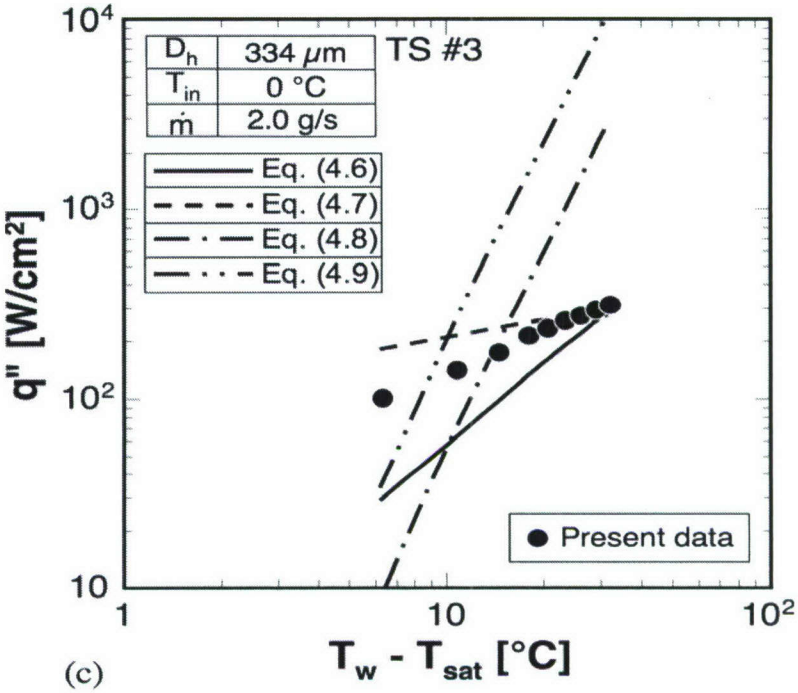

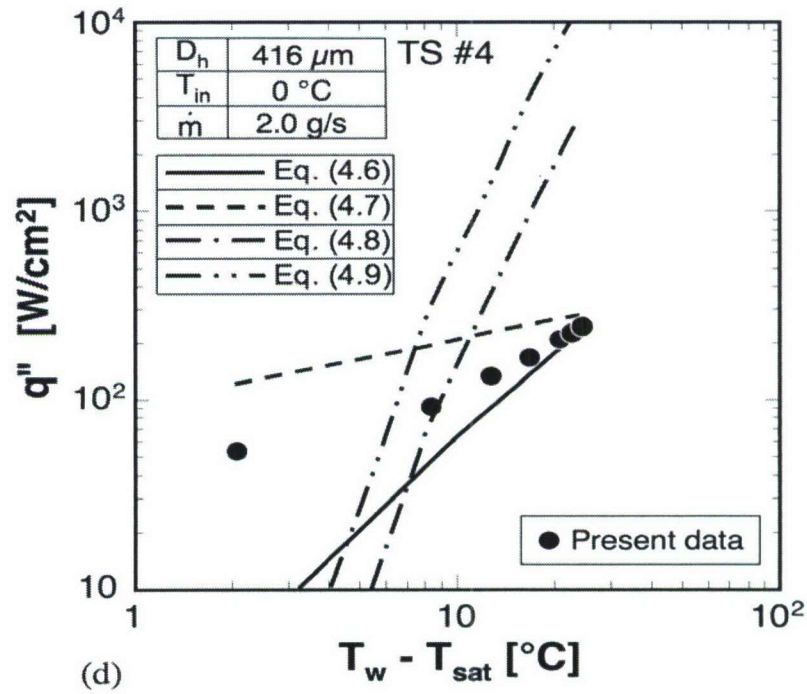

Figure II.4.8 continued.

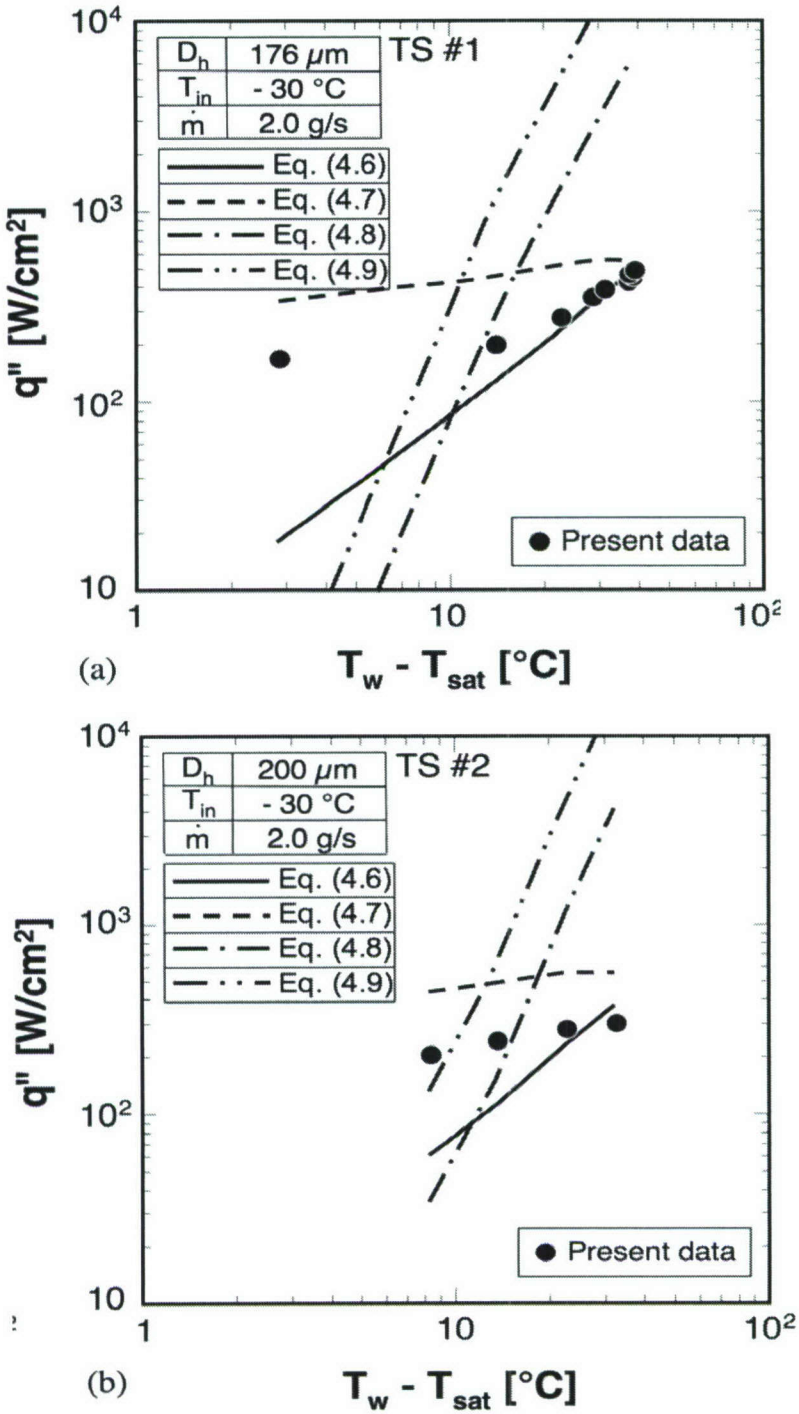

Figure II.4.9 Comparison of predictions of prior two-phase heat transfer correlations and present subcooled boiling data corresponding to T_{in} = - 30 °C for (a) TS #1, (b) TS #2, (c) TS #3, and (d) TS #4.

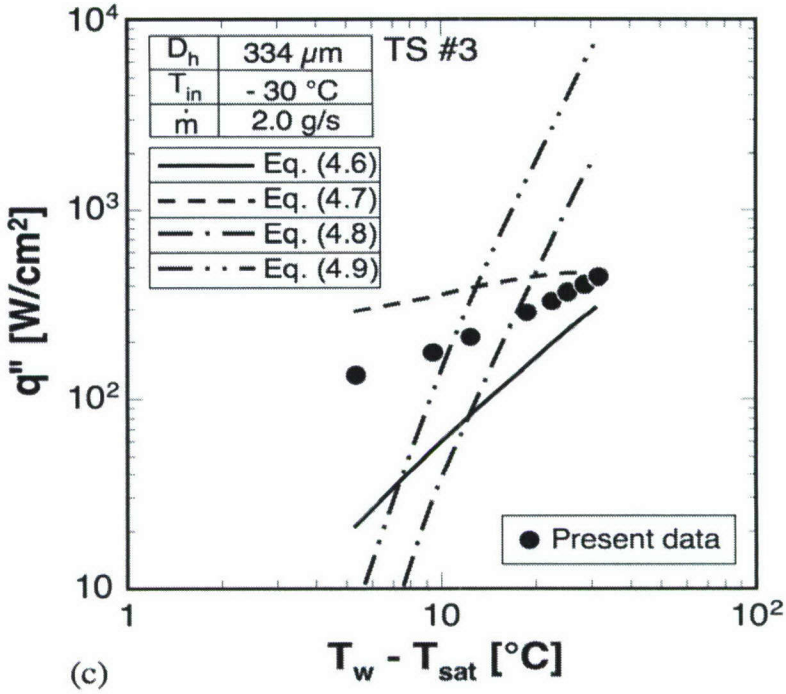

(c)

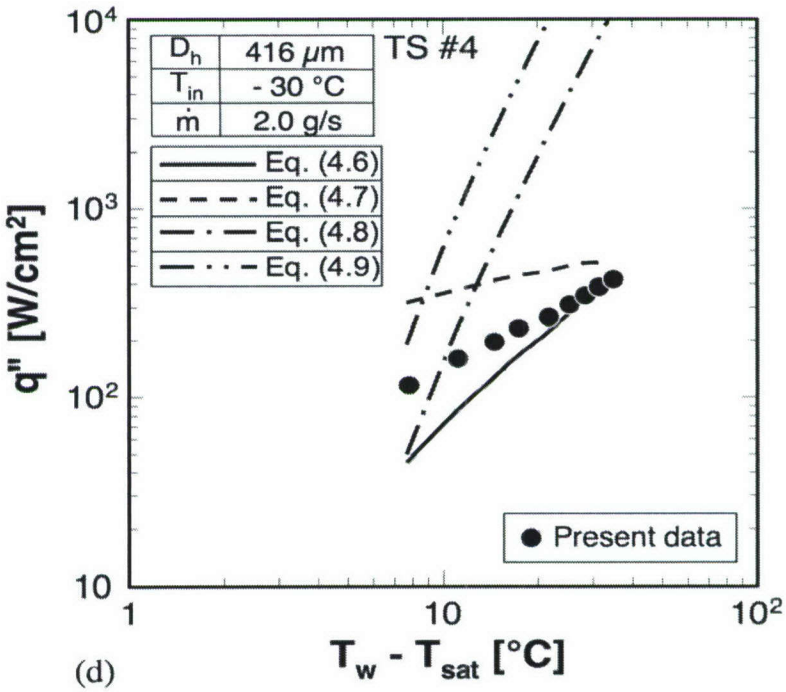

(d)

Figure II.4.9 continued.

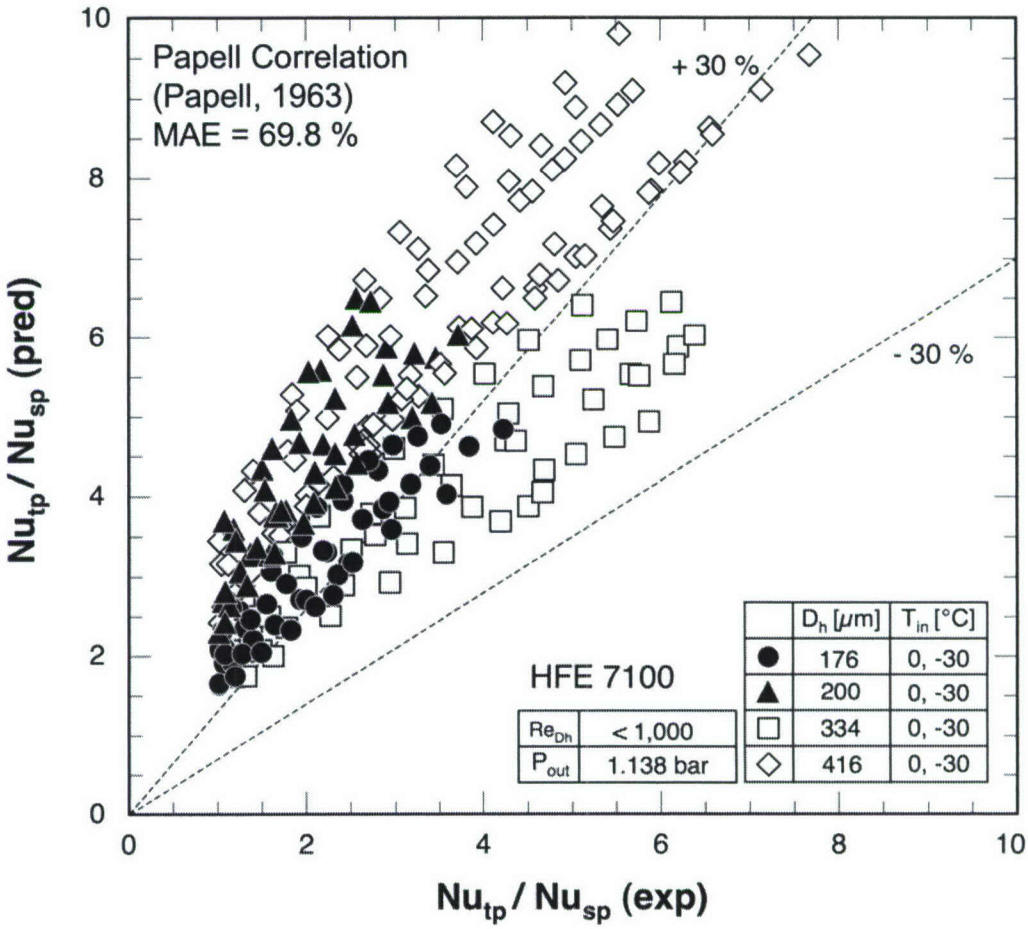

Figure II.4.10 Comparison of predictions of Papell's correlation and present subcooled boiling data.

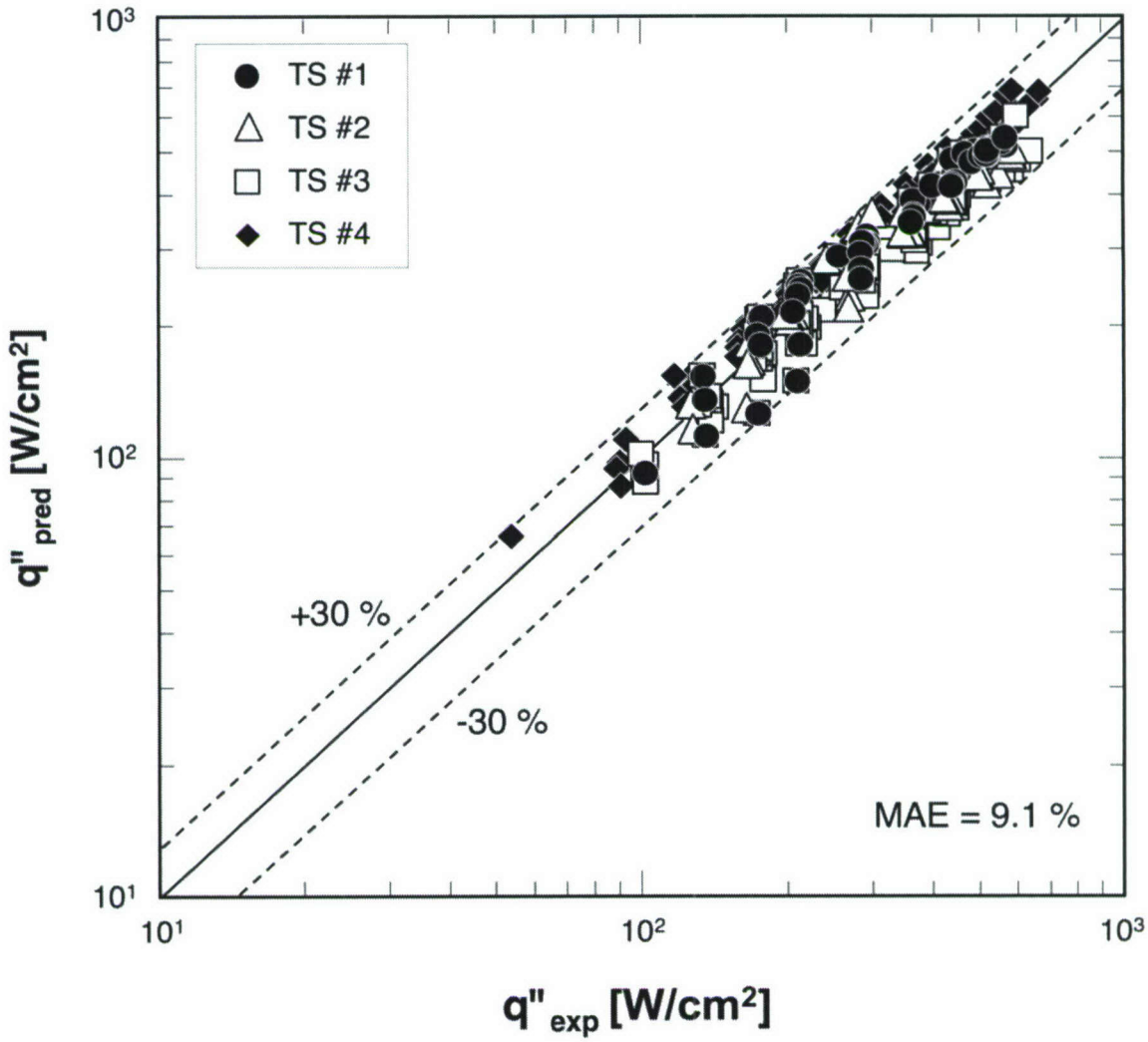

Figure II.4.11 New correlation for subcooled boiling data of four test sections.

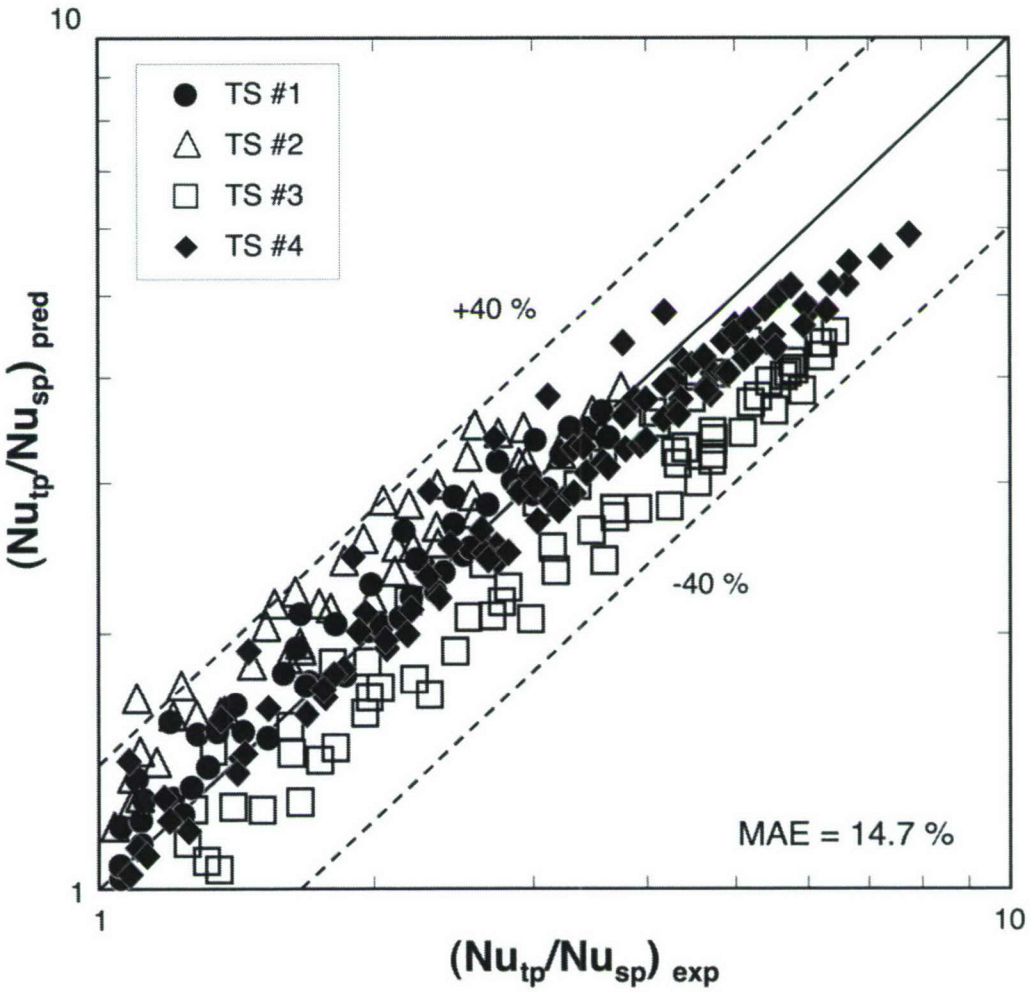

Figure II.4.12 Comparison of predictions of new normalized two-phase Nusselt number correlation and experimental data for four test sections.

II.5 DEVELOPING HOMOGENEOUS LAYER MODEL (DHLM) FOR SUBCOOLED BOILIING PRESSURE DROP

II.5.1 Developing homogeneous Layer Model (DHLM)

II.5.1.1 Model Description and Assumptions

Subcooled flow boiling is initiated when bubbles begin to nucleate in a mostly subcooled liquid flow, and extends to the axial location where thermodynamic equilibrium quality reaches zero. The subcooled flow boiling region consists of two sub-regions, a highly subcooled sub-region, and the developing subcooled sub-region. Vapor void in the highly subcooled sub-region is a wall effect since strong condensation effects along the bubble interface suppress bubble growth and prevent coalescence between bubbles. The developing subcooled sub-region is initiated at the point of bubble detachment off the heating wall. Here, bubbles are able to grow and depart into the subcooled liquid stream.

Flow visualization studies in chapter II.3 shed some light on the unique nature of subcooled boiling in micro-channels. Unlike flow in long macro-channels, the transition from single-phase liquid flow or highly subcooled flow to developing subcooled boiling in short micro-channels results from a relatively mild increase in heat flux. Furthermore, the subcooled boiling engulfs the entire length of the micro-channel at once, dominated mostly by bubbly flow and to a lesser extent slug flow. This justifies using a homogeneous flow description to model the vapor layer.

Figure II.5.1 shows a schematic representation of the *Developing Homogeneous Layer Model (DHLM)* model adopted in this study. This model is constructed specifically for developing subcooled flow boiling in micro-channels and should be

extended to neither the single-phase region nor the saturated boiling region. This model considers conditions where developed subcooled boiling engulfs the entire length of the micro-channels. Thus, it precludes an upstream single-phase region or downstream saturated boiling region along the heated wall. Extension of the developing subcooled boiling layer both upstream and downstream of the heated length as shown in Fig. II.5.1(a) will be discussed later.

DHLM assumes the flow consists of two layers, a subcooled liquid core and a homogeneous two-phase flow layer; the latter represents the bubbly region of the flow. The homogeneous layer thickens along the flow direction due to wall heating. Key assumptions of the model are as follows:

(1) The flow is one-dimensional, meaning flow velocity in each layer is constant at any axial location.

(2) The flow is steady.

(3) The liquid layer flow is laminar and incompressible, also because of the large density and relatively strong momentum of liquid relative to the two-phase layer, the liquid velocity is assumed constant along the flow direction.

(4) The two-phase layer behaves as a homogeneous two-phase mixture whose properties are weighted averages of those of liquid and vapor.

(5) There is no thermal equilibrium between the two layers. The two-phase layer is assumed to maintain saturated temperature, while the liquid layer is subcooled. In the flow direction, heat supplied from the wall increases quality in the homogenous layer and liquid temperature. Heat is also transferred between the two layers.

(6) Pressure is uniform across the flow area of the micro-channel at every axial location.

(7) As shown in Fig. II.5.1(b), an idealized flat interface is assumed between the homogeneous two-phase layer and the liquid layer to determine mean thickness of the two-phase layer from the model. As shown in Fig. II.5.1(c), the actual interface is distorted by greater void toward the sidewalls and lesser void near the center of the micro-channel because of heating from the sidewalls.

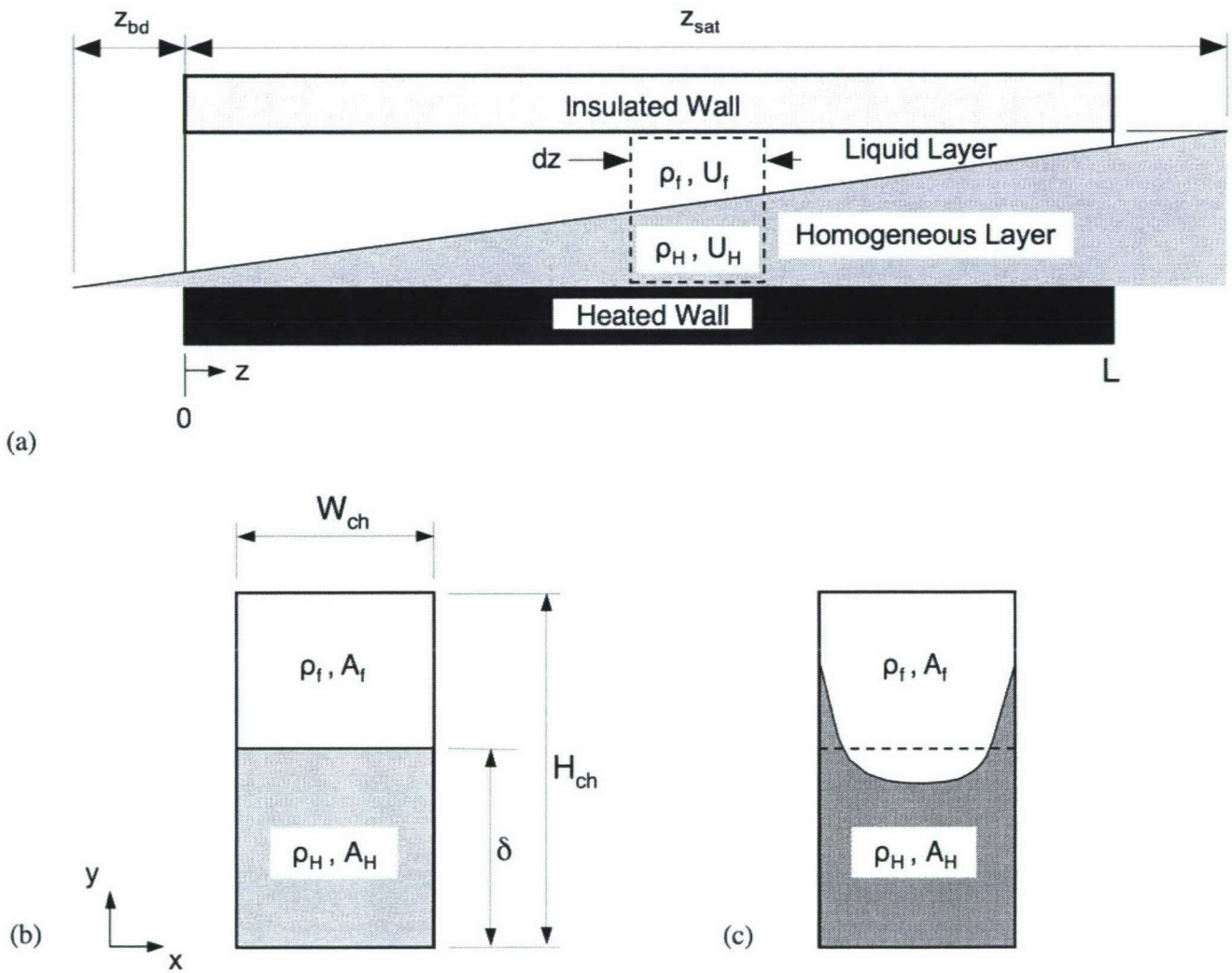

Figure II.5.1 (a) Side view and (b) cross-sectional view representation of Developing Homogeneous Layer Model (DHLM). (c) Cross-sectional view of actual interface between homogeneous two-phase layer and liquid layer in the presence of sidewall heating effects.

II.5.1.2 Control Volume Conservation Equations

Figure II.5.2(a) shows mass flow terms for a micro-channel control volume of length Δz along the flow direction. Mass conservations for the liquid layer and the homogeneous layer can be expressed, respectively, as

$$\frac{d\left(\rho_f U_f A_f\right)}{dz} + K_i = 0, \tag{II.5.1}$$

and

$$\frac{d\left(G_H A_H\right)}{dz} - K_i = 0, \tag{II.5.2}$$

where $G_H = \rho_H U_H$, the mass velocity of the homogeneous layer, and K_i is the rate of mass transfer from the liquid layer to the homogeneous layer per unit axial distance. Since liquid density is assumed constant, it can taken out of the derivative in Eq. (II.5.1).

Figure II.5.2(b) shows energy conservation for the homogeneous layer alone. Heat supplied from the wall is consumed in used in two different ways. A portion of this heat increases the temperature of the liquid mass transferred between the liquid layer and the homogeneous layers from T_f to T_{sat}. The remaining portion increases the latent heat of the homogeneous layer. Therefore, energy conservation for the homogenous layer can be expressed as

$$q''\left(W_{ch} + W_w\right) = \frac{d}{dz}\left(G_H A_H h_H\right) + K_i c_{p,f}\left(T_{sat} - T_f\right), \tag{II.5.3}$$

Because of the subcooled boiling state of the flow, the enthalpy, h_H, of the homogeneous layer requires careful assessment. This issue will be discussed in the next section.

Figure II.5.3 shows the momentum changes and forces acting on the control volume. Momentum conservation for the liquid layer and the homogeneous layer can be expressed, respectively, as

$$\frac{d\left(\rho_f U_f^2 A_f\right)}{dz} + K_i U_i = -A_f \frac{dP}{dz} - P\frac{dA_f}{dz} - \tau_{f,w}\left[W_{ch} + 2\left(H_{ch} - \delta\right)\right] - \tau_i W \tag{II.5.4}$$

and $$\frac{d\left(\rho_H U_H^2 A_H\right)}{dz} - K_i U_i = -A_H \frac{dP}{dz} - P\frac{dA_H}{dz} - \tau_{H,w}\left[W_{ch} + 2\delta\right]W + \tau_i W \,. \qquad \text{(II.5.5)}$$

Combining Eqs. (II.5.4) and (II.5.5) eliminates both the interfacial momentum and interfacial friction terms, resulting in the following equation

$$\frac{d\left(\rho_f U_f^2 A_f\right)}{dz} + \frac{d\left(\rho_H U_H^2 A_H\right)}{dz} = -A\frac{dP}{dz} - \left\{\tau_{f,w}\left[W_{ch} + 2\left(H_{ch} - \delta\right)\right] + \tau_{H,w}\left[W_{ch} + 2\delta\right]\right\}. \text{(II.5.6)}$$

Equations (II.5.1), (II.5.2), (II.5.3), and (II.5.6) are main governing equation for *DHLM*.

(a)

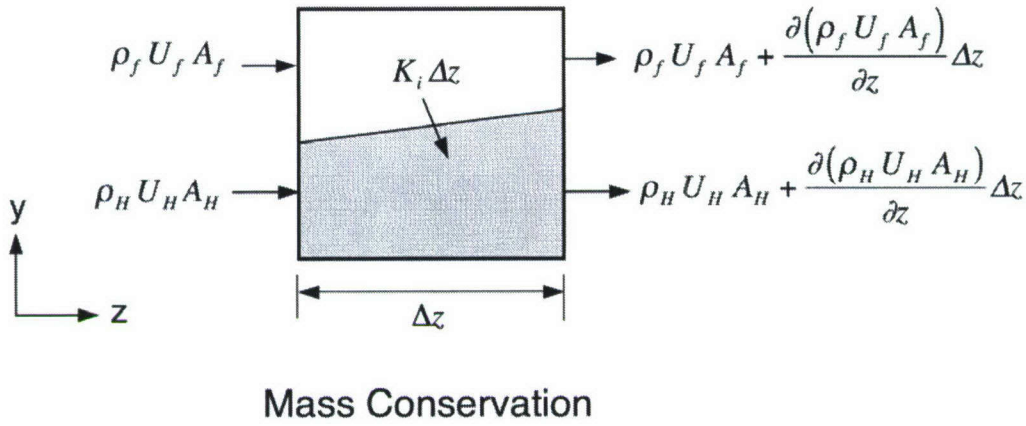

Mass Conservation

(b)

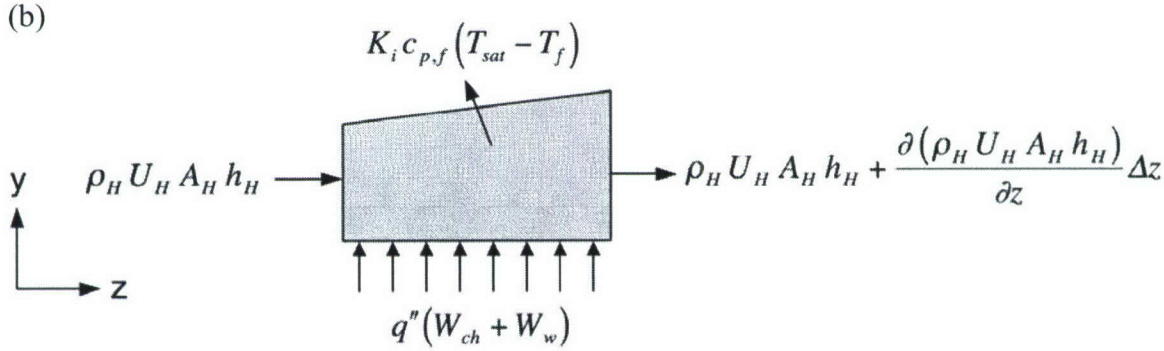

Energy Conservation

Figure II.5.2 (a) Mass conservation for liquid and homogeneous layer control volumes.
(b) Energy conservation for homogenous layer control volume.

(a)

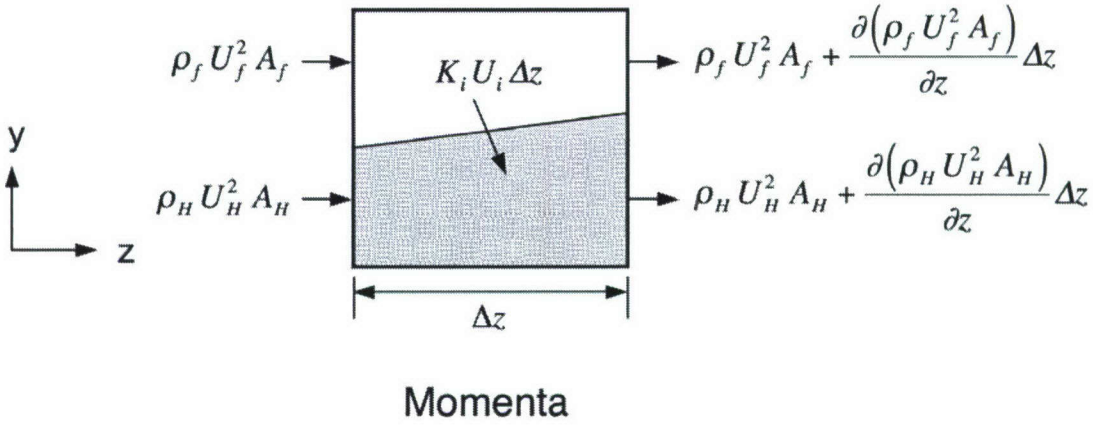

Momenta

(b)

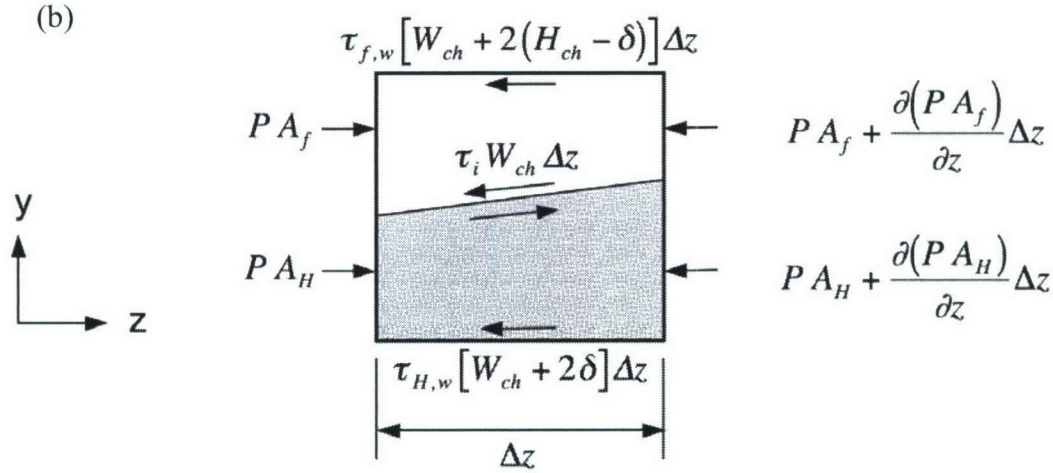

Forces

Figure II.5.3 (a) Momenta and (b) forces for liquid and homogeneous layer control volumes.

II.5.1.3 Solution Scheme

Referring to Fig. II.5.1(b) the flow areas for the liquid layer and the homogeneous layer can be expressed, respectively, as

$$A_f = W_{ch}\left(H_{ch} - \delta\right) \tag{II.5.7}$$

and

$$A_H = W_{ch}\,\delta. \tag{II.5.8}$$

Therefore, the area derivatives with respect to z can be expressed as

$$\frac{dA_f}{dz} = -W_{ch}\frac{d\delta}{dz} \tag{II.5.9}$$

and

$$\frac{dA_H}{dz} = W_{ch}\frac{d\delta}{dz}. \tag{II.5.10}$$

Based on the assumptions of *DHLM*, the liquid layer is assumed to preserve its velocity along the micro-channel. Therefore,

$$U_f = \frac{G}{\rho_f} \tag{II.5.11}$$

and

$$\frac{dU_f}{dz} = 0. \tag{II.5.12}$$

where G is mass velocity of the incoming subcooled non-boiling liquid. Since both ρ_f and U_f are constant along the flow direction, Eq. (II.5.1) yields

$$K_i = -\rho_f U_f \frac{dA_f}{dz}. \tag{II.5.13}$$

Introducing the above relation in Eq. (II.5.9) gives

$$K_i = \rho_f U_f W_{ch}\frac{d\delta}{dz}. \tag{II.5.14}$$

Combining Eq. (II.5.14) with Eqs. (II.5.2), (II.5.8) and (II.5.10) gives

$$\frac{d\delta}{dz} = \frac{\delta \dfrac{dG_H}{dz}}{\left(\rho_f U_f - G_H\right)}. \tag{II.5.15}$$

One of the key parameters in *DHLM* is the enthalpy, h_H, of the homogeneous two-phase layer. Because vapor is generated in along the micro-channel in a subcooled boiling region, thermodynamic equilibrium quality cannot be used to determine the enthalpy of the two-phase layer. Therefore, the enthalpy of this layer is defined as

$$h_H = h_f + x_H^{'} h_{fg}, \tag{II.5.16}$$

where $x_H^{'}$ is an *apparent* flow quality. Two different formulations have been recommended for apparent quality in subcooled boiling. Levy's (1967) formulation was attempted but produced unrealistic predictions for micro-channel flow. A second formulation by Kroeger and Zuber (1968) is used here.

$$x_H^{'}(z) = \frac{c_{p,f}\,\Delta T_{sub,in}\left(Z^{+} - T^{*}\right)}{h_{fg} - c_{p,f}\,\Delta T_{sub,in}\left(1 - T^{*}\right)}, \tag{II.5.17}$$

where

$$Z^{+} = \frac{z - z_{bd}}{z_{sat} - z_{bd}} \tag{II.5.18}$$

and

$$T^{*} = tanh\left(Z^{+}\right). \tag{II.5.19}$$

Now the apparent quality in homogeneous layer is set and two-phase flow apparent quality can be predetermined over whole test section domain without calculation of other governing equation variables. Quality gradient is also required later, but it can be easily obtained since all quality values are set by equation (II.5.17).

Combining Eqs. (II.5.10), (II.5.14) to (II.5.16) and (II.5.17) with energy conservation Eq. (II.5.3) yields

$$\frac{dG_H}{dz} = \frac{\left(\rho_f U_f - G_H\right)\left\{q''\left(W_{ch}+W_w\right) - W_{ch}\,\delta\, G_H\, h_{fg}\dfrac{dx_H'}{dz}\right\}}{GW_{ch}\,\delta\left[h_H + c_{p,f}\left(T_{sat}-T_f\right)\right]}. \qquad \text{(II.5.20)}$$

Another equation for homogeneous layer thickness δ can be determined by substituting Eq. (II.5.20) into (II.5.15).

$$\frac{d\delta}{dz} = \frac{q''\left(W_{ch}+W_w\right) - W_{ch}\,\delta\, G_H\, h_{fg}\dfrac{dx_H'}{dz}}{GW_{ch}\left[h_H + c_{p,f}\left(T_{sat}-T_f\right)\right]}. \qquad \text{(II.5.21)}$$

Equations (II.5.20) and (II.5.21) are coupled ordinary differential equations. Referring to Fig. II.5.1(a), these equations must satisfy the conditions

$$\delta = \begin{cases} 0 & at\ z = -z_{bd} \\ H_{ch} & at\ z = z_{sat} \end{cases} \qquad \text{(II.5.22)}$$

and

$$G_H = \begin{cases} 0 & at\ z = -z_{bd} \\ G & at\ z = z_{sat} \end{cases}. \qquad \text{(5.23)}$$

To meet those boundary conditions, the homogeneous two-phase layer is assumed to evolve from zero thickness at an *equivalent* distance $-z_{bd}$ associated with preheating the flow at the same heat flux supplied at the micro-channel. The homogeneous layer is also assumed to engulf the entire cross-section at another equivalent distance z_{sat} extending beyond the micro-channel exit and where the flow is subjected to the same heat flux supplied at the micro-channel.

Finally, Eqs. (II.5.9) and (II.5.10) are used along with $U_H = G_H/\rho_H$ to simplify momentum equation (II.5.6) to the following explicit form:

$$\frac{dP}{dz} = -\frac{1}{W_{ch}H_{ch}}\left[-\rho_f U_f^2 W_{ch}\frac{d\delta}{dz} + \rho_H U_H^2 W_{ch}\frac{d\delta}{dz} + 2\rho_H U_H W_{ch} H_{ch}\frac{dU_H}{dz} + U_H^2 W_{ch} H_{ch}\frac{d\rho_H}{dz}\right.$$
$$\left. + \left\{\tau_{f,w}\left[W_{ch} + 2\left(H_{ch}-\delta\right)\right] + \tau_{H,w}\left[W_{ch}+2\delta\right]\right\}\right]. \qquad \text{(II.5.24)}$$

Notice that solution of Eqs. (II.5.20) and (II.5.21) is not dependent on Eq. (II.5.24). Therefore Eqs. (II.5.20) and (II.5.21) can be solved first for δ and G_H. Then the variations of δ, U_H, $d\delta/dz$ and dU_H/dz with z are substituted in Eq. (II.5.24) to solve separately for pressure drop. Two-phase density and its derivative are predetermined from the apparent quality calculations.

Several additional parameters are required to solve Eqs. (II.5.20), (II.5.21) and (II.5.24). They include mixture density and mixture viscosity of the homogeneous two-phase layer, and friction factor relations for the liquid layer and the homogeneous layer are specifically related to rectangular micro-channels. These relations are summarized in Table II.5.1. A more comprehensive discussion of homogeneous flow viscosity models is provided in a previous study by Lee and Mudawar (2005a).

There are also other parameters that define the domain of the subcooled boiling region. These parameters must be determined in advance. Referring to Fig. II.5.1(a), the location of saturated boiling, which is also the downstream edge of *DHLM* domain, can be determined using a simple heat balance.

$$z_{sat} = \frac{GW_{ch} H_{ch} c_{p,f} \left(T_{sat} - T_{in}\right)}{q''\left(W_{ch} + W_w\right)}. \tag{II.5.40}$$

A key difficulty lies in the determination of z_{bd}. Two approaches are available from the literature for estimating the location of bubble departure. Both involve estimating flow subcooling, $\Delta T_{sub,bd}$, at the departure point, from z_{db} is calculated from the simple energy balance

$$-z_{bd} = z_{sat} - \frac{\Delta T_{sub,bd}}{q''} \frac{GW_{ch} H_{ch} c_{p,f}}{\left(W_{ch} + W_w\right)}. \tag{II.5.41}$$

Relations recommended by Bowring (Collier and Thome,1994) and Saha and Zuber (1974) for $\Delta T_{sub,bd}$ for macro-channels produced poor predictions for the conditions of the present study. The bubble departure point was predicted with both relations to occur in the micro-channel at much higher heat fluxes than actually measured.

An alternative relation for $\Delta T_{sub,bd}$ is suggested here that follows the same general form as the Saha and Zuber model, but ensures the occurrence of bubble departure within the micro-channel as captured experimentally in prior flow visualization studies.

$$\Delta T_{sub,bd} = \frac{q'' C_G}{h_{bd}}, \tag{II.5.42}$$

where h_{bd} is the heat transfer coefficient measured when bubble departure was first observed *inside* the micro-channel, and C_G is a dimensionless function developed specifically for rectangular micro-channels and correlated to aspect ratio, β, from data for the four different test sections used in the present study.

$$C_G = 0.632\beta + 0.014. \tag{II.5.43}$$

A key challenge is using Eqs. (II.5.42) and (II.5.43) is that the value of h_{bd} used to develop these correlations was measured experimentally for a condition that produced bubble departure inside the micro-channel. However, as illustrated in Fig. II.5.1(a), the value of h_{bd} sought in the *DHLM* is that of a pseudo heat transfer coefficient that yields bubble departure upstream of the micro-channel. This value was determined with an iterative procedure described next.

Figure II.5.4 outlines the entire solution procedure for *DHLM*. The model is initiated by guessing micro-channel inlet pressure, P_{in} at $z = 0$, then h_{bd}. Different values of h_{bd} produced different variations of δ with z. The value of h_{bd} was updated until the model yielded $\delta = H$ at $z = z_{sat}$. Then the model used this last value of h_{bd} to determine the variation of P with z. Since the present experiments were performed with a fixed outlet plenum pressure (P_{out} = 1.138 bar), the predicted micro-channel exit pressure, P_L at $z = L$, was corrected for pressure recovery due to expansion from the micro-channels to the outlet plenum in order to determine P_{out}. If this value of P_{out} matched the measured pressure, the solution was deemed convergent. If, on the other hand, the pressure values did not agree, a new value of P_{in} was entered and the entire iteration repeated. Overall, pressure differences due to recovery were quite small and

had virtually no impact on the pressure drop calculation. Details concerning two-phase pressure recovery relations are available in a paper by Qu and Mudawar (2003a).

Table II.5.1 Additional relations of *DHLM*.

	Equations
Two-phase density	$\rho_H = \dfrac{1}{\dfrac{x'}{\rho_g} + \dfrac{1-x'}{\rho_f}}$ (II.5.25)
Two-phase viscosity (McAdams model)	$\mu_H = \dfrac{1}{\dfrac{x'}{\mu_g} + \dfrac{1-x'}{\mu_f}}$ (II.5.26)
Liquid layer wall shear (Shah and London,1978)	$\tau_{f,w} = \dfrac{1}{2} f_f \rho_f U_f^2$ (II.5.27)
	$f_f Re_f = \left\{ 3.44\, z_{hy}^{+\,-0.5} + \dfrac{1.089/4 z_{hy}^{+} + K_f - 3.44/z_{hy}^{+\,0.5}}{1 + 0.000131 z_{hy}^{+\,-2}} \right\}$ (II.5.28)
	$Re_f = \dfrac{\rho_f U_f D_{h,f}}{\mu_f}$ (II.5.29)
	$D_{h,f} = \dfrac{2(H_{ch} - \delta) W_{ch}}{(H_{ch} - \delta) + W_{ch}}$ (II.5.30)
	$z_{hy}^{+} = \dfrac{z}{D_h Re_f}$ (II.5.31)
	$K_f = 24\left(1 - 1.355\beta_f + 1.947\beta_f^{\,2} - 1.701\beta_f^{\,3} + 0.956\beta_f^{\,4} - 0.254\beta_f^{\,5}\right)$ (II.5.32)
	$\beta_f = \dfrac{W_{ch}}{(H_{ch} - \delta)}$ *or* $\dfrac{(H_{ch} - \delta)}{W_{ch}}$; $\beta_f \le 1$ (II.5.33)

Table II.5.1 Continued.

	Equations
Homogeneous layer wall shear	$\tau_{H,w} = \frac{1}{2} f_H \rho_H U_H^2$ (II.5.34)
	$f_H = \frac{K_H}{\mathrm{Re}_H}$ (II.5.35)
	$Re_H = \frac{\rho_H U_H D_{h,H}}{\mu_H}$ (II.5.36)
	$D_{h,H} = \frac{2\delta W_{ch}}{\delta + W_{ch}}$ (II.5.37)
	$K_H = 24\left(1 - 1.355\beta_H + 1.947\beta_H^2 - 1.701\beta_H^3 + 0.956\beta_H^4 - 0.254\beta_H^5\right)$ (II.5.38)
	$\beta_H = \frac{W_{ch}}{\delta}$ *or* $\frac{\delta}{W_{ch}}$; $\beta_H \le 1$ (II.5.39)

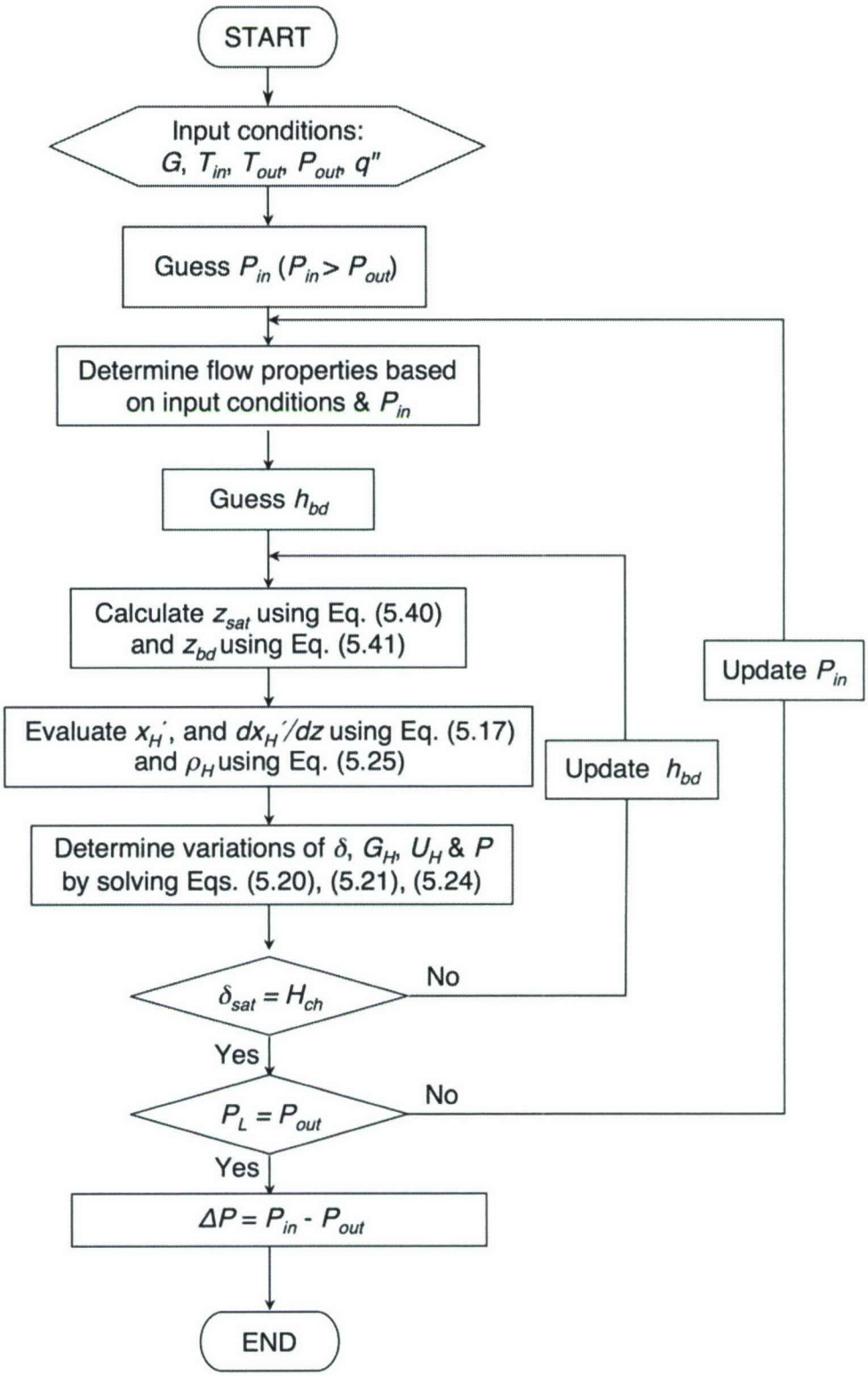

Figure II.5.4 Solving procedure for *DHLM*.

II.5.2 Model Results

II.5.2.1 Profiles of Main Variables

Figure II.5.5 shows predictions of the axial variations of the *DHLM* main variables: velocity of homogenous two-phase layer, U_H, thickness of homogeneous layer, δ, and pressure, P, for each of the four test sections. Notice that the profiles include the pseudo upstream and downstream extensions of the subcooled boiling layer; the extent of the actual micro-channel is indicated for each case. The results are based on experimentally measured heat flux, which varies slightly between the four cases. Because of the relatively high heat flux, these conditions correspond to the upper range of the nucleate boiling region, which indicated by the micro-channel length corresponding to the relatively high void fraction region of the model domain.

Pressure drop across the micro-channel is the difference between P_{in} predicted by *DHLM* at $z = 0$ minus the measured outlet pressure, P_{out}, corrected for pressure recovery. Equation (II.5.24) shows pressure drop is inversely proportional to micro-channel cross sectional area and strongly influenced by U_H. Figure II.5.5 shows decreasing hydraulic diameter, which yields a substantial increase in U_H, increases pressure drop.

II.5.2.2 Validation of Model Predictions

Figure II.5.6 compares pressure drop predictions of *DHLM* with measured pressure drop for the four test sections, two different flow rates and two inlet temperatures. Most cases are predicted quite accurately with the exception of the largest hydraulic diameter at the higher inlet temperature. This shows the model is well suited to small rectangular micro-channels and may begin to lose accuracy with large micro-channels. The model's accuracy is apparently compromised when the homogenous two-phase layer assumption begins to fall apart as the two-phase layer undergoes transition from bubbly to slug flow at higher inlet temperatures (*i.e.,* lower subcoolings), especially

at high heat fluxes. It should be noted that *DHLM* provided excellent predictions of pressure drop for all three smaller hydraulic diameters, and its predictive accuracy increased at low heat fluxes. Relatively poor predictions for the largest hydraulic diameter may be related to strong entrance effects, especially at high Reynolds numbers, causing the assumption of constant mean liquid layer velocity in the model to be violated. Another reason for the deviation, which is mainly encountered at high fluxes, concerns both the aforementioned transition form bubbly to slug flow, and the flow instabilities (even flow reversal) at conditions approaching CHF as described in the chapter II.3.

Figure II.5.7 compares the model predictions with the entire pressure drop database of this study. Excepting the large diameter data corresponding to the higher inlet temperature, good predictions are achieved for most of the 191 data points, evidenced by a mean absolute error (MAE) of 14.9%.

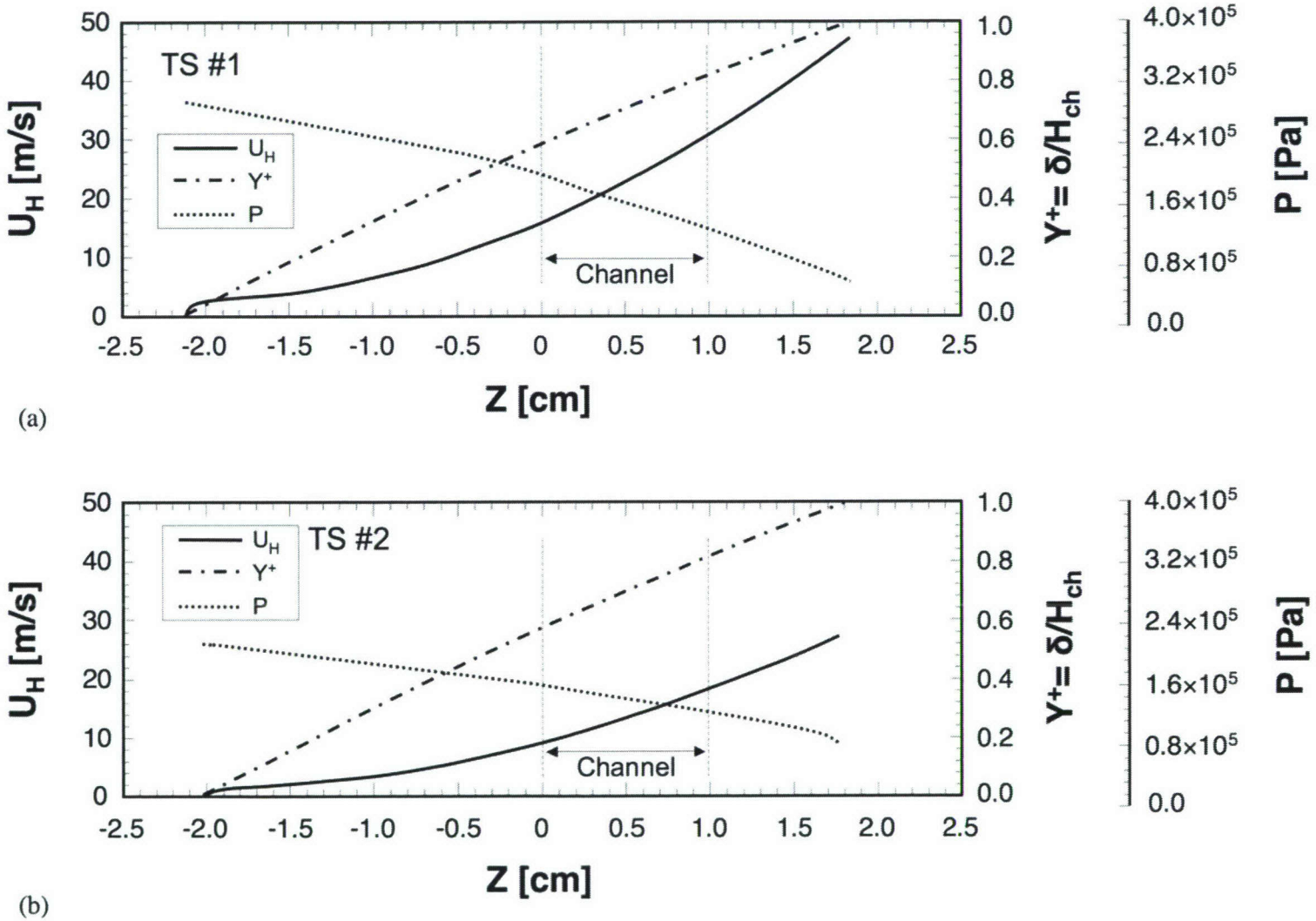

Figure II.5.5 (*DHLM* predictions for T_{in} = -30 °C and m = 5 g/s for (a) TS #1 (D_h = 176 μm) at q'' =561 W/cm^2, (b) TS #2 (D_h = 200 μm) at q'' =586 W/cm^2, (c) TS #3 (D_h = 334 μm) at q'' =560 W/cm^2, and (d) TS #4 (D_h = 416 μm) at q'' =627 W/cm^2.

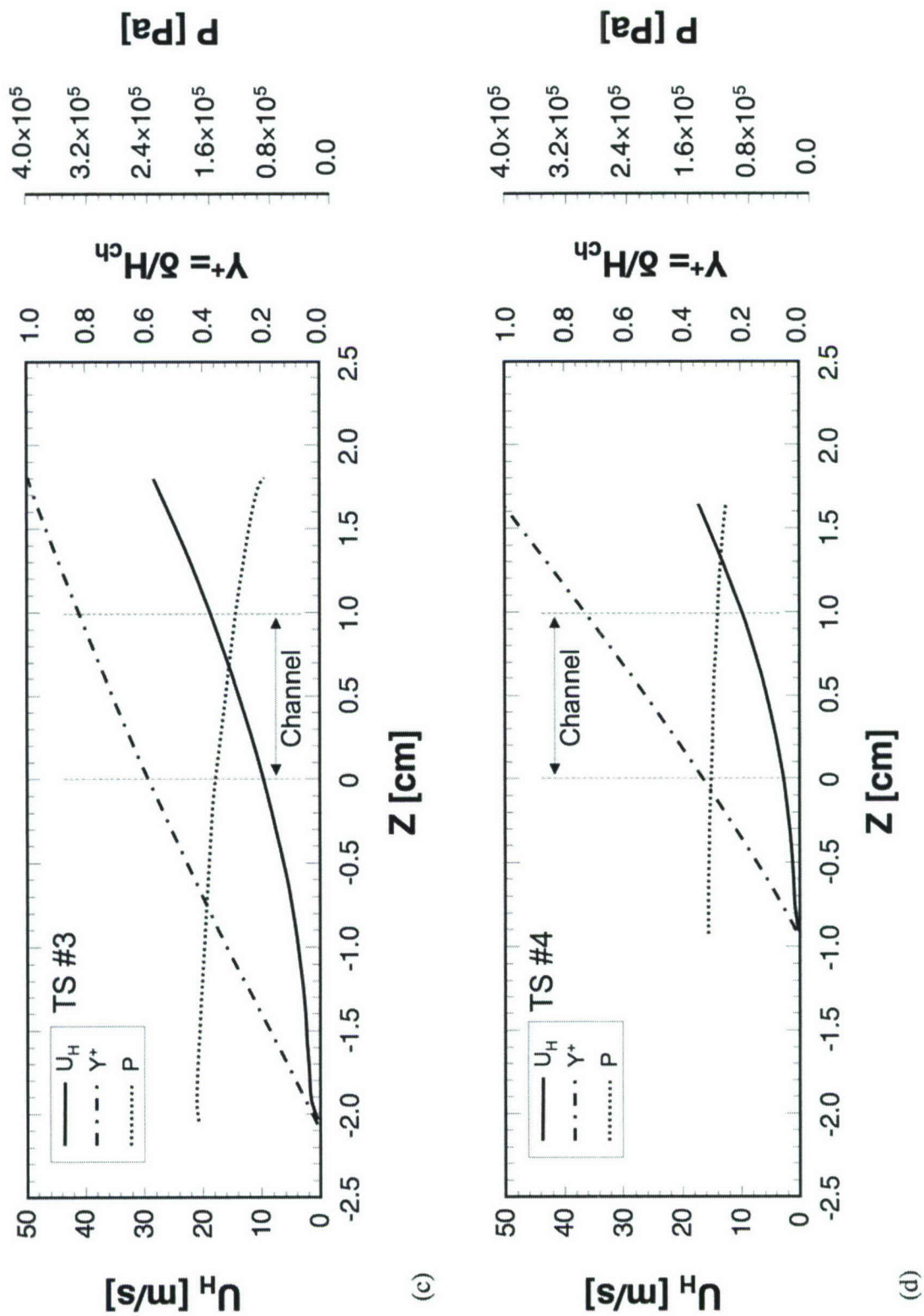

Figure II.5.5 Continued.

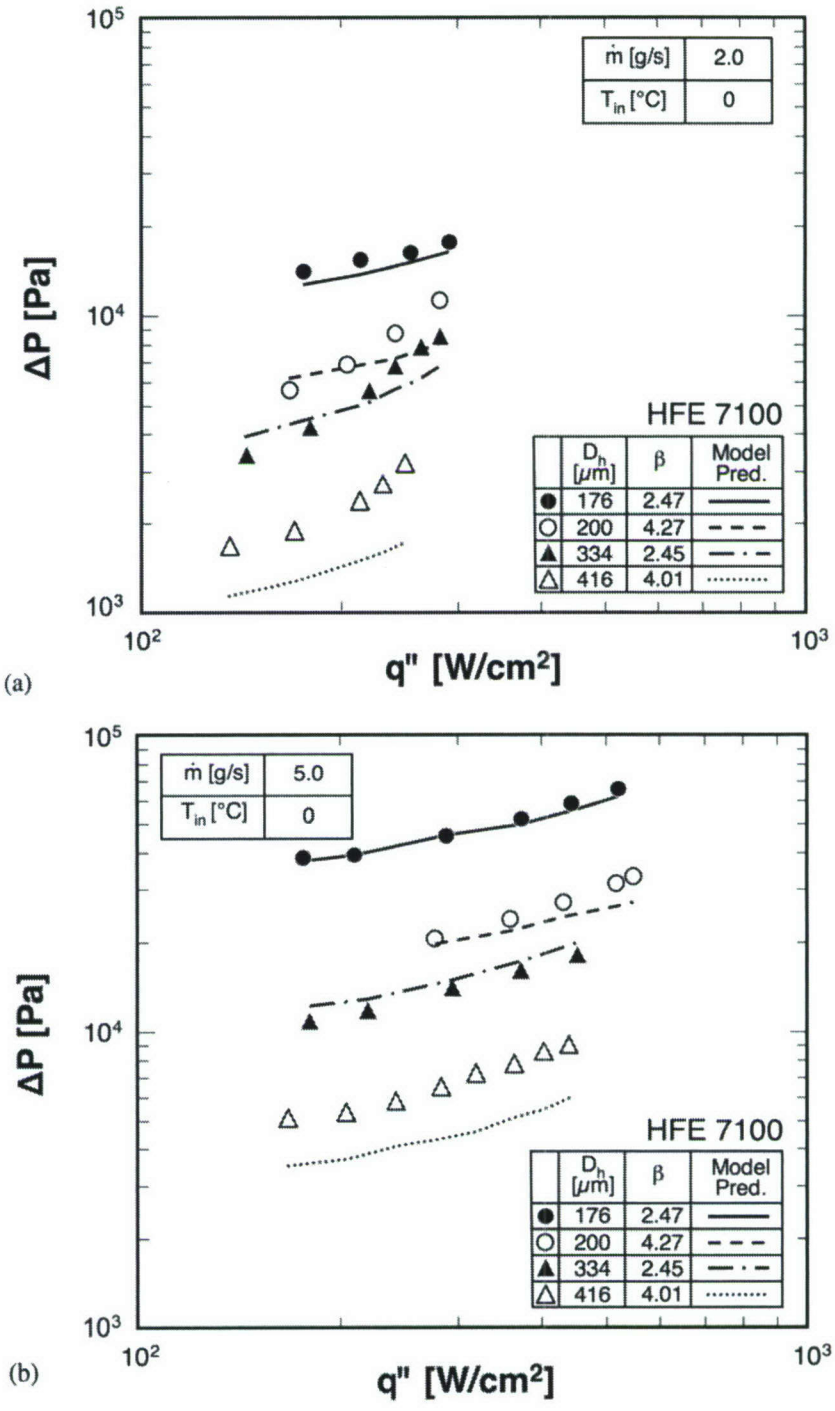

Figure II.5.6 Comparison of model predictions and measured variation of pressure drop with heat flux for (a) T_{in} = 0 °C and $\dot{m}$ = 2 g/s, (b) T_{in} = 0 °C and $\dot{m}$ = 5 g/s, (c) T_{in} = -30 °C and $\dot{m}$ = 2 g/s, and (d) T_{in} = -30 °C and $\dot{m}$ = 5 kg/s.

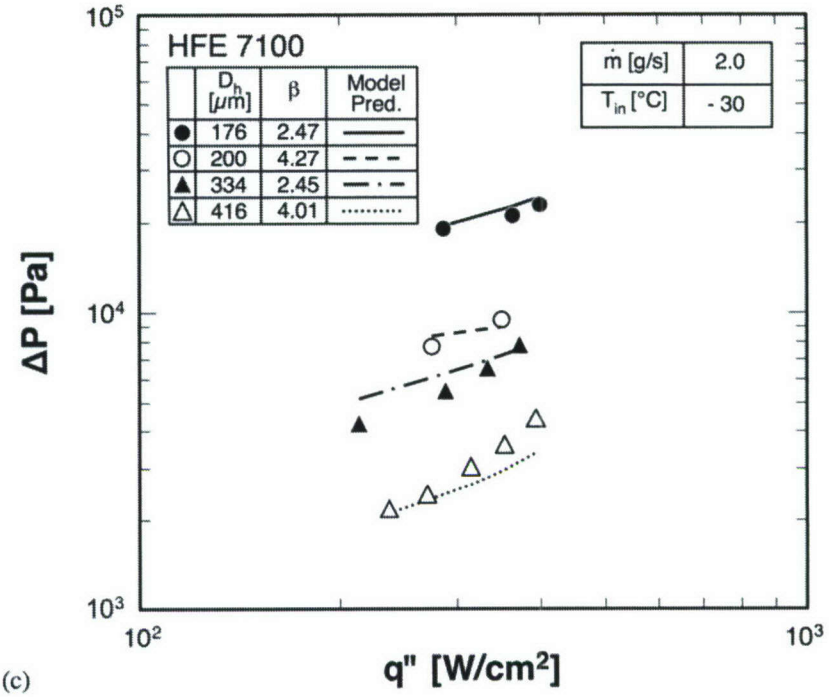

(c)

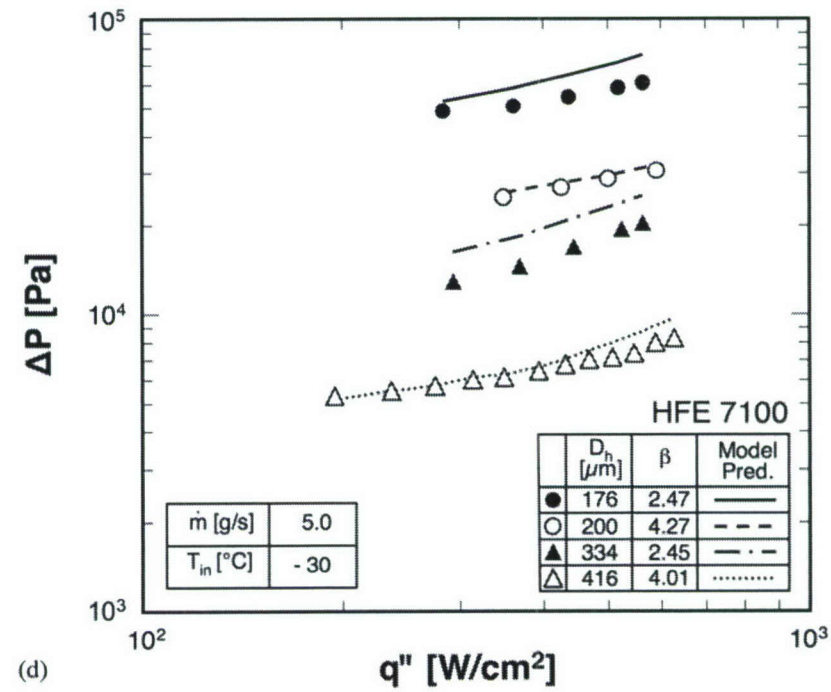

(d)

Figure II.5.6 Continued.

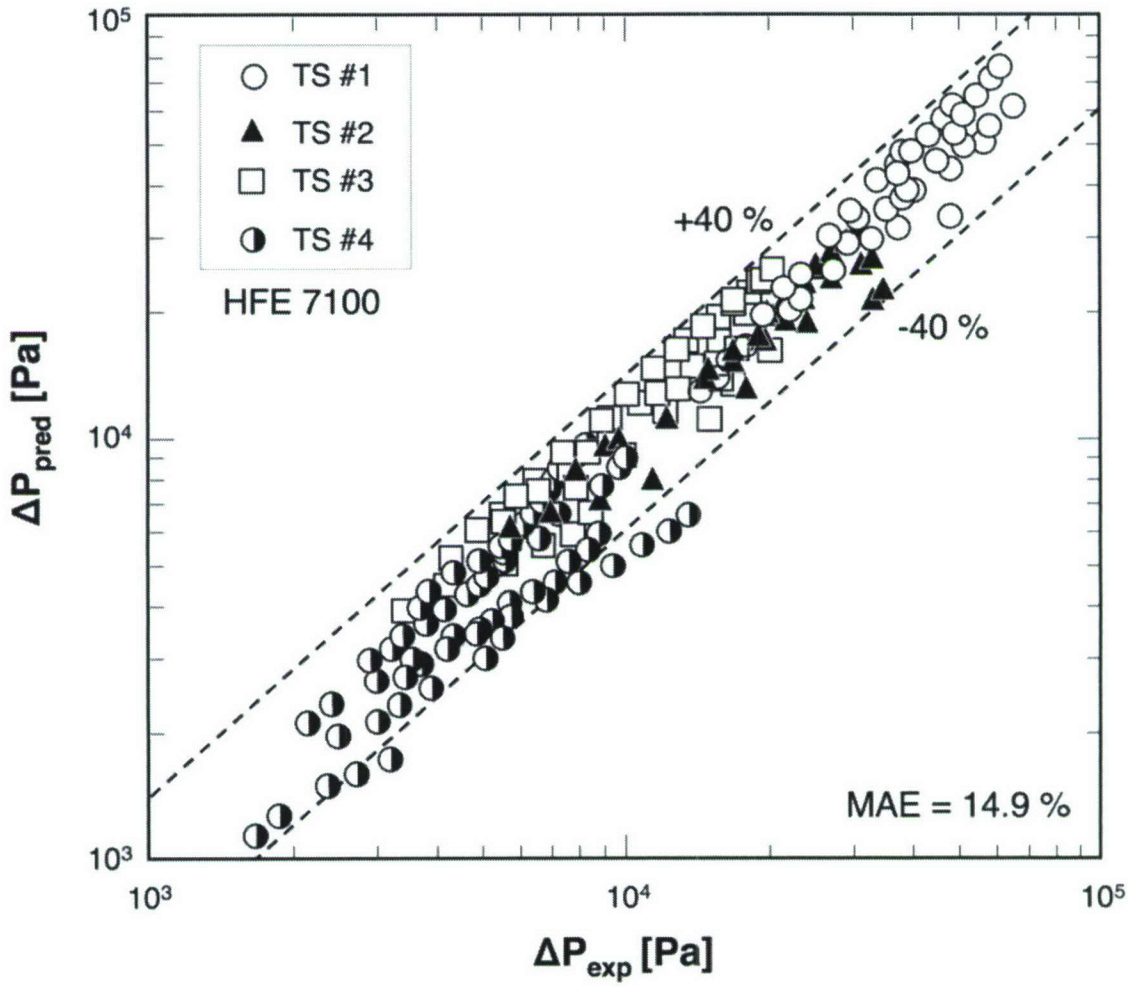

Figure II.5.7 Comparison of pressure drop predictions of *DHLM* and experimental data.

II.6 CRITICAL HEAT FLUX FOR SUBCOOLED FLOW BOILING

II.6.1 CHF Trend and Flow Visualization Results

Several key parameters were used to characterize flow conditions and CHF. Aside from total flow rate, $\dot{m}$, of the primary coolant, tests were also based on mass velocity, which is defined as

$$G = \frac{\dot{m}}{N A_{ch}}, \tag{II.6.1}$$

where N is the number of micro-channels in the heat sink, and A_{ch} the cross-sectional area of each micro-channel. Two definitions are used for heat flux as shown in Fig. II.6.1. The first is the effective heat flux, q''_{eff}, which is based on the total base area of the micro-channel heat sink. This would be equivalent to the heat flux dissipated from an electronic device to which the micro-channel heat sink is attached. The second, q''_p, is the average heat flux along the three thermally conducting walls of the rectangular micro-channel. This latter definition is used to compare present CHF values to those determined from prior CHF correlations, which are typically derived from databases for uniformly heated channels. As illustrated in Fig. II.6.1, q''_p is related to q''_{eff} by the relation

$$q''_p = \frac{q''_{eff}\left(W_{ch} + W_w\right)}{\left(W_{ch} + 2H_{ch}\right)}. \tag{II.6.2}$$

Figure II.6.2 shows representative flow boiling curves for two different micro-channel test sections and two mass flow rates. The micro-channel's mean base temperature, $\overline{T}_w$, halfway along the micro-channel was determined with a simple fin

model and the assumption of 1-D conduction using the unit cell shown in Fig. II.6.1 Details of the procedure used to determine $\overline{T}_w$ was mentioned in earlier chapter. Figure II.6.2 shows increasing the flow rate increases CHF for both test sections. Furthermore, the micro-channel with the smaller hydraulic diameter yields higher CHF values. This can be explained by the smaller micro-channel's greater mass velocity for the same mass flow rate as the larger micro-channel. However, this trend is by no means conclusive or monotonic. For example, comparing the data in Fig. II.6.2 for TS#3 at G = 1,341 kg/m^2.s with data for TS#4 at G = 1,007 kg/m^2.s shows the smaller G yielding a higher CHF value. A more effective way to assess the influence of G on CHF is to use q''_p rather than q''_{eff}. For the G = 1,341 kg/m^2.s case, q''_{eff} = 325.8 W/cm^2 but q''_p = 109.2 W/cm^2, whereas q''_{eff} = 417.0 W/cm^2 and q''_p = 82.8 W/cm^2 for the G = 1,007 kg/m^2.s case. This shows using q''_p does yield the expected trend of increasing CHF with increasing G and is therefore a more effective parameter for correlating micro-channel CHF data. Unfortunately, further verification of the benefits of smaller micro-channels was not possible for all micro-channel sizes, given the lack of CHF data for test sections TS#1 and TS#2. However, prior flow visulaization has shown very small diameters promote early transition from bubbly to slug flow, especially in narrow channels. A large increase in void fraction may compromise the magnitude of CHF.

Figure II.6.2 shows two different types of CHF, three are indicated as 'normal CHF' and one as 'pre-mature CHF' or PM-CHF. Differences between these CHF types can be best explained with the aid of images obtained with high-speed video.

Figure II.6.3 shows the typical occurrence of 'normal CHF.' Prior to CHF, there is significant near-wall bubble activity, with an abundance of liquid in the core. At CHF, bubbles suddenly coalesce into a continuous vapor blanket, thermally insulating the micro-channel walls from liquid contact. This behavior is consistent with the definition of DNB (see Fig. II.1.3), and is manifest by a sudden sharp rise in the micro-channel's base temperature.

As discussed earlier, fig. II.3.8 shows a series of images of the flow during pre-mature CHF. High void fraction appears to momentarily increase pressure drop,

preventing liquid from entering the micro-channels. This forces vapor backwards towards the inlet plenum. Vapor begins to accumulate in the inlet plenum as liquid inside the micro-channels is evaporated, causing wall temperature to rise. During the vapor back flow, pressure in the inlet plenum begins to rise until it is capable of resisting the vapor back flow. Fresh liquid is then reintroduced into the micro-channels, re-wetting the micro-channel walls and decreasing the wall temperature as the inlet temperature also decreases. This cycle is repeated several times, with the mean wall temperature increasing between cycles. Eventually, the wall temperature begins to rise more rapidly, signaling the commencement of PM-CHF. Figure II.6.4 shows transient records of the downstream wall thermocouple, the inlet and outlet pressure transducers and the Coriolis flow meter before and during PM-CHF. Notice the large increase in the amplitude of the temperature and pressure signals as well as the increase in mean wall temperature during PM-CHF. Overall, PM-CHF occurs at low mass velocities and low subcoolings. High mass velocities preclude the occurrence of PM-CHF by providing sufficiently large momentum to resist the vapor back flow. High subcooling serves to decrease vapor void fraction through stronger condensation, which greatly reduces the vapor blockage.

Figure II.6.5 shows the variation of CHF, based on heated perimeter, with inlet subcooling and mass velocity for test sections TS#3 and TS#4, including PM-CHF data. Overall, CHF increases monotonically with increases in inlet subcooling and/or mass velocity. Notice that PM-CHF is encountered mostly at low mass velocities and/or low subcoolings. Special attention is given in this study to distinguishing between normal and PM-CHF data when assessing prior correlations. Table II.6.1 provides all the CHF data measured in the present study. The database consists of 45 data points of which 13 are PM-CHF.

Table II.6.1 Present CHF data.

No.	D_h [μm]	L/D_h	G [kg/m^2.s]	T_{in} [°C]	T_o [°C]	$\Delta T_{sub,in}$ [°C]	$\Delta T_{sub,o}$ [°C]	P_{in} [bar]	P_o [bar]	x_{in}	x_o	$q''_{eff,c}$ [W/cm^2]	$q''_{p,c}$ [W/cm^2]	Notes
1	175.7	56.9	2213.9	0.04	43.82	68.28	19.75	1.3135	1.1339	-0.652	-0.206	301.1	85.3	PM-CHF
2	175.7	56.9	2215.9	-23.60	49.88	95.92	13.88	1.4810	1.1408	-0.888	-0.145	513.8	145.5	
3	200.0	50.0	1276.7	-0.13	42.99	67.46	20.72	1.2742	1.1388	-0.656	-0.216	311.4	55.0	PM-CHF
4	200.0	50.0	1282.1	-22.79	30.34	90.69	33.50	1.2968	1.1435	-0.881	-0.348	435.0	76.8	
5	200.0	50.0	1924.2	-0.30	38.16	69.2	25.66	1.3369	1.1429	-0.659	-0.268	403.5	71.3	PM-CHF
6	334.1	29.9	1338.1	19.62	50.84	46.7	13.04	1.2352	1.1451	-0.459	-0.137	210.9	70.7	PM-CHF
7	334.1	29.9	1338.3	10.14	47.29	56.12	16.45	1.2331	1.1399	-0.553	-0.172	265.6	89.0	PM-CHF
8	334.1	29.9	1341.2	-0.42	49.64	67.21	14.43	1.2534	1.1520	-0.663	-0.151	325.8	109.2	
9	334.1	29.9	1338.2	-10.46	45.15	77.5	18.51	1.2630	1.1373	-0.758	-0.193	399.6	133.9	
10	334.1	29.9	1341.1	-24.92	34.77	91.95	29.02	1.2628	1.1418	-0.901	-0.302	459.1	153.9	
11	334.1	29.9	1672.8	19.30	59.13	49.98	4.94	1.3522	1.1519	-0.464	-0.052	340.6	114.1	
12	334.1	29.9	1673.8	10.02	52.97	58.41	10.82	1.3179	1.1419	-0.555	-0.113	366.0	122.7	
13	334.1	29.9	1673.5	-0.61	47.51	68.96	16.46	1.3145	1.1484	-0.664	-0.172	423.1	141.8	
14	334.1	29.9	1673.5	-10.04	40.42	77.89	23.32	1.2949	1.1402	-0.755	-0.243	441.8	148.1	
15	334.1	29.9	1673.6	-29.66	26.61	97.59	37.18	1.2981	1.1419	-0.947	-0.386	534.4	179.1	
16	334.1	29.9	2009.9	19.29	57.83	51.29	5.96	1.4062	1.1417	-0.461	-0.062	381.7	127.9	
17	334.1	29.9	2006.4	9.73	52.71	59.96	10.99	1.3692	1.1387	-0.557	-0.115	417.7	140.0	
18	334.1	29.9	2013.3	-0.46	43.48	68.7	20.34	1.3102	1.1429	-0.660	-0.212	442.0	148.1	
19	334.1	29.9	2008.5	-9.42	37.56	77.9	26.03	1.3198	1.1345	-0.746	-0.271	479.2	160.6	
20	334.1	29.9	2017.1	-28.77	25.41	96.78	38.39	1.3010	1.1421	-0.938	-0.399	592.3	198.5	
21	334.1	29.9	2345.1	19.39	56.04	52.14	7.68	1.4464	1.1393	-0.459	-0.080	414.4	138.9	
22	334.1	29.9	2344.9	10.20	47.73	60.68	15.95	1.4187	1.1379	-0.552	-0.167	439.6	147.3	
23	334.1	29.9	2345.1	-1.17	42.15	71.32	21.51	1.3880	1.1373	-0.666	-0.225	500.0	167.6	
24	334.1	29.9	2345.5	-10.67	37.02	80.17	26.66	1.3611	1.1379	-0.760	-0.278	555.2	186.1	

Table II.6.1 Continued.

No.	D_h [μm]	L/D_h	G [kg/m^2.s]	T_{in} [°C]	T_o [°C]	$\Delta T_{sub,in}$ [°C]	$\Delta T_{sub,o}$ [°C]	P_{in} [bar]	P_o [bar]	x_{in}	x_o	$q''_{eff,c}$ [W/cm^2]	$q''_{p,c}$ [W/cm^2]	Note
25	415.9	24.0	670.5	19.41	45.96	45.2	17.88	1.1716	1.1437	-0.460	-0.187	183.1	36.3	PM-CHF
26	415.9	24.0	670.5	9.75	43.27	54.74	20.39	1.1671	1.1370	-0.556	-0.213	219.0	43.5	PM-CHF
27	415.9	24.0	671.9	-0.07	40.88	64.68	22.84	1.1714	1.1393	-0.655	-0.238	257.1	51.0	PM-CHF
28	415.9	24.0	670.2	-9.62	35.07	74.24	28.59	1.1718	1.1373	-0.749	-0.298	312.2	62.0	PM-CHF
29	415.9	24.0	671.0	-28.48	36.28	93.89	27.67	1.2010	1.1477	-0.937	-0.289	445.7	88.5	
30	415.9	24.0	838.7	19.30	50.52	46.03	13.25	1.1982	1.1412	-0.461	-0.139	253.8	50.4	PM-CHF
31	415.9	24.0	838.6	9.36	42.61	55.7	21.18	1.1881	1.1417	-0.561	-0.221	274.7	54.5	PM-CHF
32	415.9	24.0	838.8	-0.04	37.92	65.17	25.85	1.1908	1.1410	-0.656	-0.269	313.2	62.1	PM-CHF
33	415.9	24.0	838.7	-10.08	33.69	75.17	29.94	1.1892	1.1362	-0.754	-0.312	372.3	73.9	PM-CHF
34	415.9	24.0	838.7	-27.84	35.45	93.44	28.29	1.2081	1.1401	-0.928	-0.295	556.3	110.4	
35	415.9	24.0	1007.0	18.96	57.37	47.63	6.57	1.2457	1.1471	-0.466	-0.069	352.3	69.9	
36	415.9	24.0	1007.0	9.27	53.78	57.17	10.11	1.2399	1.1453	-0.564	-0.106	401.9	79.8	
37	415.9	24.0	1007.0	-0.49	43.37	66.86	20.76	1.2372	1.1542	-0.665	-0.217	417.0	82.8	
38	415.9	24.0	1007.0	-10.88	38.67	76.85	24.87	1.2219	1.1330	-0.760	-0.259	477.1	94.7	
39	415.9	24.0	1009.0	-30.17	24.75	95.55	39.07	1.2001	1.1430	-0.952	-0.406	603.1	119.7	
40	415.9	24.0	1176.0	19.51	56.02	47.68	7.88	1.2690	1.1458	-0.460	-0.083	389.2	77.2	
41	415.9	24.0	1173.0	9.43	49.34	57.33	14.40	1.2524	1.1400	-0.560	-0.151	425.6	84.5	
42	415.9	24.0	1176.0	-0.28	44.16	67.1	19.64	1.2546	1.1423	-0.658	-0.205	483.9	96.0	
43	415.9	24.0	1176.0	-10.82	36.80	77.47	26.82	1.2479	1.1356	-0.761	-0.279	541.6	107.5	
44	415.9	24.0	1176.0	-31.01	31.78	97.57	31.98	1.2447	1.1407	-0.959	-0.333	693.0	137.5	
45	415.9	24.0	1346.0	0.09	47.00	67.28	16.72	1.2757	1.1395	-0.654	-0.175	571.8	113.5	

Table II.6.2 Subcooled boiling CHF correlations.

Author(s)	Remarks	Correlations
Hall & Mudawar (2000b)	Outlet-conditions based	$Bo_c = \frac{q_c''}{G\,h_{fg}} = C_1 We_D^{C_2}\left(\frac{\rho_f}{\rho_g}\right)^{C_3}\left[1 - C_4\left(\frac{\rho_f}{\rho_g}\right)^{C_5} x_o\right]$ $C_1 = 0.0722$, $C_2 = -0.312$, $C_3 = -0.644$, $C_4 = 0.900$, $C_5 = 0.724$
Hall & Mudawar (2000b)	Inlet-conditions based	$Bo_c = \frac{q_c''}{G\,h_{fg}} = \frac{C_1 We_D^{C_2}\left(\rho_f/\rho_g\right)^{C_3}\left[1 - C_4\left(\rho_f/\rho_g\right)^{C_5} x_{e,in}^*\right]}{1 + 4\,C_1 C_4 We_D^{C_2}\left(\rho_f/\rho_g\right)^{C_3+C_5}(L/D)}$ $C_1 = 0.0722$, $C_2 = -0.312$, $C_3 = -0.644$, $C_4 = 0.900$, $C_5 = 0.724$
Hall & Mudawar (1999)	Outlet-conditions based; ultra-high heat flux	$Bo_c = \frac{q_c''}{G\,h_{fg}} = C_1 We_D^{C_2}\left(\frac{\rho_f}{\rho_g}\right)^{C_3}\left[1 - C_4\left(\frac{\rho_f}{\rho_g}\right)^{C_5} x_o\right]$ $C_1 = 0.0332$, $C_2 = -0.235$, $C_3 = -0.681$, $C_4 = 0.684$, $C_5 = 0.832$
Hall & Mudawar (1999)	Inlet-conditions based; ultra-high heat flux	$Bo_c = \frac{q_c''}{G\,h_{fg}} = \frac{C_1 We_D^{C_2}\left(\rho_f/\rho_g\right)^{C_3}\left[1 - C_4\left(\rho_f/\rho_g\right)^{C_5} x_{e,in}^*\right]}{1 + 4\,C_1 C_4 We_D^{C_2}\left(\rho_f/\rho_g\right)^{C_3+C_5}(L/D)}$ $C_1 = 0.0332$, $C_2 = -0.235$, $C_3 = -0.681$, $C_4 = 0.684$, $C_5 = 0.832$

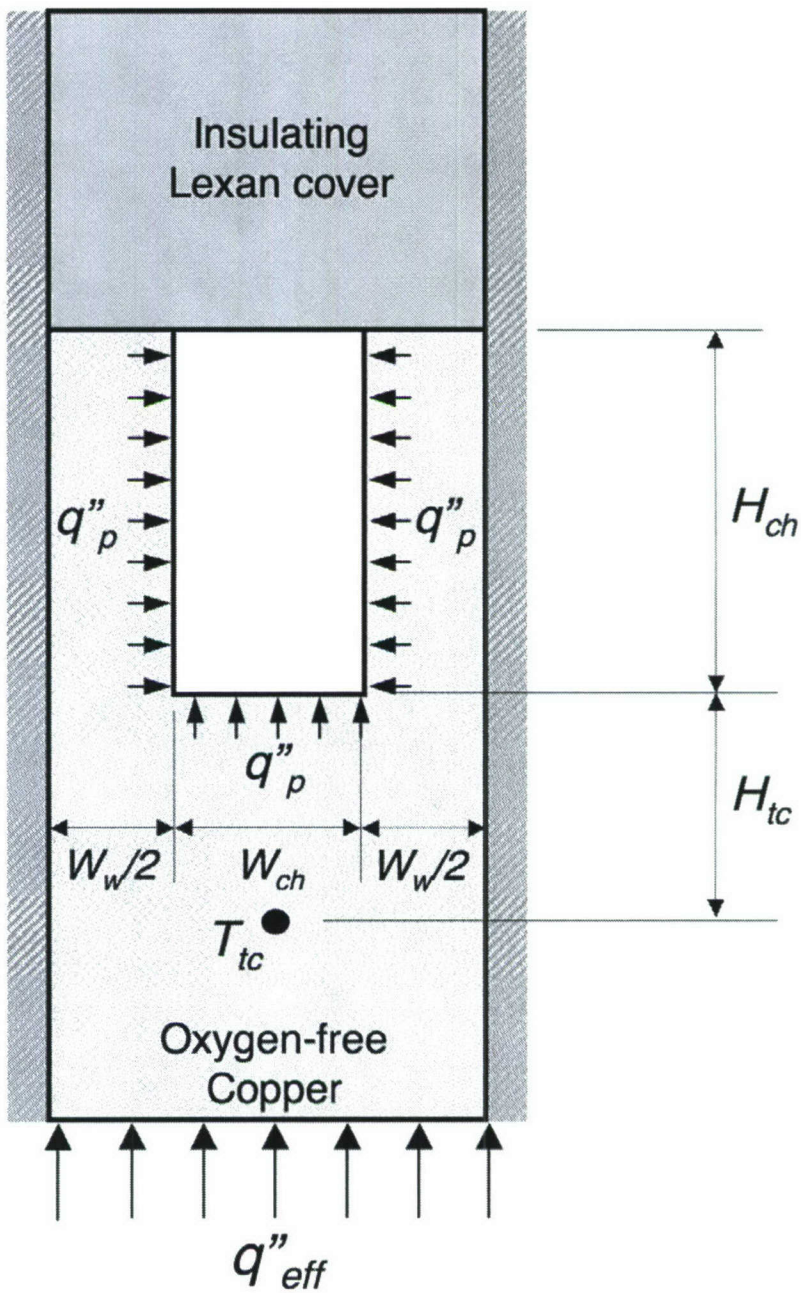

Figure II.6.1 Micro-channel unit cell.

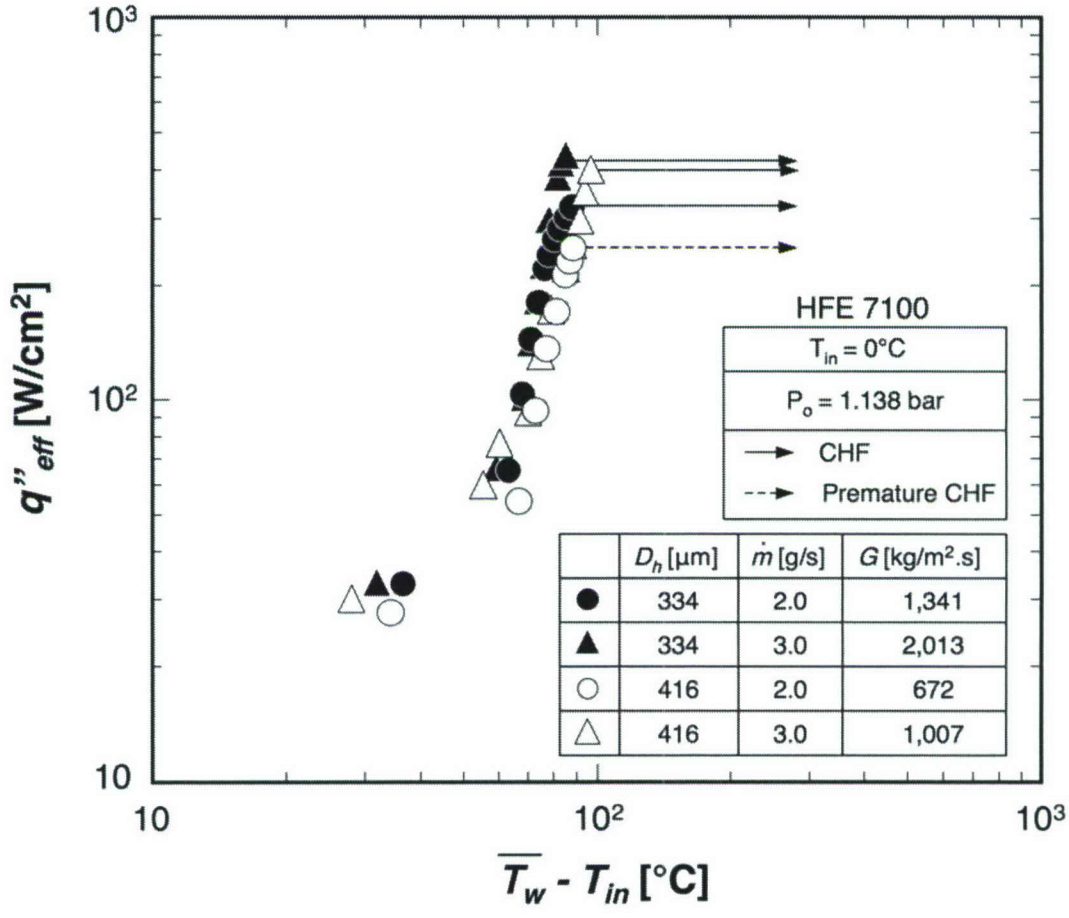

Figure II.6.2 Boiling curves for subcooled flow boiling conditions.

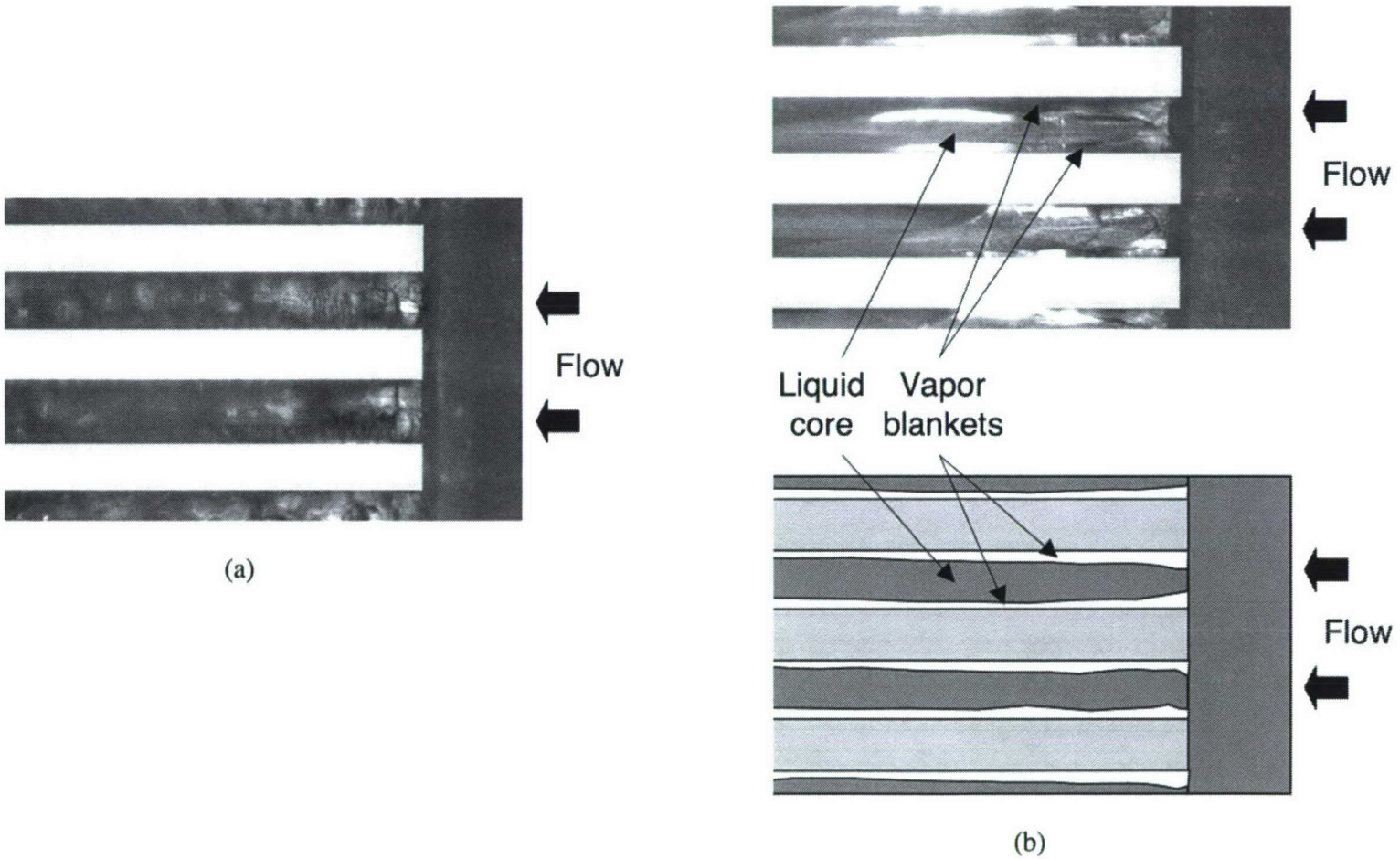

Figure II.6.3 Flow images for normal DNB with TS#3 (D_h = 334.1 μm) at T_{in} = 0°C and G = 1341 kg/m^2.s for (a) q''_{eff} = 318.3 W/cm^2, (b) $q''_{eff} > q''_{eff,c}$ = 325.8 W/cm^2.

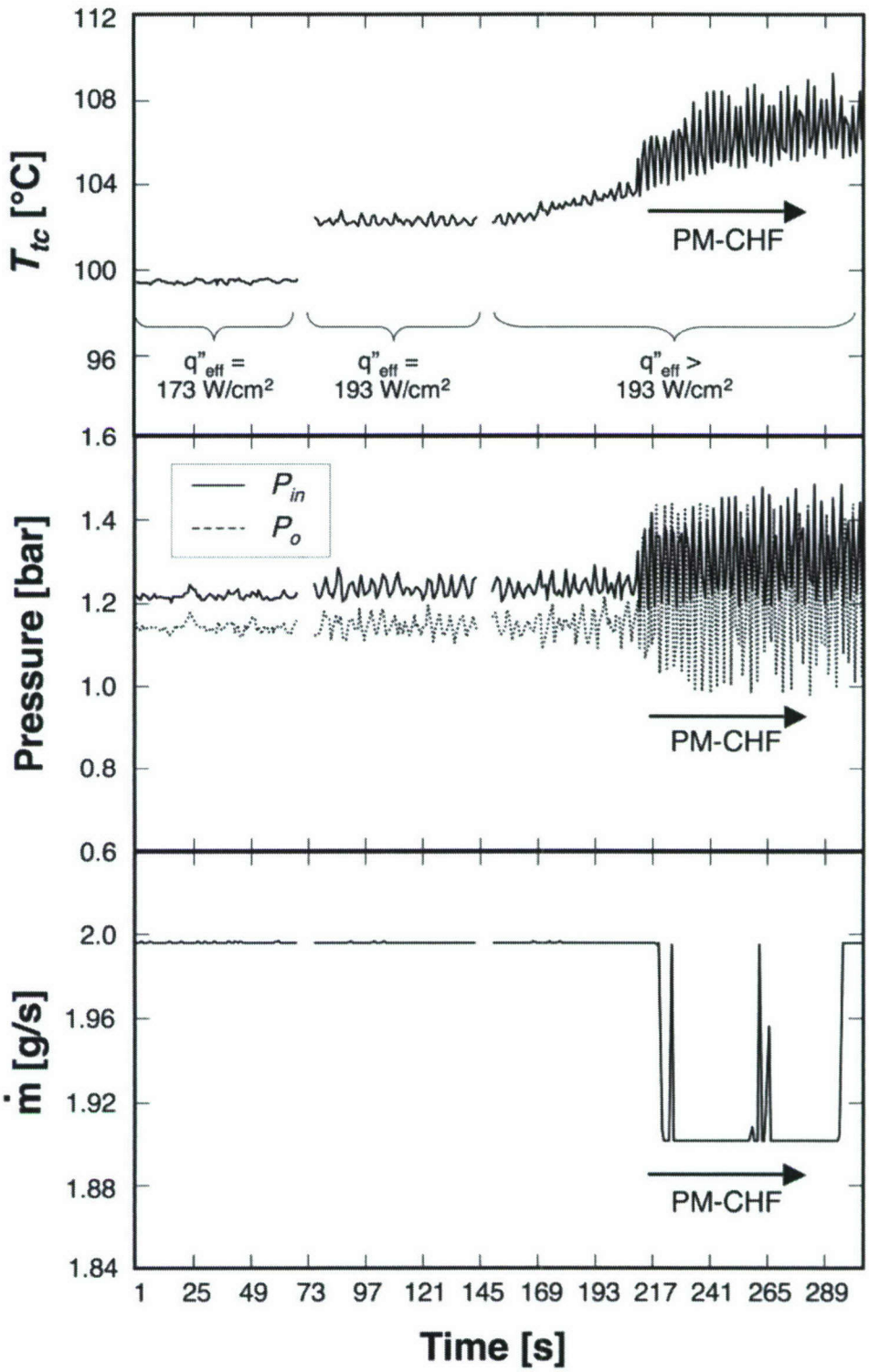

Figure II.6.4 Variations of temperature, pressure, and mass flow rate associated with premature CHF for TS#4, T_{in} = 20°C and G = 671 kg/m^2.s.

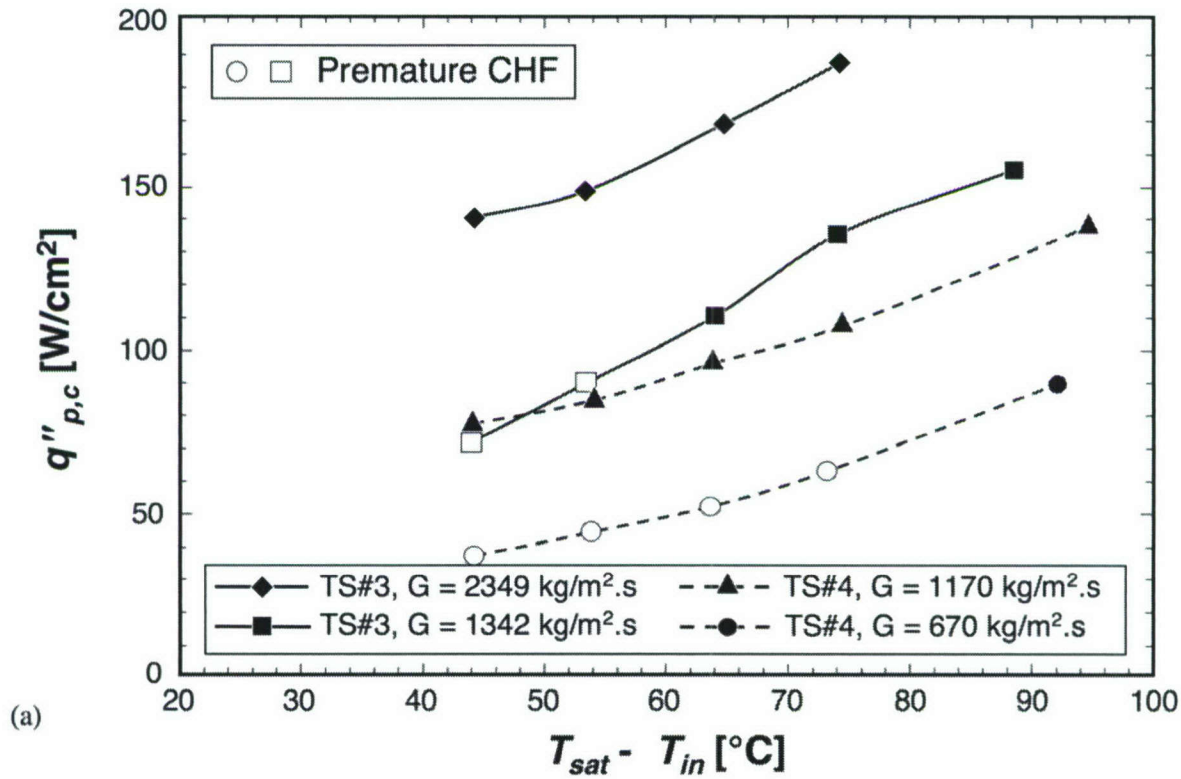

(a)

Figure II.6.5 Variation of subcooled boiling CHF with
(a) inlet subcooling and (b) mass velocity.

(b)

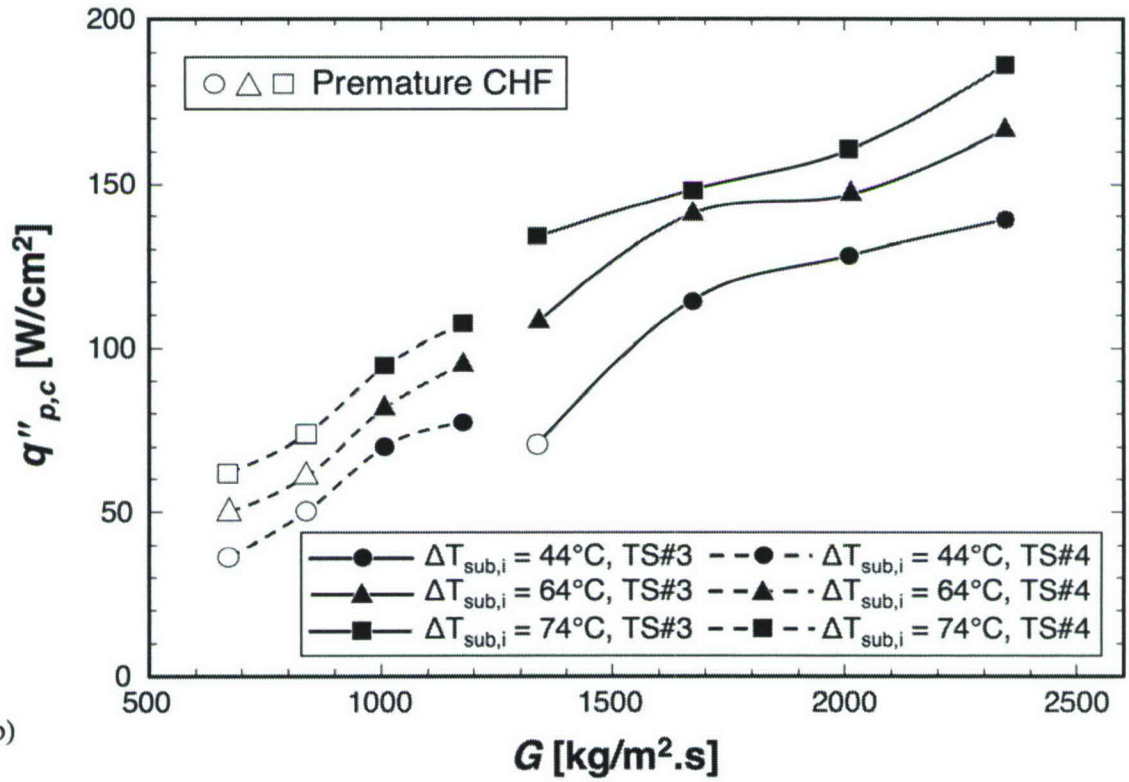

Figure II.6.5 continued.

II.6.2 New CHF Correlation

CHF correlations are based on either inlet (upstream) channel conditions or outlet (local) conditions. Pressure, mass velocity and diameter appear in both types of correlations. However, the effect of inlet quality in inlet conditions correlations is expressed in terms of inlet enthalpy (or inlet subcooling or quality); these correlations also account for quality variations along the channel through their dependence on channel length.

$$q_c'' = f(G, P, h_{in}, D, L). \tag{II.6.3}$$

The parameters in Eq. (6.3) are independent variables that are readily available for CHF determination. On the other hand, while outlet conditions correlations are also based pressure, mass flux and diameter, they account for the effects of quality through outlet enthalpy (or outlet subcooling or quality) since they are based on the premise that CHF occurs locally at the channel outlet.

$$q_c'' = f(G, P, D, h_o). \tag{II.6.4}$$

Therefore, use of an outlet conditions correlation involves indirect estimation of CHF since outlet quality must first be calculated with the CHF data point using an energy balance over the entire heated length. This is why channel length does not appear in Eq. (II.6.4).

Developing universal CHF correlations that are applicable to broad ranges of operating conditions requires amassing large CHF databases. This goal was accomplished by Hall and Mudawar (2000a, 2000b) through the Purdue University - Boiling and Two Phase Flow Laboratory (PU-BTPFL) CHF database, which was assembled with 32,544 data points from over 100 sources, of which 5544 data points are subcooled CHF. The primary objectives of their study were to (a) amass all existing water CHF databases for both vertical upflow and horizontal flow in a uniformly heated channel, (b) assess these databases on a point-by-point basis to eliminate any erroneous data, (c) compile all known subcooled CHF correlations for water flow in a uniformly

heated tube, (d) evaluate these correlations using the CHF database corrected for the erroneous data, and (e) develop simple, subcooled CHF correlations that are superior in accuracy to existing correlations and look-up tables. Hall and Mudawar recommended two correlations for subcooled (negative outlet quality) flow boiling CHF, one is inlet conditions based and the second outlet conditions. In a separate study, Mudawar *et al.* (Mudawar and Bowers, 1999, Hall and Mudawar, 1999) examined a subset of the PU-BTPFL database that involved ultra-high-flux subcooled flow boiling CHF in small diameter tubes in the range of $D = 0.406 - 2.54$ mm with relatively small L/D ratios, and recommended inlet conditions and outlet conditions correlations that are better suited for this subset. This subset includes the worlds highest CHF value of 27,600 W/cm^2 measured with a uniformly heated channel (Mudawar and Bowers, 1999). Table II.6.2 summarizes the correlations based on the entire PU-BTPFL database and on the small diameter subset. Because of the superiority of these four correlations to other published correlations has already been systematically ascertained (Hall and Mudawar, 1999, Hall and Mudawar, 2000b), these correlations are used in the present study as a starting point for developing CHF correlations for micro-channel heat sinks.

The present micro-channel heat sink configuration poses the following challenges when attempting to assess or utilize prior CHF correlations:

(1) *Working fluid*: most published CHF correlations for subcooled flow boiling are derived from water data; the present data were obtained using HFE 7100 as working fluid.

(2) *Partial circumferential heating*: while the present micro-channels are heated on three sides, prior CHF correlations are typically derived from data for uniform circumferential heating.

(3) *Channel cross-section*: most prior correlations are derived from data for circular channels; the present data involves rectangular channels.

(4) *Multi-channel interactions*: flow interactions between micro-channels can have an appreciable effect on CHF for micro-channel heat sinks. Prior CHF correlations do not account for this effect.

(5) *Small channel size*: with a few exceptions, prior CHF correlations are based on data for macro-channels that are much larger than those of micro-channel heat sinks.

(6) *Pre-mature CHF*: this phenomenon appears to be unique to micro-channel heat sinks and, therefore, cannot be predicted by prior CHF correlations.

The applicability of water-based CHF correlations to other fluids is commonly justified by the broad range of databases upon which a correlation is developed, especially when a correlation is presented in dimensionless form. Partial circumferential heating and the effects of the rectangular geometry in the present micro-channel heat sinks is accounted for by using a hydraulic diameter based on the heated perimeter,

$$D_{h,e} = \frac{4A_{ch}}{P_{h,e}} = \frac{4W_{ch}H_{ch}}{\left(W_{ch}+2H_{ch}\right)}, \tag{II.6.5}$$

and accounting for the micro-channel's aspect ratio, β, using the following approach.

For a uniformly heated channel, the single-phase convection heat transfer coefficient prevalent in the highly subcooled inlet is given by the relation (Incropera and Dewitt, 2002)

$$Nu = \frac{hD_{eq}}{k_f} = 4.36. \tag{II.6.6}$$

For a rectangular channel that is heated along three sides, the single-phase convection heat transfer coefficient can be derived from the modified relation (Shah and London, 1978)

$$Nu_3 = \frac{hD_{h,e}}{k_f} = 8.235\, f(\beta), \tag{II.6.7}$$

where $$f(\beta) = 1 - 1.833\beta + 3.767\beta^2 - 5.814\beta^3 + 5.361\beta^4 - 2.0\beta^5. \tag{II.6.8}$$

Combining Eqs. (II.6.6) and (II.6.7) provides a relation for equivalent diameter for the present micro-channel configuration.

$$D_{eq} = \frac{D_{h,e}}{1.889\, f(\beta)}. \tag{II.6.9}$$

This diameter replaces D in all We_D and L/D terms of the CHF correlations given in Table II.6.2.

The CHF correlations for micro-channel heat sinks must account for two additional effects: multi-channel interactions and small channel size. As discussed in the Introduction, these effects are closely associated with bubble confinement, which can be expressed in terms of the Weber number as suggested by Eq. (II.1.9). Accounting for the effects of the rectangular geometry and three-sided heating, the Weber number is expressed as

$$We_{D_{eq}} = \frac{G^2 D_{eq}}{\sigma \rho_f}. \tag{II.6.10}$$

Therefore, the CHF correlation for the micro-channel heat sink can be obtained by modifying the correlations provided in Table 6.2 according to the relation

$$Bo_{c,MC} = Bo_c\, f\left(We_{D_{eq}}\right), \tag{II.6.11}$$

where $Bo_{c,MC}$ is the Boiling number corresponding to CHF in the micro-channel heat sink and Bo_c is the Boiling number at CHF obtained from the correlations given in Table II.6.2.

This technique for correlating CHF data for micro-channel heat sinks only requires the determination of $f\left(We_{D_{eq}}\right)$. Using the present database for micro-channel heat sinks, this parameter was fitted as

$$f\left(We_{D_{eq}}\right) = We_{D_{eq}}^{0.121}. \tag{II.6.12}$$

Both of the inlet conditions correlations given in Table II.6.2 provided good predictions of the present CHF data. However, the ultra-high-heat-flux correlation provided a slightly better MAE of 8.0% compared to 10.7% for the other correlation. Figure II.6.6 compares the predictions of Eqs. (II.6.11) and (II.6.12) based on the ultra-high-heat-flux inlet conditions correlation to the experimental micro-channel CHF database, excluding the PM-CHF data. Figure II.6.6 shows all the data falling within ±20% from the

predictions. Figure II.6.7 shows the distributions of prediction error relative to mass velocity, quality, and length-to-diameter ratio. Due to the lack of CHF data for smaller diameter test sections, the majority of the test data are limited to L/D_h = 20 – 30. The new correlation is valid over the following ranges: G = 500 to 2500 kg/m^2.s, $x^*_{e,in}$ = -1.0 to -0.4, and P = 1.13 to 1.48 bar.

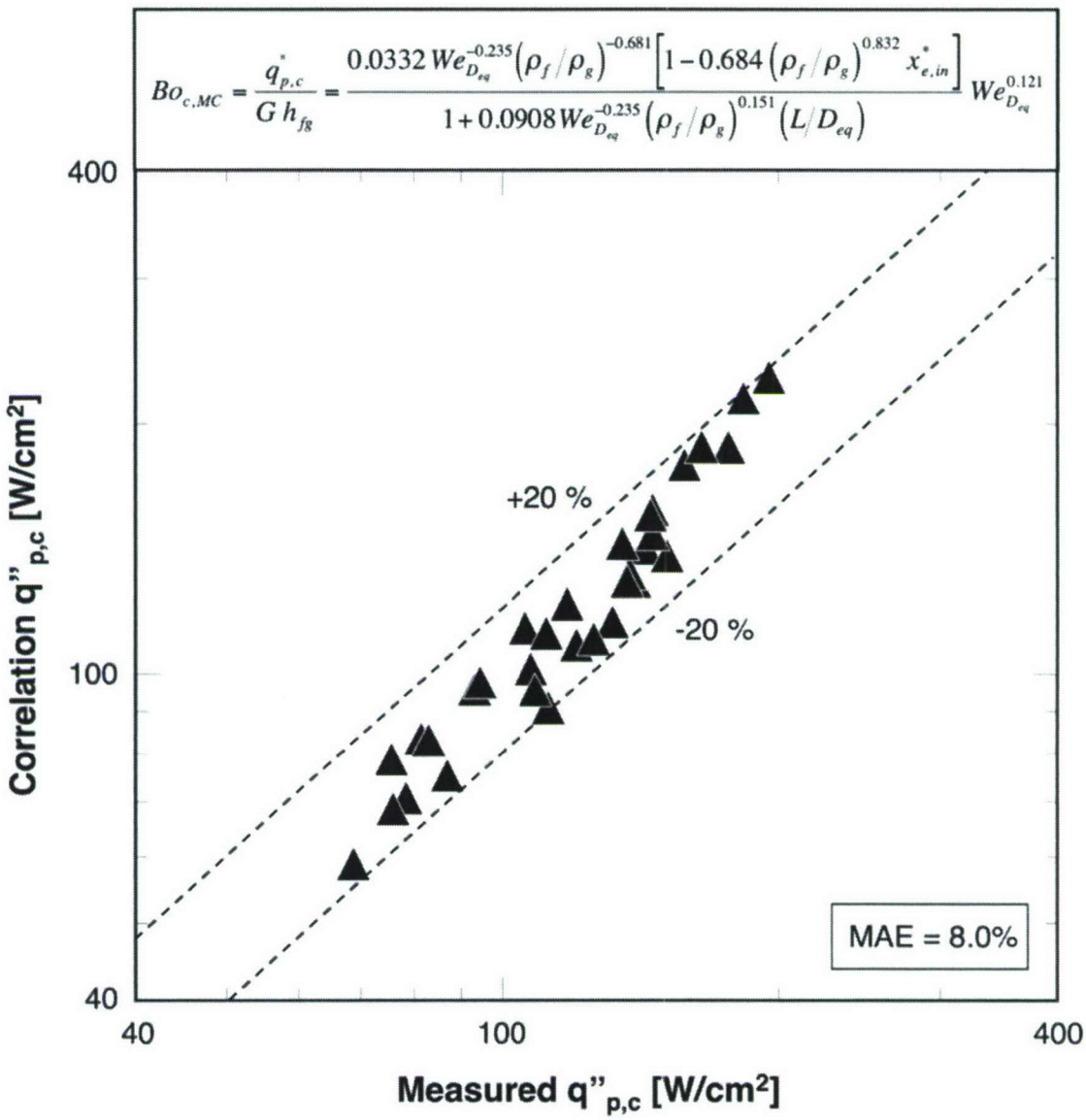

Figure II.6.6 Comparison of predictions of subcooled boiling CHF correlation and experimental data.

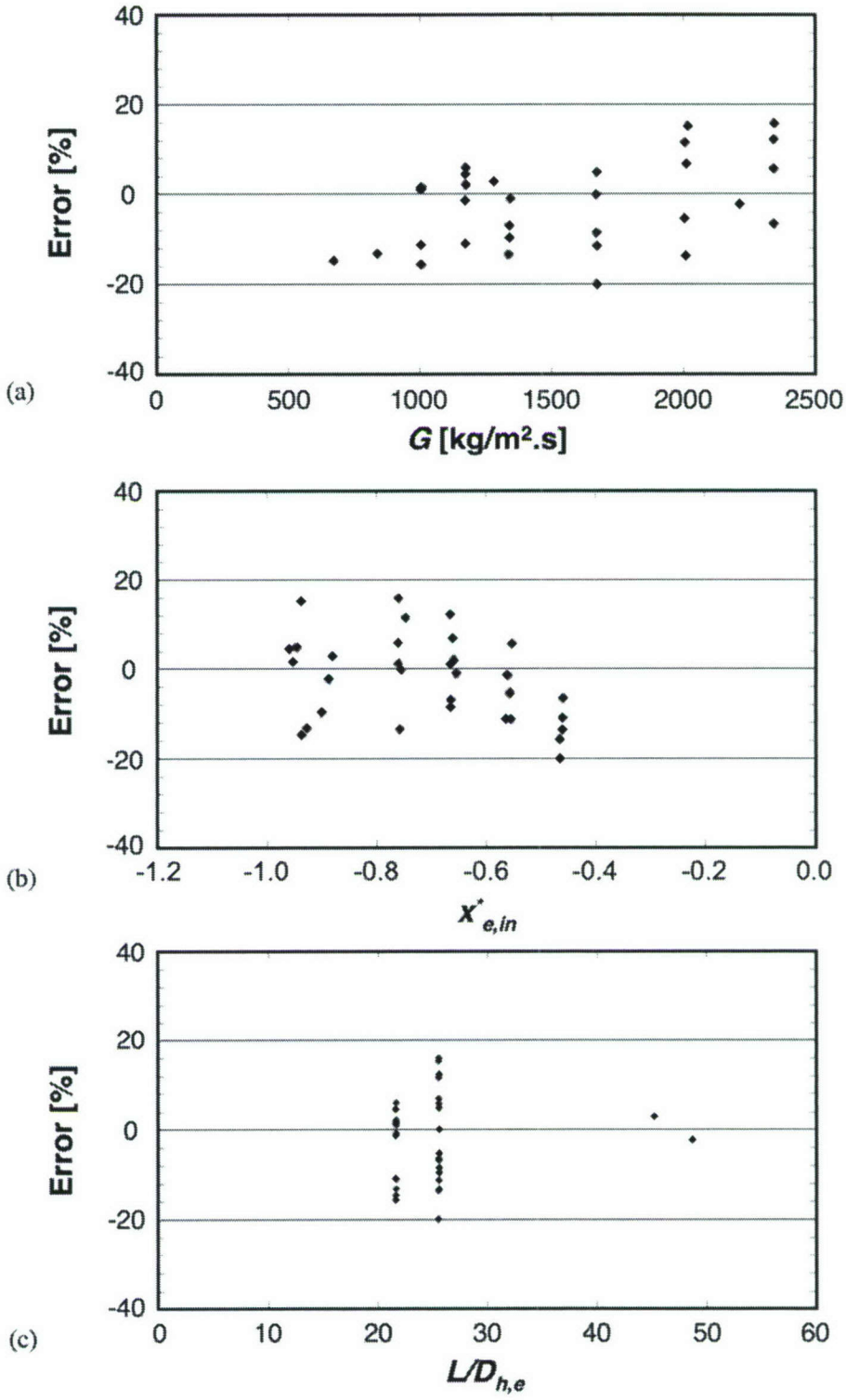

Figure II.6.7 Error distributions in predictions of subcooled CHF correlation relative to (a) mass velocity, (b) inlet quality, and (c) length-to-hydraulic-diameter ratio.

II.6.3 Strategy for Exceeding 1000 W/cm^2

The ability to dissipate 1000 W/cm^2 is a major challenge for advanced defense electronics for which the present study is intended. Ironically, efforts to experimentally demonstrate such heat dissipation is limited by the ability to construct test heaters that can endure these extreme heating conditions. Large temperature gradients between the cartridge heaters embedded in the test heater and the test surface often produce temperatures that are too high for the materials comprising the test heater, such as plastics and sealants. In the present study, tests had to terminated at about 700 W/cm^2 to avoid damaging the test module parts.

However, using the new CHF correlation, it is possible to determine operating conditions that can yield the required 1000 W/cm^2 heat dissipation. Calculations are based on the four different micro-channel geometries examined in the preset study and two inlet qualities, x_{in} = -0.65 (for T_{in} = 0°C) and x_{in} = -0.85 (for T_{in} = -20°C). Outlet pressure is fixed at P_o = 1.14 bar.

Figure II.6.8 shows conditions exist that can easily exceed 1000 W/cm^2. Results are based on G in Fig. 6.8(a) and $\dot{m}$ in Fig. 6.8(b); the later provides a more realistic comparison of different micro-channel sizes. Because of their relatively smaller heat transfer area, smaller diameter channels require higher mass fluxes to achieve 1000 W/cm^2 than larger channels. However, on a heat sink basis, smaller diameters can actually exceed 1000 W/cm^2 at lower total coolant flow rates than larger diameters. Decreasing the coolant's inlet temperature (*i.e*, increasing $\Delta T_{sub,in}$) also decreases the total flow rate required to exceed this heat flux.

Interestingly, the required coolant flow rates according to Fig. II.6.8 are quite feasible with the present indirect refrigeration system. However, aside from the aforementioned high temperatures and test module's material concerns, such flow rates were not possible for the smaller test sections because high pressure drop exceeded the capability of the primary coolant's pump. These findings provide important quantitative practical guidelines for the attainment of the thermal goal.

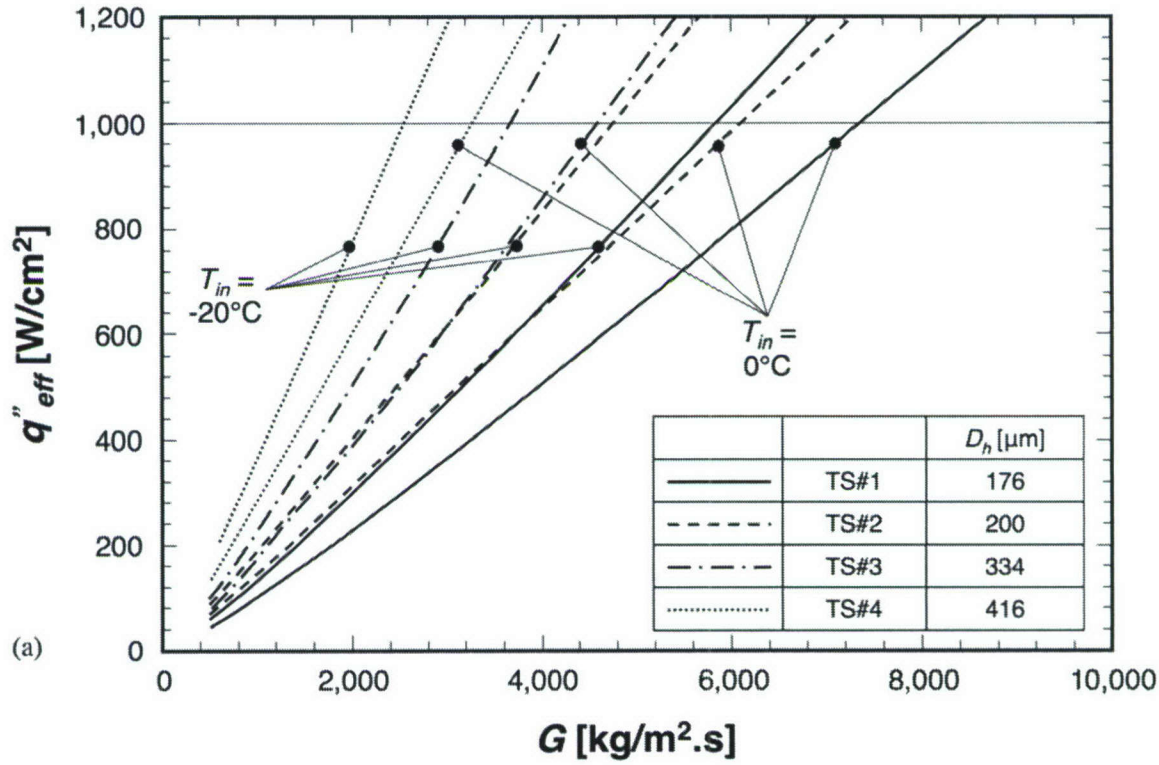

Figure II.6.8 Conditions required to exceed 1000 W/cm^2: (a) CHF versus mass velocity; (b) CHF versus mass flow rate.

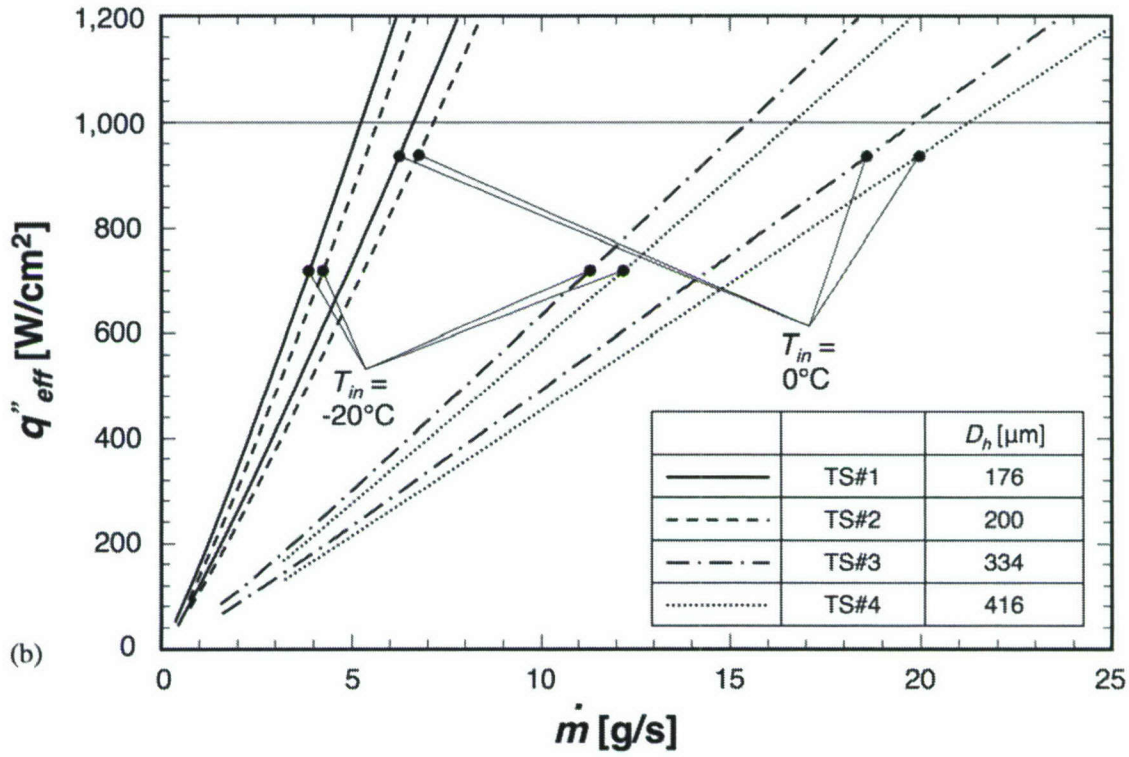

Figure II.6.8 continued.

II.7 CONCLUSIONS

7.1 System Delvelopment and Flow Visualization

A new micro-channel cooling scheme is suggested where the primary coolant passing through the micro-channel heat sink is pre-cooled to low temperature using an indirect refrigeration cooling system. The cooling performance of this system was examined for different flow rates using four different micro-channel geometries. Extensive high-speed video imaging and photomicrography were used to capture interfacial behavior with increasing heat flux up to and including CHF. Key findings from the study are as follows.

(1) Indirect refrigeration cooling is a highly effective means for removing heat from high-flux devices while maintaining low device temperatures. Unlike direct refrigeration cooling, where the micro-channel heat sink serves as evaporator in a vapor compression cycle, the present scheme decouples the quality requirements of the heat sink from those of the refrigeration loop. This decoupling alleviates compressor problems, facilitates high cooling capacity at low temperatures, and allows heat sink operation at near-ambient pressure.

(2) Cooling performance of the micro-channel heat sink can be greatly enhanced by lowering the temperature of coolant entering the heat sink. With temperatures of 0 °C or below, the heat sink could dissipate up to 100 W/cm^2 without phase change while maintaining surface temperatures below ambient. Heat fluxes as high as 700 W/cm^2 could be managed with flow boiling without the risk of burnout.

(3) Unlike most earlier two-phase heat sink studies, where annular film evaporation is the dominant mechanism for heat removal, the low coolant temperature used in the present study results in predominantly subcooled flow boiling, and outlet coolant temperature never reaches saturation. Some oblong bubbles typical of slug flow form mainly towards the outlet of the micro-channels. Decreasing the coolant temperature (*i.e.,* increasing subcooling) delays the onset of boiling, reduces bubble departure size and coalescence effects, and enhances CHF.

(4) CHF is associated with departure from nucleate boiling, caused by vapor blanket formation along the walls of the micro-channels even while abundant liquid is available in the core.

(5) Micro-channel hydraulic diameter and width play a complex role in cooling performance, and this role varies greatly with liquid subcooling. Small hydraulic diameter increases total wetted area, decreasing heat flux along the micro-channel walls. This tends to decrease void fraction along the micro-channels. On the other hand, a limit might be reached where decreasing micro-channel width causes bubbles to span the entire width and promote early transition to slug flow. These complex effects highlight the need for a comprehensive mechanistic model for subcooled flow boiling in micro-channel heat sinks.

(6) A premature form of CHF is associated with vapor flow reversal toward the inlet plenum. This is followed by development of a large vapor mass in the upstream plenum, which prevents liquid from flowing into the micro-channels. Momentary dryout ensues inside the micro-channels and wall temperatures begin to rise. The vapor buildup causes an increase in the upstream pressure, which ultimately becomes strong enough to purge the vapor mass through the micro-channels and into the outlet plenum. This process is then repeated in a cyclical manner as wall temperatures continue to rise gradually with each new cycle. This form of CHF occurs only at low mass velocities and can be eliminated by decreasing coolant temperature and/or increasing flow rate.

7.2 Experimental Results and Correlations

Experiments were performed to determine both the pressure drop and heat transfer characteristics of two-phase micro-channel flow. Unlike earlier studies of two-phase heat sinks, where annular evaporation is typically the dominant mechanism for heat removal, the present work focused on subcooled boiling characteristics. Four different test sections were tested to assess the effects of not only hydraulic diameter, but micro-channel width and aspect ratio as well. Aided by findings from the flow visualization study presented in chpter 3, the data were carefully examined for important parametric trends and compared to predictions of earlier correlations. Key findings from this study are as follows.

(1) During single-phase cooling, pressure drop decreases with increasing heat flux because of decreased liquid viscosity. After bubbles form and depart into the liquid flow, void fraction begins to increase appreciably, causing pressure drop to begin increasing with increasing heat flux. These opposite trends produce a minimum in the variation of pressure drop with heat flux.

(2) Increasing the subcooling of incoming liquid decreases two-phase pressure drop because of decreased void fraction caused by strong condensation at bubble interfaces, and decreased likelihood of bubble coalescence.

(3) The effects of hydraulic diameter on two-phase heat transfer are complicated by the relative size of bubbles and micro-channel width. While smaller hydraulic diameters tend to enhance two-phase cooling performance by increasing both mass velocity and wetted area, smaller micro-channel width can trigger early transition from bubbly to slug flow, causing a reduction in cooling effectiveness.

(4) It is quite difficult to identify correlations from the heat transfer literature that can predict pressure drop and cooling behavior of subcooled micro-channel heat sinks. This difficulty is the result of scarcity of subcooled boiling correlations in general, and the drastic differences in fluid, hydraulic diameter, and operating conditions of

the present study compared to the macro-channel heat transfer databases upon which these correlations are based. A new modified form of earlier correlations by Shah produced good predictions of the present heat transfer data.

(5) The shortage of useful correlations highlights the need for new mechanistic models of subcooled micro-channel boiling that capture the complex interfacial interactions reported in flow visualization work.

7.3 Developing homogeneous Layer Model (DHLM)

This study also examined subcooled boiling pressure drop in a micro-channel heat sink. A new control volume model is proposed in which the subcooled flow is described as consisting of two layers: a homogeneous two-phase layer near the heated wall and a subcooled bulk liquid layer. Mass, momentum and energy conservation equations are combined to predict pressure drop for thermodynamic equilibrium qualities below zero. Achieving closure in the construction of this Developing Homogeneous Layer Model (*DHLM*) required incorporating a relation for apparent quality across the two-phase layer as well as a new criterion for bubble departure. This model enables the determination of axial variations of two-phase layer thickness and velocity as well as pressure drop, and is specifically tailored to rectangular micro-channels. The model shows good predictions of pressure drop data for different mass velocities and subcoolings for four different micro-channel sizes.

7.4 Critical Heat Flux for Subcooled Flow Boiling

This study explored the critical heat flux (CHF) limit for micro-channel sinks under subcooled flow conditions using HFE 7100 as working fluid. The subcooling was achieved by pre-cooling the fluid using a low-temperature refrigeration system. Prior CHF correlations were modified to accommodate the unique features of micro-channel

heat sinks, such as rectangular geometry, three-sided heating and flow interactions between micro-channels. Key conclusions from the study are as follows:

(1) High inlet subcooling greatly reduces both bubble departure diameter and void fraction, precluding any flow pattern transitions beyond the bubbly regime. CHF is triggered by vapor blanket formation along the micro-channel walls despite the abundance of core liquid. This behavior is consistent with the mechanism of Departure from Nucleate Boiling (DNB).

(2) CHF increases with increases in mass velocity and/or subcooling. CHF also increases with decreasing hydraulic diameter for a given total coolant mass flow rate because of the increased mass velocity. Exceptions to the diameter trend are very small diameters and/or very small micro-channel widths that may promote early transition to slug flow.

(3) Weak momentum of incoming liquid at low mass velocities and small inlet subcoolings trigger a premature form of CHF caused by vapor backflow into the inlet. This type of CHF is associated with significant fluctuations in inlet and outlet pressure, as well as wall temperature.

(4) A systematic technique was developed to modify existing CHF correlations to more accurately account for the unique features of micro-channel heat sinks, including rectangular cross-section, three-sided heating, and flow interaction between micro-channels. This technique is successful at correlating the present data for different hydraulic diameters, mass velocities and inlet subcoolings.

PART III. Assessment of the Effectiveness of Nanofluids for Single-Phase and Two-Phase Heat Transfer in Micro-Channels

III.1 INTRODUCTION

Solid particles generally possess far greater thermal conductivity than common heat transfer liquids. Mixing solid particles in a liquid can therefore enhance the cooling potential of the liquid by increasing the thermal conductivity of the suspended fluid.

In the past, this goal was sought by using relatively large ('milli' or 'micro' scale) particles. While these fluids do provide the aforementioned cooling benefit, their implementation is complicated by their tendency to damage mechanical pumps and valves, as well as clog flow passages due to particle settling.

Recent developments in nanotechnology and related manufacturing techniques have made possible the production of far smaller – nano-sized - particles. Such particles greatly reduce the damage to flow loop components while providing the cooling benefits. Choi and co-workers at Argonne National Laboratory proposed the use of nanoparticles to enhance the thermal conductivity of liquids, and coined the term 'nanofluids' for the resulting mixtures [Choi (1995), Lee and Choi (1996), Lee at al (1999)]. Later studies experimentally demonstrated this enhancement effect. Lee et al. (1999) used 50 nm or smaller Al_2O_3 and CuO particles to enhance the thermal conductivity of their nanofluids. They showed the percentage enhancement in thermal conductivity was not simply a function of concentration and conductivities of the particle material and liquid, but particle size and shape as well. Xuan and Li (2000) reported that copper particles provided greater thermal conductivity enhancement than metal oxide particles. Xue (2003) showed analytically that carbon nanotubes produce the highest conductivity enhancement of all nanofluids.

The aforementioned clogging problem is perhaps most serious in micro-channel flow devices recently recommended for high-heat-flux electronic and aerospace applications. These devices offer a number of cooling advantages such as high convective heat transfer coefficients, small size and weight, and reduced coolant inventory. Nanofluids are considered an ideal fit for micro-channel devices because they are thought to virtually eliminate the clogging problem. Furthermore, they can enhance the already substantial heat transfer coefficients realized with micro-channel flow by the added benefit of greater thermal conductivity.

Investigating the combined advantages of micro-channel flow and nanofluids is precisely the goal of the present study. Those advantages are examined experimentally for both single-phase and two-phase situations, and practical conclusions are drawn concerning the implementation of nanofluids in small coolant passages.

III.2 ENHACEMENT FOR LAMINAR VERSUS TURBULENT FLOW

Aside from thermal conductivity, other fluid properties will change by the particle inclusion, and it is the combined effect of these property variations that dictates the overall enhancement effect for a nanofluid. This point is illustrated with the aid of a simple example that will also show how this effect is quite different for laminar flow as compared to turbulent flow.

Figure III.2.1 shows a fluid being heated uniformly as it flows inside a circular tube. Ignoring entrance effects for now (these effects will be discussed latter in this report), the flow is assumed both hydraulically and thermally fully developed. The Nusselt number is constant for laminar flow and follows the Dittus-Boelter equation for turbulent flow.

$$Nu = 4.36 \qquad \text{for laminar flow} \qquad \text{(III.2.1)}$$

and

$$Nu = 0.023 Re^{0.8} Pr^{0.4} \qquad \text{for turbulent flow.} \qquad \text{(III.2.2)}$$

Lee et al. (1999) showed that the thermal conductivity of Al_2O_3 nanofluids follows the two-components mixture conductivity model of Hamilton-Crosser model fairly well.

$$k_{nf} = \left[\frac{k_p + (n-1)k_{bf} - (n-1)\varphi\left(k_{bf} - k_p\right)}{k_p + (n-1)\,k_{bf} + \varphi\left(k_{bf} - k_p\right)} \right] k_{bf}, \qquad \text{(III.2.3)}$$

where k_{nf}, k_{bf} and k_p are the thermal conductivities of the nanofluid, base fluid and solid particles, respectively, φ is the volumetric concentration of nanoparticles, and n is solid particle shape factor (n = 3 for spherical particles).

Following Wen and Ding (2004), the Einstein equation is used for dynamic viscosity.

$$\frac{\mu_{nf}}{\mu_{bf}} = 1 + 2.5\varphi, \tag{III.2.4}$$

where μ_{nf} and μ_{bf} are the viscosities of the nanofluid and base fluid, respectively.

All other properties are linearized relative to nanoparticle volumetric concentration (Pak and Cho (1998)). This yields relationships for density and specific heat, respectively,

$$\rho_{nf} = (1-\varphi)\rho_{bf} + \varphi\rho_p \tag{III.2.5}$$

and

$$c_{p,nf} = (1-\varphi)c_{p,bf} + \varphi\, c_{p,p}. \tag{III.2.6}$$

The system shown in Fig. III.2.1 yields the following variations of bulk mean fluid temperature and inside wall temperature, respectively, with distance x from the tube entrance.

$$T_{m,x} = T_{in} + \frac{q"Dx}{\dot{m}c_{p,nf}} \tag{III.2.7}$$

and

$$T_{w,x} = T_{m,x} + \frac{q"}{h}. \tag{III.2.8}$$

Two kinds of base fluids are examined in this example, water and HFE-7100. The latter is a 3M dielectric fluid used in electronics cooling and general heat transfer applications. The thermal conductivity for this fluid is significantly smaller than for water. Table III.2.1 shows properties of these base fluids as well as for different concentrations of Al_2O_3.

Figure III.2.2 shows heat transfer results for the laminar case. For each base fluid, increasing nanoparticle concentration is shown in Fig. III.2.2(a) monotonically increasing the heat transfer coefficient. This is the result of the heat transfer coefficient being proportional to thermal conductivity for laminar flow. Notice that the heat transfer coefficient values with HFE-7100 are much smaller than for water. Overall, the enhancement ratio is almost the same for water and HFE 7100 nanofluids.

However, as shown in Fig. III.2.2(b), increasing nanoparticle concentration increases both fluid and wall temperatures for the nanofluids relative to their base fluid counterparts. This temperature increase is the result of the decreased specific heat of nanofluids caused by the solid particles having lower specific heat than fluids. Notice

for HFE-7100 the large axial rise in both fluid and wall temperature. This trend is the result of the small specific heat for this fluid.

Figure III.2.3 shows the results for the turbulent case. According to Eq. (2), $h \sim k^{0.6}$ for turbulent flow compared to $h \sim k$ for laminar flow. This implies the enhancement effect due to the increased thermal conductivity of nanofluids is significantly weaker for turbulent flow than for laminar. The enhancement in turbulent flow is also dependent on flow rate in addition to viscosity and specific heat. Since $h \sim k^{0.6}\mu^{-0.4}\ c_p{}^{0.4}$, and because increased nanoparticle concentration enhances viscosity and degrades specific heat, the enhancement effect of nanoparticles in turbulent flow is further reduced compared to thermal conductivity alone. This effect is quite evident in Fig. III.2.3(a).

This simple analysis shows how the enhancement effect of nanofluids is more effectively realized in laminar flow. Interestingly, most micro-channel flows of practical interest are laminar because of both their small hydraulic diameter and small flow rates. Implementing nanofluids in micro-channel devices therefore appears to be an advantageous strategy in pursuit of enhanced cooling performance.

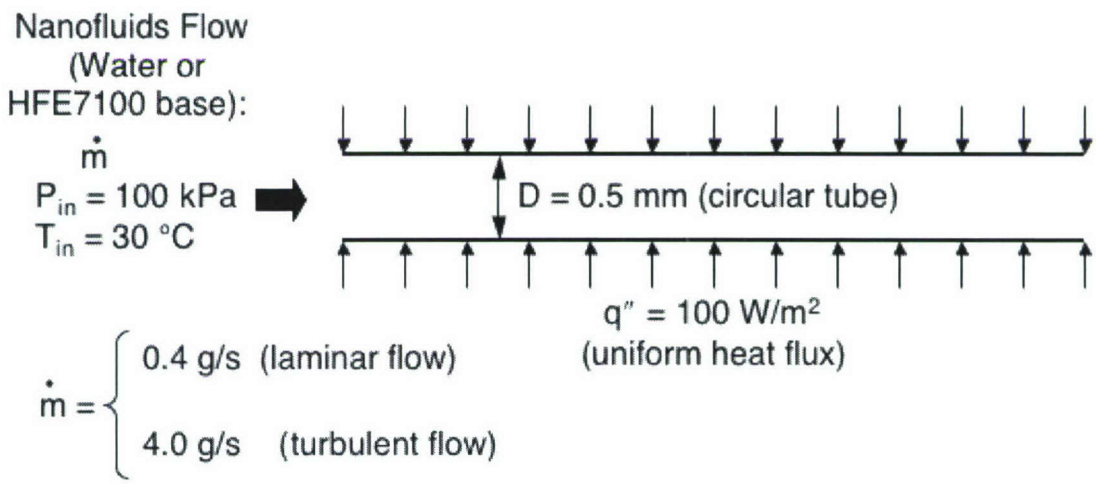

Figure III.2.1 Uniformly heated flow in circular tube.

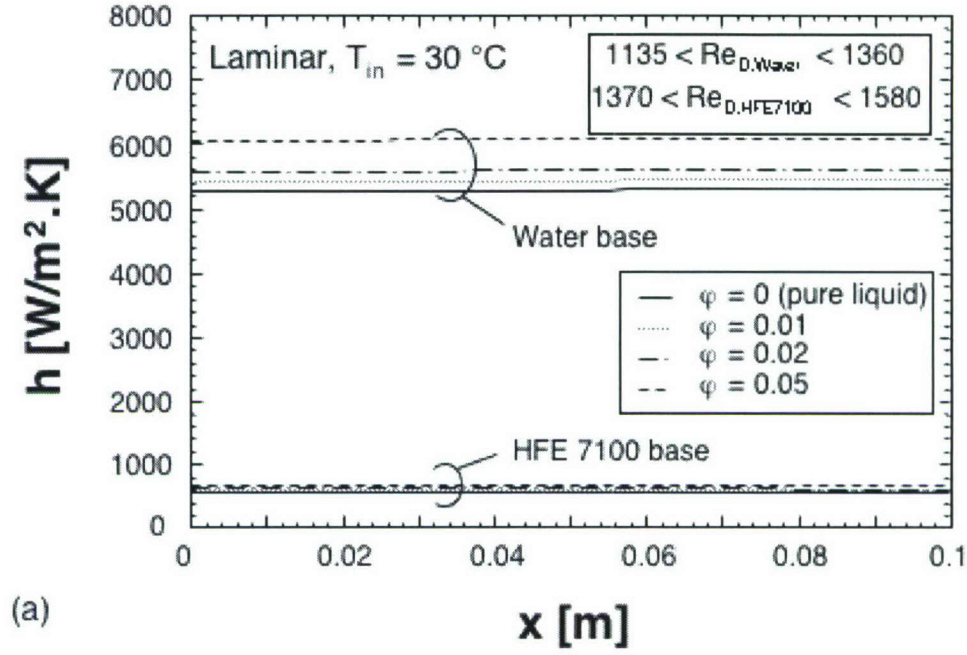

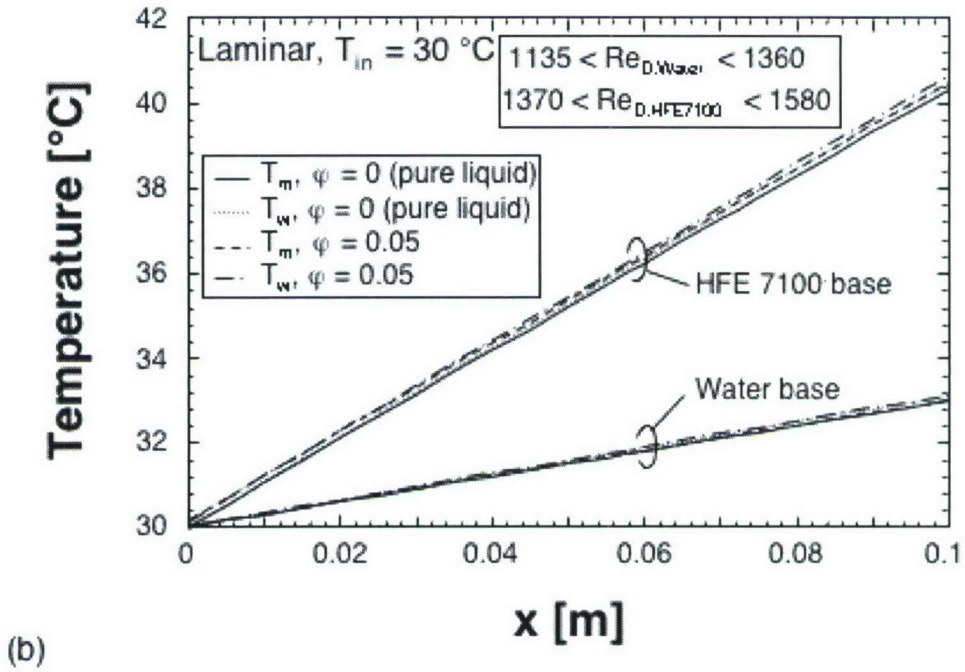

Figure III.2.2 Axial variations of (a) heat transfer coefficient and (b) bulk and wall temperatures for laminar flow and different nanoparticle concentrations in water and HFE7100 base fluids.

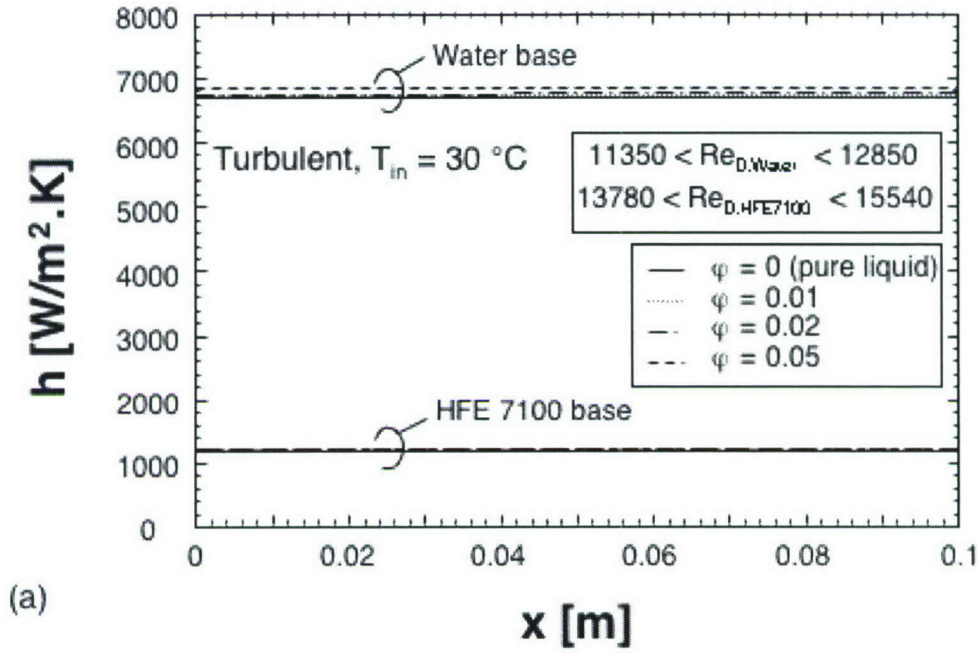

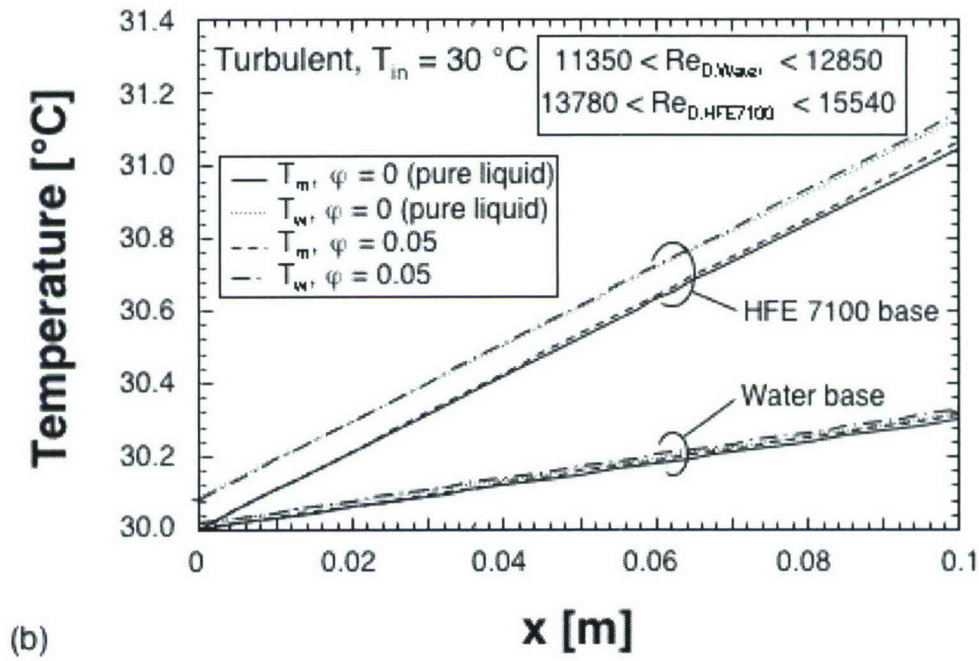

Figure III.2.3 Axial variations of (a) heat transfer coefficient and (b) bulk and wall temperatures for turbulent flow and different nanoparticle concentrations in water and HFE7100 base fluids.

Table III.2.1 Al_2O_3 nanoparticle suspension fluid properties at 30 °C and 100 kPa.

	Water Base						HFE 7100 Base					
	φ = 0%	1%	2%	3%	4%	5%	φ = 0%	1%	2%	3%	4%	5%
k_{nf} [W/m.K]	0.603	0.620	0.638	0.656	0.675	0.693	0.0678	0.0699	0.0720	0.0741	0.0763	0.0785
ρ_{nf} [kg/m^3]	995.7	1021.7	1047.7	1073.8	1099.8	1125.9	1455.4	1476.9	1498.3	1519.8	1541.2	1562.7
μ_{nf} [kg/m.s]	7.977×10^{-4}	8.177×10^{-4}	8.376×10^{-4}	8.576×10^{-4}	8.775×10^{-4}	8.974×10^{-4}	6.556×10^{-4}	6.720×10^{-4}	6.884×10^{-4}	7.048×10^{-4}	7.212×10^{-4}	7.376×10^{-4}
$c_{p,nf}$ [kJ/kg.K]	4.183	4.149	4.115	4.081	4.046	4.012	1.193	1.189	1.184	1.180	1.176	1.172

* Solid (Al_2O_3) properties: ρ_s = 3,600 kg/m^3, k_s = 36.0 W/m.K, $c_{p,s}$ = 0.765 kJ/kg.K

III.3. EXPERIMENTAL METHODS

III.3.1 Nanofluid Preparation

The solid particles used in this study were Al_2O_3. The nanofluid was produced by gas condensation by Nanophase Technologies. Insoluble solid Al_2O_3 particles with an area-averaged size of about 36 nm came dispersed in high concentration in water, which formed the base fluid. This high concentration fluid was diluted with de-ionized water to the desired specified volume concentration demanded for individual experiments.

Two volumetric concentrations of Al_2O_3 nanofluid, 1% and 2%, were tested in the present study. The particle size and shape were identical to those used by Lee et al. (1999), who measured about 6% enhancement in thermal conductivity with 2% Al_2O_3.

III.3.2 Test Loop and Operating Procedure

The enhancement effects of the Al_2O_3 nanofluids were examined with the aid of a test facility that was used in earlier studies of single-phase and two-phase micro-channel heat sink performance by Qu and Mudawar (2002, 2003, 2004). As shown in Fig. III.3.1, water was pumped from a reservoir through a filter followed by one of two parallel flowmeters, and a constant-temperature bath before entering the micro-channel test module. Exiting the test module, the fluid was passed through a water-cooled condenser before returning to the reservoir. Since the flow meters were not calibrated for the 1% and 2% Al_2O_3 concentrations, a bypass was included immediately downstream of the flowmeters to calibrate the flowmeters for these concentrations. The

calibration was achieved by dividing the mass of nanofluid accumulated in a beaker by the fill time. A precision digital bench scale was used for the mass measurements.

Figure III.3.2 shows a schematic of the micro-channel test module. Rectangular 215 μm wide by 821 μm deep grooves were milled into the top surface of an oxygen-free copper block. This block was inserted into a G-7 plastic housing and sealed atop with a polycarbonate plastic cover plate. This formed 21 parallel micro-channels with a hydraulic diameter of 341 μm and a total planform area 1 cm wide by 4.48 cm long. Heating was provided by 12 cartridge heaters that were embedded in the underside of the copper block. The G-7 housing featured inlet and exit plenums where the fluid temperature and pressure were measured with the aid of type-K thermocouples and pressure transducers, respectively.

Figure III.3.5(b) shows the detailed construction of the copper block. Notice the three deep cuts in the copper block virtually dividing the block into four cells, which helped confine the power dissipated by each set of cartridge heaters to the micro-channel flow region immediately above, thus minimizing axial heat flow. Four type K thermocouples were inserted along the flow direction to determine the channel bottom wall temperatures. A Yokogawa WT210 power meter measured electric power input to the copper block. All the facility's sensor signals were input to an HP 3852A data acquisition system.

Cooling performances of the nanofluids were benchmarked against that for pure water. The pure water experiments were performed first. The test facility was drained completely and flushed very carefully with de-ionized water before it was filled with a new fluid. Operating conditions for the study were as follows: $Re_{Dh} = 140 - 941$, $Q = 100 - 300\ W$, $T_{in} = 30\ ^{\circ}C$, $P_{in} = 1.17 - 1.36\ bar$, and $P_{out} = 1.12\ bar$.
Measurement uncertainties were $\pm\ 0.3\ ^{\circ}C$ for temperature, 0.5% for pressure, 0.1% for electrical power, and 2% for flow rate. Heat loss from the copper block was estimated at less than 5% of the electrical power input.

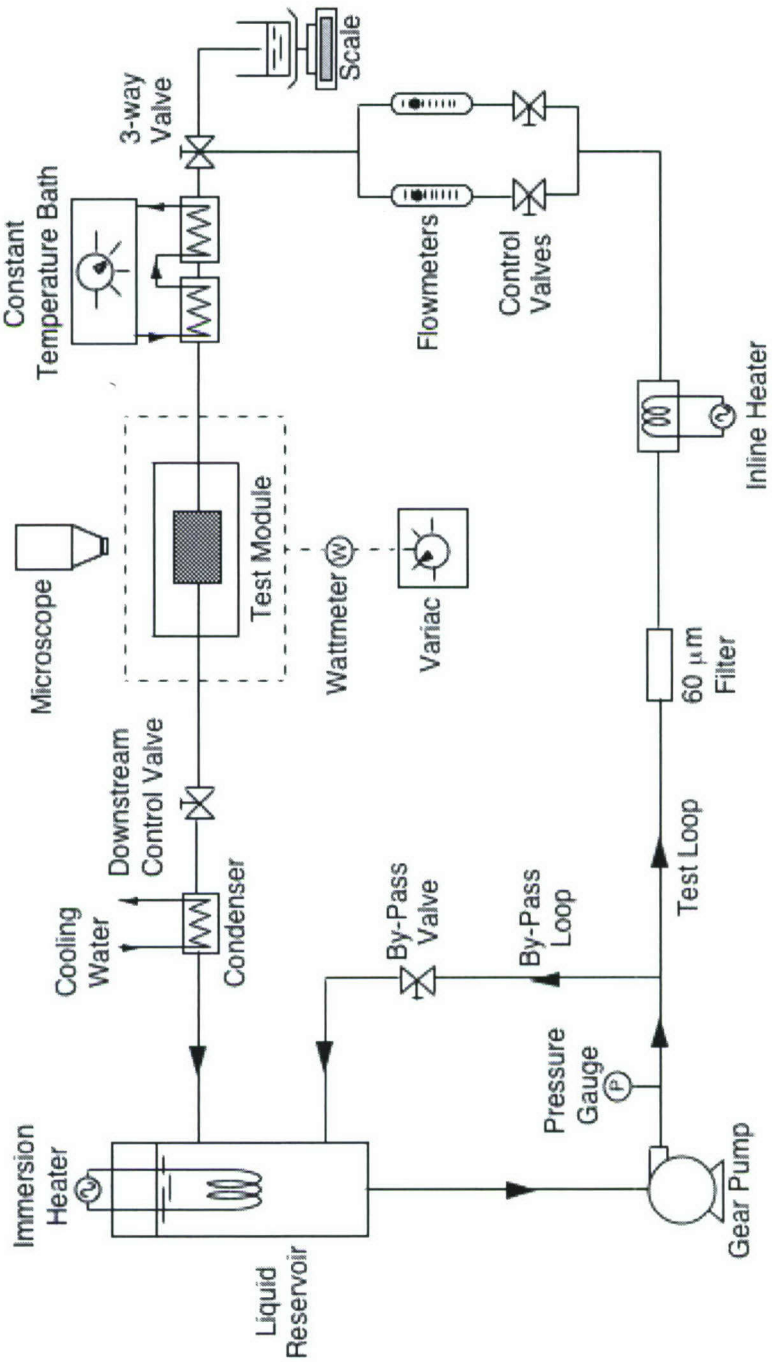

Figure III.3.1 Schematic of flow loop.

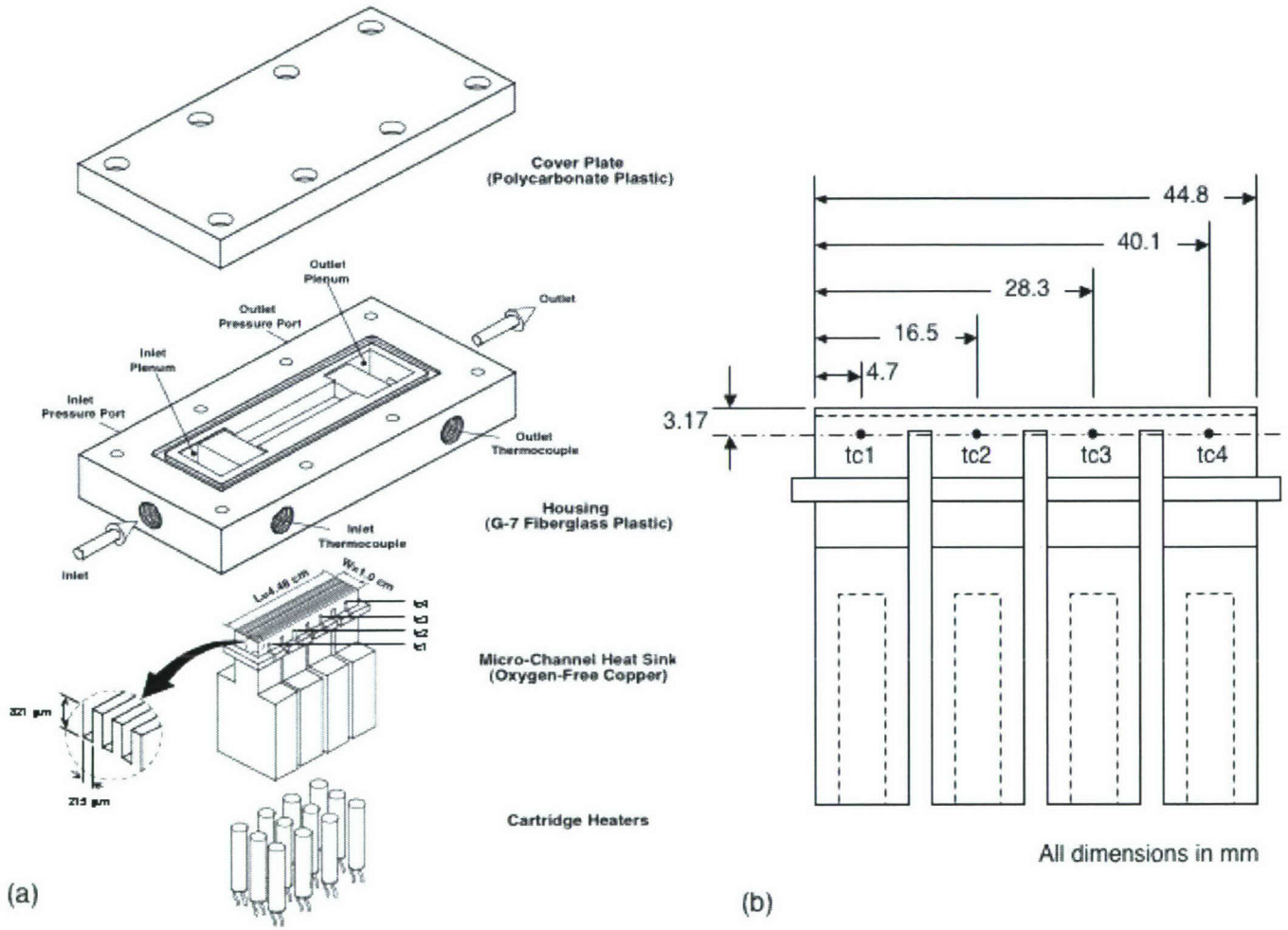

Figure III.3.2 (a) Construction of micro-channel test module and
(b) thermocouple locations in copper block inside test module.

III.4 SINGLE-PHASE RESULTS

III.4.1 Pressure Drop

Suspending solid particles in a fluid generally increases dynamic viscosity relative to the base fluid. Even with nanoparticles, this phenomenon causes a pressure drop increase in micro-channels compared to an equal mass flow rate of the base fluid.

Since the present pressure measurements were made in the inlet and outlet plenums of the test module, they included inlet contraction pressure loss and outlet expansion pressure recovery in addition to the pressure drop along the micro-channels as detailed by Qu and Mudawar (2002) for pure water.

Figure III.4.1(a) shows the variation of the measured pressure drop between the inlet and outlet plenums with Reynolds number for adiabatic flow. A strong particle concentration dependency is shown with the total pressure drop increasing with increasing nanoparticle concentration. Instead of using the viscosity relation given earlier in Eq. (III.2.4), Re_{Dh} in Fig. III.4.1(b) was based an empirical relation developed specifically for water-based Al_2O_3 nanofluids [Maiga et al. (2004)],

$$\frac{\mu_{nf}}{\mu_{bf}} = 123\varphi^2 + 7.3\varphi + 1. \qquad \text{(III.4.1)}$$

After subtracting the effects of inlet contraction and outlet expansion from the total measured pressure drop (see Qu and Mudawar (2002) for detailed calculation scheme), a single-phase micro-channel friction factor was determined from the pressure drop ΔP_{ch} calculated for the micro-channels alone.

$$f_{sp} = \frac{\Delta P_{ch} D_h}{2 L \rho_f u^2}. \qquad \text{(III.4.2)}$$

Figure III.4.1 (b) shows particle concentration does not have a clear influence on the friction factor dependence on Reynolds number. Error propagation from measurement uncertainties is estimated at 2.9% in friction factor calculation.

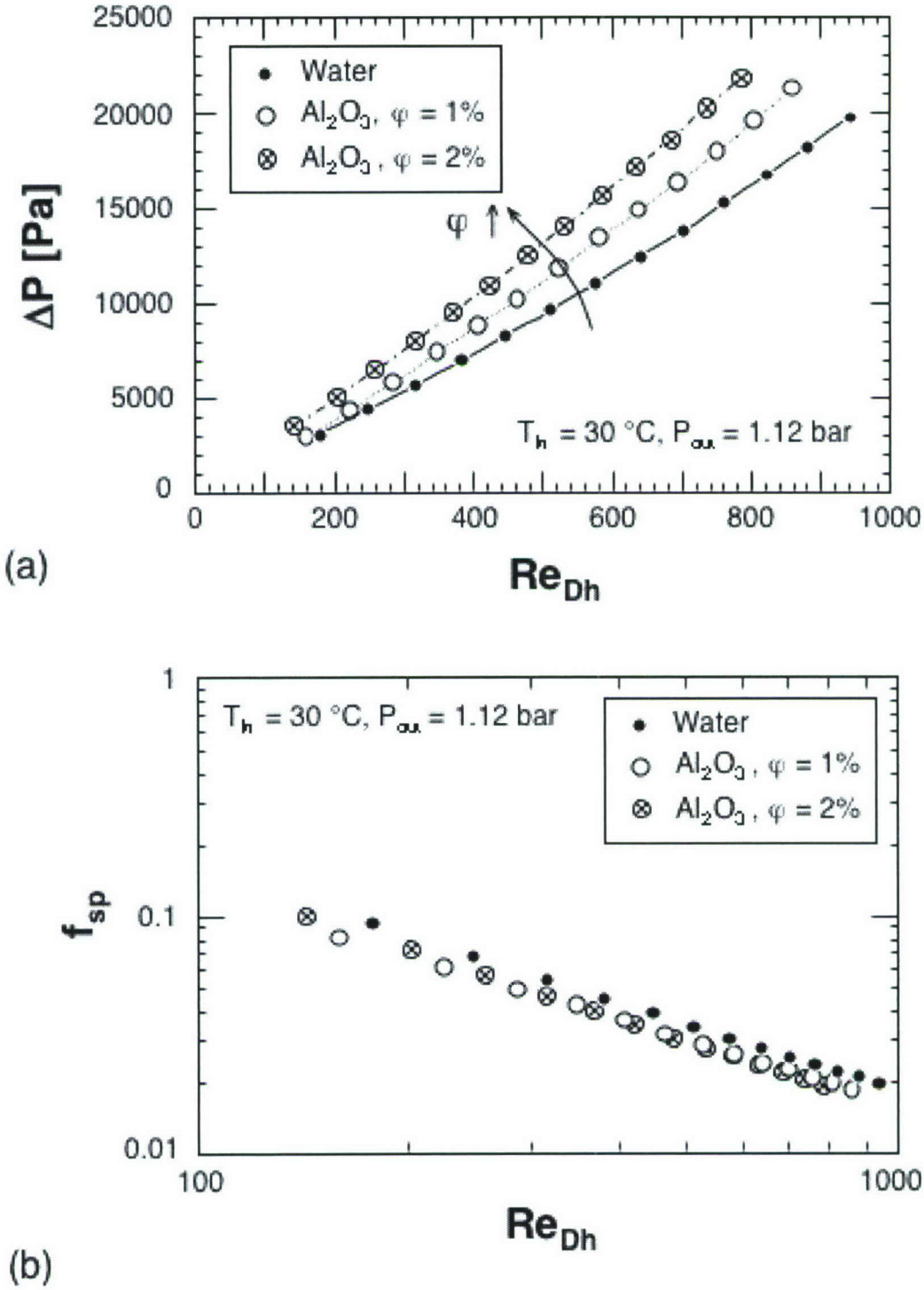

Figure III.4.1 Variations of (a) pressure drop across test module and (b) friction factor across micro-channels with Reynolds number for pure water and for 1% and 2% Al_2O_3.

III.4.2 Heat Transfer Coefficient

The single-phase heat transfer coefficient was determined from the measured fluid and heater block temperatures and the electrical power input using an analytical fin technique detailed by Qu and Mudawar (2003).

As shown in Figure I.4.1 and description in chapter I.4.1, equating the heat influx to the unit cell through the bottom solid wall to the heat efflux yields

$$q''(W_{ch} + 2W_w) = h_{sp}(T_w - T_m)(W_{ch} + 2\eta H_{ch}), \tag{III.4.3}$$

where η is the fin efficiency. Since the top wall is adiabatic, the fin efficiency is given by

$$\eta = \frac{\tanh(m H_{ch})}{m H_{ch}}, \tag{III.4.4}$$

where m is the fin parameter defined as

$$m = \sqrt{\frac{h_{sp}}{k_s W_w}}. \tag{III.4.5}$$

These three equations yields the valued of single phase heat transfer coefficient h_{sp}. The corresponding error propagation from measurement uncertainties is estimated at 5.0 %. The fin base temperature, T_w, was calculated using the assumption of one-dimensional heat diffusion between the plane of the thermocouple embedded in the copper block and the plane containing the fin base.

$$T_w = T_{tc} - \frac{q'' H_{tc}}{k_s}. \tag{III.4.6}$$

Figure III.4.2 shows the variation of the single-phase heat transfer coefficient along the flow direction for water and the two nanofluids for different power inputs. The four measurement locations correspond to the thermocouple layout shown earlier in Fig. III.3.2(b). The two upstream locations are well within the entrance region, while the third and the fourth indicate the flow is becoming thermally fully developed. The nanofluids exhibit the same spatial trend as that for pure water. Figures III.4.2(a) and 2(b) show similar trends for 1% and 2% Al_2O_3, respectively, as compared to pure water.

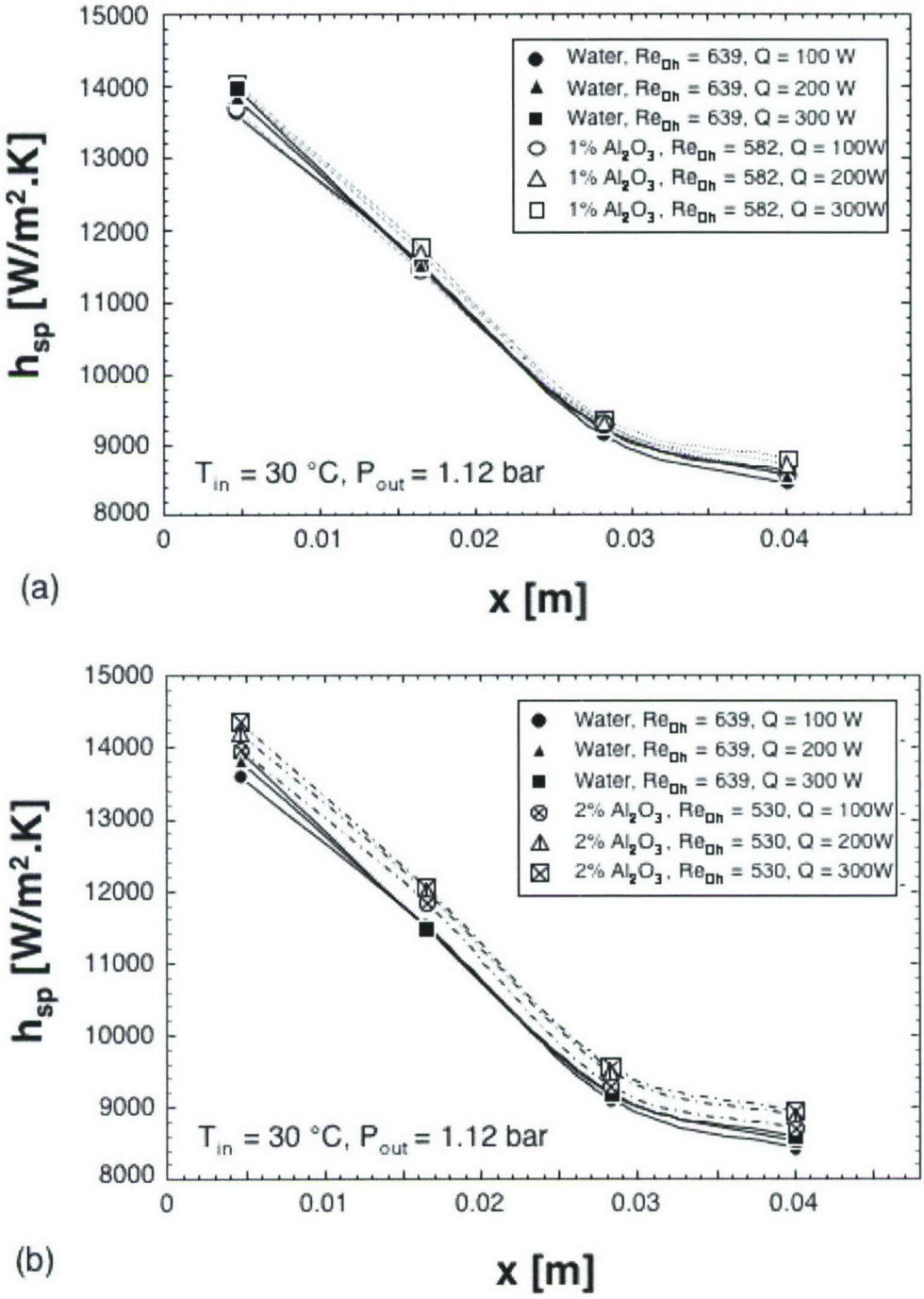

Figure III.4.2 Variation of heat transfer coefficient along micro-channel for (a) pure water and 1% Al_2O_3, and (b) pure water and 2% Al_2O_3.

In each of these figures, increasing the heat flux has a very weak effect on the heat transfer coefficient for pure water, but an appreciable effect for the nanofluid. Notice also the stronger effect of heat flux for 2% Al_2O_3, Fig. III.4.2(b), compared to 1% Al_2O_3, Fig. III.4.2(a).

Keblinski et al. (2002) suggested four possible mechanisms for heat transfer enhancement with nanofluids: Brownian motion, liquid layering at liquid/particle interface, phonon movement in nanoparticles, and nanoparticle clustering. While it is difficult to determine which of these four mechanisms has the greatest impact on enhancement, the increased dependence of the heat transfer enhancement on heat flux at higher concentrations may be one trend future research may rely upon in pursuit of mechanism identification. In any case, this increased dependence appears to alter boundary layer development for nanofluids.

Figure III.4.3 compares the heat transfer coefficient variation with Reynolds number for water, 1% Al_2O_3 and 2% Al_2O_3 for each of the four axial locations along the micro-channel heat sink. For each axial location, 2% Al_2O_3 shows the greatest heat transfer enhancement. For 1% Al_2O_3, the enhancement is obvious for the first two upstream locations, but virtually nonexistent for the two downstream locations where the thermal boundary layer is almost fully developed. In fact, the enhancement effect for both concentrations appears far more prevalent in the entrance region than the downstream fully developed region. It can therefore be concluded that nanoparticles have an appreciable effect on thermal boundary layer development.

Interestingly, this trend is a general agreement with the findings of Wen and Ding (2004) for Al_2O_3 nanofluid flow inside a much larger tube ($D = 4.5\ mm$).

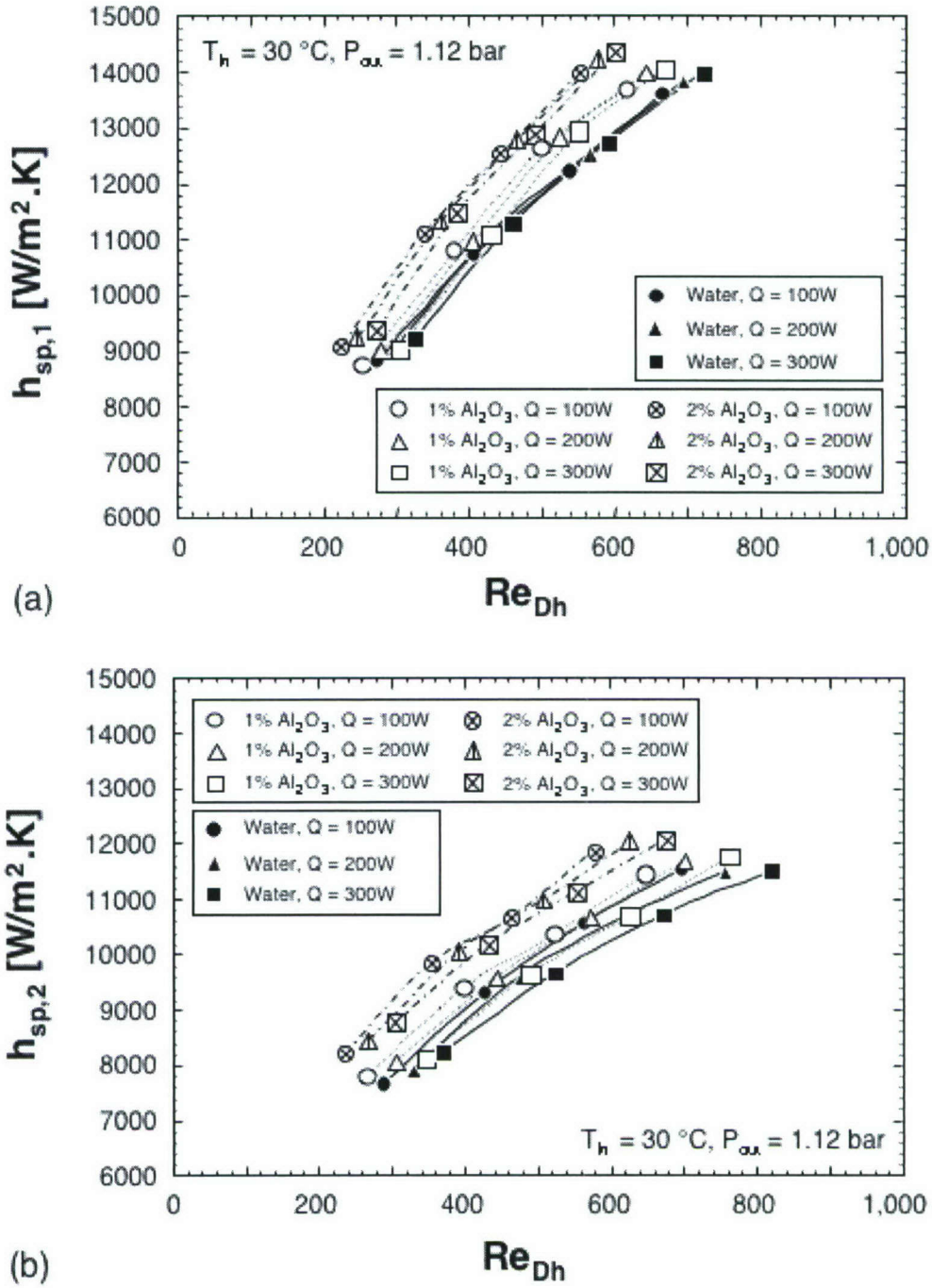

Figure III.4.3 Variation of heat transfer coefficient with Reynolds number for different heat inputs and different Al_2O_3 concentrations at measurement locations (a) tc1, (b) tc2, (c) tc3, and (d) tc4.

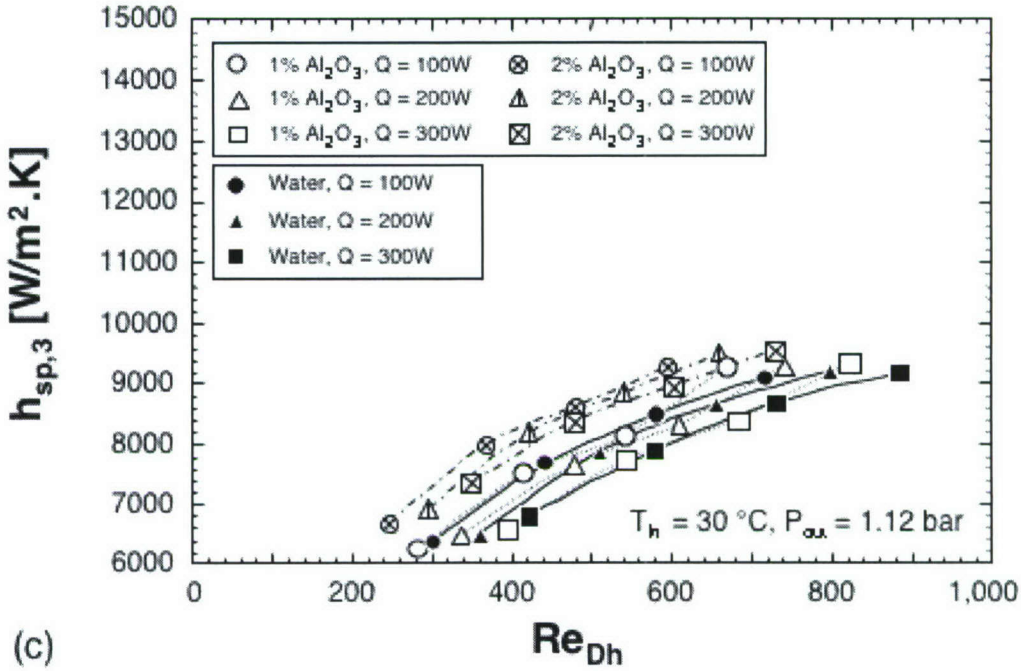

(c)

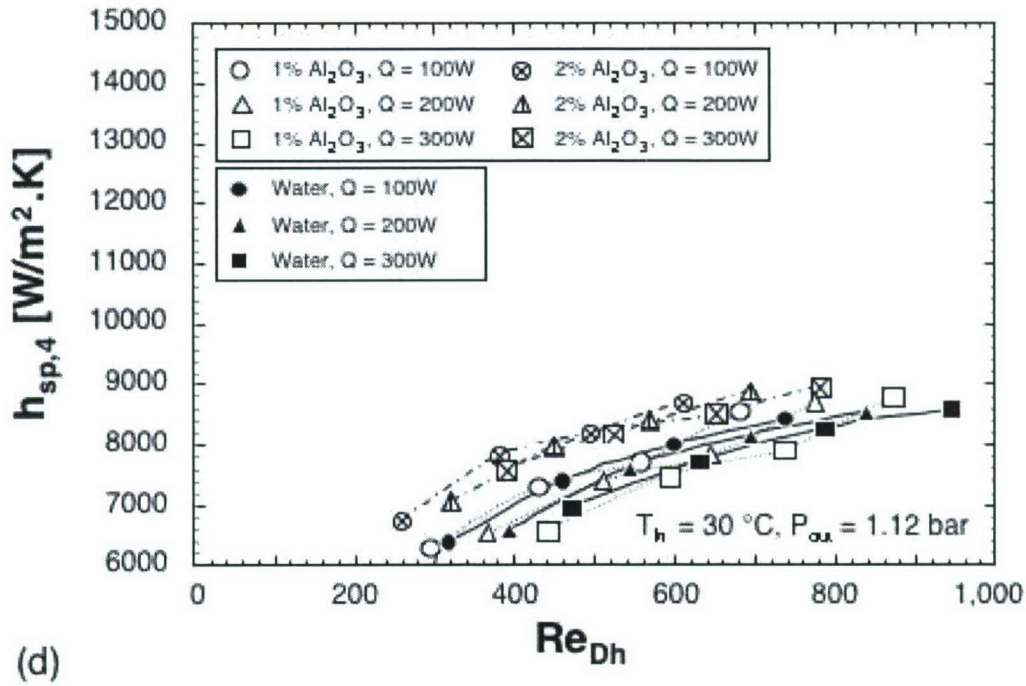

(d)

Figure III.4.3 continued.

III.4.3 Axial Variations of Fluid and Wall Temperatures

As discussed earlier, the thermal performance of a heat sink is dictated not only by the magnitude of the heat transfer coefficient, but by the wall temperature of the heat sink as well. Increasing nanoparticle concentration increases the fluid's thermal conductivity, thus increasing the heat transfer coefficient, especially for laminar flow. On the other hand, increased nanoparticle concentration also degrades specific heat, resulting in larger axial rises in both fluid and wall temperatures compared to the base fluid. Therefore, it is not immediately evident if the wall temperature actually decreases (a sign of better cooling performance) with increasing nanoparticle concentration as a result of the higher heat transfer coefficient, given this degradation in the nanofluid's specific heat.

Figure III.4.4 shows the measured variation of mean fluid temperature between the inlet and outlet of the micro-channel heat sink with mass flow rate. Shown is an increase in temperature difference with increased nanoparticle concentration due to the specific heat degradation. This effect is more pronounced for lower mass flow rates and higher heat fluxes.

Figure III.4.5 shows the net effect of increasing thermal conductivity and decreasing specific heat on the wall temperature, which is perhaps the most realistic measure of the effectiveness of a given cooling scheme. These wall temperatures were calculated using Eq. (III.4.6) with measured thermocouple data. The only noticeable decrease in wall temperature is realized near the inlet for the lower mass flow rate at the lower heat input. All other conditions and axial locations show virtually no measurable enhancement. Furthermore, any differences in the wall temperature are within the range of measurement uncertainty of the study, let alone the difficulty of achieving an exact flow rate when comparing different cases. These findings prove nanoparticles are not an effective means for enhancing single-phase cooling performance of a micro-channel heat sink.

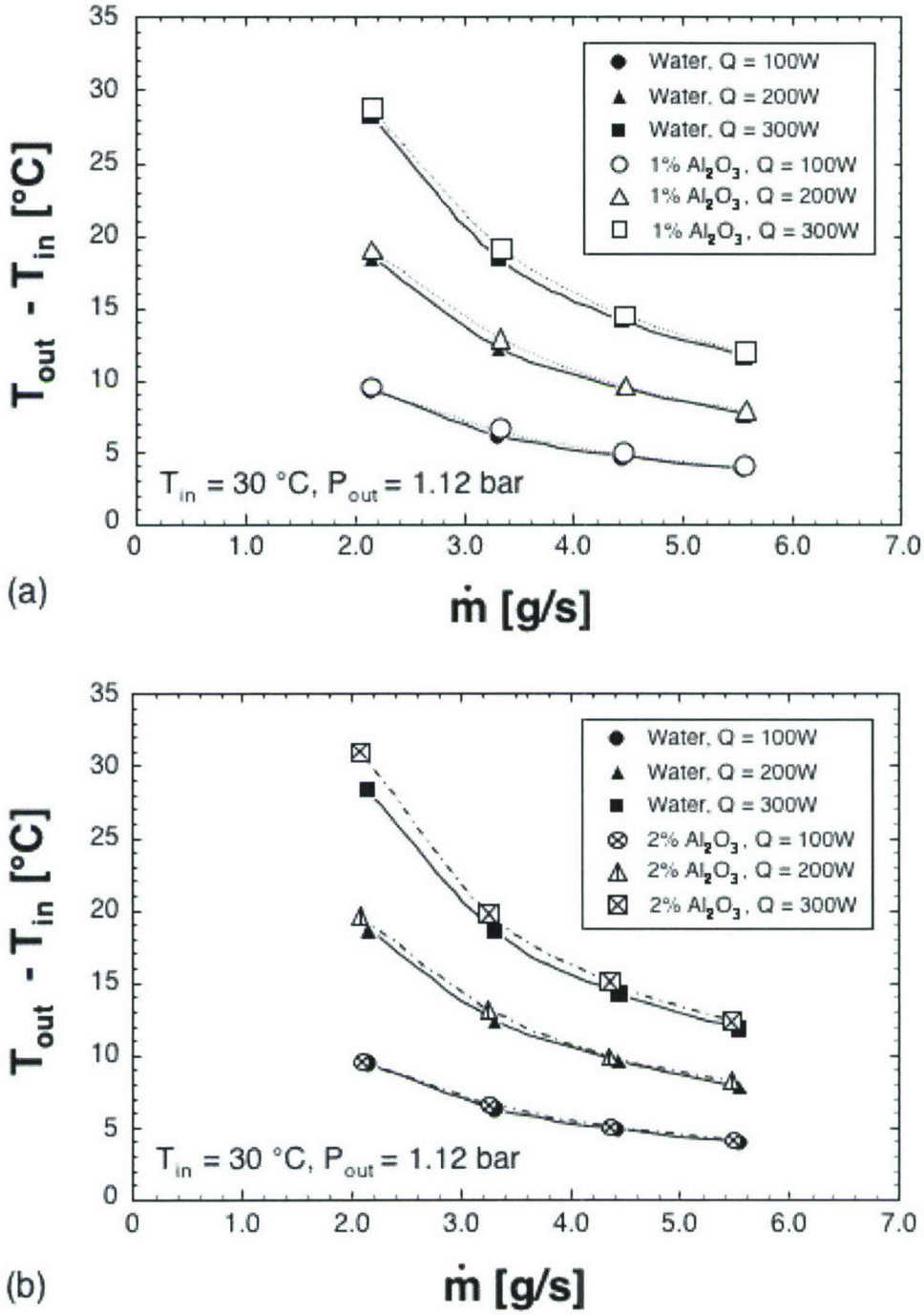

Figure III.4.4 Variation of fluid temperature rise along micro-channel for (a) pure water flow and 1% Al_2O_3, and (b) pure water and 2% Al_2O_3.

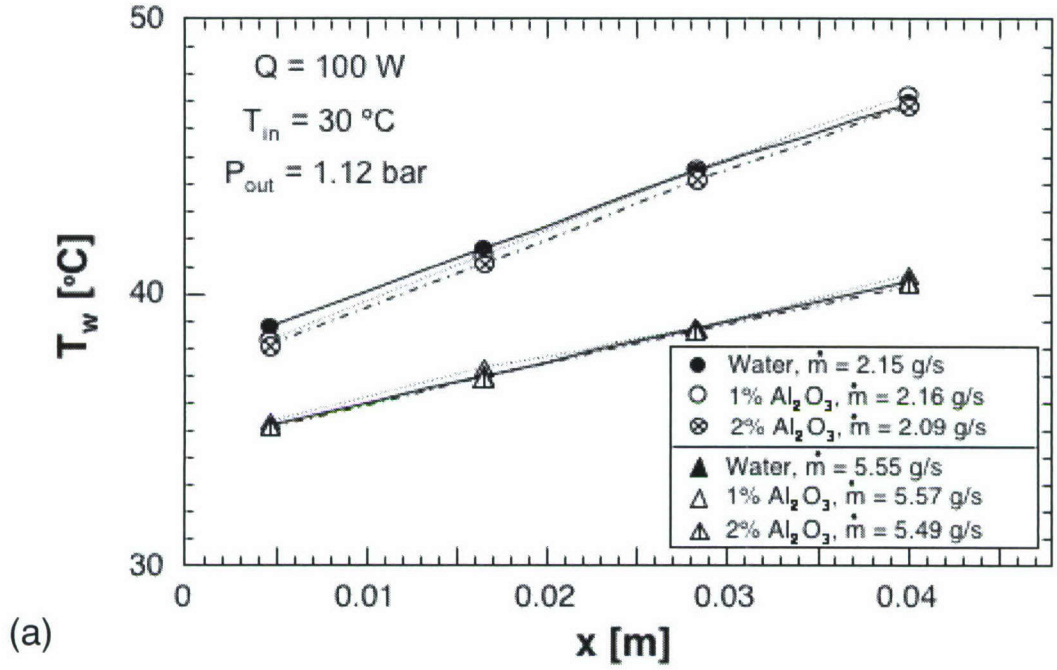

(a)

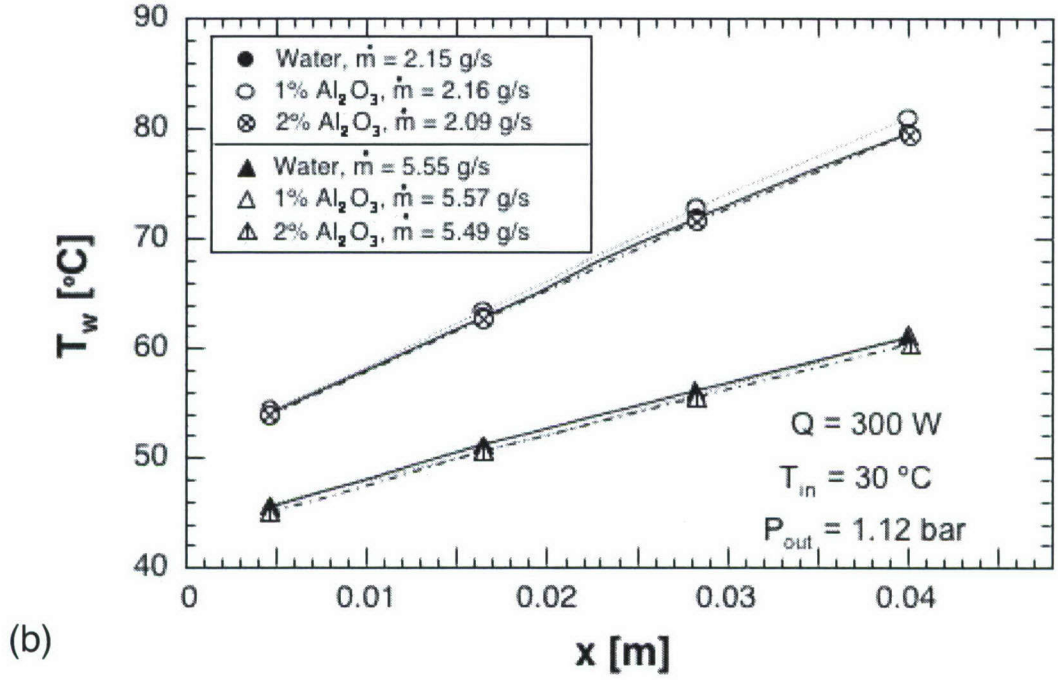

(b)

Figure III.4.5 Variation of wall temperature along micro-channel for different flow rates and Al_2O_3 concentrations and heat inputs of (a) 100 W and (b) 300 W.

III.4.4 Fluid Stability

Particle settlement is an obvious concern with solid particle suspensions that are intended for cooling applications. As mentioned earlier, nanoparticle suspensions are far more stable than suspensions of larger particles.

This issue was examined in the present study by repeating heat transfer coefficient measurements in tests that were separated by many hours. Figures III.4.6(a) and III.4.6(b) show these results for 2% Al_2O_3 for Reynolds numbers of 202 and 530, respectively. These results show fairly repeatable results over the indicated time span.

Another method of assessing nanofluid stability was to visually inspect fluid samples over an extended period of time. The samples were sealed in glass beaker for the entire period. Figure III.4.7 compares picture of 1% and 2% Al_2O_3 nanofluids taken shortly after initial mixing and 30 days later. The latter pictures show some settlement and a concentration gradient in both nanofluids. Such effects can cause long-term degradation in thermal performance due to settling inside the cooling system's reservoir. Furthermore, most cooling systems contain feedback control systems that attenuate coolant flow rate or stop it altogether in response to the fluctuating heat load of the device being cooled. Slow or zero flow rate accentuate nanoparticle settling and may even lead to clogging of individual components of the cooling loop. This issue points to the need for long-term testing of a nanofluid cooling loop before actual deployment.

Another long-term concern with nanofluids is surface abrasion. Like most metal surfaces, copper exhibits some oxidation when exposed to pure water. This effect was more pronounced with increasing surface temperature. The oxidize layer acts as an additional thermal resistance and tends to degrade the heat transfer performance. Interestingly, the micro-channel surface appeared cleaner and shinier following each single-phase experiment with the nanofluids. This phenomenon is believed to be the result of erosion of the copper surface by the nanoparticles. While this may seem an advantage for nanofluids, special attention must be paid to the possibility of the removed oxide be entrained with the flow, altering the enhancement effect of the nanoparticles, and contributing long term to particle settling or even clogging of flow passages.

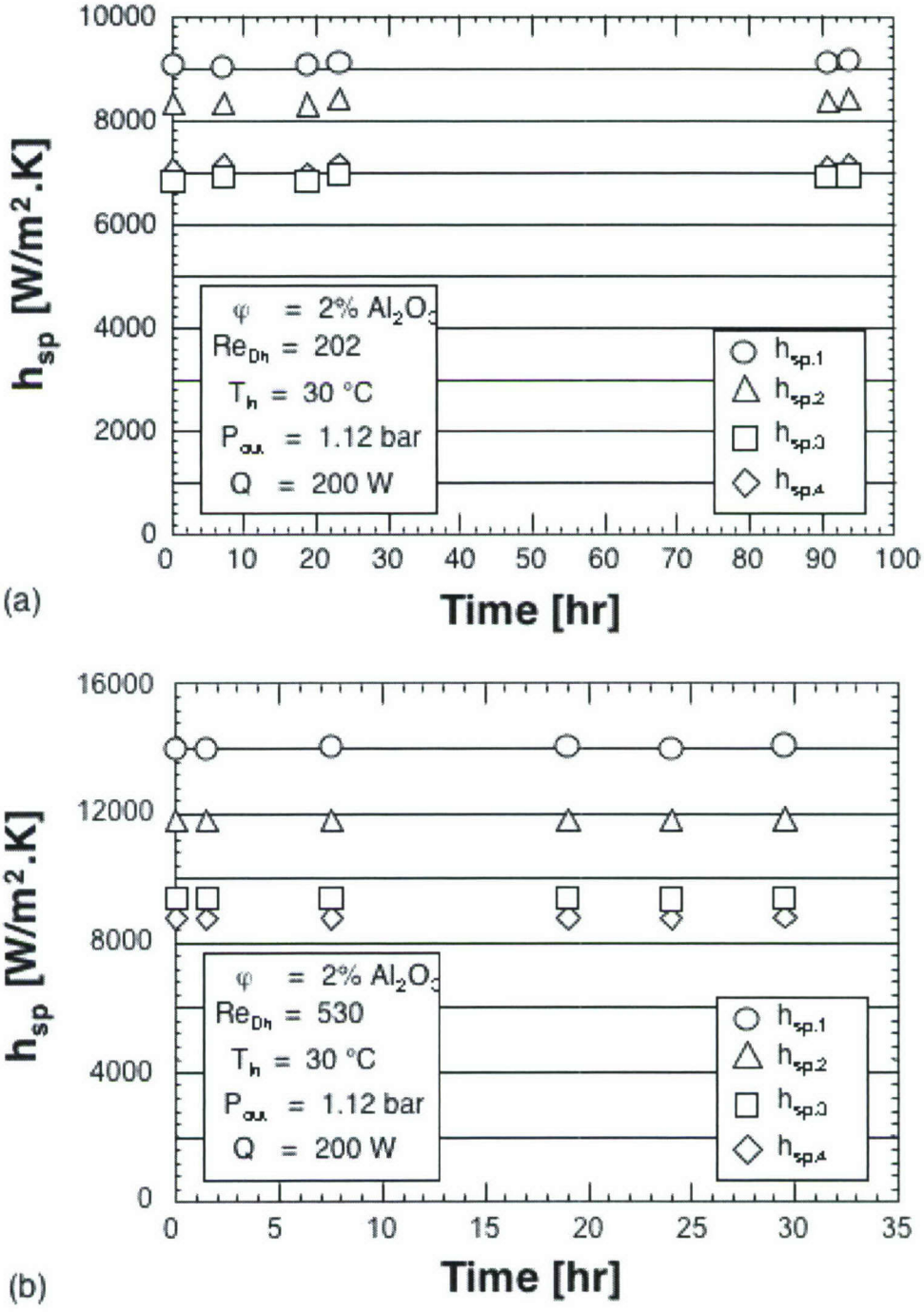

Figure III.4.6 Heat transfer coefficient versus time for 2% Al_2O_3 and Reynolds numbers of (a) 202 and (b) 530.

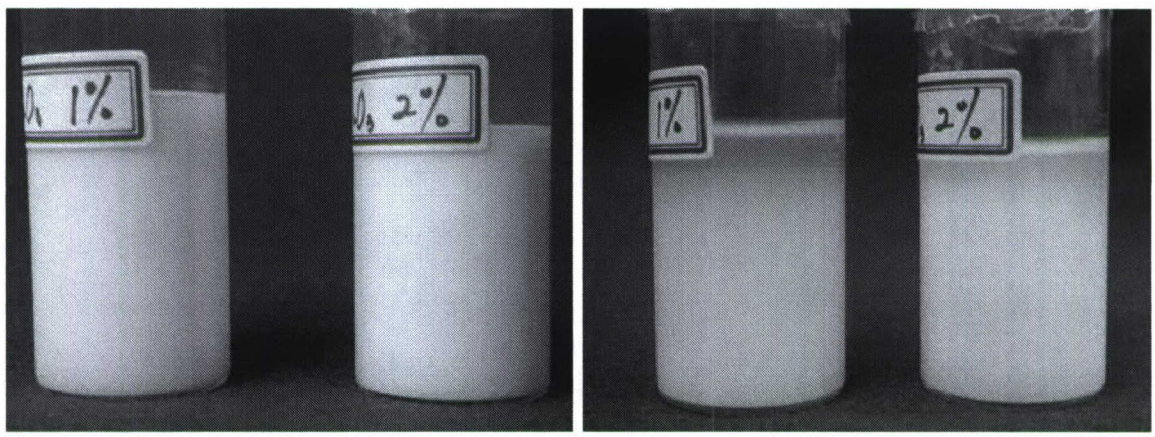

Figure III.4.7 Nanofluid settling over 30 day period.

III.5 FLOW BOILING RESULTS

Flow boiling can greatly enhance the cooling performance of a micro-channel heat sink by increasing the heat transfer coefficient. Furthermore, since flow boiling relies to a great degree on latent heat transfer, better temperature axial uniformity is realized both in the coolant and the wall compared to a single-phase heat sink. The question here is whether nanoparticles could further enhance an already superior performance.

Recently, several research articles examined the effects of nanoparticles on pool boiling [Das et al. (2003), Bang and Chang (2005), Vassallo et al. (2004)]. Degradation in nucleate boiling performance was related to surface smoothing, resulting from bubble-generated cavity filling with particles and particle deposition on the heating surface. However, nanofluids netted a measurable increase in critical heat flux (CHF).

In this research, flow boiling experiments were conducted with the micro-channel heat sink using pure water and 1% Al_2O_3. Figure III.5.1(a) shows the data for pure water follow a typical boiling curve. This curve is initiated at low heat fluxes with single-phase forced convection, followed by an appreciable slope change following the onset of boiling, and culminating in a sudden unsteady temperature rise at CHF. While single-phase forced convection proceeded in the same manner with increasing heat flux for 1% Al_2O_3, flow boiling was never achieved with this nanofluid. It appears fluid evaporation associated with the initial incipience of boiling near the channel exit caused rapid deposition of nanoparticles in the same region. Despite the small size of these particles, the deposition rate was so severe that relatively large particle clusters could be seen near the exit. This clustering effect quickly propagated upstream and filled the entire channel, preventing the coolant from entering the heat sink. The heat sink

responded with a sudden unsteady temperature rise. This phenomenon constitutes a catastrophic failure for a cooling system. Figure III.5.1(b) shows photos of the deposited particles after they were removed by a fine needle.

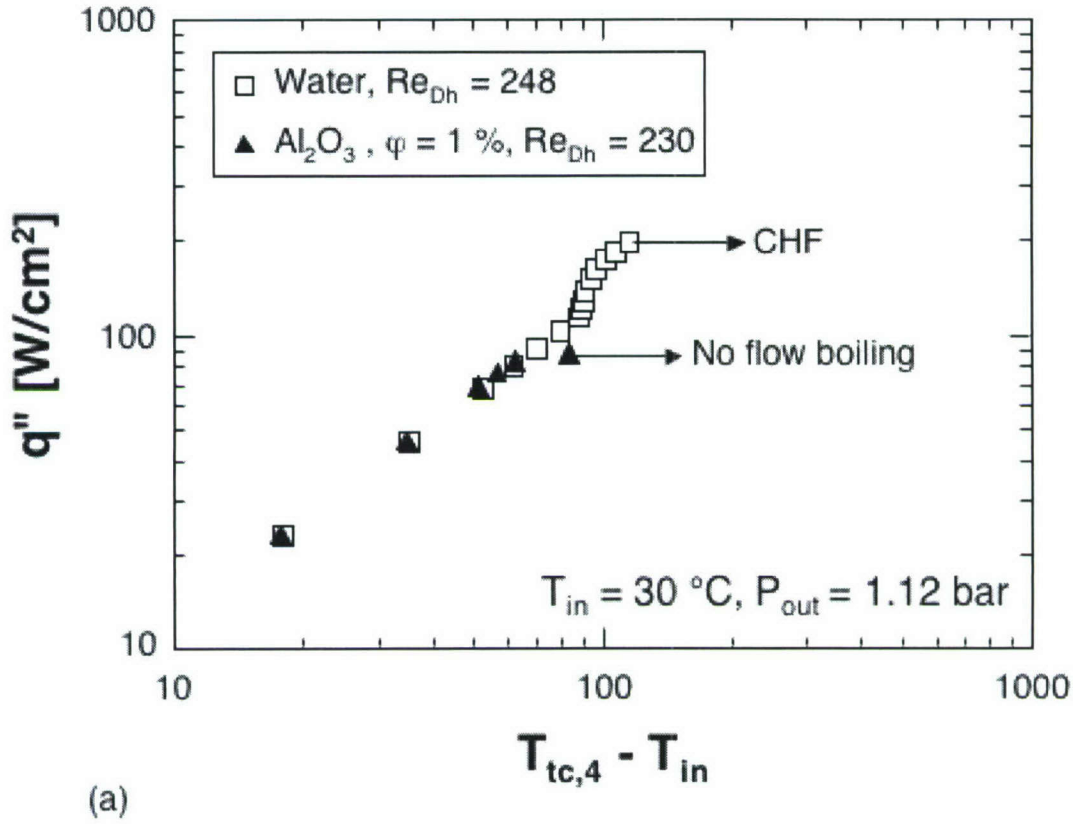

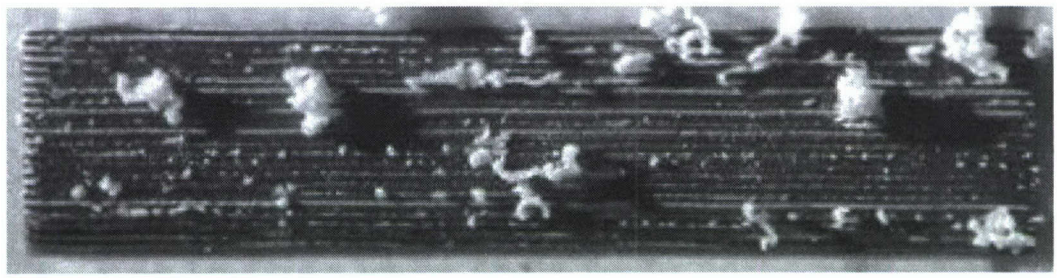

(b)

Figure III.5.1 (a) Flow boiling curve at measurement location tc4 for pure water and 1% Al_2O_3. (b) Photo of particles after being removed from micro-channels.

III.6 CONCLUSIONS

This study is an assessment of the effectiveness of Al_2O_3 nanoparticles at enhancing single-phase and two-phase heat transfer in micro-channel heat sinks. Key conclusions can be summarized as follows:

(1) The high thermal conductivity of nanoparticles relative to common pure fluids enhances the single-phase heat transfer coefficient for fully-developed laminar flow. The enhancement is far weaker for turbulent flow because of a weaker dependence of the heat transfer coefficient on thermal conductivity as well as decreased specific heat and increased viscosity with increased nanoparticle concentration.

(2) Increasing nanoparticle concentration increases single-phase pressure drop appreciably compared to pure fluids at the same Reynolds number.

(3) Higher single-phase heat transfer coefficients are achieved in the entrance region of micro-channels with increased nanoparticle concentration. However, the enhancement is weaker in the fully developed region, proving that nanoparticles have an appreciable effect on thermal boundary layer development. Higher concentrations also produce greater sensitivity to heat flux.

(4) Despite their ability to enhance to the single-phase heat transfer coefficient due to the increased thermal conductivity, the overall cooling effectiveness of nanopartcles is quite miniscule. Simultaneous degradation of the specific heat leads to larger fluid temperature rise along the micro-channel. The net effect of increasing thermal conductivity and decreasing specific heat on wall temperature is virtually nonexistent.

(5) Single-phase cooling performance with nanofluids is quite repeatable over extended durations. However, very long-term use may lead to particle settling and potential clogging of flow passages. This issue must me carefully examined by long term testing

of the entire cooling system, including variations of, or complete stoppage of the coolant flow rate, before deployment. Nanoparticles also cause erosion to metal surfaces and, while this may help maintain surface texture, the removed oxide may ultimately alter the enhancement effect of nanoparticles, accentuate settling, or even clog flow passages.

(6) Nanoparticles should not be used in two-phase micro-channel heat sinks. Once boiling commences, particles begin to deposit into relatively large clusters near the channel exit due to localized evaporation. This clustering phenomenon quickly propagates upstream to fill the entire channel, preventing coolant from entering the heat sink and causing catastrophic failure of the cooling system.

Table III.6.1 summarizes the practical implications from the present study. While this study does demonstrate the effectiveness of nanoparticles at enhancing the single-phase heat transfer coefficient by increasing the nanofluids thermal conductivity, it also shows only a miniscule enhancement in cooling effectiveness compared to the pure fluid, and reveales several important disadvantages. These disadvantages bring into question the overall merit of using nanofluids in micro-channel heat sinks. A far more effective strategy is to simply optimize micro-channel geometry in pursuit of a higher heat transfer coefficient and lower pressure drop using pure fluids [Qu and Mudawar (2005)].

Table III.6.1. Advantages and disadvantages of nanofluids.

Advantages	Disadvantages
- Higher single-phase heat transfer coefficient, especially for laminar flow, due to increased thermal conductivity	- Increased axial rise in wall temperature due to degraded specific heat - Increase pumping power due to greater pressure drop - Long-term fluid settling and potential clogging of flow passages - Possible damage to flow loop parts by erosion - Inability to sustain flow boiling - High cost of nanoparticle suspensions

LIST OF REFERENCES

LIST OF REFERENCES

Bang, I.C. and Chang, S.H., "Boiling heat transfer performance and phenomena of Al_2O_3-water nano-fluids from a plain surface in a pool", Int. J. Heat and Mass Transfer 48 (2005) 2407-2419.

Bergles, A.E. and Dormer, T. Jr., "Subcooled boiling pressure drop with water at low pressure", Int. J. Heat Mass Transfer 12, 459-470, 1969.

Bao, Z.Y., Flectcher, D.F. and Haynes, B.S., "Flow boiling heat transfer of Freon R11 and HCFC123 in narrow passages", Int. J. Heat Mass Transfer 43, pp.3347-3358, 2000.

Beattie, D.R.H. and Whalley, P.B., "A simple two-phase flow frictional pressure drop calculation method", Int. J. Multiphase Flow 8, pp.83-87, 1982.

Bowers, M.B. and Mudawar, I., "High flux boiling in low flow rate, low pressure drop mini-channel and micro-channel heat sinks", Int. J. Heat Mass Transfer 37, pp.321-332, 1994a.

Bowers, M.B. and Mudawar, I., "Two-phase electronic cooling using mini-channel and micro-channel heat sinks: Part 1- Design criteria and heat diffusion constraints", ASME J. Electronic Packaging 116, 290-297, 1994b.

Bowers, M.B. and Mudawar, I., "Two-phase electronic cooling using mini-channel and micro-channel heat sinks: Part 2 – flow rate and pressure drop constraints", ASME J. Electronic Packaging 116, pp.298-305, 1994c.

Chen, J.C., "Correlation for boiling heat transfer to saturated fluids in convective flow", I&EC Process Design Development 5, pp.322-329, 1966.

Chisholm, D., "Pressure gradients due to friction during the flow of evaporation two-phase mixtures in smooth tubes and channels", Int. J. Heat Mass Transfer 16, pp.347-358, 1973.

Choi, S.U.S., "Enhancing thermal conductivity of fluids with nanoparticles", Developments and Applications of Non-Newtonian Flows, ASME, New York, FED-Vol. 231/MD-Vol. 66 (1995) 99-105.

Collier, J.G. and Thome, J.R., "Convective Boiling and Condensation", 3rd ed., Oxford University Press, Oxford, 1994.

Das, S.K., Putra, N. and Roetzel, W., "Pool boiling of nano-fluids on horizontal narrow tubes", Int. J. Multiphase Flow 29 (2003) 1237-1247.

Hall, D. and Mudawar, I., "Critical heat flux (CHF) for water flow in tubes-I. Compilation and assessment of world CHF data", Int. J. Heat Mass Transfer 43, 2573-2604, 2000.

Hall, D. and Mudawar, I., "Critical heat flux (CHF) for water flow in tubes-II. Subcooled CHF correlations", Int. J. Heat Mass Transfer 43, 2605-2640, 2000.

Hoffman, M.A. and Kline, C.T., "Evaluation of several empirical models for predicting subcooled flow-boiling pressure drop", in: V.K. Dhir, J.C. Chen, O.C. Jones (Eds.), Multiphase Flow and Heat Transfer, 23rd National Heat Transfer Conference, ASME HTD-Vol. 47, Denver, Colorado, pp. 151-160, 1985.

Hoffman, M.A. and Wong, C.F., "Prediction of pressure drops in forced convection subcooled boiling water flows", Int. J. Heat Mass Transfer 35, 3291-3299, 1992.

Huo, X., Chen, L., Tian, Y.S. and Karayiannis, T.G., "Flow boiling and flow regimes in small diameter tubes", App. Thermal Engineering 24, pp.1225-1239, 2004.

Incropera, F.P. and Dewitt, D.P., "Fundamentals of Heat and Mass Transfer", 5th ed. Wiley, New York, 2002.

Kandlikar, S.G., "A general correlation for saturated two-phase flow boiling heat transfer inside horizontal and vertical tubes", ASME J. Heat Transfer 112, 219-228, 1990.

Kandlikar, S.G., "Heat transfer characteristics in partial boiling, fully developed boiling, and significant void flow regions of subcooled flow boiling", ASME J. Heat Transfer 120, 395-401, 1998.

Katto, Y., "General features of CHF of forced convection boiling in uniformly heated rectangular channels", Int. J. Heat Mass Transfer 24, 1413-1419, 1981.

Katto, Y. and Ohno, H., "An improved version of the generalized correlation of critical heat flux for the forced convective boiling in uniformly heated vertical tubes", Int. J. Heat Mass Transfer 27, 1641-1648, 1984.

Kawahara, A., Chung, P.M.-Y. and Kawaji, M., "Investigation of two-phase flow pattern, void fraction and pressure drop in a microchannel", Int. J. Multiphase Flow 28, pp.1411-1435, 2002.

Kays, W.K. and Crawford, M.E., "Convective Heat and Mass Transfer", 2nd Ed., McGraw-Hill, New York, pp. 275-280, 1980.

Kew, P.A. and Cornwell, K., "Correlations for the prediction of boiling heat transfer in small-diameter channels", App. Thermal Engineering 17, pp.705-715, 1997.

Keblinkski, P., Phillpot, S.R., Choi, S.U.S. and Eastman, J.A., "Mechanisms of heat flow in suspensions of nano-sized particles (nanofluids)", Int. J. Heat and Mass Transfer 45 (2002) 855-863.

Kirschman, R.K., "Cold electronics: an overview", Cryogenics 25 (1985) 115-122.

Kroeger, P.G., and Zuber, N., "An analysis of the effects of various parameters on the average void fractions in subcooled boiling", Int. J. Heat Mass Transfer 11, 211-213, 1968.

Kureta, M. and Akimoto, H., "Critical heat flux correlation for subcooled boiling flow in narrow channels", Int. J. Heat Mass Transfer 45, 4107-4115, 2002.

Kwon, Y.M. and Chang, S.H., "A mechanistic critical heat flux model for wide range of subcooled and low quality flow boiling", Nuclear Engineering Design 188, 27-47, 1999.

Lazarek, G.M. and Black, S.H., "Evaporative heat transfer, pressure drop and critical heat flux in a small vertical tube with R-113", Int. J. Heat Mass Transfer 25, 945-959, 1982.

Lee, C.H. and Mudawar, I., "A mechanistic critical heat flux model for subcooled flow boiling based on local bulk flow conditions", Int. J. Multiphase Flow 14 (1989) 711-728.

Lee, H.J. and Lee, S.Y., "Pressure drop correlations for two-phase flow within horizontal rectangular channels with small heights", Int. J. Multiphase Flow 27, pp.783-796, 2001.

Lee, H.J. and Lee, S.Y., "Heat transfer correlation for boiling flows in small rectangular horizontal channels with low aspect ratios", Int. J. Multiphase Flow 27, pp.2043-2062, 2001.

Lee, J. and Mudawar, I., "Two-phase flow in high-heat-flux micro-channel heat sink for refrigeration cooling applications: Part I - pressure drop characteristics", Int. J. Heat Mass Transfer 48, 928-940, 2005a.

Lee, J. and Mudawar, I., "Two-phase flow in high-heat-flux micro-channel heat sink for refrigeration cooling applications: Part II – heat transfer characteristics", Int. J. Heat Mass Transfer 48, 941-955, 2005b.

Lee, J. and Mudawar, I., "Implementation of microchannel evaporator for high-heat-flux refrigeration cooling applications", ASME J. Electronic Packaging 128, 30-37, 2006.

Lee, S. and Choi, S.U.S., "Application of metallic nanoparticle suspension in advanced cooling systems", Recent Advances in Solids/Structures and Applications of Metallic Materials, ASME, New York, PVP-Vol. 342/MD-Vol. 72 (1996) 227-234.

Lee,S., Choi, S.U.S, Li,S. and Eastman, J.A., "Measuring thermal conductivity of fluids containing oxide nanoparticles", ASME J. Heat Transfer 121 (1999) 280-289.

Levy, S., "Forced convection subcooled boiling – Prediction of vapor volumetric fraction," Int. J. Heat Mass Transfer 10, 951-965, 1967.

Liao, S-J., "An analytic approximation of the drag coefficient for the viscous flow past a sphere", Int. J. Non-Linear Mech. 37, 1-18, 2002.

Lin, S., Kwok, C.C.K., Li, R.Y., Chen, Z.H. and Chen, Z.Y., "Local frictional pressure drop during vaporization for R-12 through capillary tubes", Int. J. Multiphase Flow 17, pp.95-102, 1991.

Lin, S., Kew, P.A. and Cornwell, K., "Two-phase heat transfer to a refrigerant in a 1 mm diameter tube", Int. J. Refrigeration 24, pp.51-56, 2001.

Liu, Z. and Winterton, R.H.S., "A general correlation for saturated and subcooled flow boiling in tubes and annuli, based on a nucleate pool boiling equation", Int. J. Heat Mass Transfer 34, pp.2759-2766, 1991.

Lockhart, R.W. and Martinelli, R.C., "Proposed correlation of data for isothermal two-phase, two-component flow in pipes", Chemical Engineering Progress 45, pp.39-48, 1949.

Maiga, S.E.B., Nguyen, C.T., Galanis, N. and Roy, G., "Heat transfer behaviours of nanofluids in an uniformly heated tube", Superlattices and Microstructures 35 (2004) 543-557.

Mehendale, S.S. and Jacobi, A.M., "Evaporative heat transfer in mesoscale heat exchangers", ASHRAE Transactions: Symposia, Dallas, TX, pp.445-452, 2000.

Mikic, B.B., Rohsenow, W.M., and Griffith, P., "On bubble growth rates", Int. J. Heat Mass Transfer 13, pp. 657-665, 1970.

Mishima, K. and Hibiki, T., "Some characteristics of air-water two-phase flow in small diameter vertical tubes", Int. J. Multiphase Flow 22, pp.703-712, 1996.

Moles, F.D. and Shaw, J.F.G., "Boiling heat transfer to subcooled liquids under condition of forced convection", Trans. Inst. Chem. Eng. 50, 76-84, 1972.

Mukherjee, S. and Mudawar, I., "Pumpless loop for narrow channel and micro-channel boiling", ASME J. Electronic Packaging 125, pp.431-441, 2003.

Mudawar, I., "Assessment of High-Heat-Flux Thermal Management Schemes," IEEE T. Comp. & Pack. Tech. 24, pp. 122-141, 2001.

Mudawar, I. and Bowers, M.B. "Ultra-high critical heat flux (CHF) for subcooled water flow boiling - I. CHF data and parametric effects for small diameter tubes", Int. J. Heat Mass Transfer 42, 1405-1428, 1999.

Mudawar, I., El-Masri, M.A., Wu, C.S., and Ausman-Mudawar, J.R., "Boiling heat transfer and critical heat flux in high-speed rotating liquid films", Int. J. Heat Mass Transfer 28, 795-806, 1985.

Pak, B.C. and Cho, Y.I., "Hydrodynamic and heat transfer study of dispersed fluids with submicron metallic oxide particles", Exp. Heat transfer 11 (1998) 151-170.

Papell, S.S., "Subcooled boiling heat transfer under forced convection in a heated tube", NASA Technical Note D-1583, Lewis Research Center, Cleveland, OH, 1963.

Peeples, J.W., Little, W., Shcmidt, R., and Nisenoff, M. "Low temperature electronics workshop", Proceedings of 16th Semiconductor Thermal Measurement and Management Symposium, IEEE, San Jose, CA, 2000, pp. 108-109.

Qu, W. and Mudawar, I., "Experimental and numerical study of pressure drop and heat transfer in a single-phase micro-channel heat sink", Int. J. Heat Mass Transfer 45, pp.2549-2565, 2002.

Qu, W. and Mudawar, I., "Measurement and prediction of pressure drop in two-phase micro-channel heat sinks", Int. J. Heat Mass Transfer 46, pp.2737-2753, 2003 (1).

Qu, W. and Mudawar, I., "Flow boiling heat transfer in two-phase micro-channel heat sinks- I. Experimental investigation and assessment of correlation methods", Int. J. Heat Mass Transfer 46, pp.2755-2771, 2003 (2).

Qu, W. and Mudawar, I., "Measurement and correlation of critical heat flux in two-phase micro-channel heat sinks", Int. J. Heat and Mass Transfer 47 (2004) 2045-2059.

Qu, W. and Mudawar, I., "A systematic method for optimal design of two-phase micro-channel heat sinks", ASME J. Electronic Packaging 127 (2005) 381-390.

Ravigururajan, T.S., "Impact of channel geometry on two-phase flow heat transfer characteristics of refrigerants in microchannel heat exchangers", ASME J. Heat Transfer 120, pp.485-491, 1998.

Rouhani, S.Z., "Calculation of steam volume fraction in subcooled boiling", ASME J. Heat Transfer 90, 158-164, 1968.

Saha, P. and Zuber, N., "Point of net vapor generation and vapor void fraction in subcooled boiling", in: Heat Transfer 1974 Vol. 4, Proceedings of the 5th International Heat Transfer Conference, Tokyo, pp. 175-179, 1974.

Schmidt, R., "Low Temperature CMOS Experience at IBM," 16th IEEE SEMI-Therm Symp., San Jose, CA, March 21-23, pp. 112-113, 2000.

Schmidt, R.R. and Notohardjono, B.D., "High-end server low-temperature cooling", IBM J. Res. & Dev. 46 (2002) 739-751.

Shah, M.M., "A new correlation for heat transfer during boiling flow through pipes", ASHRAE Trans. 82, pp.66-86, 1976.

Shah, M.M., "A general correlation for heat transfer during subcooled boiling in pipes and annuli", ASHRAE Transactions 83, 202-217, 1977.

Shah, M.M., "Chart correlation for saturated boiling heat transfer: equation and further study", ASHRAE Trans. 88, pp.185-196, 1982.

Shah, R.K. and London, A.L., "Laminar flow forced convection in Ducts: a source book for compact heat exchanger analytical data", Advances in Heat Transfer, Supplement 1, Academic Press, New York, 1978.

Sturgis, J.C., and Mudawar, I., "Critical heat flux in a long, rectangular channel subjected to one-sided heating – II. Analysis of critical heat flux data", Int. J. Heat Mass Transfer 42, 1849-1862, 1999.

Thome, J.R., "Boiling in microchannels: a review of experiment and theory", Heat and Fluid Flow 25, 128-139, 2004.

Tong, W., Bergles, A.E., and Jensen, M.K. "Pressure drop with highly subcooled flow boiling in small-diameter tubes", Exp. Thermal Fluid Science 15, 202-212,1997.

Tran, T.N., Wambsganss, M.W. and France, D.M., "Small circular- and rectangular-channel boiling with two refrigerants", Int. J. Multiphase Flow 22, pp.485-498, 1996.

Tran, T.N., Chyu, M.-C., Wambsganss, M.W. and France, D.M., "Two-phase pressure drop of refrigerants during flow boiling in small channels: an experimental investigation and correlation development", Int. J. Multiphase Flow 26, pp.1739-1754, 2000.

Triplett, K.A., Ghiaasiaan, S.M., Abdel-Khalik, S.I., LeMouel, A. and McCord, B.N., "Gas-liquid two-phase flow in microchannels Part II: void fraction and pressure drop", Int. J. Multiphase Flow 25, pp.395-410, 1999.

Tuckerman, D.B. and Pease, R.F.W., "High-performance heat sinking for VLSI", IEEE Electron Device Letters 2, 126-129, 1981.

Vassallo, P., Kumar, R. and D'Amico, S. "Pool boiling heat transfer experiments in silica–water nano-fluids", Int. J. Heat and Mass Transfer 47 (2004) 407-411.

Wambsganss, M.W., France, D.M., Jendrzejczyk, J.A. and Tran, T.N., "Boiling heat transfer in a horizontal small-diameter tube", ASME J. Heat Transfer 115, pp.963-972, 1993.

Warrier, G.R., Dhir, V.K. and Momoda, L.A., "Heat transfer and pressure drop in narrow rectangular channels", Exp. Therm. Fluid Science 26, pp.53-64, 2002.

Weisman, J. and Pei, B.S., "Prediction of critical heat flux in flow boiling at low qualities", Int. J. Heat Mass Transfer 26, 1463-1477, 1983.

Wen, D. and Ding, Y., "Experimental investigation into convective heat transfer of nanofluids at the entrance region under laminar flow conditions", Int. J. Heat and Mass Transfer 47 (2004) 5181-5188.

Wen, D.S., Yan, Y. and Kenning, D.B.R., "Saturated flow boiling of water in a narrow channel: time-averaged heat transfer coefficient and correlations", App. Thermal Engineering 24, pp.1207-1223, 2004.

Wojtan, L., Revellin, R. and Thome, J., "Investigation of saturated critical heat flux in a single, uniformly heated micro-channel", Exp. Thermal Fluid Science 30, 765-774, 2006.

Xuan,Y., and Li,Q., "Heat transfer enhancement of nanofluids", Int. J. Heat and Fluid Flow 21 (2000) 58-64.

Xue, Q-Z., "Model for effective thermal conductivity of nanofluids", Physics Letter A 307 (2003) 313-317.

Yan, Y-Y. and Lin, T-F., "Evaporation heat transfer and pressure drop of refrigerant R-134a in a small pipe", Int. J. Heat Mass Transfer 41, pp.4183-4194, 1998.

Yu, W., France, D.M., Wambsganss, M.W. and Hull, J.R., "Two-phase pressure drop, boiling heat transfer, and critical heat flux to water in a small-diameter horizontal tube", Int. J. Multiphase Flow 28, pp.927-941, 2002.

Zhang, M. and Webb, R.L., "Correlation of two-phase friction for refrigerants in small-diameter tubes", Exp. Thermal and Fluid Science 25, pp.131-139, 2001.

Zivi, S.M., "Estimation of steady-state stem void-fraction by means of the principle of minimum entropy production", ASME J. Heat Transfer 86, pp.247-252, 1964.

APPENENDICES

Appendix A – Comparison present study with Qu and Mudawar's (2003).

Table A.1 Comparison of properties of R134a and water and respective experimental parameters.

Fluids		R134a [present study]		Water [Qu and Mudawar (2003)]
Properties		$P_{sat,Low}$ [Pa]	$P_{sat,High}$ [Pa]	P_{sat} [Pa]
		144,750	659,650	115,000
	T_{sat} [C]	-17.99	24.69	103.6
	ρ_f [kg/m^3]	1352.1	1207.9	955.8
	ρ_g [kg/m^3]	7.365	32.07	0.6721
	h_{fg} [kJ/kg]	211.5	178.1	2247.2
	μ_f [kg/m-s]	3.37E-4	1.95E-4	2.72E-4
	μ_g [kg/m-s]	1.02E-5	1.195E-5	1.239E-5
	ν_f [m^2/s]	2.490E-7	1.615E-7	2.842E-7
	ν_g [m^2/s]	13.84E-7	3.727E-7	184.4E-7
	σ [N/m]	0.01421	0.008123	0.05822
	$c_{p,f}$ [J/kg-K]	1297.3	1423.2	4222.1
	k_f [W/m-K]	0.102	0.0834	0.6661
	Pr_f	4.283	3.33	1.722
	Pr_g	0.812	0.844	1.0
Experiment Conditions	q'' [W/cm^2]	15.7 ~ 93.9		18.2 ~ 239.8
	G [kg/m^2-s]	128.16 ~ 656.72		134.9 ~ 402.7
	x_e	0.001 ~ super heat (1.360)		Subcooled ~ 0.255
	d_h [μm]	349		

Appendix B – Direct Refrigeration Cooling Experimental Data

This appendix includes all experimental data obtained in the present study. Nomenclature used in the data tables are as following:

Symbols

A	Direct current ampere applied to the compressor
COM	Compressor
CON	Condenser
DP	Pressure drop
EVA	Evaporator heat sink
G	Mass velocity [kg/m^{2}s]
In	Inlet
Out	Outlet
Q	Total heat transfer rate to the copper heat sink [W]
Q_v	Volumetric flow rate at evaporator inlet [ml/min]
q''	Heat flux through the heat sink base surface [W/cm^2]
$Temp$	Temperature
T_{amb}	Surrounding temperature
T_c	Heat sink block temperature
V	Electric voltage applied to the compressor
x_e	Thermodynamic equilibrium quality

Table B.1 q''=15.70 – 16.01 W/cm^2.

Q	q"	COM Power		Q_v	G	x_e		Temp [C]							Pressure [Pa]			
[W]	[W/cm^2]	V	A	[ml/min]	[kg/m^{2}s]	In	Out	COM In	COM Out	CON Out	EVA In	EVA Out	T_c	T_{amb}	COM Out	CON Out	EVA In	EVA DP
101.1	15.83	12.75	7.000	101.36	235.39	0.1249	0.3803	5.349	25.893	23.384	5.920	5.728	12.080	23.314	6.712E+05	6.611E+05	3.562E+05	3670.2
101.2	15.84	12.70	7.020	91.95	213.64	0.1246	0.4058	5.278	26.295	23.238	5.814	5.642	11.958	23.309	6.794E+05	6.714E+05	3.548E+05	3487.1
101.2	15.84	12.70	6.980	85.72	199.18	0.1255	0.4267	5.164	26.452	23.239	5.678	5.520	11.788	23.364	6.805E+05	6.730E+05	3.527E+05	3332.2
101.8	15.93	12.73	6.970	79.50	184.80	0.1260	0.4521	4.950	26.431	23.097	5.435	5.302	11.556	23.335	6.806E+05	6.738E+05	3.501E+05	3186.1
101.8	15.94	12.70	6.835	70.22	163.38	0.1263	0.4943	4.647	26.414	22.795	5.065	4.990	11.265	23.376	6.799E+05	6.740E+05	3.447E+05	2757.0
102.0	15.96	12.80	6.410	54.98	128.16	0.1314	0.5983	3.253	26.406	22.209	3.597	3.552	9.970	23.355	6.785E+05	6.740E+05	3.285E+05	2287.6
101.3	15.85	12.77	6.490	44.07	102.72	0.1393	0.7149	2.077	26.497	22.252	2.403	2.373	8.864	23.340	6.786E+05	6.750E+05	3.135E+05	2154.0
101.3	15.86	12.88	6.350	38.87	90.63	0.1493	0.7978	0.340	26.353	22.157	0.697	0.656	7.227	23.362	6.783E+05	6.752E+05	2.887E+05	2137.1
102.0	15.96	12.58	5.065	36.40	85.01	0.2231	0.8878	-12.249	28.435	21.655	-12.453	-12.856	-1.245	23.441	6.744E+05	6.720E+05	1.774E+05	2719.2
102.3	16.01	12.55	5.205	33.96	79.33	0.2318	0.9420	-11.869	31.567	21.573	-14.144	-14.562	-1.519	23.437	6.729E+05	6.706E+05	1.675E+05	2785.3
100.9	15.79	12.55	5.190	31.44	73.45	0.2375	0.9910	-11.262	34.784	21.506	-15.260	-15.663	-1.682	23.460	6.724E+05	6.701E+05	1.609E+05	2783.8
100.5	15.73	12.56	5.125	28.79	67.25	0.2434	1.0600	-5.361	37.577	21.484	-16.384	-16.712	-0.766	23.440	6.716E+05	6.695E+05	1.535E+05	2739.3
100.3	15.70	12.59	5.035	25.96	60.66	0.2508	1.1230	3.859	40.682	21.430	-17.824	-7.415	1.344	23.449	6.694E+05	6.674E+05	1.448E+05	2725.0

Table B.2 q''=23.52 – 23.96 W/cm^2.

Q	q"	COM Power		Q_v	G	x_e		Temp [C]							Pressure [Pa]			
[W]	[W/cm^2]	V	A	[ml/min]	[kg/m^{2}s]	In	Out	COM In	COM Out	CON Out	EVA In	EVA Out	T_c	T_{amb}	COM Out	CON Out	EVA In	EVA DP
151.6	23.73	12.68	7.120	117.19	271.60	0.1099	0.4456	8.338	26.695	24.065	8.956	8.767	17.762	23.539	6.889E+05	6.784E+05	3.950E+05	4515.2
151.5	23.72	12.76	6.980	101.48	235.29	0.1129	0.4989	7.774	26.720	23.918	8.351	8.194	17.284	23.573	6.886E+05	6.796E+05	3.871E+05	4043.1
152.0	23.80	12.79	6.810	85.82	199.13	0.1145	0.5707	7.383	26.869	23.691	7.862	7.754	16.965	23.602	6.899E+05	6.825E+05	3.808E+05	3468.4
150.2	23.52	12.90	6.535	70.31	163.36	0.1178	0.6647	6.517	27.227	23.286	6.913	6.862	16.415	23.646	6.979E+05	6.923E+05	3.699E+05	2768.1
151.9	23.78	12.85	6.385	55.10	128.18	0.1362	0.8318	3.181	27.035	22.909	3.643	3.556	14.841	23.693	6.964E+05	6.923E+05	3.291E+05	2441.4
152.3	23.84	12.52	5.505	44.08	102.72	0.2052	1.0370	-7.420	34.845	22.345	-8.451	-8.634	8.851	23.740	6.933E+05	6.903E+05	2.114E+05	3249.4
152.3	23.84	12.46	5.525	41.37	96.42	0.2082	1.0930	-5.358	39.038	22.282	-9.063	-9.252	9.236	23.746	6.905E+05	6.878E+05	2.055E+05	3264.0
153.1	23.96	12.49	5.480	38.89	90.63	0.2145	1.1560	3.516	42.525	22.320	-10.108	-10.176	10.751	23.760	6.892E+05	6.866E+05	1.979E+05	3240.0
151.4	23.70	12.49	5.425	36.47	85.01	0.2201	1.2070	7.387	44.767	22.272	-11.161	-10.089	13.855	23.747	6.890E+05	6.865E+05	1.905E+05	3256.0
151.6	23.73	12.57	5.360	34.03	79.33	0.2244	1.2660	16.405	49.552	22.241	-11.967	-3.590	27.186	23.765	6.888E+05	6.864E+05	1.839E+05	3278.1
152.4	23.86	12.59	5.270	31.51	73.45	0.2292	1.3480	19.479	50.387	22.235	-12.836	4.124	38.658	23.766	6.873E+05	6.850E+05	1.772E+05	3287.5

Table B.3 q''=31.47 – 31.78 W/cm^2.

Q	q"	COM Power		Q_v	G	x_e		Temp [C]							Pressure [Pa]			
[W]	[W/cm^2]	V	A	[ml/min]	[kg/m^{2}s]	In	Out	COM In	COM Out	CON Out	EVA In	EVA Out	T_c	T_{amb}	COM Out	CON Out	EVA In	EVA DP
201.0	31.47	12.77	6.930	148.53	343.81	0.0952	0.4516	10.748	27.026	24.448	11.556	11.213	21.997	23.632	6.954E+05	6.821E+05	4.306E+05	7007.6
202.4	31.69	12.76	6.900	132.92	307.79	0.0969	0.4965	10.456	27.204	24.343	11.204	10.909	21.796	23.636	6.989E+05	6.870E+05	4.255E+05	6271.2
203.0	31.78	12.81	6.760	117.25	271.54	0.1002	0.5529	10.022	27.304	24.306	10.683	10.449	21.585	23.692	6.992E+05	6.887E+05	4.182E+05	5536.2
202.6	31.72	12.77	6.670	101.59	235.20	0.1022	0.6229	9.976	27.776	24.415	10.503	10.346	21.729	23.720	7.075E+05	6.987E+05	4.156E+05	4690.6
202.6	31.72	12.87	6.505	85.89	199.08	0.1049	0.7174	9.273	27.719	24.047	9.702	9.612	21.679	23.733	7.067E+05	6.996E+05	4.058E+05	3893.3
201.8	31.59	12.51	6.300	70.34	163.35	0.1164	0.8523	6.903	27.768	23.481	7.343	7.275	21.830	23.759	7.045E+05	6.993E+05	3.739E+05	3071.1
201.9	31.61	12.54	5.595	55.03	128.16	0.1853	1.0800	3.276	33.966	22.518	-4.814	-4.756	20.164	23.779	6.973E+05	6.937E+05	2.409E+05	3871.8

Table B.4 q''=39.03 – 39.50 W/cm^2.

Q	q"	COM Power		Q_v	G	x_e		Temp [C]							Pressure [Pa]			
[W]	[W/cm^2]	V	A	[ml/min]	[kg/m^{2}s]	In	Out	COM In	COM Out	CON Out	EVA In	EVA Out	T_c	T_{amb}	COM Out	CON Out	EVA In	EVA DP
250.2	39.17	12.75	7.045	179.41	414.92	0.0783	0.4509	13.334	27.377	24.727	14.298	13.843	26.185	23.352	7.057E+05	6.889E+05	4.691E+05	9466.3
251.5	39.38	12.68	6.880	164.06	379.50	0.0805	0.4886	13.025	27.377	24.660	13.915	13.510	26.096	23.408	7.043E+05	6.890E+05	4.647E+05	8626.2
250.9	39.27	12.72	6.725	148.57	343.77	0.0832	0.5311	12.621	27.430	24.579	13.436	13.090	25.718	23.457	7.053E+05	6.916E+05	4.579E+05	7703.8
251.0	39.29	12.72	6.680	132.99	307.73	0.0857	0.5849	12.327	27.650	24.578	13.076	12.785	25.587	23.535	7.082E+05	6.961E+05	4.525E+05	6925.0
250.8	39.27	12.76	6.645	117.38	271.42	0.0886	0.6531	12.311	28.282	24.822	12.935	12.731	26.023	23.566	7.223E+05	7.119E+05	4.515E+05	5942.5
250.3	39.18	12.80	6.565	101.68	235.13	0.0913	0.7399	12.033	28.481	24.812	12.523	12.388	26.398	23.628	7.233E+05	7.145E+05	4.446E+05	4988.1
249.3	39.03	12.88	6.330	86.00	199.02	0.0978	0.8568	10.914	28.565	24.565	11.306	11.240	27.558	23.680	7.232E+05	7.160E+05	4.291E+05	4043.1
252.3	39.50	12.46	5.885	70.41	163.33	0.1625	1.0580	0.319	40.949	23.846	0.516	0.540	27.243	23.791	7.214E+05	7.164E+05	2.940E+05	4496.6
251.1	39.30	12.50	5.825	58.19	135.17	0.1748	1.2360	21.345	48.643	23.382	-2.035	0.356	56.096	23.867	7.150E+05	7.111E+05	2.667E+05	4505.9

Table B.5 q''=46.87 – 47.19 W/cm^2.

Q	q"	COM Power		Q_v	G	x_e		Temp [C]							Pressure [Pa]			
[W]	[W/cm^2]	V	A	[ml/min]	[kg/m^{2}s]	In	Out	COM In	COM Out	CON Out	EVA In	EVA Out	T_c	T_{amb}	COM Out	CON Out	EVA In	EVA DP
299.4	46.87	12.55	6.740	209.37	485.32	0.0589	0.4441	15.048	26.569	23.987	16.218	15.606	29.528	21.942	6.893E+05	6.681E+05	4.985E+05	12364.8
300.0	46.96	12.60	6.600	194.24	450.53	0.0606	0.4750	14.670	26.582	23.790	15.765	15.215	29.270	21.975	6.875E+05	6.682E+05	4.921E+05	11394.5
301.4	47.19	12.63	6.515	178.99	415.44	0.0627	0.5124	14.234	26.504	23.584	15.257	14.769	28.928	22.025	6.856E+05	6.680E+05	4.848E+05	10481.2
301.3	47.16	12.61	6.585	163.69	379.95	0.0637	0.5542	14.145	26.559	23.563	15.097	14.670	28.979	22.028	6.860E+05	6.698E+05	4.814E+05	9595.9
300.5	47.05	12.59	6.475	148.22	344.17	0.0668	0.6049	13.695	26.515	23.448	14.555	14.202	28.440	22.058	6.849E+05	6.703E+05	4.732E+05	8677.1
301.2	47.16	12.63	6.330	132.64	308.10	0.0699	0.6702	13.242	26.536	23.326	13.995	13.728	28.634	22.087	6.843E+05	6.717E+05	4.660E+05	7479.3
300.7	47.07	12.70	6.115	116.96	271.82	0.0719	0.7493	12.947	26.505	23.193	13.545	13.345	29.047	22.100	6.823E+05	6.714E+05	4.593E+05	6328.8
300.2	47.00	12.77	5.885	101.29	235.44	0.0754	0.8538	12.498	26.555	23.108	12.970	12.851	30.252	22.166	6.816E+05	6.723E+05	4.505E+05	5208.2
301.0	47.12	12.53	5.570	85.62	199.24	0.0876	1.0010	10.233	26.088	22.785	10.872	10.669	37.305	22.228	6.809E+05	6.741E+05	4.207E+05	4099.5
301.2	47.16	12.49	5.715	76.26	177.70	0.1322	1.1270	3.470	37.173	22.346	3.628	3.533	34.794	22.260	6.782E+05	6.724E+05	3.281E+05	4927.4

Table B.6 q″=54.59 – 55.09 W/cm^2.

Q	q"	COM Power		Q_v	G	x_e		Temp [C]							Pressure [Pa]			
[W]	[W/cm^2]	V	A	[ml/min]	[kg/m^{2}s]	In	Out	COM In	COM Out	CON Out	EVA In	EVA Out	T_c	T_{amb}	COM Out	CON Out	EVA In	EVA DP
350.3	54.84	12.41	6.725	239.36	554.20	0.043	0.443	17.479	27.255	24.360	18.763	18.063	33.749	22.263	7.058E+05	6.807E+05	5.407E+05	14664.5
351.4	55.02	12.53	6.570	224.50	519.74	0.047	0.473	17.110	27.307	24.397	18.335	17.685	33.620	22.300	7.054E+05	6.824E+05	5.344E+05	13617.0
350.3	54.84	12.53	6.520	209.48	485.18	0.048	0.502	16.805	27.209	24.261	17.969	17.369	33.306	22.299	7.043E+05	6.826E+05	5.284E+05	12901.0
349.4	54.70	12.50	6.600	194.41	450.30	0.050	0.536	16.652	27.245	24.247	17.728	17.194	33.077	22.348	7.029E+05	6.831E+05	5.245E+05	11822.8
350.0	54.80	12.54	6.535	179.19	415.20	0.052	0.579	16.362	27.260	24.135	17.342	16.890	32.895	22.371	7.018E+05	6.837E+05	5.168E+05	10821.2
349.3	54.69	12.61	6.355	163.86	379.74	0.055	0.628	15.877	27.227	24.080	16.793	16.392	32.708	22.386	7.008E+05	6.842E+05	5.086E+05	9866.1
348.7	54.59	12.65	6.195	148.36	344.01	0.058	0.687	15.494	27.186	23.922	16.296	15.983	32.689	22.423	6.993E+05	6.846E+05	5.016E+05	8778.7
349.1	54.66	12.72	5.980	132.77	307.96	0.060	0.762	15.257	27.158	23.822	15.923	15.698	32.955	22.457	6.962E+05	6.834E+05	4.953E+05	7484.2
352.1	55.13	12.78	5.785	117.11	271.68	0.062	0.863	14.997	27.231	23.771	15.520	15.379	34.866	22.471	6.956E+05	6.844E+05	4.885E+05	6188.8
351.4	55.02	12.71	5.610	101.39	235.36	0.068	0.985	14.105	27.108	23.549	14.540	14.425	38.427	22.491	6.931E+05	6.838E+05	4.744E+05	4982.1
351.9	55.09	12.63	5.760	85.66	199.22	0.117	1.166	11.021	36.195	22.962	6.667	6.474	46.296	22.470	6.901E+05	6.834E+05	3.698E+05	5548.2

Table B.7 q''=62.43 – 62.86 W/cm^2.

Q	q"	COM Power		Q_v	G	x_e		Temp [C]							Pressure [Pa]			
[W]	[W/cm^2]	V	A	[ml/min]	[kg/m^{2}s]	In	Out	COM In	COM Out	CON Out	EVA In	EVA Out	T_c	T_{amb}	COM Out	CON Out	EVA In	EVA DP
400.1	62.63	12.59	6.980	268.94	622.59	0.0301	0.4407	19.101	27.286	24.414	20.551	19.731	36.979	22.012	7.087E+05	6.792E+05	5.711E+05	17457.0
399.5	62.54	12.56	7.065	254.25	588.35	0.0314	0.4646	19.125	27.356	24.538	20.508	19.740	36.969	22.060	7.080E+05	6.801E+05	5.698E+05	16583.6
399.3	62.51	12.61	6.760	239.37	554.18	0.0346	0.4923	18.611	27.282	24.385	19.934	19.223	36.576	22.057	7.068E+05	6.807E+05	5.602E+05	15648.5
400.4	62.68	12.70	6.580	224.50	519.74	0.0373	0.5251	18.330	27.329	24.400	19.578	18.936	36.519	22.070	7.067E+05	6.826E+05	5.557E+05	14609.5
400.0	62.62	12.74	6.455	209.49	485.17	0.0392	0.5598	18.015	27.309	24.278	19.203	18.607	36.435	22.109	7.054E+05	6.828E+05	5.495E+05	13668.4
399.1	62.48	12.73	6.360	194.42	450.29	0.0413	0.5996	17.829	27.346	24.282	18.931	18.403	36.041	22.114	7.032E+05	6.824E+05	5.428E+05	12611.2
401.1	62.80	12.79	6.235	179.17	415.22	0.0423	0.6491	17.575	27.264	24.091	18.588	18.136	36.113	22.144	7.021E+05	6.830E+05	5.375E+05	11461.9
401.0	62.78	12.82	6.130	163.80	379.81	0.0441	0.7054	17.256	27.200	23.922	18.170	17.790	36.367	22.146	7.002E+05	6.830E+05	5.318E+05	10227.9
401.5	62.86	12.51	5.965	148.33	344.04	0.0447	0.7744	17.222	27.207	23.821	17.992	17.692	36.869	22.137	6.983E+05	6.830E+05	5.279E+05	9004.8
400.6	62.72	12.65	5.660	132.73	308.00	0.0481	0.8584	16.758	27.188	23.669	17.367	17.178	38.076	22.138	6.955E+05	6.822E+05	5.181E+05	7466.7
399.8	62.59	12.72	5.490	117.03	271.76	0.0523	0.9649	16.029	27.055	23.440	16.550	16.388	41.514	22.139	6.934E+05	6.821E+05	5.069E+05	6279.9
400.3	62.67	12.44	5.550	104.44	242.70	0.0736	1.0820	12.552	26.644	23.231	13.346	13.031	48.707	22.105	6.924E+05	6.834E+05	4.550E+05	5685.9
398.8	62.43	12.38	5.765	91.84	213.71	0.1030	1.2210	20.919	33.316	22.774	8.565	8.290	66.232	22.117	6.822E+05	6.751E+05	3.895E+05	6089.6

Table B.8 q''=70.34 – 70.83 W/cm^2.

Q	q"	COM Power		Q_v	G	x_e		Temp [C]							Pressure [Pa]			
[W]	[W/cm^2]	V	A	[ml/min]	[kg/m^{2}s]	In	Out	COM In	COM Out	CON Out	EVA In	EVA Out	T_c	T_{amb}	COM Out	CON Out	EVA In	EVA DP
452.4	70.83	12.44	6.640	283.55	656.72	0.0161	0.4599	20.686	27.239	24.265	22.216	21.333	40.003	21.299	7.102E+05	6.775E+05	6.027E+05	20112.6
449.3	70.34	12.48	6.570	268.81	622.77	0.0175	0.4812	20.451	27.348	24.177	21.948	21.094	39.707	21.390	7.129E+05	6.820E+05	5.975E+05	19051.9
451.3	70.65	12.49	6.600	254.13	588.53	0.0206	0.5120	20.261	27.483	24.295	21.682	20.884	39.852	21.474	7.130E+05	6.840E+05	5.936E+05	17957.0
451.5	70.68	12.51	6.370	239.35	554.21	0.0234	0.5439	20.028	27.482	24.347	21.364	20.651	39.780	21.507	7.128E+05	6.854E+05	5.869E+05	16804.1
452.2	70.80	12.58	6.215	224.45	519.80	0.0256	0.5798	19.763	27.553	24.300	21.020	20.375	39.702	21.576	7.105E+05	6.849E+05	5.802E+05	15654.2
451.9	70.74	12.46	6.045	209.40	485.28	0.0269	0.6183	19.448	27.397	24.083	20.628	20.049	39.532	21.608	7.072E+05	6.833E+05	5.732E+05	14563.1
451.7	70.71	12.49	6.015	194.27	450.48	0.0280	0.6631	19.225	27.303	23.900	20.299	19.800	39.526	21.663	7.049E+05	6.830E+05	5.676E+05	13212.1
451.5	70.68	12.49	5.875	179.09	415.31	0.0303	0.7172	18.981	27.287	23.878	19.977	19.537	39.676	21.664	7.032E+05	6.832E+05	5.620E+05	11975.5
451.3	70.66	12.64	5.615	163.75	379.88	0.0315	0.7805	18.876	27.236	23.756	19.689	19.353	40.260	21.680	7.018E+05	6.840E+05	5.579E+05	10457.3
451.0	70.61	12.63	5.480	148.30	344.08	0.0335	0.8581	18.684	27.308	23.721	19.39f3	19.139	41.322	21.716	7.008E+05	6.848E+05	5.520E+05	9128.8
450.7	70.55	12.69	5.325	132.71	308.02	0.0372	0.9545	18.205	27.249	23.604	18.771	18.577	43.879	21.724	6.998E+05	6.858E+05	5.431E+05	7722.5
450.6	70.55	12.68	5.130	118.64	275.35	0.0422	1.0650	17.394	26.900	23.645	18.140	17.833	52.570	21.810	6.995E+05	6.881E+05	5.320E+05	5882.4
451.5	70.68	12.47	5.850	102.84	239.09	0.0824	1.2300	24.049	41.166	23.085	11.931	11.701	70.324	21.818	6.919E+05	6.831E+05	4.356E+05	6592.7

Table B.9 q''=78.17 – 78.70 W/cm^2.

Q	q"	COM Power		Q_v	G	x_e		Temp [C]							Pressure [Pa]			
[W]	[W/cm^2]	V	A	[ml/min]	[kg/m^{2}s]	In	Out	COM In	COM Out	CON Out	EVA In	EVA Out	T_c	T_{amb}	COM Out	CON Out	EVA In	EVA DP
500.9	78.41	12.69	6.515	283.60	656.64	0.0082	0.5020	21.738	27.525	24.374	23.331	22.387	42.821	21.376	7.174E+05	6.830E+05	6.225E+05	21233.8
501.5	78.52	12.64	6.425	268.87	622.68	0.0093	0.5292	21.632	27.627	24.300	23.116	22.277	42.718	21.406	7.164E+05	6.841E+05	6.192E+05	20205.4
499.3	78.17	12.74	6.280	254.07	588.61	0.0105	0.5567	21.446	27.574	24.191	22.856	22.091	42.488	21.423	7.154E+05	6.848E+05	6.142E+05	19060.7
502.5	78.67	12.45	6.180	239.28	554.30	0.0122	0.5944	21.367	27.589	24.222	22.675	21.999	42.799	21.490	7.164E+05	6.877E+05	6.131E+05	17822.0
502.7	78.70	12.56	6.080	224.40	519.86	0.0134	0.6332	21.289	27.618	24.200	22.504	21.902	42.810	21.508	7.126E+05	6.858E+05	6.064E+05	16412.5
502.6	78.68	12.55	6.015	209.41	485.27	0.0149	0.6771	21.074	27.585	24.098	22.206	21.669	42.977	21.527	7.115E+05	6.864E+05	6.012E+05	15047.6
501.1	78.45	12.59	5.940	194.31	450.44	0.0170	0.7265	20.776	27.537	24.005	21.835	21.354	42.998	21.535	7.091E+05	6.861E+05	5.941E+05	13542.8
500.1	78.29	12.64	5.800	179.09	415.33	0.0189	0.7847	20.534	27.418	23.861	21.454	21.044	43.145	21.545	7.057E+05	6.850E+05	5.874E+05	12038.0
501.8	78.56	12.75	5.500	163.75	379.87	0.0202	0.8588	20.375	27.467	23.772	21.188	20.847	44.051	21.551	7.035E+05	6.847E+05	5.811E+05	10458.1
502.2	78.62	12.83	5.235	148.25	344.13	0.0226	0.9462	20.025	27.353	23.579	20.676	20.399	47.783	21.521	7.033E+05	6.864E+05	5.757E+05	8898.3
501.8	78.56	12.86	4.955	132.66	308.08	0.0266	1.0540	19.399	27.152	23.427	20.005	19.757	53.361	21.536	6.987E+05	6.846E+05	5.623E+05	7146.9
500.4	78.34	12.63	5.680	116.96	271.82	0.0548	1.1940	17.341	28.717	23.200	15.961	15.571	65.161	21.575	6.965E+05	6.852E+05	4.929E+05	7069.7

Table B.10 q''=86.09 – 86.32 W/cm^2.

Q	q"	COM Power		Q_v	G	x_e		Temp [C]							Pressure [Pa]			
[W]	[W/cm^2]	V	A	[ml/min]	[kg/m^{2}s]	In	Out	COM In	COM Out	CON Out	EVA In	EVA Out	T_c	T_{amb}	COM Out	CON Out	EVA In	EVA DP
551.4	86.32	12.44	6.150	254.65	587.79	0.0028	0.6128	23.611	28.768	25.370	25.021	24.237	46.737	21.769	7.410E+05	7.094E+05	6.545E+05	19162.4
551.2	86.30	12.40	6.085	239.87	553.49	0.0050	0.6512	23.565	28.838	25.465	24.850	24.166	46.660	21.819	7.392E+05	7.092E+05	6.490E+05	18065.6
550.0	86.10	12.38	5.995	224.94	519.13	0.0079	0.6929	23.292	28.843	25.407	24.417	23.871	46.698	21.852	7.380E+05	7.101E+05	6.420E+05	16507.2
551.0	86.27	12.43	5.900	209.88	484.64	0.0094	0.7426	22.995	28.778	25.242	24.056	23.556	46.933	21.853	7.378E+05	7.119E+05	6.371E+05	15178.1
550.1	86.12	12.45	5.760	194.74	449.87	0.0106	0.7976	22.846	28.760	25.127	23.796	23.342	47.302	21.975	7.403E+05	7.166E+05	6.338E+05	13814.8
550.5	86.18	12.55	5.525	179.59	414.69	0.0130	0.8661	22.756	28.895	25.247	23.611	23.211	48.189	22.035	7.369E+05	7.154E+05	6.272E+05	11981.0
550.0	86.11	12.72	5.235	164.21	379.31	0.0151	0.9448	22.588	28.959	25.157	23.264	22.944	51.952	22.058	7.365E+05	7.172E+05	6.207E+05	10090.1
549.9	86.09	12.71	5.045	148.69	343.63	0.0179	1.0410	22.122	28.808	25.002	22.731	22.440	56.767	22.137	7.348E+05	7.175E+05	6.113E+05	8615.8
551.0	86.26	12.49	5.755	133.06	307.65	0.0375	1.1670	19.097	30.264	24.859	20.038	19.604	68.174	22.219	7.373E+05	7.231E+05	5.689E+05	7659.0

Table B.11 q''=93.75 – 93.94 W/cm^2.

Q	q"	COM Power		Q_v	G	x_e		Temp [C]							Pressure [Pa]			
[W]	[W/cm^2]	V	A	[ml/min]	[kg/m^{2}s]	In	Out	COM In	COM Out	CON Out	EVA In	EVA Out	T_c	T_{amb}	COM Out	CON Out	EVA In	EVA DP
598.8	93.75	12.67	5.455	194.86	449.72	0.0012	0.8643	24.407	29.302	25.422	25.270	24.869	51.747	22.319	7.459E+05	7.213E+05	6.596E+05	13431.8
599.9	93.91	12.81	5.215	179.57	414.71	0.0020	0.9382	24.053	29.003	25.221	24.969	24.459	54.742	22.229	7.390E+05	7.161E+05	6.507E+05	12059.1
600.0	93.94	12.69	4.765	164.21	379.31	0.0047	1.0250	23.886	28.908	25.151	24.559	24.245	60.069	22.210	7.358E+05	7.153E+05	6.448E+05	10248.8

Appendix C – Indirect Refrigeration Cooling Experimental Data

This appendix includes all experimental data obtained in the present study. Nomenclature used in the data tables are as following:

Symbols

D_h	Channel hydraulic diameter
DP	Pressure drop
$\dot{m}$	Total mass flow rate to test section
P_{in}	Channel inlet pressure
P_{out}	Channel outlet pressure
q''_c	Heat flux through the heat sink base surface [W/cm^2]
q''	Heat loss compensated base heat flux [W/cm^2]
$h_{1,2,3}$	Reduced heat transfer coefficients [W/m^2.K]
T_{in}	Channel inlet temperature
T_{out}	Channel outlet temperature
T_{sat}	Saturated temperature
$T_{tc,1,2,3}$	Thermocouple temperature reading
$T_{w,1,2,3}$	Calculated wall temperatures
TS	Test Section
Q	Total heat transfer rate to the copper heat sink [W]

Table C.1 Test data, TS#1, Tin = 0 °C, m = 2.0 g/s.

- Test Section : 1
- D_h : 175.7 [μm]
- Number of Channels : 24
- Mass flow rate : 2.0 [g/s]
- T_{in} : 0 [°C]
- P_{out} : 16.5 [psia]
- T_{sat} (@ P_{out}) : 63.59 [°C]

Measurement data

No	T_{tc1} [°C]	T_{tc2} [°C]	T_{tc3} [°C]	T_{in} [°C]	T_{out} [°C]	P_{in} [psia]	P_{out} [psia]	Q [W]	$\dot{m}$ [g/s]
1	0.1473	0.0842	0.0496	-0.0766	0.2684	19.2307	16.5038	**-0.0125**	2.0009
2	26.1107	26.3999	26.5078	-0.1256	5.5995	18.8934	16.5067	**20.2194**	2.0009
3	50.3435	51.6182	52.2555	0.2487	11.2586	18.6444	16.5121	**39.4442**	2.0009
4	75.6755	76.6654	77.1851	-0.3306	15.0863	18.4771	16.5280	**60.7468**	2.0009
5	88.3635	89.8897	90.7368	0.0115	21.0421	18.4553	16.5179	**78.3760**	2.0008
6	97.7525	99.9211	101.1682	-0.2676	26.7867	18.6466	16.5607	**99.9737**	2.0009
7	105.7212	108.1399	109.7667	-0.4029	31.8289	18.8186	16.5488	**119.6504**	2.0010
8	112.8943	115.5949	117.5498	0.0213	38.9370	18.8414	16.4531	**140.7919**	2.0010
9	119.1716	122.2678	124.4650	0.0402	43.8230	19.0500	16.4463	**159.5940**	1.9995
10	*125.6432*	*128.8189*	*131.0246*	*-5.4428*	*47.0075*	*20.4302*	*16.9311*	***170.5692***	*2.0431*

Reduced Data

No	DP [Pa]	q''_e [W/cm^2]	q" [W/cm^2]	q"/q''_e	h_1 [W/m^2 K]	h_2 [W/m^2 K]	h_3 [W/m^2 K]	T_{w1} [°C]	T_{w2} [°C]	T_{w3} [°C]
1	18801.6		0.0							
2	16456.0	40.4	**34.280**	84.8%	**5071.1**	**4995.7**	**4968.1**	22.00	22.30	22.40
3	14702.0	78.9	**66.056**	83.7%	**5139.4**	**4965.8**	**4883.3**	42.40	43.70	44.30
4	13438.5	121.5	**101.645**	83.7%	**5174.5**	**5084.3**	**5038.2**	63.50	64.40	65.00
5	13358.2	156.8	**133.980**	85.5%	**6210.2**	**6059.4**	**5978.8**	72.20	73.70	74.60
6	14381.8	199.9	**175.205**	87.6%	**7930.8**	**7666.3**	**7522.1**	76.60	78.70	80.00
7	15649.6	239.3	**213.160**	89.1%	**9538.7**	**9189.4**	**8968.6**	79.90	82.30	84.00
8	16466.3	281.6	**254.495**	90.4%	**11725.4**	**11235**	**10905**	82.10	84.70	86.70
9	17952.1	319.2	**291.105**	91.2%	**13592.5**	**12937.1**	**12509.1**	83.90	86.90	89.10
10										

Table C.2 Test data, TS#1, Tin = 0 °C, m = 3.0 g/s.

- Test Section : 1
- D_h : 175.7 [μm]
- Number of Channels : 24
- Mass flow rate : 3.0 [g/s]
- T_{in} : 0 [°C]
- P_{out} : 16.5 [psia]
- T_{sat} (@ P_{out}) : 63.59 [°C]

Measurement data									
No	T_{tc1} [°C]	T_{tc2} [°C]	T_{tc3} [°C]	T_{in} [°C]	T_{out} [°C]	P_{in} [psia]	P_{out} [psia]	Q [W]	$\dot{m}$ [g/s]
1	0.1820	0.1211	0.0758	-0.1515	-0.1484	20.4486	16.5219	**-0.0174**	3.0036
2	24.3945	24.6130	24.6953	-0.3032	3.7384	20.1656	16.5201	**20.7347**	3.0036
3	47.4851	47.9895	48.2355	-0.1689	7.5825	19.9457	16.5157	**40.5177**	3.0036
4	69.7015	70.4805	70.8789	0.0886	11.3565	19.6604	16.4834	**60.2703**	3.0036
5	86.5060	87.5880	88.1612	-0.0778	15.0044	19.6354	16.5733	**78.9117**	3.0036
6	99.2566	100.9011	101.8349	-0.0620	18.4564	19.7760	16.5608	**101.4538**	3.0036
7	105.6107	107.8295	109.2778	0.1901	21.6346	19.8988	16.5055	**118.9736**	3.0038
8	117.8787	121.2407	123.6738	0.1347	29.8339	20.4982	16.5224	**160.7535**	3.0039
9	130.1949	134.4001	137.9901	0.0085	37.6711	21.3343	16.5491	**199.8370**	3.0039
10	137.5055	142.2625	146.6475	0.0465	40.3977	22.0454	16.6007	**222.1887**	3.0030
11	144.4101	149.5842	154.4091	-0.1292	42.7080	23.4670	16.4542	**240.7670**	3.0041
12	151.1684	156.7523	162.1289	-0.2941	50.2580	24.3895	16.5202	**261.5952**	3.0040
13	154.5731	160.5200	166.4072	0.0519	53.4147	24.0446	16.5530	**277.6440**	3.0041

Reduced Data										
No	DP [Pa]	q''_e [W/cm^2]	q" [W/cm^2]	q''/q''_e	h_1 [W/m^2 K]	h_2 [W/m^2 K]	h_3 [W/m^2 K]	T_{w1} [°C]	T_{w2} [°C]	T_{w3} [°C]
1	27073.9		0.0							
2	25134.3	41.5	**35.593**	85.8%	**5511.9**	**5446.9**	**5422.8**	20.16	20.38	20.46
3	23648.9	81.0	**68.780**	84.9%	**5525**	**5447.2**	**5410.1**	39.26	39.76	40.01
4	21904.6	120.5	**102.165**	84.8%	**5644.1**	**5559.9**	**5517.7**	57.43	58.21	58.61
5	21112.5	157.8	**134.920**	85.5%	**6143.7**	**6039**	**5985**	70.25	71.33	71.90
6	22168.2	202.9	**176.850**	87.2%	**7374.3**	**7200.8**	**7105.8**	77.89	79.53	80.46
7	23396.2	237.9	**210.520**	88.5%	**8728.1**	**8454.9**	**8285.7**	80.14	82.35	83.79
8	27411.9	321.5	**291.945**	90.8%	**12487.5**	**11888.4**	**11489.6**	82.47	85.81	88.22
9	32992.9	399.7	**367.700**	92.0%	**16009.7**	**15045.3**	**14309.4**	85.49	89.66	93.22
10	37540.1	444.4	**410.885**	92.5%	**17774.1**	**16580.9**	**15614.6**	87.49	92.20	96.55
11	48351.6	481.5	**446.480**	92.7%	**18943.2**	**17593.7**	**16497.7**	89.99	95.11	99.89
12	54257.4	523.2	**487.310**	93.1%	**21367**	**19684.8**	**18297.6**	91.70	97.23	102.54
13	51653.2	555.3	**518.985**	93.5%	**23629**	**21590.3**	**19891.2**	91.20	97.08	102.90

Table C.3 Test data, TS#1, Tin = 0 °C, m = 4.0 g/s.

- Test Section : 1
- D_h : 175.7 [μm]
- Number of Channels : 24
- Mass flow rate : 4.0 [g/s]
- T_{in} : 0 [°C]
- P_{out} : 16.5 [psia]
- T_{sat} (@ P_{out}) : 63.59 [°C]

Measurement data									
No	T_{tc1} [°C]	T_{tc2} [°C]	T_{tc3} [°C]	T_{in} [°C]	T_{out} [°C]	P_{in} [psia]	P_{out} [psia]	Q [W]	$\dot{m}$ [g/s]
1	1.0307	0.9759	0.9204	-0.1728	-0.0531	21.5454	16.5050	**0.0787**	4.0034
2	21.8196	22.0018	22.0673	-0.0448	2.5200	21.2946	16.5082	**19.9291**	4.0063
3	43.2828	43.7214	43.8372	-0.0814	5.5566	21.1390	16.5127	**39.5355**	4.0065
4	64.9969	65.7895	66.2188	-0.0206	8.5037	20.9401	16.4910	**60.8993**	4.0061
5	82.8474	83.8828	84.6696	0.3570	11.1879	20.7408	16.4779	**78.9909**	4.0033
6	97.0832	98.5850	99.5885	0.3339	14.3368	20.7518	16.4849	**99.5911**	4.0052
7	105.9673	108.0396	109.5658	0.1650	17.5791	20.9952	16.5258	**120.6460**	4.0063
8	117.6143	121.0280	123.8698	0.0086	23.3391	21.6661	16.5189	**160.7570**	4.0062
9	128.7521	133.2218	137.2568	0.1229	29.1252	22.3530	16.4819	**199.0826**	4.0049
10	141.3524	146.7559	151.9027	-0.0324	33.8167	23.5053	16.4899	**238.4407**	4.0037
11	154.0875	160.2468	166.4825	-0.0753	40.0185	24.6984	16.4647	**281.6510**	4.0064

Reduced Data										
No	DP [Pa]	q''_e [W/cm^2]	q" [W/cm^2]	q''/q''_e	h_1 [W/m^2 K]	h_2 [W/m^2 K]	h_3 [W/m^2 K]	T_{w1} [°C]	T_{w2} [°C]	T_{w3} [°C]
1	34752.6		0.0							
2	33001.0	39.9	**34.659**	87.0%	**6017.6**	**5951.2**	**5927.7**	17.70	17.90	17.90
3	31896.6	79.1	**67.888**	85.9%	**5982**	**5901.6**	**5880.7**	35.20	35.60	35.70
4	30675.4	121.8	**104.510**	85.8%	**6197.1**	**6096.3**	**6043**	52.50	53.20	53.70
5	29392.0	158.0	**135.760**	85.9%	**6393.8**	**6285.9**	**6206.3**	66.50	67.50	68.30
6	29419.6	199.2	**173.195**	87.0%	**7205.4**	**7050.6**	**6950.8**	76.20	77.70	78.70
7	30815.6	241.3	**213.100**	88.3%	**8575**	**8331.1**	**8160.1**	80.20	82.20	83.80
8	35488.7	321.5	**291.060**	90.5%	**11882.8**	**11329.5**	**10906.7**	82.30	85.70	88.50
9	40479.7	398.2	**365.485**	91.8%	**15197.7**	**14269.1**	**13523.2**	84.30	88.80	92.80
10	48369.7	476.9	**441.305**	92.5%	**18173.1**	**16861.9**	**15777.6**	87.60	92.90	98.00
11	56769.4	563.3	**525.455**	93.3%	**21992.8**	**20178.7**	**18623.4**	89.90	96.00	102.20

Table C.4 Test data, TS#1, Tin = 0 °C, m = 5.0 g/s.

- Test Section : 1
- D_h : 175.7 [μm]
- Number of Channels : 24
- Mass flow rate : 5.0 [g/s]
- T_{in} : 0 [°C]
- P_{out} : 16.5 [psia]
- T_{sat} (@ P_{out}) : 63.59 [°C]

Measurement data									
No	T_{tc1} [°C]	T_{tc2} [°C]	T_{tc3} [°C]	T_{in} [°C]	T_{out} [°C]	P_{in} [psia]	P_{out} [psia]	Q [W]	$\dot{m}$ [g/s]
1	0.5671	0.5035	0.4391	-0.2078	-0.1922	23.1126	16.4888	**0.0835**	5.0040
2	20.2456	20.4314	20.4963	-0.1038	1.8617	22.8585	16.5062	**19.7482**	5.0090
3	40.5089	40.9553	41.0804	-0.1794	4.3686	22.6609	16.4910	**39.9351**	5.0090
4	61.6591	62.4223	62.8635	0.2703	6.9689	22.1075	16.5132	**59.3879**	5.0091
5	80.4361	81.3729	82.0611	0.3073	9.5889	22.0164	16.4790	**79.0508**	5.0090
6	96.6426	97.9706	98.8395	-0.1590	11.4709	22.0442	16.4873	**101.0655**	5.0090
7	105.7321	107.4710	108.7136	-0.2923	13.7381	22.1830	16.5019	**119.0780**	5.0058
8	119.0181	122.0522	124.6699	0.1669	18.0896	23.0570	16.4983	**159.5676**	5.0090
9	131.5436	135.8756	139.7797	0.2829	22.7434	24.0026	16.5132	**203.0768**	5.0091
10	142.5415	147.8610	152.9151	-0.0976	27.7668	24.9475	16.4918	**239.6060**	5.0091
11	153.8438	160.1197	166.5450	-0.1876	32.5040	26.0227	16.5354	**279.6714**	5.0089

Reduced Data										
No	DP [Pa]	q''_e [W/cm^2]	q'' [W/cm^2]	q''/q''_e	h_1 [W/m^2 K]	h_2 [W/m^2 K]	h_3 [W/m^2 K]	T_{w1} [°C]	T_{w2} [°C]	T_{w3} [°C]
1	45669.4		0.0							
2	43797.4	39.5	**34.694**	87.8%	**6509.5**	**6430.5**	**6403.3**	16.12	16.31	16.37
3	42539.8	79.9	**69.391**	86.9%	**6588.3**	**6491.3**	**6464.7**	32.22	32.67	32.79
4	38570.8	118.8	**102.350**	86.2%	**6395.6**	**6290**	**6230.5**	49.39	50.15	50.59
5	38179.3	158.1	**136.455**	86.3%	**6609.5**	**6505.7**	**6431.4**	64.01	64.95	65.63
6	38313.3	202.1	**175.975**	87.1%	**7226.3**	**7090.4**	**7004.2**	75.39	76.71	77.58
7	39170.1	238.2	**209.650**	88.0%	**8163.9**	**7974.3**	**7844.1**	80.37	82.10	83.33
8	45220.8	319.1	**287.585**	90.1%	**11044.4**	**10611.1**	**10263.7**	84.13	87.14	89.74
9	51638.1	406.2	**371.850**	91.6%	**14389.7**	**13592.1**	**12945.4**	86.32	90.62	94.49
10	58300.3	479.2	**442.510**	92.3%	**17201.9**	**16042.5**	**15077.1**	88.62	93.89	98.90
11	65412.6	559.3	**520.365**	93.0%	**20502.9**	**18875**	**17455.9**	90.31	96.52	102.87

Table C.5 Test data, TS#1, Tin = 0 °C, m = 10.0 g/s.

• Test Section	:	1	• Mass flow rate	:	10.0 [g/s]
• D_h	:	175.7 [μm]	• T_{in}	:	0 [°C]
• Number of Channels	:	24	• P_{out}	:	16.5 [psia]
			• T_{sat} (@ P_{out})	:	63.59 [°C]

Measurement data									
No	T_{tc1} [°C]	T_{tc2} [°C]	T_{tc3} [°C]	T_{in} [°C]	T_{out} [°C]	P_{in} [psia]	P_{out} [psia]	Q [W]	$\dot{m}$ [g/s]
1	0.8149	0.7577	0.7011	-0.0910	-0.2701	32.8350	16.4846	**-0.0131**	9.9765
2	32.1087	32.5610	32.6821	-0.1534	1.8600	32.3065	16.5069	**40.0214**	9.9893
3	65.0633	66.1521	66.9648	-0.0150	4.5579	32.0209	16.5384	**80.3939**	9.9755
4	94.0275	95.6171	96.7067	0.1869	7.1359	32.3438	16.4972	**122.5141**	9.9779
5	116.2606	118.4997	120.2963	0.1010	7.9291	32.6632	16.5027	**159.6846**	9.9944
6	131.3704	135.0176	138.3000	0.0642	9.8019	33.8192	16.4835	**201.2990**	9.9916
7	142.7222	147.5558	152.0209	0.0399	11.5945	35.2491	16.4846	**240.2592**	9.9748
8	152.9201	159.0868	165.3987	0.0528	14.3125	36.1011	16.5079	**280.3009**	9.9748
9	157.8048	164.4822	171.7583	-0.2484	15.2307	36.6280	16.5090	**299.0118**	9.9764

Reduced Data										
No	DP [Pa]	q''_e [W/cm^2]	q" [W/cm^2]	q''/q''_e	h_1 [W/m^2 K]	h_2 [W/m^2 K]	h_3 [W/m^2 K]	T_{w1} [°C]	T_{w2} [°C]	T_{w3} [°C]
1	112732.7		0.0							
2	108934.9	80.0	**71.870**	89.8%	**9095.4**	**8915.5**	**8868.5**	23.54	23.99	24.11
3	106748.1	160.8	**143.260**	89.1%	**9020.0**	**8807.6**	**8655.4**	47.87	48.96	49.77
4	109258.4	245.0	**219.460**	89.6%	**9877.8**	**9635.8**	**9476.6**	67.54	69.12	70.20
5	111422.8	319.4	**287.500**	90.0%	**10695.0**	**10391.7**	**10160.5**	81.40	83.63	85.41
6	119525.4	402.6	**366.635**	91.1%	**12939.1**	**12381.1**	**11918.5**	86.79	90.41	93.66
7	129376.8	480.5	**441.785**	91.9%	**15420.0**	**14561.4**	**13849.1**	88.89	93.68	98.10
8	135090.2	560.6	**519.390**	92.6%	**18372.9**	**17073.7**	**15921.4**	89.52	95.61	101.85
9	138715.5	598.0	**555.545**	92.9%	**19665.3**	**18168.6**	**16777.2**	89.93	96.53	103.71

Table C.6 Test data, TS#1, Tin = -30 °C, m = 2.0 g/s.

- Test Section : 1
- D_h : 175.7 [μm]
- Number of Channels : 24
- Mass flow rate : 2.0 [g/s]
- T_{in} : -30 [°C]
- P_{out} : 16.5 [psia]
- T_{sat} (@ P_{out}) : 63.59 [°C]

Measurement data

No	T_{tc1} [°C]	T_{tc2} [°C]	T_{tc3} [°C]	T_{in} [°C]	T_{out} [°C]	P_{in} [psia]	P_{out} [psia]	Q [W]	$\dot{m}$ [g/s]
1	-30.9220	-30.9641	-30.9716	-29.7068	-29.8150	21.0250	16.5112	**-0.0085**	2.0010
2	-5.3073	-5.1164	-5.0492	-29.7581	-24.7665	20.4299	16.5013	**20.7624**	2.0009
3	18.4313	18.8620	18.9795	-30.2710	-20.7972	19.9951	16.5136	**40.5325**	2.0008
4	44.1359	44.7862	44.9471	-29.7779	-15.6685	19.5060	16.4742	**60.8255**	2.0009
5	66.7721	67.5233	67.9299	-29.6772	-10.6460	19.2740	16.5166	**80.5694**	2.0010
6	85.5364	86.5842	87.3795	-30.3501	-6.4441	19.2303	16.5001	**101.3583**	2.0009
7	99.8295	101.2993	102.2814	-29.6253	-3.3407	19.1260	16.5270	**118.9941**	2.0010
8	116.1058	118.6403	120.7603	-29.4250	7.0255	19.3878	16.5656	**160.7355**	2.0011
9	129.3876	132.9101	136.0452	-27.9672	16.0463	19.6556	16.5354	**200.3304**	2.0012
10	135.6229	139.6044	142.9290	-26.8142	23.5138	19.9430	16.5488	**218.3158**	2.0012
11	144.8761	149.5182	153.7472	-25.5577	31.8082	21.2106	16.5720	**239.1286**	2.0013
12	149.4052	153.9377	158.1887	-24.7110	38.4755	21.7500	16.5788	**252.0907**	2.0013
13	148.9977	154.2228	159.1702	-24.0973	43.9683	21.5023	16.5815	**258.9866**	2.0013
14	152.9333	158.3890	163.6036	-23.6047	49.8755	21.4807	16.5464	**270.6988**	2.0013
15	*159.7982*	*165.3246*	*170.7806*	*-23.2584*	*51.3414*	*20.6876*	*16.5807*	***283.4470***	*2.0081*

Reduced Data

No	DP [Pa]	q''_e [W/cm^2]	q" [W/cm^2]	q''/q''_e	h_1 [W/m^2 K]	h_2 [W/m^2 K]	h_3 [W/m^2 K]	T_{w1} [°C]	T_{w2} [°C]	T_{w3} [°C]
1	31121.7		0.0							
2	27086.8	41.5	**37.200**	89.6%	**6051.8**	**5986.3**	**5963.5**	-9.70	-9.50	-9.40
3	24004.5	81.1	**70.149**	86.5%	**5623.0**	**5555.5**	**5537.3**	10.10	10.50	10.60
4	20903.8	121.7	**103.785**	85.3%	**5442.3**	**5377.7**	**5361.9**	31.70	32.40	32.50
5	19011.1	161.1	**137.175**	85.1%	**5560.1**	**5501.2**	**5469.8**	50.30	51.10	51.50
6	18823.9	202.7	**173.700**	85.7%	**5981.2**	**5906.3**	**5850.7**	64.60	65.70	66.40
7	17919.8	238.0	**205.150**	86.2%	**6411.1**	**6309.3**	**6243.0**	75.00	76.50	77.50
8	19458.5	321.5	**285.370**	88.8%	**8836.8**	**8600.2**	**8411.8**	81.50	84.00	86.10
9	21513.1	400.7	**362.345**	90.4%	**11438.5**	**11009.8**	**10654.4**	85.30	88.80	91.90
10	23402.1	436.6	**397.830**	91.1%	**12933.2**	**12372.8**	**11940.9**	87.20	91.20	94.50
11	31982.1	478.3	**438.040**	91.6%	**14352.6**	**13628.0**	**13028.9**	91.50	96.10	100.30
12	35654.4	504.2	**463.955**	92.0%	**15663.0**	**14868.3**	**14192.9**	92.80	97.30	101.50
13	33928.0	518.0	**478.700**	92.4%	**17254.5**	**16189.8**	**15296.2**	90.60	95.80	100.70
14	34020.6	541.4	**501.935**	92.7%	**18623.6**	**17394.9**	**16363.0**	91.70	97.10	102.20
15										

Table C.7 Test data, TS#1, Tin = -30 °C, m = 3.0 g/s.

- Test Section : 1
- D_h : 175.7 [μm]
- Number of Channels : 24
- Mass flow rate : 3.0 [g/s]
- T_{in} : -30 [°C]
- P_{out} : 16.5 [psia]
- T_{sat} (@ P_{out}) : 63.59 [°C]

Measurement data									
No	T_{tc1} [°C]	T_{tc2} [°C]	T_{tc3} [°C]	T_{in} [°C]	T_{out} [°C]	P_{in} [psia]	P_{out} [psia]	Q [W]	$\dot{m}$ [g/s]
1	-29.9294	-29.9883	-30.0480	-30.0829	-30.4925	21.7757	16.4903	**-0.0673**	3.0036
2	-6.8466	-6.6708	-6.6076	-30.2058	-27.4232	21.3181	16.4812	**20.2397**	3.0036
3	14.6593	15.0670	15.1787	-30.0662	-24.3649	20.9771	16.5125	**40.5514**	3.0029
4	36.9702	37.6457	37.8131	-29.8051	-20.5424	20.6799	16.4894	**60.3043**	3.0037
5	59.4014	60.3872	61.0761	-29.8022	-16.9297	20.4539	16.5074	**80.0553**	3.0036
6	79.8538	81.2865	82.2153	-29.6749	-12.6358	20.2693	16.5172	**100.3416**	3.0038
7	96.3615	98.1403	99.3828	-29.9556	-8.5115	20.1937	16.5173	**122.3118**	3.0038
8	114.1377	117.0409	119.5148	-29.6220	-2.7956	20.3886	16.4947	**159.7309**	3.0037
9	126.0016	130.2165	133.7677	-29.7554	1.7938	20.8256	16.5057	**201.2237**	3.0038
10	138.2410	143.4419	148.2723	-29.8718	7.3224	21.4008	16.4934	**242.4521**	3.0039
11	150.4532	156.4848	162.3101	-28.8887	15.2496	21.9672	16.5633	**281.3318**	3.0040
12	156.2397	162.8605	169.4304	-28.4270	20.0396	22.1117	16.5570	**303.8353**	3.0041

Reduced Data										
No	DP [Pa]	q''_e [W/cm^2]	q" [W/cm^2]	q''/q''_e	h_1 [W/m^2 K]	h_2 [W/m^2 K]	h_3 [W/m^2 K]	T_{w1} [°C]	T_{w2} [°C]	T_{w3} [°C]
1	36442.0		0.0							
2	33349.6	40.5	**36.265**	89.6%	**5856.3**	**5798.2**	**5777.6**	-11.12	-10.95	-10.88
3	30782.4	81.1	**70.928**	87.5%	**6058.7**	**5985.3**	**5965.5**	6.24	6.65	6.76
4	28893.0	120.6	**104.300**	86.5%	**5997.9**	**5917.0**	**5897.3**	24.53	25.20	25.37
5	27210.5	160.1	**137.520**	85.9%	**5929.1**	**5841.7**	**5782.2**	42.92	43.90	44.59
6	25869.7	200.7	**172.430**	85.9%	**6142.2**	**6033.9**	**5965.8**	59.10	60.53	61.45
7	25348.0	244.6	**212.070**	86.7%	**6743.8**	**6612.4**	**6523.7**	70.75	72.52	73.76
8	26846.9	319.5	**282.485**	88.4%	**8432.4**	**8183.8**	**7983.2**	79.90	82.79	85.24
9	29784.6	402.4	**362.845**	90.2%	**10895.7**	**10433.4**	**10073.2**	81.92	86.10	89.63
10	33835.7	484.9	**442.885**	91.3%	**13392.9**	**12695.1**	**12109.1**	84.32	89.47	94.25
11	37258.5	562.7	**518.425**	92.1%	**16003.6**	**15027.4**	**14191.4**	87.20	93.16	98.92
12	38298.1	607.7	**562.640**	92.6%	**17854.7**	**16636.6**	**15581.8**	87.52	94.06	100.54

Table C.8 Test data, TS#1, Tin = -30 °C, m = 4.0 g/s.

- Test Section : 1
- D_h : 175.7 [μm]
- Number of Channels : 24
- Mass flow rate : 4.0 [g/s]
- T_{in} : -30 [°C]
- P_{out} : 16.5 [psia]
- T_{sat} (@ P_{out}) : 63.59 [°C]

Measurement data									
No	T_{tc1} [°C]	T_{tc2} [°C]	T_{tc3} [°C]	T_{in} [°C]	T_{out} [°C]	P_{in} [psia]	P_{out} [psia]	Q [W]	$\dot{m}$ [g/s]
1	-29.4480	-29.5009	-29.5546	-29.8917	-30.2309	23.6934	16.5129	**-0.0673**	4.0063
2	-7.4967	-7.3245	-7.2643	-29.9162	-28.1164	23.1620	16.5227	**20.3094**	4.0062
3	11.9456	12.3428	12.4403	-30.2856	-25.7403	22.8078	16.5330	**40.0723**	4.0049
4	35.6725	36.3746	36.5608	-30.2169	-21.9106	22.4024	16.5193	**61.1152**	4.0065
5	56.4250	57.4090	58.1400	-30.0089	-18.5274	22.0823	16.5142	**80.7301**	4.0066
6	73.7069	74.9604	75.8409	-30.1929	-16.4213	22.0179	16.5234	**100.3776**	4.0063
7	92.2763	93.8201	94.8970	-29.6824	-14.1644	21.7365	16.4860	**120.7046**	4.0064
8	111.9634	114.5537	116.7200	-30.1369	-10.1497	21.9304	16.5001	**160.5473**	4.0064
9	126.8058	130.7242	134.0792	-29.7943	-1.5171	22.2843	16.4806	**201.7393**	4.0073
10	138.5985	143.6518	148.3293	-29.7909	4.7026	22.7965	16.5076	**239.7473**	4.0065
11	150.7396	156.8154	162.8120	-29.8023	8.2644	23.2444	16.4778	**280.2705**	4.0064
12	156.1167	162.6936	169.4273	-29.4893	9.4022	23.5504	16.4847	**299.5782**	4.0064

Reduced Data										
No	DP [Pa]	q''_e [W/cm^2]	q" [W/cm^2]	q''/q''_e	h_1 [W/m^2 K]	h_2 [W/m^2 K]	h_3 [W/m^2 K]	T_{w1} [°C]	T_{w2} [°C]	T_{w3} [°C]
1	49507.6		0.0							
2	45775.9	40.6	**36.561**	90.0%	**6071.5**	**6010.9**	**5990.0**	-11.80	-11.60	-11.60
3	43263.2	80.1	**70.600**	88.1%	**6390.9**	**6311.0**	**6291.7**	3.60	4.00	4.10
4	40562.8	122.2	**106.120**	86.8%	**6181.6**	**6093.8**	**6070.9**	23.00	23.70	23.90
5	38390.7	161.5	**139.570**	86.4%	**6237.6**	**6142.6**	**6073.8**	39.70	40.70	41.40
6	37883.1	200.8	**174.030**	86.7%	**6542.1**	**6435.5**	**6362.7**	52.80	54.00	54.90
7	36201.0	241.4	**209.465**	86.8%	**6740.2**	**6624.7**	**6546.4**	67.00	68.50	69.60
8	37441.1	321.1	**283.810**	88.4%	**8330.6**	**8114.3**	**7941.9**	77.60	80.20	82.30
9	40015.1	403.5	**363.215**	90.0%	**10633.4**	**10222.8**	**9895.6**	82.70	86.60	89.90
10	43360.7	479.5	**436.790**	91.1%	**12879.7**	**12242.0**	**11705.6**	85.40	90.40	95.10
11	46654.1	560.5	**515.180**	91.9%	**15137.6**	**14250.0**	**13470.5**	87.90	93.90	99.80
12	48716.3	599.2	**552.525**	92.2%	**16257.5**	**15230.2**	**14304.7**	88.60	95.10	101.80

Table C.9 Test data, TS#1, Tin = -30 °C, m = 5.0 g/s.

- Test Section : 1
- D_h : 175.7 [μm]
- Number of Channels : 24
- Mass flow rate : 5.0 [g/s]
- T_{in} : -30 [°C]
- P_{out} : 16.5 [psia]
- T_{sat} (@ P_{out}) : 63.59 [°C]

Measurement data									
No	T_{tc1} [°C]	T_{tc2} [°C]	T_{tc3} [°C]	T_{in} [°C]	T_{out} [°C]	P_{in} [psia]	P_{out} [psia]	Q [W]	$\dot{m}$ [g/s]
1	-28.9044	-28.9529	-29.0021	-30.1055	-29.6336	25.6017	16.4962	**-0.0672**	5.0061
2	-8.4244	-8.2439	-8.1790	-29.8743	-27.8458	25.0539	16.4837	**20.3071**	5.0088
3	9.7653	10.1643	10.2690	-29.7422	-25.9082	24.6693	16.5082	**40.0704**	5.0089
4	31.9324	32.6325	32.8112	-30.1291	-23.0105	24.2030	16.5067	**61.0158**	5.0056
5	52.3047	53.3061	54.0570	-29.7770	-20.2798	23.9349	16.5155	**81.2408**	5.0130
6	68.1758	69.5521	70.5328	-29.8005	-19.2581	23.7608	16.5028	**99.8503**	5.0091
7	86.0490	87.5146	88.5423	-29.5876	-17.6965	23.5543	16.4738	**120.1415**	5.0091
8	110.9292	113.3083	115.2481	-29.7528	-14.1417	23.6563	16.5097	**160.2447**	5.0090
9	125.8125	129.4971	132.5905	-30.0904	-9.0045	23.9776	16.5361	**200.3490**	5.0111
10	138.3801	143.2792	147.7025	-29.8348	-2.4591	24.4237	16.4898	**239.5251**	5.0090
11	151.0998	157.1505	163.1132	-29.6460	-3.1822	25.0382	16.5148	**281.4875**	5.0092
12	157.5588	164.2627	171.1849	-29.8022	-0.0648	25.3745	16.4828	**304.6870**	5.0091

Reduced Data										
No	DP [Pa]	q''_e [W/cm^2]	q" [W/cm^2]	q''/q''_e	h_1 [W/m^2 K]	h_2 [W/m^2 K]	h_3 [W/m^2 K]	T_{w1} [°C]	T_{w2} [°C]	T_{w3} [°C]
1	62780.7		0.0							
2	59089.7	40.6	**36.894**	90.8%	**6558.8**	**6485.4**	**6459.4**	-12.77	-12.59	-12.53
3	56269.0	80.1	**71.336**	89.0%	**7006.8**	**6911.4**	**6886.8**	1.31	1.71	1.82
4	53064.0	122.0	**106.960**	87.6%	**6688.3**	**6586.7**	**6561.3**	19.18	19.88	20.06
5	51154.8	162.5	**141.685**	87.2%	**6714.4**	**6604.2**	**6523.8**	35.35	36.35	37.09
6	50041.8	199.7	**174.305**	87.3%	**6950.9**	**6819.3**	**6728.6**	47.25	48.62	49.59
7	48818.3	240.3	**209.770**	87.3%	**7114.9**	**6992.8**	**6909.7**	60.77	62.23	63.25
8	49274.5	320.5	**283.100**	88.3%	**8235.8**	**8040.7**	**7888.4**	76.64	79.01	80.93
9	51307.6	400.7	**359.705**	89.8%	**10178.3**	**9819.9**	**9537.8**	82.12	85.77	88.84
10	54702.5	479.1	**435.510**	90.9%	**12384.6**	**11809.4**	**11334.2**	85.36	90.21	94.59
11	58766.8	563.0	**515.910**	91.6%	**14283.6**	**13494.8**	**12798.4**	88.14	94.13	100.02
12	61305.9	609.4	**560.955**	92.1%	**15652.5**	**14694.5**	**13821.1**	89.03	95.65	102.48

Table C.10 Test data, TS#2, Tin = 0 °C, m = 2.0 g/s.

- Test Section : 2
- D_h : 200.0 [μm]
- Number of Channels : 24
- Mass flow rate : 2.0 [g/s]
- T_{in} : 0 [°C]
- P_{out} : 16.5 [psia]
- T_{sat} (@ P_{out}) : 63.59 [°C]

Measurement data									
No	T_{tc1} [°C]	T_{tc2} [°C]	T_{tc3} [°C]	T_{in} [°C]	T_{out} [°C]	P_{in} [psia]	P_{out} [psia]	Q [W]	$\dot{m}$ [g/s]
1	-0.2298	-0.3106	-0.2533	-0.1136	0.8261	17.4438	16.5026	**0.0166**	2.0009
2	23.6603	23.7834	24.3360	0.1072	5.3275	17.3367	16.4797	**20.2474**	2.0011
3	46.7920	47.1040	48.1753	0.2584	10.0213	17.3078	16.5153	**40.5637**	2.0011
4	68.3668	68.8497	70.4351	-0.0580	14.8265	17.2287	16.5006	**60.2879**	2.0012
5	82.4749	82.7381	85.4796	0.1272	19.8305	17.2834	16.5503	**79.4960**	2.0013
6	90.9457	90.9860	95.2712	-0.0552	21.8457	17.3405	16.5117	**101.0356**	2.0006
7	98.9253	99.0358	104.1623	-0.0468	27.6387	17.5327	16.5245	**120.3123**	2.0012
8	107.3531	107.4699	113.5197	0.1083	33.6233	17.7847	16.5029	**139.8735**	1.9966
9	115.5328	115.6031	122.7017	-0.2145	39.0941	18.1554	16.4988	**160.6621**	2.0012
10	119.5477	119.5983	127.2576	-0.1345	42.9863	18.4812	16.5169	**170.7606**	1.9930
11	*124.1332*	*123.9752*	*132.2385*	*-0.1715*	*46.8302*	*18.8067*	*16.5398*	***182.2537***	*2.0012*

Reduced Data										
No	DP [Pa]	q''_e [W/cm^2]	q" [W/cm^2]	q''/q''_e	h_1 [W/m^2 K]	h_2 [W/m^2 K]	h_3 [W/m^2 K]	T_{w1} [°C]	T_{w2} [°C]	T_{w3} [°C]
1	6489.5		0.0							
2	5908.7	40.5	**31.822**	78.6%	**3295.5**	**3271.9**	**3170.1**	20.10	20.20	20.70
3	5464.4	81.1	**62.897**	77.5%	**3274.1**	**3244.4**	**3146.1**	39.60	39.90	41.00
4	5020.1	120.6	**93.484**	77.5%	**3338.6**	**3306.4**	**3205.0**	57.70	58.10	59.70
5	5054.9	159.0	**126.960**	79.9%	**3947.8**	**3929.7**	**3750.2**	67.90	68.20	70.90
6	5713.9	202.1	**167.240**	82.8%	**4977.2**	**4973.8**	**4640.5**	71.70	71.80	76.00
7	6951.8	240.6	**204.220**	84.9%	**6030.3**	**6019.2**	**5547.3**	75.40	75.50	80.60
8	8837.7	279.7	**241.690**	86.4%	**7057.8**	**7044.3**	**6408.8**	79.50	79.60	85.60
9	11422.0	321.3	**281.555**	87.6%	**8140.4**	**8131.1**	**7291.5**	83.00	83.10	90.10
10	13543.0	341.5	**301.235**	88.2%	**8773.1**	**8765.9**	**7791.0**	84.70	84.80	92.40
11										

Table C.11 Test data, TS#2, Tin = 0 °C, m = 3.0 g/s.

- Test Section : 2
- D_h : 200.0 [μm]
- Number of Channels : 24
- Mass flow rate : 3.0 [g/s]
- T_{in} : 0 [°C]
- P_{out} : 16.5 [psia]
- T_{sat} (@ P_{out}) : 63.59 [°C]

Measurement data									
No	T_{tc1} [°C]	T_{tc2} [°C]	T_{tc3} [°C]	T_{in} [°C]	T_{out} [°C]	P_{in} [psia]	P_{out} [psia]	Q [W]	$\dot{m}$ [g/s]
1	0.4369	0.3695	0.4194	0.1373	0.6395	17.9620	16.5036	**0.0930**	3.0039
2	21.7845	21.8931	22.4978	-0.0518	3.3572	17.8945	16.5164	**20.3121**	3.0037
3	42.4267	42.7066	43.8502	-0.0727	6.8061	17.7869	16.4880	**40.0968**	3.0038
4	62.6214	63.0905	64.8019	-0.0101	9.5853	17.7626	16.4983	**60.9427**	3.0038
5	79.9677	80.5987	82.8122	-0.0992	13.4641	17.7290	16.4765	**80.1524**	3.0178
6	89.5581	89.8003	93.7325	0.1928	17.1968	17.8258	16.5092	**101.5420**	3.0038
7	97.4127	97.5041	102.7803	0.1829	20.8506	17.9197	16.5116	**121.8371**	3.0038
8	109.1301	109.2400	116.4676	-0.1780	25.3037	18.2562	16.4822	**159.0226**	2.9970
9	123.2437	123.1101	132.7207	-0.0611	33.8201	19.1308	16.5244	**201.0199**	3.0037
10	126.3504	126.5168	136.8118	-0.2992	38.1556	19.3904	16.5766	**215.2380**	3.0039
11	*132.4827*	*132.6500*	*143.8001*	*-6.0313*	*41.0466*	*20.1180*	*16.7436*	***232.3970***	*3.0019*

Reduced Data										
No	DP [Pa]	q''_e [W/cm^2]	q" [W/cm^2]	q''/q''_e	h_1 [W/m^2 K]	h_2 [W/m^2 K]	h_3 [W/m^2 K]	T_{w1} [°C]	T_{w2} [°C]	T_{w3} [°C]
1	10055.0		0.0							
2	9501.6	40.6	**32.396**	79.7%	**3537.1**	**3513.6**	**3388.0**	18.10	18.20	18.80
3	8955.6	80.2	**63.344**	79.0%	**3575.5**	**3543.9**	**3420.2**	35.20	35.50	36.60
4	8716.6	121.9	**96.516**	79.2%	**3710.0**	**3672.6**	**3542.4**	51.60	52.10	53.80
5	8635.4	160.3	**128.000**	79.8%	**3933.9**	**3891.3**	**3749.0**	65.30	65.90	68.10
6	9077.3	203.1	**167.940**	82.7%	**4937.1**	**4917.4**	**4617.8**	70.20	70.50	74.40
7	9708.8	243.7	**206.530**	84.8%	**5950.5**	**5941.7**	**5473.9**	73.60	73.70	79.00
8	12231.2	318.0	**278.045**	87.4%	**7915.3**	**7901.4**	**7084.0**	77.00	77.10	84.30
9	17970.2	402.0	**359.405**	89.4%	**10300.3**	**10322.5**	**8938.7**	81.60	81.50	91.00
10	19400.4	430.5	**387.985**	90.1%	**11593.6**	**11561.4**	**9864.9**	81.40	81.60	91.80
11										

Table C.12 Test data, TS#2, Tin = 0 °C, m = 4.0 g/s.

• Test Section	:	2	• Mass flow rate	:	4.0 [g/s]
• D_h	:	200.0 [μm]	• T_{in}	:	0 [°C]
• Number of Channels	:	24	• P_{out}	:	16.5 [psia]
			• T_{sat} (@ P_{out})	:	63.59 [°C]

Measurement data									
No	T_{tc1} [°C]	T_{tc2} [°C]	T_{tc3} [°C]	T_{in} [°C]	T_{out} [°C]	P_{in} [psia]	P_{out} [psia]	Q [W]	$\dot{m}$ [g/s]
1	0.2763	0.2139	0.2587	-0.0264	0.0163	19.0994	16.4993	**0.0652**	4.0025
2	19.3681	19.4722	20.0829	0.0247	2.7297	18.8949	16.4835	**20.2866**	4.0040
3	38.2656	38.5545	39.7379	-0.2669	5.1708	18.8125	16.5113	**40.6034**	4.0065
4	56.2396	56.7170	58.4825	0.0844	8.2411	18.7084	16.4863	**60.8931**	4.0086
5	73.0800	73.7046	76.0146	0.2257	10.8537	18.6102	16.4825	**79.9545**	4.0065
6	89.7785	90.5587	93.5230	0.0511	14.9744	18.5991	16.5196	**101.0835**	4.0025
7	97.7678	98.3123	102.6576	-0.0175	17.6818	18.6358	16.5017	**120.1431**	4.0057
8	110.1687	110.2033	117.5393	-0.0093	24.2835	18.9078	16.4628	**160.1802**	4.0041
9	121.0121	121.3219	131.0156	-0.0941	29.4580	19.3624	16.5030	**200.8320**	4.0066
10	132.0786	132.5217	144.4862	0.1325	36.5521	19.9974	16.5026	**239.8663**	4.0066
11	144.6807	145.2696	158.9395	-0.1584	43.0217	21.3693	16.5511	**279.3519**	4.0067
12	149.9850	150.5507	165.0349	-0.1459	44.4004	21.6507	16.5752	**298.7309**	4.0002

Reduced Data										
No	DP [Pa]	q''_e [W/cm^2]	q" [W/cm^2]	q"/q''_e	h_1 [W/m^2 K]	h_2 [W/m^2 K]	h_3 [W/m^2 K]	T_{w1} [°C]	T_{w2} [°C]	T_{w3} [°C]
1	17927.3		0.0							
2	16625.9	40.6	**33.461**	82.5%	**4248.8**	**4217.3**	**4041.5**	15.60	15.70	16.30
3	15866.5	81.2	**66.060**	81.3%	**4209.1**	**4165.8**	**3997.3**	30.70	31.00	32.20
4	15321.2	121.8	**99.373**	81.6%	**4403.4**	**4351.5**	**4169.5**	44.90	45.40	47.10
5	14670.1	159.9	**130.570**	81.7%	**4483.9**	**4430.3**	**4242.7**	58.10	58.70	61.00
6	14338.1	202.2	**166.415**	82.3%	**4766.2**	**4707.0**	**4494.6**	70.60	71.40	74.40
7	14714.3	240.3	**202.015**	84.1%	**5584.0**	**5537.1**	**5189.1**	74.50	75.00	79.40
8	16857.6	320.4	**279.790**	87.3%	**7808.9**	**7804.7**	**7000.0**	77.90	77.90	85.20
9	19715.1	401.7	**358.945**	89.4%	**10279.9**	**10229.1**	**8857.1**	79.50	79.80	89.40
10	24095.6	479.7	**435.525**	90.8%	**12937.9**	**12843.2**	**10724.6**	81.60	82.00	93.90
11	33219.8	558.7	**511.930**	91.6%	**15241.7**	**15093.9**	**12319.7**	85.20	85.80	99.30
12	34994.0	597.5	**549.365**	91.9%	**16389.5**	**16236.7**	**13105.6**	86.10	86.60	101.00

Table C.13 Test data, TS#2, Tin = 0 °C, m = 5.0 g/s.

- Test Section : 2
- D_h : 200.0 [μm]
- Number of Channels : 24
- Mass flow rate : 5.0 [g/s]
- T_{in} : 0 [°C]
- P_{out} : 16.5 [psia]
- T_{sat} (@ P_{out}) : 63.59 [°C]

Measurement data									
No	T_{tc1} [°C]	T_{tc2} [°C]	T_{tc3} [°C]	T_{in} [°C]	T_{out} [°C]	P_{in} [psia]	P_{out} [psia]	Q [W]	$\dot{m}$ [g/s]
1	0.2672	0.2051	0.2622	0.0027	-0.2868	19.8737	16.5051	**0.0655**	5.0092
2	17.9165	18.0197	18.6387	-0.1133	1.7179	19.6444	16.4715	**20.2758**	5.0092
3	35.9642	36.2463	37.4488	0.0130	3.9750	19.5417	16.4890	**40.6032**	5.0093
4	52.6682	53.1291	54.9153	-0.0344	6.0429	19.4463	16.4765	**60.8236**	5.0092
5	68.6520	69.2850	71.6295	0.1065	8.3221	19.3210	16.4595	**80.0756**	5.0093
6	84.7548	85.5229	88.4026	0.3488	10.1409	19.1831	16.4958	**99.8657**	5.0092
7	97.5228	98.2179	102.1726	-0.0963	13.3299	19.1350	16.4771	**120.7504**	5.0077
8	109.6383	109.7045	116.7395	0.0654	19.8492	19.4853	16.5158	**159.5666**	5.0101
9	121.5311	121.1819	131.1425	0.4417	24.5719	19.9465	16.4985	**201.6525**	5.0094
10	130.8616	131.3146	143.0666	0.0173	29.7231	20.4435	16.5002	**238.4855**	5.0092
11	141.9034	142.5119	156.5509	-0.0083	34.9990	21.0812	16.5285	**282.4761**	5.0100
12	146.3127	146.9619	161.8697	-0.2992	37.3431	21.3062	16.5074	**298.5630**	5.0093

Reduced Data										
No	DP [Pa]	q''_e [W/cm^2]	q" [W/cm^2]	q"/q''_e	h_1 [W/m^2 K]	h_2 [W/m^2 K]	h_3 [W/m^2 K]	T_{w1} [°C]	T_{w2} [°C]	T_{w3} [°C]
1	23225.5		0.0							
2	21876.0	40.6	**33.916**	83.6%	**4615.1**	**4578.8**	**4372.2**	14.08	14.18	14.80
3	21047.5	81.2	**67.023**	82.5%	**4594.8**	**4545.1**	**4345.0**	28.34	28.62	29.82
4	20476.3	121.6	**100.521**	82.6%	**4758.0**	**4700.1**	**4488.5**	41.20	41.66	43.44
5	19728.9	160.2	**132.485**	82.7%	**4863.8**	**4800.9**	**4581.4**	53.48	54.11	56.45
6	18528.2	199.7	**165.405**	82.8%	**4946.6**	**4883.4**	**4660.1**	65.76	66.52	69.39
7	18325.5	241.5	**202.550**	83.9%	**5436.8**	**5380.3**	**5079.8**	74.20	74.89	78.82
8	20473.5	319.1	**277.815**	87.1%	**7528.2**	**7520.6**	**6793.7**	77.57	77.63	84.62
9	23772.8	403.3	**359.660**	89.2%	**9884.1**	**9937.5**	**8608.9**	79.91	79.56	89.44
10	27187.9	477.0	**431.595**	90.5%	**12254.0**	**12166.4**	**10262.5**	80.82	81.27	92.92
11	31389.7	565.0	**517.850**	91.7%	**15301.3**	**15149.2**	**12322.2**	81.75	82.35	96.24
12	33086.3	597.1	**549.265**	92.0%	**16389.2**	**16214.0**	**13016.9**	82.46	83.10	97.84

Table C.14 Test data, TS#2, Tin = 0 °C, m = 10.0 g/s.

- Test Section : 2
- D_h : 200.0 [μm]
- Number of Channels : 24
- Mass flow rate : 10.0 [g/s]
- T_{in} : 0 [°C]
- P_{out} : 16.5 [psia]
- T_{sat} (@ P_{out}) : 63.59 [°C]

Measurement data									
No	T_{tc1} [°C]	T_{tc2} [°C]	T_{tc3} [°C]	T_{in} [°C]	T_{out} [°C]	P_{in} [psia]	P_{out} [psia]	Q [W]	$\dot{m}$ [g/s]
1	-0.5147	-0.0373	0.1101	-0.1856	-0.6190	24.2319	16.5029	**0.0326**	9.9754
2	27.7975	28.1053	29.9242	-0.0319	1.6300	23.8161	16.5113	**39.6357**	9.9880
3	55.4778	55.1756	58.7591	0.2415	4.8364	23.5487	16.5018	**80.0201**	9.9746
4	82.4010	81.3651	86.2699	0.2850	7.8166	23.4233	16.5053	**120.1257**	9.9906
5	104.6473	103.2775	109.5207	0.0189	9.6558	23.5962	16.5191	**161.8798**	9.9916
6	118.1886	117.2058	125.1851	-0.0576	11.4525	23.7875	16.5383	**198.1601**	10.0050
7	131.3301	131.5175	142.6862	-0.2147	13.4757	23.4328	16.5599	**240.5024**	10.0011
8	141.5824	141.6600	155.0062	0.0394	17.1212	23.9246	16.5044	**278.8097**	9.9976
9	152.2735	152.6844	168.5661	-0.1950	19.5903	23.0669	16.5017	**320.2507**	10.0081

Reduced Data										
No	DP [Pa]	q''_e [W/cm^2]	q" [W/cm^2]	q"/q''_e	h_1 [W/m^2 K]	h_2 [W/m^2 K]	h_3 [W/m^2 K]	T_{w1} [°C]	T_{w2} [°C]	T_{w3} [°C]
1	53289.2									
2	50365.2	79.3	**68.583**	86.5%	**6506.1**	**6400.5**	**5840.5**	20.00	20.30	22.10
3	48587.0	160.0	**138.515**	86.6%	**6810.7**	**6868.3**	**6242.8**	39.70	39.40	42.90
4	47698.0	240.3	**208.180**	86.7%	**6985.6**	**7125.0**	**6509.9**	58.50	57.50	62.30
5	48795.1	323.8	**283.335**	87.5%	**7739.4**	**7905.6**	**7201.0**	72.00	70.60	76.80
6	49981.3	396.3	**351.390**	88.7%	**9022.3**	**9151.8**	**8196.8**	77.60	76.60	84.50
7	47387.4	481.0	**431.635**	89.7%	**10753.5**	**10725.5**	**9282.5**	81.30	81.50	92.50
8	51160.8	557.6	**506.235**	90.8%	**12809.6**	**12795.5**	**10765.5**	82.80	82.90	96.10
9	45265.5	640.5	**586.640**	91.6%	**14969.1**	**14882.0**	**12151.5**	84.00	84.40	100.10

Table C.15 Test data, TS#2, Tin = -30 °C, m = 2.0 g/s.

- Test Section : 2
- D_h : 200.0 [μm]
- Number of Channels : 24
- Mass flow rate : 2.0 [g/s]
- T_{in} : -30 [°C]
- P_{out} : 16.5 [psia]
- T_{sat} (@ P_{out}) : 63.59 [°C]

Measurement data									
No	T_{tc1} [°C]	T_{tc2} [°C]	T_{tc3} [°C]	T_{in} [°C]	T_{out} [°C]	P_{in} [psia]	P_{out} [psia]	Q [W]	$\dot{m}$ [g/s]
1	-31.0447	-31.1141	-31.0246	-29.7274	-29.4784	17.9171	16.4976	**0.0412**	2.0011
2	-7.9979	-7.8516	-7.3041	-29.7556	-26.4747	17.8083	16.5114	**20.2351**	2.0015
3	12.8990	13.2465	14.2537	-30.1483	-23.6224	17.6918	16.4931	**40.1536**	2.0011
4	33.4109	33.9636	35.4568	-29.8811	-18.5531	17.5926	16.4852	**59.7598**	2.0012
5	54.3265	55.0954	57.1056	-30.0594	-11.6070	17.5655	16.5122	**80.0439**	1.9995
6	73.5214	74.4399	77.0333	-30.0456	-6.9275	17.4810	16.4728	**100.8228**	2.0011
7	90.2362	91.1211	94.6968	-29.8594	-2.9003	17.5367	16.5337	**122.2919**	1.9998
8	101.6351	101.9518	108.5780	-29.1865	11.8351	17.6804	16.5408	**160.0018**	2.0010
9	117.2384	117.6796	126.2467	-25.9342	16.7812	17.9997	16.5995	**199.0922**	2.0012
10	133.9868	134.0886	144.9647	-22.7856	30.3431	18.8082	16.5847	**238.3375**	2.0014
11	*139.1841*	*139.8762*	*150.3436*	*-32.7508*	*38.1061*	*19.1609*	*16.6203*	***250.1665***	*1.9948*

Reduced Data										
No	DP [Pa]	q''_e [W/cm^2]	q'' [W/cm^2]	q''/q''_e	h_1 [W/m^2 K]	h_2 [W/m^2 K]	h_3 [W/m^2 K]	T_{w1} [°C]	T_{w2} [°C]	T_{w3} [°C]
1	9786.8									
2	8941.6	40.5	**33.682**	83.2%	**3708.5**	**3675.0**	**3555.0**	-11.80	-11.60	-11.10
3	8264.9	80.3	**64.518**	80.3%	**3569.0**	**3530.7**	**3424.2**	5.60	6.00	7.00
4	7635.5	119.5	**95.582**	80.0%	**3675.9**	**3632.3**	**3519.5**	22.50	23.10	24.60
5	7261.9	160.1	**128.120**	80.0%	**3809.0**	**3760.5**	**3639.3**	39.70	40.50	42.50
6	6950.9	201.6	**162.040**	80.4%	**3974.3**	**3924.5**	**3790.3**	55.00	55.90	58.40
7	6915.5	244.6	**198.635**	81.2%	**4277.2**	**4231.8**	**4057.7**	67.40	68.30	71.80
8	7857.5	320.0	**273.965**	85.6%	**6339.0**	**6313.0**	**5814.1**	70.10	70.40	77.00
9	9653.5	398.2	**348.295**	87.5%	**7836.9**	**7793.5**	**7037.0**	77.00	77.40	85.90
10	15330.6	476.7	**424.420**	89.0%	**9701.5**	**9688.9**	**8505.6**	84.80	84.90	95.60
11										

Table C.16 Test data, TS#2, Tin = -30 °C, m = 3.0 g/s.

• Test Section	:	2	• Mass flow rate	:	3.0 [g/s]
• D_h	:	200.0 [μm]	• T_{in}	:	-30 [°C]
• Number of Channels	:	24	• P_{out}	:	16.5 [psia]
			• T_{sat} (@ P_{out})	:	63.59 [°C]

Measurement data									
No	T_{tc1} [°C]	T_{tc2} [°C]	T_{tc3} [°C]	T_{in} [°C]	T_{out} [°C]	P_{in} [psia]	P_{out} [psia]	Q [W]	$\dot{m}$ [g/s]
1	-30.2583	-30.3170	-30.1988	-29.8245	-27.2526	19.4235	16.5074	**0.0714**	3.0038
2	-11.0086	-10.8765	-10.2346	-30.2221	-25.0246	19.1492	16.5178	**20.2909**	3.0039
3	7.8337	8.1504	9.3151	-29.9002	-22.0845	18.8744	16.5063	**40.0589**	3.0008
4	27.3737	27.8861	29.5635	-29.8815	-20.0078	18.7167	16.5022	**59.8602**	3.0040
5	45.5787	46.3031	48.5507	-30.3044	-16.0833	18.5968	16.5178	**80.2908**	3.0040
6	63.0224	63.9524	66.7376	-30.3780	-10.0144	18.5059	16.4835	**100.9211**	3.0038
7	78.9342	80.0787	83.3290	-29.6916	-6.0713	18.3940	16.4733	**119.0518**	3.0038
8	97.9699	98.6501	104.4882	-30.2671	-4.8375	18.5539	16.5080	**159.5432**	3.0038
9	113.3984	113.7452	122.2348	-30.2754	2.2709	18.6854	16.5185	**200.2242**	3.0038
10	125.3539	125.3850	136.4792	-30.3803	9.9072	18.9562	16.5068	**240.1444**	3.0038
11	136.1496	136.1868	149.3780	-29.7661	16.3630	19.2877	16.5218	**277.9899**	3.0039
12	*147.9888*	*148.1071*	*163.4876*	*-27.8486*	*26.7622*	*19.6606*	*16.5018*	***320.0158***	*3.0038*

Reduced Data										
No	DP [Pa]	q''_e [W/cm^2]	q" [W/cm^2]	q''/q''_e	h_1 [W/m^2 K]	h_2 [W/m^2 K]	h_3 [W/m^2 K]	T_{w1} [°C]	T_{w2} [°C]	T_{w3} [°C]
1	20106.0		0.0							
2	18143.2	40.6	**35.548**	87.6%	**5096.6**	**5042.6**	**4795.8**	-15.00	-14.90	-14.20
3	16327.8	80.1	**67.321**	84.0%	**4636.7**	**4580.3**	**4384.1**	0.20	0.50	1.70
4	15268.5	119.7	**98.516**	82.3%	**4320.4**	**4266.2**	**4098.2**	16.20	16.70	18.40
5	14334.1	160.6	**131.995**	82.2%	**4434.0**	**4374.0**	**4197.6**	30.50	31.30	33.50
6	13944.0	201.8	**166.800**	82.6%	**4699.9**	**4631.5**	**4438.0**	43.90	44.90	47.60
7	13242.4	238.1	**197.110**	82.8%	**4803.8**	**4729.5**	**4530.5**	56.30	57.50	60.70
8	14106.3	319.1	**270.600**	84.8%	**5829.7**	**5782.1**	**5403.2**	66.80	67.50	73.30
9	14939.7	400.4	**348.095**	86.9%	**7307.3**	**7277.6**	**6618.8**	73.20	73.50	81.90
10	16888.2	480.3	**425.915**	88.7%	**9113.6**	**9110.2**	**8041.2**	76.00	76.10	87.10
11	19070.4	556.0	**500.090**	89.9%	**10977.6**	**10972.6**	**9444.0**	78.10	78.20	91.20
12	21779.0	640.0	**583.500**	91.2%	**13630.4**	**13609.4**	**11339.8**	80.10	80.20	95.40

Table C.17 Test data, TS#2, Tin = -30 °C, m = 4.0 g/s.

• Test Section	:	2	• Mass flow rate	:	4.0 [g/s]
• D_h	:	200.0 [μm]	• T_{in}	:	-30 [°C]
• Number of Channels	:	24	• P_{out}	:	16.5 [psia]
			• T_{sat} (@ P_{out})	:	63.59 [°C]

Measurement data									
No	T_{tc1} [°C]	T_{tc2} [°C]	T_{tc3} [°C]	T_{in} [°C]	T_{out} [°C]	P_{in} [psia]	P_{out} [psia]	Q [W]	$\dot{m}$ [g/s]
1	-29.8759	-29.9351	-29.8083	-29.9266	-28.5367	20.4529	16.5122	**0.0691**	4.0065
2	-11.3081	-11.1924	-10.5294	-29.9394	-26.0834	20.0507	16.4979	**20.2924**	4.0066
3	6.3216	6.6139	7.8303	-30.2516	-24.2582	19.7621	16.5021	**40.0648**	3.9965
4	24.2362	24.7269	26.4698	-30.1919	-22.7570	19.5651	16.5021	**59.8649**	3.9992
5	41.8227	42.4926	44.8283	-30.3402	-20.1060	19.4178	16.5101	**80.1622**	4.0067
6	56.9156	57.7421	60.6189	-30.1777	-18.3204	19.3976	16.5099	**99.9592**	4.0065
7	75.1707	76.2088	79.7006	-29.5744	-14.0318	19.2562	16.5131	**122.0522**	4.0057
8	100.7249	102.0262	106.6103	-30.0997	-9.8664	19.1553	16.4908	**159.1089**	4.0037
9	113.6603	114.0819	122.2155	-29.7950	-2.0883	19.3922	16.5035	**200.3329**	4.0048
10	125.0137	125.0119	135.7640	-29.8736	-0.6310	19.6413	16.4929	**237.6832**	4.0065
11	136.2421	136.3941	149.5860	-30.2668	4.7239	19.9556	16.4852	**279.9895**	4.0064
12	146.0753	146.3172	161.6378	-29.6150	11.6028	20.2488	16.5088	**320.3266**	4.0012

Reduced Data										
No	DP [Pa]	q''_e [W/cm^2]	q" [W/cm^2]	q"/q''_e	h_1 [W/m^2 K]	h_2 [W/m^2 K]	h_3 [W/m^2 K]	T_{w1} [°C]	T_{w2} [°C]	T_{w3} [°C]
1	27170.8		0.0							
2	24496.0	40.6	**35.523**	87.5%	**5055.3**	**5008.7**	**4757.4**	-15.30	-15.20	-14.50
3	22476.5	80.1	**67.506**	84.2%	**4698.5**	**4645.2**	**4435.6**	-1.30	-1.00	0.20
4	21118.5	119.7	**99.405**	83.0%	**4552.0**	**4495.1**	**4303.8**	13.00	13.40	15.20
5	20047.5	160.3	**132.710**	82.8%	**4616.2**	**4556.3**	**4359.1**	26.70	27.40	29.70
6	19909.9	199.9	**166.120**	83.1%	**4830.5**	**4766.0**	**4554.1**	37.90	38.80	41.60
7	18913.2	244.1	**203.390**	83.3%	**4998.0**	**4927.2**	**4703.2**	51.90	52.90	56.40
8	18371.4	318.2	**267.165**	84.0%	**5388.3**	**5310.0**	**5051.3**	69.90	71.20	75.80
9	19917.0	400.7	**347.260**	86.7%	**7095.8**	**7061.6**	**6462.2**	73.50	74.00	82.00
10	21707.4	475.4	**418.745**	88.1%	**8394.2**	**8394.3**	**7489.8**	76.50	76.50	87.20
11	23927.3	560.0	**501.170**	89.5%	**10235.5**	**10217.8**	**8881.8**	78.10	78.20	91.30
12	25786.4	640.7	**580.930**	90.7%	**12438.0**	**12402.2**	**10487.8**	78.50	78.80	93.90

Table C.18 Test data, TS#2, Tin = -30 °C, m = 5.0 g/s.

- Test Section : 2
- D_h : 200.0 [μm]
- Number of Channels : 24
- Mass flow rate : 5.0 [g/s]
- T_{in} : -30 [°C]
- P_{out} : 16.5 [psia]
- T_{sat} (@ P_{out}) : 63.59 [°C]

Measurement data									
No	T_{tc1} [°C]	T_{tc2} [°C]	T_{tc3} [°C]	T_{in} [°C]	T_{out} [°C]	P_{in} [psia]	P_{out} [psia]	Q [W]	$\dot{m}$ [g/s]
1	-29.7875	-29.8480	-29.7015	-30.3196	-29.3233	21.5414	16.4964	**0.0771**	5.0092
2	-11.8664	-11.7617	-11.0765	-30.0073	-27.0334	21.0649	16.5034	**20.2904**	5.0064
3	4.7281	5.0058	6.2695	-30.0443	-25.3906	20.7439	16.4934	**40.0552**	5.0095
4	21.3699	21.8282	23.6404	-29.9021	-24.3988	20.4995	16.4961	**59.8600**	5.0092
5	38.7566	39.3920	41.7732	-29.6086	-21.5111	20.3032	16.5175	**80.3242**	5.0047
6	55.2003	55.9573	59.0576	-29.9623	-18.9144	20.1979	16.4771	**101.5434**	5.0040
7	69.3717	70.3031	73.8621	-29.9648	-16.3255	20.0973	16.4884	**120.1632**	5.0069
8	96.7499	98.0207	102.6754	-29.8401	-11.1867	19.9883	16.5210	**158.9930**	5.0069
9	113.9394	114.6661	122.1412	-29.8563	-7.5888	20.1799	16.5199	**201.0493**	5.0059
10	125.6020	125.8222	136.2132	-30.0521	-2.1274	20.4294	16.4913	**240.2047**	5.0091
11	135.4410	135.5174	148.3632	-30.2180	2.6397	20.6977	16.4648	**277.5944**	5.0066
12	147.1985	147.6051	163.0491	-30.1551	4.8663	21.0066	16.5015	**323.6944**	4.9952

Reduced Data										
No	DP [Pa]	q''_e [W/cm^2]	q" [W/cm^2]	q''/q''_e	h_1 [W/m^2 K]	h_2 [W/m^2 K]	h_3 [W/m^2 K]	T_{w1} [°C]	T_{w2} [°C]	T_{w3} [°C]
1	34784.3		0.0							
2	31450.2	40.6	**35.571**	87.7%	**5084.4**	**5041.8**	**4779.5**	-15.86	-15.75	-15.07
3	29306.7	80.1	**68.104**	85.0%	**4975.2**	**4918.9**	**4677.9**	-2.95	-2.68	-1.42
4	27601.8	119.7	**100.610**	84.0%	**4902.8**	**4841.8**	**4614.9**	9.97	10.42	12.23
5	26101.6	160.6	**134.465**	83.7%	**4963.9**	**4899.1**	**4670.6**	23.45	24.09	26.46
6	25654.0	203.1	**170.080**	83.7%	**5114.4**	**5049.7**	**4800.6**	35.78	36.53	39.62
7	24882.3	240.3	**201.850**	84.0%	**5270.8**	**5199.6**	**4944.3**	46.26	47.18	50.73
8	23906.3	318.0	**268.770**	84.5%	**5654.1**	**5570.4**	**5283.9**	65.80	67.06	71.69
9	25234.6	402.1	**347.225**	86.4%	**6852.5**	**6797.8**	**6282.2**	73.82	74.54	81.95
10	27152.4	480.4	**423.185**	88.1%	**8400.5**	**8380.1**	**7513.7**	76.59	76.81	87.10
11	29184.8	555.2	**496.200**	89.4%	**10036.1**	**10027.5**	**8756.0**	77.87	77.94	90.66
12	31061.9	647.4	**585.510**	90.4%	**11933.0**	**11878.0**	**10110.3**	79.12	79.52	94.78

Table C.19 Test data, TS#3, Tin = 0 °C, m = 2.0 g/s.

- Test Section : 3
- D_h : 334.1 [μm]
- Number of Channels : 11
- Mass flow rate : 2.0 [g/s]
- T_{in} : 0 [°C]
- P_{out} : 16.5 [psia]
- T_{sat} (@ P_{out}) : 63.59 [°C]

Measurement data

No	T_{tc1} [°C]	T_{tc2} [°C]	T_{tc3} [°C]	T_{in} [°C]	T_{out} [°C]	P_{in} [psia]	P_{out} [psia]	Q [W]	$\dot{m}$ [g/s]
1	0.5656	0.9192	0.9955	0.0578	0.2531	16.9280	16.5135	**0.0362**	1.9996
2	39.6468	40.3468	41.2066	0.2360	5.5995	16.8477	16.4833	**20.8148**	1.9972
3	69.5796	70.4318	72.0193	-0.0188	10.8396	16.8763	16.5324	**40.5631**	1.9955
4	78.4088	79.0405	81.4594	-0.3557	16.5396	16.9737	16.5478	**60.3142**	2.0008
5	86.5621	87.1012	90.4362	0.0333	23.4760	16.9848	16.4919	**80.9577**	2.0010
6	93.4923	93.9853	98.1570	-0.1995	28.7580	17.1523	16.5476	**99.2805**	2.0010
7	100.6327	101.0712	106.1370	-0.1032	34.3996	17.3287	16.5206	**119.9366**	2.0009
8	104.9395	105.4223	111.0290	0.2994	36.8539	17.4947	16.5221	**130.5429**	1.9998
9	109.7574	110.2734	116.4506	0.1185	39.5059	17.6801	16.5572	**142.6451**	2.0009
10	114.0207	114.5977	121.2453	0.1220	41.9630	17.8143	16.5890	**152.0200**	2.0009
11	118.6659	119.3102	126.4281	-0.2755	45.1818	17.9466	16.6251	**162.1250**	2.0009
12	123.3224	124.0367	131.6882	-0.4150	49.6360	18.1785	16.7083	**171.9848**	2.0010
13	*132.9614*	*134.1476*	*141.0376*	*0.0726*	*44.9235*	*17.9207*	*16.7040*	***180.1757***	*2.0009*

Reduced Data

No	DP [Pa]	q''_e [W/cm^2]	q" [W/cm^2]	q"/q''_e	h_1 [W/m^2 K]	h_2 [W/m^2 K]	h_3 [W/m^2 K]	T_{w1} [°C]	T_{w2} [°C]	T_{w3} [°C]
1	2857.4		0.0							
2	2512.4	41.6	32.719	78.6%	3340.7	3271.0	3189.3	35.96	36.66	37.52
3	2371.3	81.1	64.899	80.0%	3858.0	3800.6	3698.2	62.23	63.08	64.67
4	2936.1	120.6	102.340	84.8%	5912.3	5848.8	5617.7	66.80	67.43	69.84
5	3398.3	161.9	142.750	88.2%	8303.0	8226.3	7781.7	70.34	70.88	74.20
6	4168.8	198.6	178.195	89.7%	10344.7	10257.5	9574.6	73.21	73.70	77.86
7	5571.2	239.9	218.275	91.0%	12803.2	12706.2	11684.0	75.75	76.19	81.23
8	6705.9	261.1	238.680	91.4%	13904.6	13789.6	12581.2	77.71	78.19	83.77
9	7742.5	285.3	261.920	91.8%	15063.1	14931.8	13520.8	79.85	80.36	86.50
10	8447.9	304.0	279.890	92.1%	15869.9	15717.6	14152.7	82.03	82.61	89.21
11	9111.2	324.2	299.205	92.3%	16720.4	16544.1	14817.7	84.44	85.08	92.15
12	10136.7	344.0	318.270	92.5%	17739.7	17533.2	15588.0	86.88	87.59	95.19
13										

Table C.20 Test data, TS#3, Tin = 0 °C, m = 3.0 g/s.

• Test Section	:	3	• Mass flow rate	:	3.0 [g/s]
• D_h	:	334.1 [μm]	• T_{in}	:	0 [°C]
• Number of Channels	:	11	• P_{out}	:	16.5 [psia]
			• T_{sat} (@ P_{out})	:	63.59 [°C]

Measurement data									
No	T_{tc1} [°C]	T_{tc2} [°C]	T_{tc3} [°C]	T_{in} [°C]	T_{out} [°C]	P_{in} [psia]	P_{out} [psia]	Q [W]	$\dot{m}$ [g/s]
1	1.3847	1.3174	1.4086	0.0988	-0.0152	17.2175	16.5396	**0.0143**	3.0035
2	34.8080	35.4669	36.3536	-0.1230	3.3662	17.1318	16.5010	**20.3471**	3.0036
3	65.8261	66.7099	68.4495	-0.0769	6.1028	17.0946	16.5026	**40.5536**	3.0036
4	79.0171	79.8482	82.3574	-0.0717	10.2492	17.1312	16.5173	**59.3936**	3.0035
5	86.4256	86.9676	90.2427	0.1556	16.0301	17.2165	16.5121	**79.5746**	3.0036
6	93.4888	93.8345	97.9544	-0.1578	20.2128	17.3119	16.5167	**100.0412**	3.0036
7	100.4246	100.7507	105.8812	-0.3983	23.0339	17.4265	16.4791	**122.2912**	3.0036
8	111.6838	111.8177	118.5666	0.3217	30.4948	17.9538	16.5142	**158.9351**	3.0036
9	125.0890	124.8396	133.3836	-0.1751	39.9648	18.7753	16.6001	**202.2511**	3.0038
10	130.9171	130.4656	139.7293	0.2014	43.0441	18.9527	16.5076	**219.2725**	3.0037
11	134.6627	134.2117	144.0591	-0.4551	43.4759	19.0033	16.5765	**229.9066**	3.0038
12	*139.6457*	*139.6552*	*149.0666*	*-0.2265*	*43.3385*	*18.8931*	*16.5801*	***241.7226***	*3.0037*

Reduced Data										
No	DP [Pa]	q''_e [W/cm^2]	q" [W/cm^2]	q''/q''_e	h_1 [W/m^2 K]	h_2 [W/m^2 K]	h_3 [W/m^2 K]	T_{w1} [°C]	T_{w2} [°C]	T_{w3} [°C]
1	4673.5		0.0							
2	4349.6	40.7	**32.784**	80.6%	**3752.8**	**3670.3**	**3564.8**	31.12	31.78	32.67
3	4081.5	81.1	**65.321**	80.5%	**3982**	**3919.1**	**3800.9**	58.43	59.32	61.05
4	4232.9	118.8	**100.013**	84.2%	**5414.8**	**5343.3**	**5138.3**	67.67	68.50	71.00
5	4856.8	159.1	**139.185**	87.5%	**7575.8**	**7509.9**	**7135**	70.61	71.15	74.41
6	5483.3	200.1	**178.715**	89.3%	**9673.7**	**9620.2**	**9025.7**	73.15	73.49	77.60
7	6531.9	244.6	**221.855**	90.7%	**11929.6**	**11867.8**	**10974.3**	75.14	75.46	80.57
8	9925.3	317.9	**293.180**	92.2%	**16157**	**16121.7**	**14525.6**	78.19	78.33	85.03
9	14997.6	404.5	**377.715**	93.4%	**21312.4**	**21401.4**	**18722**	81.82	81.58	90.05
10	16858.1	438.5	**410.680**	93.6%	**23151.4**	**23326.8**	**20188.2**	83.83	83.38	92.56
11	16732.4	459.8	**430.910**	93.7%	**23744.9**	**23920.4**	**20595.6**	85.22	84.77	94.53
12										

Table C.21 Test data, TS#3, Tin = 0 °C, m = 4.0 g/s.

- Test Section : 3
- D_h : 334.1 [μm]
- Number of Channels : 11
- Mass flow rate : 4.0 [g/s]
- T_{in} : 0 [°C]
- P_{out} : 16.5 [psia]
- T_{sat} (@ P_{out}) : 63.59 [°C]

Measurement data

No	T_{tc1} [°C]	T_{tc2} [°C]	T_{tc3} [°C]	T_{in} [°C]	T_{out} [°C]	P_{in} [psia]	P_{out} [psia]	Q [W]	$\dot{m}$ [g/s]
1	1.0761	1.3300	1.4175	0.0344	-0.1037	17.5316	16.4955	**-0.0211**	4.0048
2	31.7190	32.3099	33.2054	0.0725	2.5377	17.4903	16.4872	**20.2383**	4.0061
3	60.0615	60.9537	62.7448	-0.0543	5.2851	17.5009	16.4983	**40.5492**	4.0061
4	77.0810	77.9968	80.5601	0.0877	8.6832	17.5095	16.4745	**60.3450**	4.0062
5	85.3174	85.9385	89.2021	-0.1739	11.7324	17.6508	16.5441	**79.9435**	4.0059
6	92.1776	92.5363	96.5755	-0.2442	13.9125	17.7217	16.5132	**100.3050**	4.0041
7	99.3289	99.4610	104.3667	-0.5018	18.0551	17.8917	16.5501	**120.5160**	4.0061
8	111.1772	111.1952	117.6723	0.1212	24.5446	18.3359	16.5732	**158.6087**	4.0062
9	124.5561	124.3247	132.5268	-0.1830	31.4991	18.8557	16.5508	**200.0444**	4.0063
10	138.7964	138.4711	148.5032	0.0489	37.0574	19.4652	16.5426	**240.5354**	4.0064
11	*147.9899*	*148.0565*	*157.5757*	*0.2477*	*35.4183*	*19.2851*	*16.5205*	***258.5881***	*4.0377*

Reduced Data

No	DP [Pa]	q''_e [W/cm^2]	q'' [W/cm^2]	q''/q''_e	h_1 [W/m^2 K]	h_2 [W/m^2 K]	h_3 [W/m^2 K]	T_{w1} [°C]	T_{w2} [°C]	T_{w3} [°C]
1	7143.1		0.0							
2	6915.6	40.5	33.308	82.3%	4221.1	4128.9	3996.7	27.98	28.57	29.46
3	6912.7	81.1	66.740	82.3%	4523.3	4443.2	4290.8	52.52	53.41	55.20
4	7136.4	120.7	102.410	84.9%	5683.8	5599.1	5375.0	65.46	66.38	68.94
5	7630.6	159.9	139.705	87.4%	7465.1	7392.1	7031.1	69.44	70.06	73.32
6	8332.3	200.6	178.960	89.2%	9404.7	9352.4	8800.6	71.82	72.17	76.20
7	9250.1	241.0	218.015	90.5%	11373.8	11350.6	10551.1	74.49	74.62	79.50
8	12153.1	317.2	292.060	92.1%	15409.5	15405.2	13989.9	77.82	77.84	84.27
9	15891.8	400.1	372.295	93.1%	19569.5	19640.1	17412.4	81.92	81.69	89.82
10	20150.3	481.1	450.360	93.6%	23041.2	23154.9	20095.2	87.08	86.76	96.70
11										

Table C.22 Test data, TS#3, Tin = 0 °C, m = 5.0 g/s.

- Test Section : 3
- D_h : 334.1 [μm]
- Number of Channels : 11
- Mass flow rate : 5.0 [g/s]
- T_{in} : 0 [°C]
- P_{out} : 16.5 [psia]
- T_{sat} (@ P_{out}) : 63.59 [°C]

Measurement data									
No	T_{tc1} [°C]	T_{tc2} [°C]	T_{tc3} [°C]	T_{in} [°C]	T_{out} [°C]	P_{in} [psia]	P_{out} [psia]	Q [W]	$\dot{m}$ [g/s]
1	0.6153	0.8725	0.9867	-0.0203	-0.2561	18.1496	16.5015	**-0.0133**	5.0086
2	27.3454	27.9468	28.9477	-0.1615	2.1046	18.0958	16.5165	**20.7590**	5.0128
3	53.5591	54.5380	56.4863	-0.2708	3.8438	17.9931	16.4971	**41.6274**	5.0091
4	73.5260	74.6925	77.4704	-0.0553	6.6922	17.9692	16.4825	**60.2141**	5.0091
5	84.6963	85.6433	89.0265	0.1692	9.5612	17.9957	16.5221	**79.4706**	5.0079
6	92.4900	93.0770	97.2475	-0.2835	12.0084	18.1128	16.5570	**100.8894**	5.0092
7	99.4208	99.7648	104.8102	-0.3711	14.7956	18.1981	16.5069	**121.4432**	5.0095
8	111.6756	111.6710	118.2964	-0.0066	19.7415	18.5195	16.5134	**159.7527**	5.0092
9	123.7233	123.5132	131.8670	0.2815	24.5935	18.8057	16.5194	**199.7076**	5.0091
10	136.5298	135.9068	145.9306	-0.2261	29.7088	19.1302	16.5285	**241.5103**	5.0017
11	142.8778	141.9941	152.7418	-0.2481	33.1594	18.9962	16.4829	**261.2571**	5.0091
12	149.3104	148.4076	159.9271	0.1655	35.2902	18.9930	16.4635	**279.2209**	5.0092
13	*158.2736*	*157.5550*	*169.8070*	*-0.6831*	*36.6376*	*18.9457*	*16.5001*	***300.4553***	*5.0485*

Reduced Data										
No	DP [Pa]	q''_e [W/cm^2]	q" [W/cm^2]	q"/q''_e	h_1 [W/m^2 K]	h_2 [W/m^2 K]	h_3 [W/m^2 K]	T_{w1} [°C]	T_{w2} [°C]	T_{w3} [°C]
1	11363.0		0.0							
2	10888.8	41.5	**35.415**	85.3%	**5356.4**	**5215.0**	**4995.5**	23.37	23.97	24.97
3	10314.3	83.3	**70.404**	84.6%	**5443.1**	**5323.1**	**5099.4**	45.61	46.59	48.53
4	10250.8	120.4	**102.635**	85.2%	**5942.9**	**5825.8**	**5564.7**	61.89	63.06	65.83
5	10160.0	158.9	**138.650**	87.2%	**7359.2**	**7250.8**	**6888.5**	68.94	69.89	73.26
6	10727.1	201.8	**179.815**	89.1%	**9278.1**	**9195.3**	**8647.6**	72.03	72.61	76.77
7	11660.1	242.9	**219.400**	90.3%	**11186.9**	**11129.0**	**10343.6**	74.42	74.76	79.78
8	13831.5	319.5	**294.020**	92.0%	**14875.4**	**14876.5**	**13533.2**	78.09	78.08	84.66
9	15763.3	399.4	**371.165**	92.9%	**18765.4**	**18824.5**	**16728.9**	81.22	81.01	89.30
10	17937.8	483.0	**452.380**	93.7%	**22687.1**	**22898.3**	**19915.5**	84.60	83.99	93.92
11	17328.9	522.5	**490.640**	93.9%	**24633.8**	**24960.4**	**21494.6**	86.50	85.62	96.26
12	17440.8	558.4	**525.120**	94.0%	**26015.0**	**26362.3**	**22524.4**	88.90	88.00	99.40
13										

Table C.23 Test data, TS#3, Tin = 0 °C, m = 10.0 g/s.

- Test Section : 3
- D_h : 334.1 [μm]
- Number of Channels : 11
- Mass flow rate : 10.0 [g/s]
- T_{in} : 0 [°C]
- P_{out} : 16.5 [psia]
- T_{sat} (@ P_{out}) : 63.59 [°C]

Measurement data									
No	T_{tc1} [°C]	T_{tc2} [°C]	T_{tc3} [°C]	T_{in} [°C]	T_{out} [°C]	P_{in} [psia]	P_{out} [psia]	Q [W]	$\dot{m}$ [g/s]
1	-0.0426	0.2102	0.3011	-0.1031	-0.4999	21.3884	16.5240	**0.0000**	10.0111
2	37.3716	38.1252	40.0149	0.0000	1.7436	21.1683	16.5353	**40.5174**	10.0171
3	71.0516	72.2311	75.9932	0.0691	4.2376	20.9567	16.5204	**80.0254**	10.0122
4	93.7011	94.8333	100.2106	0.0655	5.9156	20.8772	16.5465	**119.5369**	9.9956
5	106.7689	107.0301	113.9008	-0.0150	9.4846	21.0493	16.5174	**160.8766**	10.0044
6	118.5435	118.1895	126.7041	0.1402	12.2064	21.3772	16.5264	**201.9082**	10.0218
7	-0.0426	0.2102	0.3011	-0.1031	-0.4999	21.3884	16.5240	**0.0000**	10.0111
8	142.5065	141.1293	152.4398	-0.0628	16.5024	21.3512	16.5223	**280.0970**	10.0231
9	155.7792	154.3243	167.2990	-0.3658	20.5472	20.9852	16.5329	**320.9165**	10.0170
10	162.8375	161.2757	175.0141	-0.2486	21.6883	20.7702	16.5380	**340.0616**	10.0228

Reduced Data										
No	DP [Pa]	q''_e [W/cm^2]	q" [W/cm^2]	q''/q''_e	h_1 [W/m^2 K]	h_2 [W/m^2 K]	h_3 [W/m^2 K]	T_{w1} [°C]	T_{w2} [°C]	T_{w3} [°C]
1	**33538.9**									
2	**31943.3**	**81.0**	**72.307**	**89.2%**	**8692.1**	**8463.7**	**7940.7**	**29.23**	**29.99**	**31.87**
3	**30587.0**	**160.1**	**142.740**	**89.2%**	**9241.1**	**9036.0**	**8438.5**	**54.88**	**56.06**	**59.81**
4	**29858.8**	**239.1**	**216.005**	**90.4%**	**11194.0**	**11002.4**	**10175.5**	**69.12**	**70.24**	**75.59**
5	**31246.7**	**321.8**	**296.080**	**92.0%**	**14976.8**	**14918.5**	**13531.5**	**72.98**	**73.24**	**80.06**
6	**33444.7**	**403.8**	**375.585**	**93.0%**	**18819.5**	**18918.7**	**16791.1**	**75.58**	**75.23**	**83.67**
7	**34776.9**	**475.6**	**445.000**	**93.6%**	**21842.6**	**22123.0**	**19344.4**	**78.23**	**77.36**	**87.06**
8	**33294.7**	**560.2**	**526.690**	**94.0%**	**25131.3**	**25627.5**	**22051.7**	**81.99**	**80.62**	**91.81**
9	**30697.3**	**641.8**	**605.420**	**94.3%**	**28219.2**	**28793.2**	**24371.2**	**86.05**	**84.61**	**97.42**
10	**29180.2**	**680.1**	**642.190**	**94.4%**	**29181.1**	**29802.3**	**25100.9**	**88.78**	**87.24**	**100.79**

Table C.24 Test data, TS#3, Tin = 0 °C, m = 15.0 g/s.

- Test Section : 3
- D_h : 334.1 [μm]
- Number of Channels : 11
- Mass flow rate : 15.0 [g/s]
- T_{in} : 0 [°C]
- P_{out} : 16.5 [psia]
- T_{sat} (@ P_{out}) : 63.59 [°C]

Measurement data									
No	T_{tc1} [°C]	T_{tc2} [°C]	T_{tc3} [°C]	T_{in} [°C]	T_{out} [°C]	P_{in} [psia]	P_{out} [psia]	Q [W]	$\dot{m}$ [g/s]
1	-0.0498	0.1580	0.2456	0.0420	-0.3671	27.5141	16.5019	**0.0000**	15.0194
2	27.7193	28.2526	30.1812	-0.0662	1.0340	27.0345	16.4668	**40.2984**	14.9886
3	55.8259	56.7826	60.5210	0.2200	2.9189	26.5691	16.4881	**80.0031**	14.9913
4	79.5097	80.6210	86.2997	0.0097	4.1719	26.0590	16.4871	**119.7017**	14.9887
5	99.0425	99.8895	107.0336	-0.1615	5.5301	25.6144	16.4819	**160.8951**	15.0034
6	116.1639	116.3240	124.6715	-0.0142	6.4945	24.8193	16.5032	**200.5511**	15.0068
7	129.3292	128.8192	138.4182	0.2574	8.5685	24.2979	16.5210	**239.5619**	15.0052
8	142.9762	141.9890	153.0967	-0.0796	10.3935	23.7981	16.4963	**282.8337**	15.0173
9	156.1821	154.1808	166.7271	0.0511	12.1150	22.9697	16.5057	**320.9790**	15.0079
10	163.6136	161.4578	174.7197	-0.3749	12.4303	22.4911	16.5081	**342.9258**	15.0083

Reduced Data										
No	DP [Pa]	q''_e [W/cm^2]	q" [W/cm^2]	q"/q''_e	h_1 [W/m^2 K]	h_2 [W/m^2 K]	h_3 [W/m^2 K]	T_{w1} [°C]	T_{w2} [°C]	T_{w3} [°C]
1	75926.4									
2	72861.6	80.6	**74.392**	92.3%	**13559.8**	**13178.4**	**11961.6**	19.36	19.90	21.82
3	69505.9	160.0	**146.660**	91.7%	**13388.2**	**13049.4**	**11875.4**	39.26	40.21	43.94
4	65996.0	239.4	**220.000**	91.9%	**14463.2**	**14156.4**	**12771.8**	54.54	55.65	61.30
5	62965.8	321.8	**297.580**	92.5%	**16496.2**	**16270.1**	**14583.6**	65.14	65.98	73.07
6	57337.1	401.1	**372.875**	93.0%	**18435.0**	**18391.9**	**16397.2**	73.53	73.69	81.96
7	53619.6	479.1	**447.960**	93.5%	**21277.6**	**21430.9**	**18872.1**	77.98	77.47	86.98
8	50344.0	565.7	**531.215**	93.9%	**24317.6**	**24645.7**	**21396.8**	81.93	80.95	91.94
9	44567.6	642.0	**604.695**	94.2%	**26529.7**	**27232.8**	**23352.4**	86.53	84.55	96.94
10	41250.8	685.9	**646.650**	94.3%	**27551.0**	**28314.9**	**24188.4**	89.03	86.90	99.99

Table C.25 Test data, TS#3, Tin = 0 °C, m = 20.0 g/s.

- Test Section : 3
- D_h : 334.1 [μm]
- Number of Channels : 11
- Mass flow rate : 20.0 [g/s]
- T_{in} : 0 [°C]
- P_{out} : 16.5 [psia]
- T_{sat} (@ P_{out}) : 63.59 [°C]

Measurement data									
No	T_{tc1} [°C]	T_{tc2} [°C]	T_{tc3} [°C]	T_{in} [°C]	T_{out} [°C]	P_{in} [psia]	P_{out} [psia]	Q [W]	$\dot{m}$ [g/s]
1	0.1958	0.4391	0.3811	0.1691	-0.1447	34.0283	16.6276	**0.0000**	20.0221
2	24.8769	25.3891	26.8395	0.1166	0.9639	33.4430	16.6164	**40.4645**	19.9927
3	47.8988	48.7659	51.8214	-0.2647	1.9038	32.8943	16.6229	**80.5126**	20.0022
4	64.6690	65.4824	70.5545	0.0331	3.5153	32.6224	16.6341	**119.6369**	19.9954
5	90.0025	91.2290	97.8382	0.2117	4.9717	30.0715	16.6285	**161.5437**	20.0002
6	114.4544	116.1384	124.4568	-0.0476	5.8421	27.7838	16.5966	**199.2230**	20.0001
7	128.5276	129.5854	139.1309	-0.1123	6.6836	27.5917	16.5878	**239.8705**	19.9969
8	143.6143	143.7528	154.6302	-0.0964	8.3007	26.3812	16.5894	**279.9474**	19.9951
9	157.7523	156.4364	168.7069	-0.1978	9.2368	25.1200	16.5890	**322.3832**	20.0007
10	164.6089	162.9959	175.9847	-0.4944	9.0867	24.4272	16.5709	**342.7855**	20.0014

Reduced Data										
No	DP [Pa]	q''_e [W/cm^2]	q" [W/cm^2]	q''/q''_e	h_1 [W/m^2 K]	h_2 [W/m^2 K]	h_3 [W/m^2 K]	T_{w1} [°C]	T_{w2} [°C]	T_{w3} [°C]
1	119973.6									
2	116015.3	80.9	**75.523**	93.3%	**16476.6**	**15946.6**	**14615.3**	16.40	16.91	18.36
3	112187.0	161.0	**149.710**	93.0%	**17180.9**	**16687.5**	**15153.8**	31.02	31.88	34.93
4	110235.7	239.3	**223.830**	93.5%	**20789.0**	**20333.5**	**17889.0**	39.34	40.15	45.20
5	92686.7	323.1	**301.190**	93.2%	**19735.5**	**19276.9**	**17131.9**	55.75	56.97	63.53
6	77132.9	398.4	**370.185**	92.9%	**18583.0**	**18130.1**	**16182.1**	72.14	73.81	82.06
7	75869.1	479.7	**448.260**	93.4%	**21202.7**	**20894.0**	**18467.9**	77.15	78.20	87.65
8	67512.0	559.9	**524.780**	93.7%	**23240.6**	**23198.6**	**20319.2**	83.30	83.44	94.20
9	58819.1	644.8	**606.605**	94.1%	**25647.7**	**26074.2**	**22572.9**	87.86	86.56	98.68
10	54167.4	685.6	**645.690**	94.2%	**26556.1**	**27083.9**	**23346.7**	90.12	88.53	101.34

Table C.26 Test data, TS#3, Tin = -30 °C, m = 2.0 g/s.

- Test Section : 3
- D_h : 334.1 [μm]
- Number of Channels : 11
- Mass flow rate : 2.0 [g/s]
- T_{in} : -30 [°C]
- P_{out} : 16.5 [psia]
- T_{sat} (@ P_{out}) : 63.59 [°C]

Measurement data									
No	T_{tc1} [°C]	T_{tc2} [°C]	T_{tc3} [°C]	T_{in} [°C]	T_{out} [°C]	P_{in} [psia]	P_{out} [psia]	Q [W]	$\dot{m}$ [g/s]
1	-28.7845	-28.8572	-28.6466	-30.0675	-28.7567	17.1506	16.4877	**0.0292**	2.0009
2	6.3407	6.8796	7.8472	-29.9176	-24.2402	17.0664	16.5019	**20.2476**	2.0009
3	39.4110	40.2235	41.9920	-29.9504	-20.6316	17.0114	16.5012	**40.0238**	2.0009
4	68.6847	69.6955	72.3234	-29.9234	-14.1033	17.0075	16.5477	**59.2306**	2.0009
5	79.8734	80.7446	84.1039	-29.9045	-11.0046	16.9980	16.5147	**79.2413**	2.0009
6	88.1130	88.7059	92.9230	-30.1279	-1.7519	17.0724	16.5099	**100.9071**	1.9999
7	94.6484	95.0887	100.0687	-30.1350	1.6347	17.1365	16.5163	**119.9170**	2.0011
8	107.7806	108.1637	114.9423	-29.8857	12.0369	17.3115	16.5106	**158.2220**	2.0009
9	115.6743	115.9277	123.6516	-28.7908	18.8788	17.5235	16.5677	**180.9489**	2.0009
10	122.3365	122.4058	130.9241	-27.7439	22.9795	17.7097	16.5688	**200.7875**	2.0010
11	129.0695	129.0072	138.4440	-26.2250	28.3751	18.0503	16.5601	**219.4003**	2.0009
12	135.7390	135.6153	146.0642	-24.9199	34.7731	18.3160	16.5602	**239.9254**	2.0009
13	*141.7126*	*141.7326*	*152.4446*	*-27.3260*	*27.3460*	*18.3545*	*16.5448*	***253.1042***	*2.2916*

Reduced Data										
No	DP [Pa]	q''_e [W/cm^2]	q" [W/cm^2]	q"/q"$_e$	h_1 [W/m^2 K]	h_2 [W/m^2 K]	h_3 [W/m^2 K]	T_{w1} [°C]	T_{w2} [°C]	T_{w3} [°C]
1	4570.1									
2	3892.6	40.5	**33.886**	83.7%	**3861.4**	**3792.0**	**3673.5**	2.56	3.10	4.06
3	3517.3	80.0	**65.105**	81.3%	**3832.5**	**3778.7**	**3666.5**	32.08	32.89	34.66
4	3169.6	118.5	**96.521**	81.5%	**4088.9**	**4037.4**	**3909.5**	57.75	58.76	61.39
5	3332.0	158.5	**133.985**	84.5%	**5332.2**	**5277.8**	**5078.0**	64.67	65.53	68.88
6	3878.3	201.8	**176.210**	87.3%	**7129.9**	**7079.5**	**6740.2**	68.08	68.67	72.87
7	4276.3	239.8	**212.940**	88.8%	**8575.6**	**8530.8**	**8053.9**	70.41	70.85	75.80
8	5522.2	316.4	**287.375**	90.8%	**11750.5**	**11696.2**	**10812.7**	74.98	75.36	82.09
9	6589.8	361.9	**331.685**	91.7%	**13813.5**	**13770.5**	**12577.3**	77.75	78.01	85.67
10	7866.2	401.6	**370.410**	92.2%	**15553.0**	**15539.6**	**14054.6**	79.93	80.00	88.45
11	10274.5	438.8	**406.685**	92.7%	**17332.7**	**17346.3**	**15501.9**	82.45	82.39	91.75
12	12105.9	479.9	**446.870**	93.1%	**19572.2**	**19603.6**	**17266.5**	84.45	84.33	94.68
13										

Table C.27 Test data, TS#3, Tin = -30 °C, m = 3.0 g/s.

- Test Section : 3
- D_h : 334.1 [μm]
- Number of Channels : 11
- Mass flow rate : 3.0 [g/s]
- T_{in} : -30 [°C]
- P_{out} : 16.5 [psia]
- T_{sat} (@ P_{out}) : 63.59 [°C]

Measurement data									
No	T_{tc1} [°C]	T_{tc2} [°C]	T_{tc3} [°C]	T_{in} [°C]	T_{out} [°C]	P_{in} [psia]	P_{out} [psia]	Q [W]	$\dot{m}$ [g/s]
1	-27.4352	-27.5229	-27.2843	-30.1250	-29.5346	17.5255	16.5024	**0.0002**	3.0035
2	4.5984	4.6546	5.6615	-29.8606	-27.1213	17.4136	16.5014	**20.7724**	3.0036
3	34.9334	35.1559	37.0160	-29.6902	-24.3001	17.3639	16.5272	**40.0149**	3.0036
4	62.8545	63.7912	66.6381	-29.6903	-21.0106	17.2894	16.5134	**59.1973**	3.0037
5	78.4044	79.4136	82.8856	-29.7942	-17.7223	17.2758	16.4834	**78.3919**	3.0037
6	87.5909	88.2980	92.5251	-30.0864	-14.3676	17.3338	16.4817	**100.3582**	3.0037
7	94.1626	94.5682	99.5138	-30.4160	-8.2855	17.4322	16.5002	**120.7886**	3.0036
8	106.1113	106.1632	112.7582	-29.5467	-0.1354	17.5576	16.4855	**158.8722**	2.9999
9	118.8481	118.7557	127.1691	-30.0024	8.1550	17.8572	16.5136	**200.4148**	3.0037
10	131.5352	131.1234	141.2608	-30.1811	11.5460	18.3895	16.5222	**240.0613**	3.0037
11	142.2377	141.4821	153.1759	-29.7635	18.3995	18.7648	16.5101	**277.9377**	3.0037
12	148.6154	147.7303	160.4692	-28.8390	22.7368	19.0056	16.5177	**298.5500**	3.0034
13	151.2337	148.6324	163.2639	-28.7734	25.4100	18.8691	16.5650	**310.4715**	3.0094
14	*151.2124*	*149.0621*	*163.7546*	*-28.8821*	*23.3398*	*19.0523*	*16.5248*	***320.1885***	*3.0019*

Reduced Data										
No	DP [Pa]	q''_e [W/cm^2]	q" [W/cm^2]	q"/q"$_e$	h_1 [W/m^2 K]	h_2 [W/m^2 K]	h_3 [W/m^2 K]	T_{w1} [°C]	T_{w2} [°C]	T_{w3} [°C]
1	7054.1		0.0							
2	6289.2	41.5	**35.153**	84.6%	**4071.9**	**4064.1**	**3927.8**	0.68	0.73	1.74
3	5768.5	80.0	**65.980**	82.4%	**4090.2**	**4073.5**	**3938.7**	27.51	27.73	29.59
4	5350.4	118.4	**97.256**	82.1%	**4258.2**	**4206.9**	**4058.1**	51.85	52.79	55.63
5	5463.6	156.8	**131.905**	84.1%	**5122.4**	**5063.4**	**4870.3**	63.44	64.44	67.91
6	5875.0	200.7	**173.930**	86.7%	**6559.3**	**6507.7**	**6215.7**	67.82	68.52	72.73
7	6425.5	241.6	**213.750**	88.5%	**8164.9**	**8127.6**	**7698.0**	69.83	70.24	75.16
8	7391.6	317.7	**287.975**	90.6%	**11203.0**	**11196.3**	**10406.0**	73.25	73.30	79.86
9	9263.2	400.8	**368.660**	92.0%	**14516.7**	**14532.3**	**13235.0**	76.67	76.58	84.92
10	12874.5	480.1	**445.260**	92.7%	**17194.2**	**17275.3**	**15477.4**	80.47	80.06	90.11
11	15545.4	555.9	**519.065**	93.4%	**20517.8**	**20700.0**	**18198.3**	82.60	81.85	93.42
12	17153.4	597.1	**559.475**	93.7%	**22443.1**	**22680.2**	**19686.4**	84.26	83.38	95.98
13	15886.3	620.9	**583.175**	93.9%	**23869.3**	**24641.4**	**20848.2**	84.12	81.55	96.00
14										

Table C.28 Test data, TS#3, Tin = -30 °C, m = 4.0 g/s.

- Test Section : 3
- D_h : 334.1 [μm]
- Number of Channels : 11
- Mass flow rate : 4.0 [g/s]
- T_{in} : -30 [°C]
- P_{out} : 16.5 [psia]
- T_{sat} (@ P_{out}) : 63.59 [°C]

Measurement data

No	T_{tc1} [°C]	T_{tc2} [°C]	T_{tc3} [°C]	T_{in} [°C]	T_{out} [°C]	P_{in} [psia]	P_{out} [psia]	Q [W]	$\dot{m}$ [g/s]
1	-27.3716	-27.8147	-27.2058	-30.1166	-30.3237	18.0577	16.5006	**0.0085**	4.0070
2	2.5921	2.1627	3.6562	-29.9681	-27.1551	17.8490	16.4739	**20.2346**	4.0062
3	30.3585	30.5934	33.0457	-29.8738	-24.7851	17.7487	16.4713	**40.0075**	4.0063
4	57.9614	58.3204	61.8855	-30.0180	-22.1074	17.6773	16.4847	**59.9808**	4.0062
5	79.7691	80.1751	84.7046	-29.6454	-19.3860	17.6307	16.4711	**81.6570**	4.0055
6	88.2648	88.2945	93.5877	-29.9561	-16.6978	17.7117	16.5001	**101.9005**	4.0062
7	95.4181	95.1249	101.1523	-29.9575	-14.0715	17.8098	16.5163	**121.1069**	4.0062
8	107.4403	107.5784	114.0599	-29.7621	-8.4497	17.9610	16.5020	**159.1415**	4.0062
9	119.3998	119.2701	127.6115	-30.0789	-4.0934	18.1811	16.5212	**200.7503**	4.0064
10	130.5750	130.1070	140.0755	-30.0267	2.2476	18.4687	16.5192	**239.9382**	4.0065
11	141.6422	140.7724	152.3071	-29.5279	8.4496	18.7722	16.4951	**280.3424**	4.0066
12	146.8353	145.7890	158.0879	-29.9522	10.0941	18.9517	16.4988	**300.0109**	4.0065
13	152.5164	151.2667	164.4192	-30.2127	12.4898	19.1832	16.5418	**321.5811**	4.0050
14	157.6321	156.1977	170.1338	-30.1226	14.8140	19.3310	16.5677	**340.5657**	4.0059

Reduced Data

No	DP [Pa]	q''_e [W/cm^2]	q" [W/cm^2]	q"/q''_e	h_1 [W/m^2 K]	h_2 [W/m^2 K]	h_3 [W/m^2 K]	T_{w1} [°C]	T_{w2} [°C]	T_{w3} [°C]
1	10735.6									
2	9481.0	40.5	**34.622**	85.6%	**4287.6**	**4356.6**	**4125.6**	-1.27	-1.70	-0.21
3	8808.0	80.0	**67.055**	83.8%	**4521.6**	**4500.4**	**4290.0**	22.82	23.06	25.51
4	8222.4	120.0	**100.103**	83.4%	**4657.2**	**4634.2**	**4417.2**	46.65	47.01	50.57
5	7995.0	163.3	**137.945**	84.5%	**5271.9**	**5247.7**	**4991.9**	64.11	64.52	69.03
6	8353.9	203.8	**176.650**	86.7%	**6555.4**	**6553.3**	**6192.1**	68.18	68.21	73.48
7	8918.3	242.2	**213.450**	88.1%	**7802.4**	**7827.3**	**7345.4**	71.12	70.82	76.82
8	10059.0	318.3	**287.050**	90.2%	**10474.6**	**10459.0**	**9775.2**	74.68	74.82	81.25
9	11444.4	401.5	**368.115**	91.7%	**13426.9**	**13445.7**	**12334.8**	77.28	77.15	85.43
10	13441.5	479.9	**444.580**	92.6%	**16465.7**	**16550.4**	**14915.6**	79.60	79.14	89.01
11	15699.5	560.7	**522.970**	93.3%	**19787.4**	**19981.3**	**17683.9**	81.56	80.70	92.11
12	16912.3	600.0	**561.250**	93.5%	**21267.2**	**21518.4**	**18894.5**	82.29	81.26	93.42
13	18211.5	643.2	**603.335**	93.8%	**23012.0**	**23339.2**	**20300.7**	83.07	81.83	94.82
14	19052.4	681.1	**640.385**	94.0%	**24612.9**	**25018.3**	**21567.2**	83.85	82.43	96.18

Table C.29 Test data, TS#3, Tin = -30 °C, m = 5.0 g/s.

- Test Section : 3
- D_h : 334.1 [μm]
- Number of Channels : 11
- Mass flow rate : 5.0 [g/s]
- T_{in} : -30 [°C]
- P_{out} : 16.5 [psia]
- T_{sat} (@ P_{out}) : 63.59 [°C]

Measurement data

No	T_{tc1} [°C]	T_{tc2} [°C]	T_{tc3} [°C]	T_{in} [°C]	T_{out} [°C]	P_{in} [psia]	P_{out} [psia]	Q [W]	$\dot{m}$ [g/s]
1	-27.5709	-27.6425	-27.4371	-29.9614	-30.2096	18.8063	16.5156	**0.0107**	5.0089
2	0.1680	0.2805	1.2708	-29.9768	-28.5374	18.5789	16.4963	**20.2340**	5.0089
3	27.0335	27.3490	29.2109	-29.8610	-26.3754	18.3989	16.4846	**40.6315**	5.0018
4	52.7562	53.3194	56.0368	-29.8787	-24.2421	18.2770	16.4878	**60.8499**	5.0090
5	73.6701	74.8880	78.5562	-30.0962	-22.4330	18.1672	16.4894	**79.4984**	5.0090
6	84.8731	85.9659	90.2867	-30.1989	-20.1744	18.1716	16.5149	**99.1019**	5.0071
7	92.3102	93.0123	97.9276	-30.3808	-17.1624	18.2144	16.5240	**119.5550**	5.0091
8	106.2369	106.4341	112.9968	-30.1680	-11.5851	18.3693	16.5115	**161.6949**	5.0057
9	117.4239	117.2387	125.3681	-29.7889	-4.1595	18.6064	16.4924	**200.0932**	5.0090
10	129.0663	128.6226	138.2927	-30.3004	0.1234	18.9741	16.5257	**238.7012**	5.0090
11	142.2159	141.4246	152.6936	-30.0570	4.8175	19.3133	16.4880	**279.3204**	5.0090
12	149.1169	148.2854	160.4725	-29.9392	7.3483	19.4596	16.5072	**299.6639**	5.0090
13	160.0056	160.3268	173.2444	-29.7285	10.3013	19.1039	16.5078	**319.9809**	5.0090

Reduced Data

No	DP [Pa]	q''_e [W/cm^2]	q" [W/cm^2]	q''/q''_e	h_1 [W/m^2 K]	h_2 [W/m^2 K]	h_3 [W/m^2 K]	T_{w1} [°C]	T_{w2} [°C]	T_{w3} [°C]
1	15793.7		0.0							
2	14359.1	40.5	**35.053**	86.6%	**4645.9**	**4625.4**	**4452.0**	-3.74	-3.63	-2.64
3	13198.3	81.3	**69.033**	85.0%	**4929.3**	**4896.4**	**4711.1**	19.28	19.60	21.46
4	12335.9	121.7	**102.920**	84.6%	**5109.7**	**5067.5**	**4873.5**	41.14	41.70	44.41
5	11567.9	159.0	**134.775**	84.8%	**5393.6**	**5316.6**	**5097.2**	58.39	59.61	63.26
6	11422.7	198.2	**171.310**	86.4%	**6419.4**	**6342.3**	**6054.5**	65.41	66.50	70.80
7	11655.3	239.1	**210.800**	88.2%	**7791.8**	**7732.2**	**7339.5**	68.32	69.02	73.91
8	12808.9	323.4	**292.190**	90.4%	**10667.4**	**10644.7**	**9940.8**	72.90	73.09	79.61
9	14575.4	400.2	**367.110**	91.7%	**13680.2**	**13708.1**	**12579.5**	75.44	75.26	83.32
10	16880.8	477.4	**441.845**	92.6%	**16357.8**	**16437.5**	**14858.6**	78.42	77.98	87.56
11	19479.9	558.6	**520.340**	93.1%	**19050.2**	**19214.3**	**17114.7**	82.43	81.65	92.79
12	20356.3	599.3	**559.685**	93.4%	**20332.6**	**20515.1**	**18129.8**	84.73	83.91	95.95
13	17899.8	640.0	**597.595**	93.4%	**20689.5**	**20622.0**	**18230.7**	91.12	91.44	104.20

Table C.30 Test data, TS#3, Tin = -30 °C, m = 10.0 g/s.

- Test Section : 3
- D_h : 334.1 [μm]
- Number of Channels : 11
- Mass flow rate : 10.0 [g/s]
- T_{in} : -30 [°C]
- P_{out} : 16.5 [psia]
- T_{sat} (@ P_{out}) : 63.59 [°C]

Measurement data

No	T_{tc1} [°C]	T_{tc2} [°C]	T_{tc3} [°C]	T_{in} [°C]	T_{out} [°C]	P_{in} [psia]	P_{out} [psia]	Q [W]	$\dot{m}$ [g/s]
1	-28.5213	-28.3993	-28.1446	-30.2204	-31.2205	22.2769	16.5189	**0.0000**	10.0022
2	12.2909	12.9550	14.9316	-30.1402	-28.6281	21.6514	16.5006	**40.5047**	9.9976
3	51.4678	52.7238	56.6129	-30.0270	-25.9817	21.2400	16.5041	**80.5437**	10.0027
4	84.0024	85.7754	91.4005	-29.7334	-23.9607	20.9170	16.4815	**118.9685**	10.0161
5	103.7080	104.9229	112.0933	-29.6760	-21.1463	20.8988	16.4989	**161.2734**	10.0057
6	114.8572	115.1339	123.5339	-29.6316	-18.8361	20.9576	16.5092	**198.5993**	10.0085
7	126.2927	125.7404	135.5592	-29.8031	-16.7841	20.8696	16.4801	**239.2861**	10.0016
8	139.0040	137.8318	149.0553	-30.0908	-14.1548	20.8055	16.5282	**280.4093**	10.0020
9	151.7357	150.1348	162.8440	-30.2590	-11.8144	20.5025	16.4939	**319.0163**	10.0186
10	166.0269	163.5074	177.7290	-30.4278	-10.3451	20.1526	16.5274	**358.8907**	10.0177

Reduced Data

No	DP [Pa]	q''_e [W/cm^2]	q" [W/cm^2]	q"/q"$_e$	h_1 [W/m^2 K]	h_2 [W/m^2 K]	h_3 [W/m^2 K]	T_{w1} [°C]	T_{w2} [°C]	T_{w3} [°C]
1	39700.5									
2	35513.8	81.0	**72.317**	89.3%	**7320.4**	**7176.9**	**6781.1**	4.21	4.87	6.84
3	32652.5	161.1	**142.255**	88.3%	**7632.6**	**7482.6**	**7053.6**	35.41	36.67	40.54
4	30581.3	237.9	**210.880**	88.6%	**8268.8**	**8101.6**	**7613.3**	60.05	61.81	67.41
5	30336.2	322.5	**290.810**	90.2%	**10369.7**	**10238.3**	**9526.1**	70.54	71.75	78.87
6	30670.5	397.2	**363.050**	91.4%	**12788.7**	**12752.0**	**11729.0**	73.36	73.63	81.96
7	30264.3	478.6	**441.950**	92.3%	**15433.7**	**15522.0**	**14087.2**	75.66	75.11	84.84
8	29490.6	560.8	**521.315**	93.0%	**17874.3**	**18088.7**	**16225.7**	79.14	77.98	89.08
9	27637.9	638.0	**595.605**	93.4%	**19920.8**	**20239.7**	**17957.4**	83.18	81.60	94.16
10	24995.0	717.8	**672.060**	93.6%	**21589.5**	**22115.3**	**19442.6**	88.48	85.99	100.02

Table C.31 Test data, TS#3, Tin = -30 °C, m = 15.0 g/s.

- Test Section : 3
- D_h : 334.1 [μm]
- Number of Channels : 11
- Mass flow rate : 15.0 [g/s]
- T_{in} : -30 [°C]
- P_{out} : 16.5 [psia]
- T_{sat} (@ P_{out}) : 63.59 [°C]

Measurement data

No	T_{tc1} [°C]	T_{tc2} [°C]	T_{tc3} [°C]	T_{in} [°C]	T_{out} [°C]	P_{in} [psia]	P_{out} [psia]	Q [W]	$\dot{m}$ [g/s]
1	-29.3109	-28.9118	-28.6781	-30.1871	-31.0660	27.4853	16.4975	**0.0000**	14.9883
2	5.3480	6.2446	8.3005	-29.9184	-29.4873	26.6214	16.5187	**40.5917**	15.0145
3	36.8727	38.4559	42.2956	-29.7584	-27.8348	25.9501	16.4882	**80.4994**	14.9946
4	65.9044	67.5616	73.2979	-29.9592	-26.4016	25.3875	16.4689	**119.8445**	14.9883
5	88.2377	89.6907	97.0186	-29.7992	-24.4092	24.9091	16.4751	**161.1491**	14.9778
6	107.7216	108.6953	117.2125	-30.1016	-23.8603	24.4328	16.4719	**199.0531**	14.9883
7	125.2627	125.2965	135.1283	-30.0164	-21.1269	23.6511	16.4847	**239.1991**	15.0029
8	138.7922	138.2394	149.5182	-30.1305	-19.0357	23.1833	16.5122	**281.8452**	14.9999
9	150.9418	148.9942	161.4659	-30.3498	-18.4752	22.6236	16.5305	**317.8772**	15.0026
10	164.5138	162.0241	175.9790	-30.2229	-17.6871	21.9090	16.5441	**359.5808**	14.9886

Reduced Data

No	DP [Pa]	q''_e [W/cm^2]	q" [W/cm^2]	q"/q''_e	h_1 [W/m^2 K]	h_2 [W/m^2 K]	h_3 [W/m^2 K]	T_{w1} [°C]	T_{w2} [°C]	T_{w3} [°C]
1	75757.9									
2	69655.4	81.2	**74.228**	91.4%	**9467.2**	**9155.6**	**8513.3**	-2.94	-2.04	0.01
3	65237.4	161.0	**145.915**	90.6%	**10129.4**	**9809.0**	**9110.0**	20.45	22.03	25.86
4	61491.4	239.7	**217.045**	90.6%	**10687.0**	**10434.4**	**9645.1**	41.34	42.99	48.70
5	58150.8	322.3	**294.135**	91.3%	**12333.7**	**12115.1**	**11121.0**	54.80	56.24	63.52
6	54889.0	398.1	**365.225**	91.7%	**13516.8**	**13374.4**	**12245.4**	66.03	67.00	75.45
7	49410.2	478.4	**441.405**	92.3%	**15204.8**	**15199.6**	**13818.0**	74.70	74.73	84.48
8	45995.8	563.7	**523.520**	92.9%	**17593.2**	**17690.1**	**15903.2**	78.68	78.13	89.29
9	42010.3	635.8	**592.920**	93.3%	**19270.1**	**19635.9**	**17507.6**	82.71	80.79	93.10
10	36989.7	719.2	**673.070**	93.6%	**21224.7**	**21725.7**	**19187.0**	86.87	84.41	98.17

Table C.32 Test data, TS#3, Tin = -30 °C, m = 20.0 g/s.

- Test Section : 3
- D_h : 334.1 [μm]
- Number of Channels : 11
- Mass flow rate : 20.0 [g/s]
- T_{in} : -30 [°C]
- P_{out} : 16.5 [psia]
- T_{sat} (@ P_{out}) : 63.59 [°C]

Measurement data

No	T_{tc1} [°C]	T_{tc2} [°C]	T_{tc3} [°C]	T_{in} [°C]	T_{out} [°C]	P_{in} [psia]	P_{out} [psia]	Q [W]	$\dot{m}$ [g/s]
1	-28.9678	-28.9467	-28.7192	-29.8796	-30.7719	34.9393	16.5777	**0.0000**	19.9945
2	-0.4436	-0.0501	1.9433	-29.8047	-29.8648	33.9041	16.6416	**39.9178**	19.9946
3	26.2995	27.0305	30.8385	-29.7902	-28.7880	32.9586	16.6263	**79.9843**	19.9945
4	49.1410	49.9658	55.4274	-29.8439	-27.6976	32.2384	16.5964	**119.9302**	19.9922
5	70.6227	71.3622	78.2080	-29.8348	-26.6456	31.6267	16.5785	**160.7013**	19.9984
6	95.1772	95.8363	104.3755	-29.7102	-25.6947	29.7267	16.5614	**199.0519**	19.9948
7	119.8776	120.7000	130.7426	-29.8410	-23.8302	27.6065	16.4963	**239.3122**	19.9949
8	135.0170	135.2654	146.6936	-29.9892	-23.0802	26.3841	16.4945	**278.7763**	19.9963
9	148.5491	147.4052	160.0548	-30.2089	-23.0840	25.2304	16.4808	**319.0165**	19.9948
10	163.3528	161.4452	175.5324	-30.0516	-21.9175	24.1673	16.5179	**363.9077**	19.9949

Reduced Data

No	DP [Pa]	q''_e [W/cm^2]	q" [W/cm^2]	q"/q''_e	h_1 [W/m^2 K]	h_2 [W/m^2 K]	h_3 [W/m^2 K]	T_{w1} [°C]	T_{w2} [°C]	T_{w3} [°C]
1	126598.7									
2	119020.8	79.8	**74.490**	93.3%	**12116.9**	**11890.5**	**10862.2**	-8.74	-8.35	-6.36
3	112607.3	160.0	**147.740**	92.4%	**13022.9**	**12778.5**	**11639.1**	9.71	10.44	14.23
4	107847.4	239.9	**221.785**	92.5%	**14455.6**	**14228.7**	**12888.8**	24.12	24.94	30.38
5	103754.1	321.4	**297.990**	92.7%	**15823.0**	**15641.1**	**14137.0**	36.86	37.60	44.40
6	90771.4	398.1	**368.500**	92.6%	**15741.4**	**15611.5**	**14103.5**	53.22	53.88	62.34
7	76602.1	478.6	**442.625**	92.5%	**15936.1**	**15798.1**	**14286.7**	69.23	70.05	79.99
8	68186.4	557.6	**517.920**	92.9%	**17599.2**	**17555.5**	**15755.9**	75.58	75.83	87.14
9	60326.3	638.0	**595.115**	93.3%	**19415.7**	**19631.3**	**17484.2**	80.09	78.96	91.46
10	52740.1	727.8	**681.445**	93.6%	**21516.3**	**21903.7**	**19332.8**	84.76	82.88	96.77

Table C.33 Test data, TS#4, Tin = 0 °C, m = 2.0 g/s.

- Test Section : 4
- D_h : 415.9 [μm]
- Number of Channels : 11
- Mass flow rate : 2.0 [g/s]
- T_{in} : 0 [°C]
- P_{out} : 16.5 [psia]
- T_{sat} (@ P_{out}) : 63.59 [°C]

Measurement data									
No	T_{tc1} [°C]	T_{tc2} [°C]	T_{tc3} [°C]	T_{in} [°C]	T_{out} [°C]	P_{in} [psia]	P_{out} [psia]	Q [W]	$\dot{m}$ [g/s]
1	0.1853	0.1868	0.2156	0.1213	0.7131	16.7422	16.5070	0.0000	1.9996
2	35.6566	35.7120	36.5801	-0.0740	6.8783	16.7304	16.5310	20.1796	1.9945
3	69.3606	69.4819	71.0943	-0.1006	12.5094	16.6738	16.5026	39.9432	1.9948
4	79.2101	79.3717	81.2293	-0.1593	17.5056	16.7076	16.5011	61.0237	2.0071
5	87.6904	87.8799	89.7961	-0.0360	24.9508	16.7733	16.5304	82.6733	2.0008
6	95.1671	95.3677	97.1733	-0.2222	30.8244	16.8122	16.5397	100.2943	1.9974
7	102.7152	103.0216	105.5001	-0.1443	36.6156	16.8933	16.5485	122.2312	2.0009
8	106.2357	106.5801	109.1059	-0.1650	38.9514	16.9440	16.5484	131.3240	1.9967
9	109.8973	110.2729	112.7863	-0.0688	40.8847	16.9901	16.5235	141.3482	1.9999
10	*111.7939*	*112.2115*	*114.7772*	*-0.0234*	*42.6776*	*17.0418*	*16.5249*	***151.5652***	*1.9741*

Reduced Data										
No	DP [Pa]	q''_e [W/cm^2]	q'' [W/cm^2]	q''/q''_e	h_1 [W/m^2 K]	h_2 [W/m^2 K]	h_3 [W/m^2 K]	T_{w1} [°C]	T_{w2} [°C]	T_{w3} [°C]
1	1621.4	0	0.0							
2	1374.9	40.4	27.479	68.1%	1876.7	1873.1	1818.9	32.88	32.94	33.81
3	1180.3	79.9	53.767	67.3%	1876.6	1872.6	1821.2	63.90	64.02	65.63
4	1423.5	122.0	93.092	76.3%	3098.9	3090.5	2997.6	69.74	69.90	71.75
5	1674.5	165.3	134.980	81.6%	4511.3	4497	4357.3	73.93	74.12	76.03
6	1878.9	200.6	168.840	84.2%	5583.4	5564.8	5403.6	77.93	78.13	79.93
7	2377.5	244.5	211.265	86.4%	7033.3	6997.5	6721.1	81.11	81.42	83.88
8	2727.8	262.6	228.750	87.1%	7578.4	7535.4	7234.1	82.83	83.17	85.68
9	3217.5	282.7	247.980	87.7%	8165.5	8115.3	7794.6	84.50	84.88	87.38
10										

Table C.34 Test data, TS#4, Tin = 0 °C, m = 3.0 g/s.

- Test Section : 4
- D_h : 415.9 [μm]
- Number of Channels : 11
- Mass flow rate : 3.0 [g/s]
- T_{in} : 0 [°C]
- P_{out} : 16.5 [psia]
- T_{sat} (@ P_{out}) : 63.59 [°C]

Measurement data									
No	T_{tc1} [°C]	T_{tc2} [°C]	T_{tc3} [°C]	T_{in} [°C]	T_{out} [°C]	P_{in} [psia]	P_{out} [psia]	Q [W]	$\dot{m}$ [g/s]
1	0.576881	0.577318	0.585634	0.015936	0.301179	17.00151	16.60179	**0**	3.05532
2	30.34922	30.37804	30.82959	-0.101085	3.960301	16.7467	16.40775	**20.21218**	2.956887
3	59.28207	59.39361	60.87548	-0.36292	7.824928	16.79919	16.4844	**40.53408**	2.956486
4	67.03109	67.13452	68.32394	0.556011	11.50526	16.81382	16.52209	**49.85563**	3.052429
5	77.31541	77.49516	79.31262	0.211415	13.10857	16.79817	16.48727	**59.72888**	2.967542
6	86.21818	86.38824	87.9188	0.293367	15.08587	16.86571	16.52944	**79.48434**	3.005673
7	94.1807	94.38445	96.03293	-0.037037	18.59926	16.8002	16.43776	**100.6733**	2.933877
8	102.8127	103.0892	105.1167	-0.161603	22.38322	16.96697	16.52775	**121.7075**	2.988234
9	108.7017	109.1618	112.2409	-0.058724	27.28865	17.11368	16.62689	**139.3054**	2.949948
10	114.6146	115.2155	118.9067	-0.142901	30.54053	17.2806	16.7121	**157.2975**	2.968856
11	122.0228	122.6936	126.495	0.154027	35.31362	17.31401	16.57499	**182.7845**	3.003403
12	127.5528	128.4137	132.9332	0.099713	38.87358	17.32222	16.52098	**200.1702**	3.003401
13	*132.578*	*133.8048*	*139.7941*	*-1.350537*	*40.30583*	*17.46215*	*16.60021*	***210.5933***	*3.015598*

Reduced Data										
No	DP [Pa]	q''_e [W/cm^2]	q'' [W/cm^2]	q''/q''_e	h_1 [W/m^2 K]	h_2 [W/m^2 K]	h_3 [W/m^2 K]	T_{w1} [°C]	T_{w2} [°C]	T_{w3} [°C]
1	2756.0		0.0							
2	2337.0	40.4	29.339	72.6%	2328.0	2325.3	2284.2	27.39	27.42	27.87
3	2170.4	81.1	58.391	72.0%	2378.1	2372.7	2302.9	53.36	53.47	54.95
4	2011.4	99.7	75.083	75.3%	2853.8	2848.1	2785.0	59.41	59.51	60.70
5	2143.6	119.5	90.514	75.8%	2991.8	2982.9	2895.7	68.11	68.29	70.10
6	2318.5	159.0	127.310	80.1%	3973.9	3963.4	3870.8	73.24	73.41	74.94
7	2499.0	201.3	167.730	83.3%	5107.1	5091.3	4966.6	77.06	77.26	78.90
8	3028.3	243.4	207.460	85.2%	6120.0	6095.1	5918.4	81.60	81.87	83.89
9	3356.3	278.6	241.595	86.7%	7197.3	7148.3	6836.6	83.97	84.42	87.49
10	3919.6	314.6	276.275	87.8%	8204.0	8131.5	7712.6	86.29	86.89	90.56
11	5095.4	365.6	326.175	89.2%	9840.2	9741.8	9219.4	88.54	89.20	92.98
12	5524.4	400.3	359.865	89.9%	10894.9	10755.0	10075.9	90.57	91.42	95.91
13										

Table C.35 Test data, TS#4, Tin = 0 °C, m = 4.0 g/s.

- Test Section : 4
- D_h : 415.9 [μm]
- Number of Channels : 11
- Mass flow rate : 4.0 [g/s]
- T_{in} : 0 [°C]
- P_{out} : 16.5 [psia]
- T_{sat} (@ P_{out}) : 63.59 [°C]

Measurement data

No	T_{tc1} [°C]	T_{tc2} [°C]	T_{tc3} [°C]	T_{in} [°C]	T_{out} [°C]	P_{in} [psia]	P_{out} [psia]	Q [W]	$\dot{m}$ [g/s]
1	-0.159485	-0.136284	0.304539	0.006923	0.18253	17.0351	16.50468	**0**	4.004219
2	28.53984	28.59176	29.40519	0.033186	3.282261	16.99372	16.4957	**20.14906**	4.006057
3	56.82082	56.96852	58.66708	0.063935	6.502368	16.98226	16.5148	**39.74445**	4.006607
4	76.49398	76.7095	79.02951	0.357823	10.26175	16.95088	16.51686	**59.05548**	4.003857
5	88.45388	88.63984	90.52006	-0.155666	13.37248	17.01754	16.54887	**80.51196**	4.001185
6	94.13675	94.29782	95.92651	-0.178632	16.61264	17.06491	16.56327	**98.84563**	4.008848
7	100.5608	100.7253	102.2923	-0.233991	19.72872	17.11282	16.57098	**119.9479**	4.006293
8	107.669	107.8564	109.5427	-0.240043	20.4007	17.1739	16.562	**141.6338**	4.006299
9	114.4785	114.71	116.5829	-0.084175	23.9833	17.30119	16.59242	**162.454**	4.005733
10	120.2944	120.5707	122.5963	-0.327567	26.96271	17.37348	16.53839	**181.1798**	4.00625
11	126.4299	126.7471	128.8697	-0.117475	30.49168	17.52684	16.53339	**201.5158**	4.006292
12	132.0329	132.4004	134.6575	-0.212642	33.4249	17.68584	16.51933	**220.3307**	4.006231
13	138.4967	138.9314	141.3944	-0.120946	37.25849	17.89041	16.51951	**241.8041**	4.004041
14	144.1296	144.6264	147.2348	-0.211609	40.30501	18.11048	16.53026	**260.8207**	4.006205
15	150.7802	151.365	154.2202	-0.109698	43.89882	18.32991	16.52929	**281.1359**	4.006171
16	156.7412	157.4486	160.6714	0.087158	46.99813	18.50207	16.52691	**299.5289**	4.006251
17	*163.6342*	*164.0863*	*168.6665*	*0.047839*	*47.49181*	*18.50184*	*16.53954*	***321.1955***	*4.005576*

Reduced Data

No	DP [Pa]	q''_e [W/cm^2]	q" [W/cm^2]	q"/q''_e	h_1 [W/m^2 K]	h_2 [W/m^2 K]	h_3 [W/m^2 K]	T_{w1} [°C]	T_{w2} [°C]	T_{w3} [°C]
1	3657.1		0.0							
2	3433.7	40.3	29.882	74.2%	2533.0	2527.4	2442.8	25.53	25.58	26.39
3	3223.0	79.5	57.724	72.6%	2448.0	2440.3	2355.2	50.97	51.12	52.82
4	2992.4	118.1	89.009	75.4%	2907.8	2897.5	2791.5	67.44	67.66	69.97
5	3231.4	161.0	127.970	79.5%	3801.3	3790.8	3687.7	75.41	75.59	77.47
6	3458.7	197.7	163.580	82.7%	4868.2	4856.5	4741.5	77.44	77.60	79.22
7	3735.8	239.9	204.370	85.2%	6075.2	6060.4	5922.5	79.67	79.83	81.39
8	4218.9	283.3	245.660	86.7%	7102.2	7083.0	6914.8	82.52	82.71	84.39
9	4886.7	324.9	286.080	88.0%	8253.4	8225.9	8010.3	85.15	85.38	87.25
10	5757.7	362.4	322.245	88.9%	9276.3	9239.6	8979.3	87.22	87.50	89.51
11	6849.6	403.0	361.780	89.8%	10480.6	10432.9	10123.7	89.25	89.57	91.68
12	8042.8	440.7	398.280	90.4%	11564.6	11503.5	11141.5	91.07	91.43	93.67
13	9452.0	483.6	440.135	91.0%	12870.9	12790.0	12350.1	93.17	93.60	96.05
14	10895.2	521.6	477.060	91.5%	14001.8	13901.1	13395.2	94.95	95.45	98.03
15	12414.8	562.3	516.310	91.8%	15129.6	15002.1	14408.9	97.49	98.07	100.90
16	13618.2	599.1	551.870	92.1%	16158.8	15994.7	15287.0	99.72	100.42	103.61
17										

Table C.36 Test data, TS#4, Tin = 0 °C, m = 5.0 g/s.

- Test Section : 4
- D_h : 415.9 [μm]
- Number of Channels : 11
- Mass flow rate : 5.0 [g/s]
- T_{in} : 0 [°C]
- P_{out} : 16.5 [psia]
- T_{sat} (@ P_{out}) : 63.59 [°C]

Measurement data									
No	T_{tc1} [°C]	T_{tc2} [°C]	T_{tc3} [°C]	T_{in} [°C]	T_{out} [°C]	P_{in} [psia]	P_{out} [psia]	Q [W]	$\dot{m}$ [g/s]
1	0.440988	0.442231	0.465855	0.058454	0.130554	17.33576	16.54545	**0**	5.012116
2	25.37858	25.42177	26.16378	-0.02662	2.467137	17.26732	16.51494	**19.64372**	5.008682
3	50.02368	50.1183	51.60079	0.085194	5.187305	17.21804	16.50527	**40.02882**	5.014944
4	73.98829	74.16003	76.63047	0.051426	8.312456	17.16488	16.52067	**59.67617**	5.008712
5	86.39626	86.56362	88.78714	-0.011382	10.82533	17.22022	16.54479	**81.10575**	5.008862
6	93.99479	94.13856	95.91183	0.009696	12.66829	17.2845	16.56277	**100.8657**	5.008818
7	100.0187	100.1609	101.7961	-0.148743	14.61938	17.26832	16.50516	**120.0545**	5.008889
8	105.9066	106.0569	107.6746	-0.0962	18.42732	17.33173	16.49976	**139.6412**	5.008843
9	111.8974	112.0602	113.7065	-0.145508	21.51951	17.47608	16.54478	**160.6619**	5.00677
10	116.7472	116.9192	118.5583	-0.132233	23.93667	17.59933	16.56529	**178.8915**	5.004972
11	122.5063	122.6863	124.3055	-0.058118	27.16217	17.63327	16.52499	**201.7571**	5.008933
12	127.9359	128.134	129.8224	-0.097604	29.4289	17.77876	16.56176	**221.5572**	5.008961
13	133.4668	133.6758	135.3664	-0.261744	31.88111	17.901	16.61768	**240.7354**	5.005372
14	138.7037	139.0378	141.6089	-0.436358	33.86974	17.87016	16.54502	**258.4648**	5.008983
15	145.9598	146.5948	151.2516	-0.25872	36.09202	17.91224	16.56064	**282.1314**	5.009076
16	152.6478	153.6616	160.7582	-0.622614	39.0871	17.92127	16.56322	**302.7733**	5.009007
17	159.6446	161.1464	171.1967	-0.647046	42.19062	17.94203	16.58905	**321.8921**	5.005632

Reduced Data										
No	DP [Pa]	q''_e [W/cm^2]	q'' [W/cm^2]	q''/q''_e	h_1 [W/m^2 K]	h_2 [W/m^2 K]	h_3 [W/m^2 K]	T_{w1} [°C]	T_{w2} [°C]	T_{w3} [°C]
1	5449.0		0.0							
2	5187.5	39.3	30.073	76.5%	2887.5	2881.5	2782	22.35	22.39	23.14
3	4914.4	80.1	61.107	76.3%	3012.1	3005.1	2898.7	43.84	43.94	45.42
4	4441.7	119.4	90.925	76.2%	3050.6	3041.8	2920.4	64.74	64.92	67.38
5	4656.9	162.2	129.590	79.9%	3910.3	3900.4	3773.6	73.19	73.36	75.57
6	4976.2	201.7	167.045	82.8%	4874.2	4863.9	4741.1	76.94	77.09	78.85
7	5261.8	240.1	203.980	85.0%	5885.8	5873.7	5738.3	79.17	79.31	80.94
8	5736.2	279.3	242.190	86.7%	7045.9	7030.5	6869.1	81.12	81.27	82.88
9	6421.1	321.3	283.110	88.1%	8282.1	8262.4	8068.7	82.89	83.05	84.69
10	7129.4	357.8	318.670	89.1%	9402.7	9378.9	9158.4	84.066	84.237	85.865
11	7641.3	403.5	363.640	90.1%	10928.2	10898.8	10641.4	85.17	85.348	86.955
12	8390.9	443.1	402.170	90.8%	12134.3	12098.3	11799.7	86.599	86.795	88.471
13	8848.2	481.5	439.240	91.2%	13257.3	13215.8	12889.6	88.275	88.482	90.159
14	9136.6	516.9	473.520	91.6%	14238.7	14168	13646.3	89.939	90.27	92.819
15	9318.9	564.3	518.650	91.9%	15440	15296.5	14320.6	92.478	93.107	97.719
16	9363.4	605.5	558.090	92.2%	16453.9	16213.9	14710.9	95.03	96.034	103.057
17	9328.5	643.8	594.115	92.3%	17229.1	16865.8	14778.5	98.231	99.716	109.656

Table C.37 Test data, TS#4, Tin = 0 °C, m = 10.0 g/s.

• Test Section	:	4	• Mass flow rate	:	10.0 [g/s]
• D_h	:	415.9 [μm]	• T_{in}	:	0 [°C]
• Number of Channels	:	11	• P_{out}	:	16.5 [psia]
			• T_{sat} (@ P_{out})	:	63.59 [°C]

Measurement data

No	T_{tc1} [°C]	T_{tc2} [°C]	T_{tc3} [°C]	T_{in} [°C]	T_{out} [°C]	P_{in} [psia]	P_{out} [psia]	Q [W]	$\dot{m}$ [g/s]
1	0.192827	0.193739	0.211051	-0.06679	-0.214643	18.69744	16.49885	**0**	10.01647
2	37.61766	37.70533	39.07886	0.06581	2.54003	18.62171	16.51718	**40.49212**	10.01311
3	73.04158	73.28039	76.02674	0.037047	5.222668	18.54242	16.5232	**80.5631**	10.0223
4	96.92705	97.20925	100.2471	0.081129	8.018157	18.4309	16.45919	**121.1288**	10.01333
5	110.8012	111.0416	113.4724	0.089722	10.32119	18.57808	16.50978	**161.0226**	9.987545
6	121.4605	121.6682	123.7675	0.16726	13.08633	18.70881	16.53987	**198.9039**	9.990765
7	133.2536	133.4539	135.3619	0.077632	15.32805	18.87674	16.52229	**240.9335**	9.993966
8	144.762	144.9711	146.8525	0.25109	18.28646	19.17823	16.54258	**282.2119**	10.00882
9	153.9463	154.3206	157.3493	0.179042	20.76289	19.5037	16.5571	**320.0253**	9.989195
10	164.0655	164.4852	167.5634	0.012582	23.37205	19.76484	16.57777	**359.5657**	9.999134
11	170.8496	171.3115	174.4025	-0.261928	25.04392	19.87154	16.54606	**385.2911**	10.02276

Reduced Data

No	DP [Pa]	q''_e [W/cm^2]	q" [W/cm^2]	q"/q''_e	h_1 [W/m^2 K]	h_2 [W/m^2 K]	h_3 [W/m^2 K]	T_{w1} [°C]	T_{w2} [°C]	T_{w3} [°C]
1	15158.7		0.0							
2	14510.2	81.0	67.106	82.9%	4670.8	4656.5	4443.5	30.84	30.93	32.30
3	13922.1	161.1	133.365	82.8%	4830.1	4809.3	4581.4	59.49	59.72	62.46
4	13594.5	242.3	205.880	85.0%	5950.5	5926.3	5677.5	75.90	76.18	79.20
5	14260.5	322.0	281.800	87.5%	7726.6	7701.2	7453.7	81.94	82.18	84.59
6	14954.3	397.8	355.190	89.3%	9668.7	9641.6	9375.1	85.00	85.21	87.29
7	16233.4	481.9	436.300	90.5%	11705.9	11674.7	11385.2	88.37	88.56	90.46
8	18172.2	564.4	516.280	91.5%	13776.3	13738.3	13405	91.54	91.74	93.61
9	20316.1	640.1	589.800	92.1%	15906.1	15827	15214.6	93.04	93.41	96.41
10	21974.1	719.1	666.775	92.7%	18057.7	17956.9	17250.9	95.09	95.50	98.54
11	22928.4	770.6	716.595	93.0%	19377.8	19259.3	18501.9	96.63	97.08	100.13

Table C.38 Test data, TS#4, Tin = 0 °C, m = 15.0 g/s.

- Test Section : 4
- D_h : 415.9 [μm]
- Number of Channels : 11
- Mass flow rate : 15.0 [g/s]
- T_{in} : 0 [°C]
- P_{out} : 16.5 [psia]
- T_{sat} (@ P_{out}) : 63.59 [°C]

Measurement data									
No	T_{tc1} [°C]	T_{tc2} [°C]	T_{tc3} [°C]	T_{in} [°C]	T_{out} [°C]	P_{in} [psia]	P_{out} [psia]	Q [W]	$\dot{m}$ [g/s]
1	0.510219	0.510861	0.523054	0.121111	-0.086766	20.57812	16.50815	**0.034897**	15.01678
2	30.62393	30.73766	32.51954	0.029885	1.561532	20.47126	16.51152	**40.40043**	14.99944
3	60.09612	60.37073	63.52876	0.009854	3.354712	20.35834	16.49719	**80.07017**	15.02163
4	87.64318	87.99727	91.80897	0.048916	5.16923	20.2191	16.474	**119.042**	15.03101
5	100.0978	100.4997	104.5637	0.131655	6.373315	20.09943	16.45596	**141.0101**	15.02251
6	108.5451	108.9074	112.5707	0.001473	6.993636	20.1935	16.54419	**160.8014**	15.00253
7	120.4396	120.7004	123.1847	-0.101614	8.519583	20.32301	16.54593	**200.8443**	15.01096
8	131.9456	132.1786	134.2749	-0.091544	10.14918	20.47439	16.57456	**241.502**	15.0144
9	141.111	141.4518	144.2092	0.092436	11.95827	20.59566	16.5419	**279.7831**	15.02955
10	150.987	151.3568	154.0682	0.030599	13.99914	20.62984	16.56271	**319.4765**	15.02506
11	162.7616	163.2085	166.1994	0.041718	15.45963	20.69058	16.58485	**363.4509**	15.03335
12	172.9922	173.5073	176.6712	0.002992	17.81536	20.59485	16.53307	**401.7183**	15.01405

Reduced Data										
No	DP [Pa]	q''_e [W/cm^2]	q" [W/cm^2]	q"/q''_e	h_1 [W/m^2 K]	h_2 [W/m^2 K]	h_3 [W/m^2 K]	T_{w1} [°C]	T_{w2} [°C]	T_{w3} [°C]
1	28061.5		0.0							
2	27301.5	80.8	69.808	86.4%	6376.2	6343	5865.6	23.59	23.70	25.48
3	26621.8	160.1	137.730	86.0%	6456.1	6414.6	5973.7	46.13	46.41	49.56
4	25821.5	238.1	205.105	86.1%	6677	6638.6	6252.2	66.73	67.09	70.88
5	25120.9	282.0	244.660	86.8%	7133.7	7092.1	6697.2	75.09	75.49	79.54
6	25161.1	321.6	281.500	87.5%	7771.8	7733.1	7362.7	79.72	80.08	83.73
7	26042.0	401.7	358.465	89.2%	9623.5	9590	9282.3	83.65	83.91	86.37
8	26888.4	483.0	436.965	90.5%	11521.8	11486.7	11179.9	87.00	87.23	89.31
9	27949.8	559.6	511.515	91.4%	13613.9	13552.9	13078.3	88.41	88.75	91.48
10	28041.9	639.0	588.735	92.1%	15737.1	15660.5	15120.4	90.22	90.59	93.27
11	28308.0	726.9	673.710	92.7%	17801.7	17698.6	17037.6	93.08	93.52	96.48
12	28005.0	803.4	747.715	93.1%	19707.5	19576.7	18809.7	95.52	96.02	99.14

Table C.39 Test data, TS#4, Tin = 0 °C, m = 20.0 g/s.

- Test Section : 4
- D_h : 415.9 [μm]
- Number of Channels : 11
- Mass flow rate : 20.0 [g/s]
- T_{in} : 0 [°C]
- P_{out} : 16.5 [psia]
- T_{sat} (@ P_{out}) : 63.59 [°C]

Measurement data									
No	T_{tc1} [°C]	T_{tc2} [°C]	T_{tc3} [°C]	T_{in} [°C]	T_{out} [°C]	P_{in} [psia]	P_{out} [psia]	Q [W]	$\dot{m}$ [g/s]
1	-0.153986	-0.136069	0.204359	-0.079714	-0.296111	22.74066	16.54969	**0.02135**	20.00213
2	27.62953	27.73447	29.37839	-0.002232	1.141139	22.56726	16.54301	**40.09406**	19.99166
3	54.56247	54.80854	57.63839	-0.078695	2.413622	22.39618	16.53574	**80.05812**	19.9884
4	80.80457	81.15135	84.88437	-0.009696	3.794748	22.28051	16.54762	**120.1158**	20.01246
5	104.2348	104.6949	109.3471	-0.014797	5.144863	22.08171	16.53657	**160.2175**	20.02125
6	121.586	121.9567	125.7057	0.011261	6.547368	21.97923	16.52155	**203.9888**	19.99503
7	132.7251	133.0424	136.0652	-0.110507	7.598503	22.00766	16.52672	**239.2297**	19.99497
8	143.5344	143.8132	146.3232	0.045898	9.069458	22.09226	16.51805	**280.721**	20.01539
9	153.1573	153.4665	155.9677	0.003015	10.18022	22.23806	16.51884	**318.846**	19.99622
10	163.4071	163.8653	167.2259	-0.10821	11.06472	22.44372	16.51736	**362.5248**	20.02144
11	173.6284	174.1135	177.3601	-0.203439	12.62563	22.55517	16.5392	**403.5734**	20.00813

Reduced Data										
No	DP [Pa]	q''_e [W/cm^2]	q'' [W/cm^2]	q''/q''_e	h_1 [W/m^2 K]	h_2 [W/m^2 K]	h_3 [W/m^2 K]	T_{w1} [°C]	T_{w2} [°C]	T_{w3} [°C]
1	42685.2		0.0							
2	41535.8	80.2	70.469	87.9%	7403.2	7362.4	6777.4	20.53	20.64	22.28
3	40406.4	160.1	140.080	87.5%	7499.6	7450.4	6927.3	40.38	40.62	43.44
4	39526.9	240.2	210.205	87.5%	7684.8	7636.4	7150.7	59.40	59.75	63.47
5	38232.4	320.4	281.700	87.9%	8159.6	8105.6	7597.2	75.42	75.88	80.50
6	37629.4	408.0	363.890	89.2%	9584.3	9537.9	9092.4	84.23	84.60	88.32
7	37789.8	478.5	431.190	90.1%	10971.6	10927.6	10525.9	88.37	88.68	91.68
8	38432.9	561.4	511.665	91.1%	12952.1	12906.8	12513.2	90.80	91.07	93.56
9	39432.7	637.7	585.515	91.8%	14770.6	14713.8	14269.3	92.70	93.01	95.48
10	40860.8	725.0	670.320	92.5%	16969.1	16872.5	16195.7	94.07	94.52	97.84
11	41478.6	807.1	750.140	92.9%	19010.1	18895.7	18164.1	95.89	96.37	99.57

Table C.40 Test data, TS#4, Tin = -30 °C, m = 2.0 g/s.

• Test Section	:	4	• Mass flow rate	:	2 [g/s]
• D_h	:	415.9 [μm]	• T_{in}	:	-30 [°C]
• Number of Channels	:	11	• P_{out}	:	16.5 [psia]
			• T_{sat} (@ P_{out})		63.59 [°C]

Measurement data									
No	T_{tc1} [°C]	T_{tc2} [°C]	T_{tc3} [°C]	T_{in} [°C]	T_{out} [°C]	P_{in} [psia]	P_{out} [psia]	Q [W]	$\dot{m}$ [g/s]
1	-31.4602	-31.4411	-31.0786	-30.0800	-28.8539	16.8989	16.4949	**0.0000**	2.0007
2	0.1127	0.1880	1.3667	-30.0621	-23.4858	16.8379	16.5101	**19.6153**	2.0008
3	33.4340	33.5523	35.1238	-29.9782	-18.2480	16.7805	16.5083	**39.9330**	2.0008
4	70.3483	70.5786	73.2271	-30.0953	-10.9911	16.7917	16.5642	**60.7761**	2.0042
5	80.6745	80.9043	83.2281	-29.8669	-9.6115	16.7732	16.5473	**78.8679**	2.0008
6	89.0195	89.2376	91.2000	-29.7692	0.4327	16.8066	16.5267	**101.9174**	2.0008
7	96.2706	96.5137	98.4814	-29.9865	5.2533	16.8467	16.5590	**121.6788**	1.9984
8	102.6413	102.9240	104.9967	-30.1413	10.0462	16.8197	16.5062	**140.0760**	2.0034
9	110.2104	110.5403	112.7478	-29.9711	15.5621	16.8555	16.5045	**159.6389**	2.0009
10	117.8042	118.2306	120.8499	-29.9339	19.0870	17.0197	16.5832	**180.6934**	2.0008
11	124.5051	125.0110	127.8782	-29.8661	22.5242	17.1396	16.6208	**200.8201**	2.0009
12	131.2926	131.8829	134.9815	-29.2875	29.2573	17.2742	16.6413	**220.8390**	1.9979
13	138.2671	138.9468	142.2652	-28.4794	36.2834	17.4196	16.6461	**239.5550**	1.9980
14	*141.3076*	*142.1477*	*145.9747*	*-30.5140*	*37.8405*	*17.4381*	*16.6344*	***257.9563***	*2.0009*

Reduced Data										
No	DP [Pa]	q''_e [W/cm^2]	q" [W/cm^2]	q''/q''_e	h_1 [W/m^2 K]	h_2 [W/m^2 K]	h_3 [W/m^2 K]	T_{w1} [°C]	T_{w2} [°C]	T_{w3} [°C]
1	2785.4	0.0	0.0							
2	2260.3	39.2	30.013	76.5%	2542.2	2534	2413.2	-2.89	-2.81	-1.63
3	1877.0	79.9	57.589	72.1%	2247.5	2242.3	2175.3	27.63	27.74	29.31
4	1568.3	121.6	84.882	69.8%	2081	2075.1	2009.6	61.73	61.95	64.60
5	1557.5	157.7	117.370	74.4%	2688.5	2681.4	2611.7	68.73	68.95	71.27
6	1929.7	203.8	162.670	79.8%	3817.2	3807.4	3721.6	72.43	72.65	74.60
7	1983.5	243.4	200.765	82.5%	4686.4	4673.1	4568.3	75.77	76.01	77.97
8	2161.4	280.2	236.420	84.4%	5529.9	5511.6	5381.4	78.47	78.75	80.81
9	2419.6	319.3	270.045	84.6%	6262.8	6238.9	6083.7	82.55	82.88	85.08
10	3009.1	361.4	314.330	87.0%	7243.6	7208.2	6998.2	85.56	85.99	88.59
11	3577.0	401.6	353.065	87.9%	8105.1	8058.4	7803.5	88.24	88.74	91.59
12	4363.7	441.7	392.360	88.8%	9172	9109.3	8793.7	90.94	91.53	94.60
13	5332.9	479.1	429.225	89.6%	10195.7	10114.3	9735	94.07	94.74	98.03
14										

Table C.41 Test data, TS#4, Tin = -30 °C, m = 3.0 g/s.

- Test Section : 4
- D_h : 415.9 [μm]
- Number of Channels : 11
- Mass flow rate : 3 [g/s]
- T_{in} : -30 [°C]
- P_{out} : 16.5 [psia]
- T_{sat} (@ P_{out}) 63.59 [°C]

Measurement data									
No	T_{tc1} [°C]	T_{tc2} [°C]	T_{tc3} [°C]	T_{in} [°C]	T_{out} [°C]	P_{in} [psia]	P_{out} [psia]	Q [W]	$\dot{m}$ [g/s]
1	-30.61856	-30.61388	-30.52494	-30.1565	-29.95601	17.12808	16.50373	**0**	3.003194
2	-0.814706	-0.770074	-0.003209	-29.8863	-25.38783	17.01221	16.49593	**19.52935**	3.003274
3	28.93894	29.04342	30.68025	-29.94142	-21.30121	16.95366	16.50157	**40.50779**	3.003306
4	56.85208	57.02142	59.45742	-30.03132	-18.27882	16.91209	16.50677	**60.70905**	3.003277
5	78.29474	78.53116	81.67218	-29.86193	-13.81721	16.88332	16.50555	**80.47711**	3.003308
6	87.25082	87.50381	90.62407	-30.26386	-10.07103	16.91995	16.52003	**101.0796**	3.003335
7	96.01388	96.28095	99.35225	-30.01393	-6.308916	16.93078	16.50896	**123.1344**	3.003274
8	102.7897	103.0691	106.0777	-30.07294	-1.935167	17.02734	16.55893	**142.0907**	3.00341
9	109.2422	109.4784	111.8663	-29.79809	-0.279192	17.02731	16.5316	**160.7459**	3.00339
10	115.7237	115.9564	118.1726	-30.19693	1.786237	17.06962	16.51541	**181.3712**	3.00089
11	122.4271	122.7003	125.1583	-30.00342	4.659206	17.15709	16.55296	**202.0605**	3.003327
12	127.7707	128.111	131.0113	-30.16195	7.416452	17.19344	16.51886	**220.5242**	3.003403
13	130.7532	131.1056	133.9565	-30.09941	8.935128	17.2415	16.52534	**230.4896**	3.003348
14	133.7245	134.3035	138.7589	-30.19584	10.28313	17.25832	16.51292	**241.2178**	3.005021
15	137.8783	138.5417	143.4066	-30.15327	13.10493	17.32572	16.54416	**254.948**	3.003309
16	139.7675	140.4746	145.4245	-29.93715	15.48568	17.31409	16.50871	**259.9889**	3.003269
17	143.8571	144.739	150.6409	-29.80856	17.93537	17.32165	16.51128	**271.2521**	2.99322
18	145.8752	146.9526	153.8553	-30.37011	17.78095	17.38871	16.55721	**280.2983**	3.003361
19	149.6092	150.8999	158.8283	-30.16845	19.6244	17.40426	16.57903	**290.3825**	3.003323
20	152.44	153.7582	161.5314	-30.04183	21.29562	17.35311	16.532	**300.0213**	3.003299
21	158.0322	159.7279	169.3366	-30.09495	23.88419	17.37687	16.55047	**313.0487**	3.003415
22	160.8472	162.5097	171.5726	-30.16999	24.7545	17.40615	16.5775	**321.6362**	3.003387
23	*170.8633*	*172.3075*	*179.6159*	*-29.71283*	*29.05068*	*17.33788*	*16.56043*	***343.5413***	*3.003384*

Reduced Data										
No	DP [Pa]	q''_e [W/cm^2]	q" [W/cm^2]	q"/q''_e	h_1 [W/m^2 K]	h_2 [W/m^2 K]	h_3 [W/m^2 K]	T_{w1} [°C]	T_{w2} [°C]	T_{w3} [°C]
1	4304.7		0.0							
2	3559.6	39.1	29.994	76.8%	2547.2	2542.4	2461.8	-3.81	-3.77	-3.00
3	3117.1	81.0	60.129	74.2%	2508.2	2502.7	2419.7	22.88	22.99	24.62
4	2794.6	121.4	89.273	73.5%	2510.2	2504.2	2421.0	47.81	47.98	50.41
5	2604.6	161.0	120.780	75.0%	2788.2	2780.6	2683.1	66.00	66.24	69.37
6	2757.4	202.2	159.480	78.9%	3568.9	3558.7	3438.6	70.99	71.25	74.36
7	2908.3	246.3	201.310	81.7%	4414.9	4402.0	4258.6	75.46	75.72	78.78
8	3229.6	284.2	238.020	83.8%	5204.6	5188.7	5023.7	78.45	78.73	81.72
9	3417.8	321.5	273.720	85.1%	5904.0	5889.0	5741.5	81.21	81.45	83.82
10	3821.1	362.7	313.560	86.4%	6697.0	6680.4	6526.4	83.57	83.80	86.01
11	4165.4	404.1	353.505	87.5%	7516.9	7495.2	7305.2	86.13	86.40	88.84
12	4651.1	441.0	389.210	88.2%	8294.9	8265.0	8018.5	87.77	88.10	90.98
13	4937.8	461.0	408.685	88.7%	8722.1	8689.5	8434.5	88.73	89.08	91.90
14	5139.3	482.4	429.135	89.0%	9167.6	9111.5	8701.1	89.57	90.14	94.57
15	5388.7	509.9	455.820	89.4%	9786.7	9717.7	9240.3	90.94	91.60	96.43
16	5552.9	520.0	465.920	89.6%	10070.9	9994.8	9492.9	91.78	92.48	97.39
17	5587.3	542.5	487.530	89.9%	10514.2	10415.6	9800.6	93.60	94.48	100.33
18	5733.0	560.6	504.675	90.0%	10845.0	10721.6	9992.7	93.84	94.90	101.74
19	5689.8	580.8	523.950	90.2%	11211.5	11059.7	10210.2	95.55	96.82	104.68
20	5661.4	600.0	542.650	90.4%	11650.4	11488.9	10620.5	96.42	97.72	105.42
21	5697.8	626.1	566.850	90.5%	11989.1	11779.4	10716.9	99.45	101.13	110.64
22	5713.4	643.3	583.495	90.7%	12287.0	12077.3	11048.7	100.52	102.16	111.13
23										

Table C.42 Test data, TS#4, Tin = -30 °C, m = 4.0 g/s.

• Test Section	:	4	• Mass flow rate	:	4 [g/s]
• D_h	:	415.9 [μm]	• T_{in}	:	-30 [°C]
• Number of Channels	:	11	• P_{out}	:	16.5 [psia]
			• T_{sat} (@ P_{out})		63.59 [°C]

Measurement data									
No	T_{tc1} [°C]	T_{tc2} [°C]	T_{tc3} [°C]	T_{in} [°C]	T_{out} [°C]	P_{in} [psia]	P_{out} [psia]	Q [W]	$\dot{m}$ [g/s]
1	-29.21389	-29.20733	-29.08279	-30.04629	-30.5846	17.338	16.53082	**0**	4.006075
2	-2.641575	-2.590967	-1.798096	-30.43141	-26.43825	17.18729	16.48567	**20.08233**	4.006173
3	23.64631	23.7778	25.28997	-29.82145	-22.77155	17.12668	16.51305	**39.92062**	4.006086
4	52.91068	53.13503	55.55004	-29.97921	-19.32412	17.06441	16.51519	**60.76602**	4.00608
5	77.05355	77.39058	80.79831	-30.14918	-15.87912	17.01332	16.50903	**81.54133**	4.006124
6	86.931	87.20726	90.00059	-30.09817	-12.66412	17.0678	16.56335	**100.6278**	4.005711
7	94.67559	94.93098	97.36387	-29.8311	-10.03375	17.07591	16.53773	**121.6667**	4.009103
8	100.1858	100.4443	102.7704	-29.79286	-7.53397	17.10736	16.54573	**138.5465**	4.006181
9	112.4629	112.75	115.0724	-29.83111	-0.777508	17.16953	16.53587	**178.842**	4.003692
10	119.4846	119.8093	122.1908	-29.68616	1.199498	17.25155	16.53135	**200.8007**	4.005398
11	131.3223	131.6884	134.1385	-29.78031	5.612688	17.5038	16.5465	**240.7693**	4.00626
12	142.045	142.4968	145.2721	-29.98128	11.32508	17.57154	16.51633	**278.8784**	4.006316
13	153.502	154.1967	158.1335	-29.98079	17.54749	17.83275	16.53222	**319.0274**	4.006208
14	161.8029	162.4382	165.7734	-30.14531	20.79743	17.96929	16.55175	**341.556**	4.006252
15	165.7431	166.6747	171.223	-30.23455	22.95594	18.01461	16.55953	**357.9889**	4.006308

Reduced Data										
No	DP [Pa]	q''_e [W/cm^2]	q'' [W/cm^2]	q''/q''_e	h_1 [W/m^2 K]	h_2 [W/m^2 K]	h_3 [W/m^2 K]	T_{w1} [°C]	T_{w2} [°C]	T_{w3} [°C]
1	5565.3	0.0	0.0							
2	4837.5	40.2	31.649	78.8%	2835.5	2829	2731.6	-5.80	-5.75	-4.96
3	4230.8	79.8	61.111	76.5%	2830	2821.3	2725.6	17.50	17.63	19.14
4	3786.8	121.5	91.068	74.9%	2700.1	2691.1	2597.9	43.69	43.92	46.33
5	3476.9	163.1	123.060	75.5%	2851.8	2840.6	2732.7	64.53	64.87	68.27
6	3478.1	201.3	158.215	78.6%	3499.4	3488.7	3384.1	70.80	71.08	73.86
7	3710.6	243.3	198.440	81.6%	4315	4303	4192.1	74.42	74.67	77.09
8	3872.3	277.1	230.810	83.3%	4996.5	4982.5	4860.3	76.59	76.85	79.17
9	4368.9	357.7	309.030	86.4%	6716.1	6695.2	6531	80.80	81.08	83.39
10	4965.7	401.6	351.260	87.5%	7556.7	7530.4	7343.3	83.44	83.76	86.13
11	6600.4	481.5	428.600	89.0%	9175	9139.2	8907.3	87.24	87.61	90.04
12	7275.4	557.8	502.775	90.1%	10866.6	10814.1	10502.3	90.24	90.68	93.43
13	8966.9	638.1	580.695	91.0%	12686.3	12591.5	12079.9	93.54	94.23	98.12
14	9773.6	683.1	623.900	91.3%	13402.7	13312.7	12859.2	97.29	97.91	101.21
15	10032.4	716.0	655.855	91.6%	14231.2	14090.2	13440.2	97.87	98.79	103.29

Table C.43 Test data, TS#4, Tin = -30 °C, m = 5.0 g/s.

- Test Section : 4
- D_h : 415.9 [μm]
- Number of Channels : 11
- Mass flow rate : 5 [g/s]
- T_{in} : -30 [°C]
- P_{out} : 16.5 [psia]
- T_{sat} (@ P_{out}) 63.59 [°C]

Measurement data									
No	T_{tc1} [°C]	T_{tc2} [°C]	T_{tc3} [°C]	T_{in} [°C]	T_{out} [°C]	P_{in} [psia]	P_{out} [psia]	Q [W]	$\dot{m}$ [g/s]
1	-29.26479	-29.26006	-29.17025	-29.85238	-30.36789	17.60886	16.5139	**0**	5.008874
2	-4.06209	-4.01989	-3.294809	-29.74069	-26.90278	17.47784	16.50837	**19.63553**	5.011415
3	20.2441	20.33513	21.76137	-30.12987	-24.46113	17.36681	16.49438	**39.71694**	5.008701
4	47.10862	47.25906	49.4231	-30.19921	-21.72194	17.29117	16.49573	**61.25459**	5.008799
5	72.14747	72.38024	75.47283	-29.80541	-20.01951	17.2086	16.47043	**82.09917**	5.008735
6	85.00935	85.26451	88.41158	-29.94326	-16.52523	17.23906	16.4974	**100.5938**	5.008833
7	92.83244	93.06015	95.67877	-30.16118	-14.74118	17.30838	16.54186	**119.8479**	5.008752
8	100.055	100.2683	102.564	-30.33217	-12.30743	17.33204	16.53337	**141.9947**	5.00887
9	106.1902	106.4318	108.6061	-30.37372	-9.064833	17.32965	16.50172	**161.8385**	5.008789
10	112.2039	112.4685	114.6099	-30.44262	-6.500375	17.38927	16.52228	**181.8336**	5.008788
11	117.3426	117.6295	119.7336	-29.54405	-3.120405	17.42182	16.54049	**199.8319**	5.008862
12	123.86	124.1952	126.4379	-29.71159	-0.679426	17.49102	16.56642	**222.7451**	5.008947
13	129.075	129.4563	131.7992	-30.34937	0.792437	17.5056	16.5373	**242.0887**	5.006383
14	134.4897	134.9092	137.3825	-30.49008	2.954267	17.56356	16.5547	**261.0899**	5.008936
15	140.1287	140.6259	143.4434	-30.0943	6.579869	17.57867	16.55188	**281.0018**	5.008932
16	146.1313	146.674	149.5229	-29.8617	9.07258	17.56709	16.50679	**301.3706**	5.008966
17	153.1506	154.0047	158.244	-29.4672	11.69722	17.64254	16.49092	**322.8179**	5.008921
18	160.5331	161.5495	166.449	-30.52976	14.21746	17.76162	16.55997	**343.7209**	5.016132
19	167.5645	168.7313	174.1977	-29.73915	17.33535	17.76054	16.55756	**362.9756**	5.009056

Reduced Data										
No	DP [Pa]	q''_e [W/cm^2]	q'' [W/cm^2]	q''/q''_e	h_1 [W/m^2 K]	h_2 [W/m^2 K]	h_3 [W/m^2 K]	T_{w1} [°C]	T_{w2} [°C]	T_{w3} [°C]
1	7549.5		0.0							
2	6684.3	39.3	31.355	79.8%	3012.9	3006.8	2905.1	-7.19	-7.15	-6.43
3	6015.2	79.4	61.792	77.8%	3036.8	3030.0	2927.1	14.03	14.12	15.55
4	5484.4	122.5	94.248	76.9%	3012.7	3005.4	2904.7	37.58	37.73	39.89
5	5089.5	164.2	125.690	76.5%	3029.5	3021.0	2912.3	59.37	59.61	62.69
6	5113.6	201.2	158.285	78.7%	3503.6	3493.7	3376.0	68.88	69.14	72.27
7	5284.9	239.7	194.345	81.1%	4172.7	4162.5	4048.7	73.00	73.23	75.83
8	5506.7	284.0	236.945	83.4%	5030.3	5018.9	4899.6	75.84	76.05	78.33
9	5708.4	323.7	275.315	85.1%	5845.7	5830.7	5699.4	78.02	78.26	80.42
10	5977.7	363.7	314.005	86.3%	6654.9	6636.3	6489.6	80.03	80.29	82.42
11	6076.6	399.7	349.380	87.4%	7501.1	7478.1	7313.7	81.51	81.79	83.88
12	6374.9	445.5	393.715	88.4%	8443.7	8413.6	8217.3	83.42	83.76	85.98
13	6676.2	484.2	431.190	89.1%	9214.3	9177.0	8954.4	84.75	85.12	87.45
14	6955.9	522.2	467.995	89.6%	9999.3	9954.9	9700.7	86.33	86.75	89.20
15	7079.5	562.0	506.930	90.2%	10951.3	10893.1	10574.7	87.91	88.40	91.19
16	7310.5	602.7	546.500	90.7%	11818.4	11749.9	11403.0	89.78	90.31	93.13
17	7940.1	645.6	587.420	91.0%	12621.7	12507.9	11971.8	92.50	93.35	97.54
18	8285.1	687.4	626.970	91.2%	13202.9	13064.3	12435.2	95.71	96.72	101.56
19	8294.2	726.0	663.940	91.5%	13891.9	13726.1	12999.0	98.84	99.99	105.39

Table C.44 Test data, TS#4, Tin = -30 °C, m = 10.0 g/s.

- Test Section : 4
- D_h : 415.9 [μm]
- Number of Channels : 11
- Mass flow rate : 10 [g/s]
- T_{in} : -30 [°C]
- P_{out} : 16.5 [psia]
- T_{sat} (@ P_{out}) 63.59 [°C]

Measurement data

No	T_{tc1} [°C]	T_{tc2} [°C]	T_{tc3} [°C]	T_{in} [°C]	T_{out} [°C]	P_{in} [psia]	P_{out} [psia]	Q [W]	$\dot{m}$ [g/s]
1	-28.94625	-28.92658	-28.55277	-29.91419	-30.01247	19.10662	16.48891	**0**	10.00388
2	10.06039	10.15426	11.62481	-29.95879	-27.28619	18.8	16.50537	**39.96467**	9.999815
3	49.26107	49.56121	53.01276	-29.98698	-24.42162	18.563	16.50848	**79.95457**	10.02219
4	86.67479	87.09939	91.67013	-29.85818	-21.3105	18.35912	16.48065	**119.412**	9.998959
5	101.5363	102.0013	106.7027	-29.99244	-19.98219	18.38271	16.51668	**142.3135**	9.980607
6	109.4256	109.842	114.0518	-30.12099	-18.94611	18.45768	16.5038	**161.2728**	9.999309
7	119.7453	120.078	123.248	-30.08662	-16.15126	18.46956	16.51808	**198.0055**	10.00517
8	131.7339	132.0198	134.5933	-29.77171	-12.6505	18.50179	16.4805	**243.3369**	10.01195
9	142.8795	143.1825	145.634	-29.91665	-10.14579	18.51158	16.42967	**283.2892**	10.00513
10	153.4229	153.7623	156.251	-29.96117	-7.757389	18.69367	16.53339	**320.1576**	10.00583
11	164.7865	165.1746	167.7717	-29.85097	-5.3253	18.8144	16.50143	**364.0471**	9.993099
12	170.3607	170.9354	174.4656	-30.04309	-3.705767	18.93412	16.518	**389.1373**	10.00655

Reduced Data

No	DP [Pa]	q''_e [W/cm^2]	q" [W/cm^2]	q"/q''_e	h_1 [W/m^2 K]	h_2 [W/m^2 K]	h_3 [W/m^2 K]	T_{w1} [°C]	T_{w2} [°C]	T_{w3} [°C]
1	18048.5		0.0							
2	15820.9	79.9	66.340	83.0%	4243.8	4231	4040.5	3.41	3.51	4.97
3	14165.4	159.9	130.595	81.7%	4231.9	4211.3	3988.4	36.05	36.35	39.79
4	12951.6	238.8	194.695	81.5%	4322.2	4301.9	4094.5	66.83	67.25	71.80
5	12865.8	284.6	234.940	82.5%	4716.6	4694.6	4483.6	77.52	77.98	82.66
6	13471.6	322.5	270.460	83.9%	5259	5237.8	5032.5	81.73	82.14	86.33
7	13455.0	396.0	341.575	86.3%	6612.5	6591.3	6396	84.69	85.02	88.17
8	13936.3	486.7	429.685	88.3%	8352	8328.9	8126.8	87.54	87.82	90.38
9	14354.3	566.6	506.955	89.5%	9783.7	9755.3	9531.6	90.63	90.93	93.36
10	14894.6	640.3	578.125	90.3%	11067	11031.4	10777.3	93.73	94.07	96.53
11	15947.4	728.1	663.085	91.1%	12706.3	12659.7	12356.3	96.18	96.56	99.13
12	16658.6	778.3	712.030	91.5%	13778.5	13703.2	13257.9	96.62	97.18	100.67

Table C.45 Test data, TS#4, Tin = -30 °C, m = 15.0 g/s.

- Test Section : 4
- D_h : 415.9 [μm]
- Number of Channels : 11
- Mass flow rate : 15 [g/s]
- T_{in} : -30 [°C]
- P_{out} : 16.5 [psia]
- T_{sat} (@ P_{out}) 63.59 [°C]

Measurement data									
No	T_{tc1} [°C]	T_{tc2} [°C]	T_{tc3} [°C]	T_{in} [°C]	T_{out} [°C]	P_{in} [psia]	P_{out} [psia]	Q [W]	$\dot{m}$ [g/s]
1	-29.69727	-29.67671	-29.28609	-30.16319	-30.60289	22.36184	16.51252	**0.059335**	15.00458
2	4.880825	5.002909	6.915571	-30.02115	-28.53925	20.94945	16.49272	**41.15267**	15.01152
3	38.22763	38.521	41.89476	-29.73092	-26.39428	20.58369	16.50171	**80.10349**	15.01184
4	70.20006	70.66478	75.66733	-29.74656	-24.52774	20.32843	16.49705	**120.1537**	14.99949
5	98.80666	99.33263	104.6508	-29.9662	-22.8425	20.12868	16.50675	**158.1637**	15.01868
6	116.2341	116.6686	121.062	-29.76038	-20.62184	20.12701	16.52084	**199.8086**	15.01522
7	128.7835	129.1228	132.3551	-29.76596	-18.68627	20.16516	16.49442	**239.9691**	15.00041
8	140.0564	140.3499	142.9911	-29.76848	-17.39129	20.23276	16.50275	**280.1976**	15.02628
9	149.335	149.7839	153.4162	-29.67472	-15.58801	20.32748	16.50921	**320.1646**	15.01661
10	158.6373	159.1328	162.7661	-30.08124	-14.32946	20.31947	16.47692	**358.9507**	15.00489
11	170.505	171.0395	174.6167	-29.95405	-12.62434	20.27515	16.45091	**404.6726**	15.00798

Reduced Data										
No	DP [Pa]	q''_e [W/cm^2]	q'' [W/cm^2]	q''/q''_e	h_1 [W/m^2 K]	h_2 [W/m^2 K]	h_3 [W/m^2 K]	T_{w1} [°C]	T_{w2} [°C]	T_{w3} [°C]
1	40329.6		0.0							
2	30728.1	82.3	70.778	86.0%	5401.4	5376.3	5010.5	-2.20	-2.08	-0.17
3	28144.2	160.2	135.575	84.6%	5324.9	5294.2	4965.8	24.54	24.84	28.20
4	26416.4	240.3	203.125	84.5%	5479.2	5445	5102.1	49.56	50.03	55.01
5	24972.3	316.3	268.015	84.7%	5678.1	5646.6	5346.9	71.42	71.94	77.23
6	24863.7	399.6	345.805	86.5%	6821.3	6792.2	6511.7	80.77	81.21	85.57
7	25308.8	479.9	422.915	88.1%	8149.5	8123	7879.1	85.31	85.64	88.85
8	25717.5	560.4	500.400	89.3%	9515.9	9489.6	9258.8	88.51	88.80	91.42
9	26326.0	640.3	578.230	90.3%	11098.7	11051.4	10683.2	89.67	90.12	93.71
10	26493.4	717.9	653.570	91.0%	12562.7	12503.8	12087.5	91.09	91.58	95.17
11	26367.2	809.3	742.055	91.7%	14221	14149.4	13688.2	93.65	94.18	97.70

Table C.46 Test data, TS#4, Tin = -30 °C, m = 20.0 g/s.

- Test Section : 4
- D_h : 415.9 [μm]
- Number of Channels : 11
- Mass flow rate : 20 [g/s]
- T_{in} : -30 [°C]
- P_{out} : 16.5 [psia]
- T_{sat} (@ P_{out}) 63.59 [°C]

Measurement data

No	T_{tc1} [°C]	T_{tc2} [°C]	T_{tc3} [°C]	T_{in} [°C]	T_{out} [°C]	P_{in} [psia]	P_{out} [psia]	Q [W]	$\dot{m}$ [g/s]
1	-29.0179	-29.01297	-28.91936	-30.11121	-30.64377	24.1072	16.50336	**0.067207**	19.99479
2	1.243495	1.332453	2.726127	-30.1217	-29.23822	23.57589	16.48004	**40.06184**	20.00112
3	31.72266	31.97804	34.91482	-29.9891	-27.65463	23.13728	16.49328	**81.73373**	19.99592
4	60.48919	60.87755	65.05814	-29.99093	-26.23261	22.8347	16.47384	**120.458**	19.99512
5	86.79924	87.36065	93.0371	-29.90517	-24.8201	22.56567	16.4488	**160.3238**	19.99136
6	111.5991	112.2233	118.5342	-29.98657	-23.57409	22.39827	16.47844	**201.8583**	19.99514
7	126.1964	126.722	131.7286	-29.81834	-22.10669	22.37411	16.45883	**240.2273**	19.99511
8	139.6959	140.1264	144.0006	-30.05078	-20.9144	22.39361	16.44142	**283.3493**	19.99961
9	148.7822	149.3188	153.6601	-29.98204	-19.6345	22.48142	16.47728	**319.1556**	19.99513
10	159.4231	159.965	163.9393	-29.74934	-18.16531	22.47962	16.47191	**359.0831**	19.99511
11	170.7002	171.2547	174.9654	-29.85716	-16.60711	22.5967	16.49654	**404.176**	19.99516

Reduced Data

No	DP [Pa]	q''_e [W/cm^2]	q'' [W/cm^2]	q''/q''_e	h_1 [W/m^2 K]	h_2 [W/m^2 K]	h_3 [W/m^2 K]	T_{w1} [°C]	T_{w2} [°C]	T_{w3} [°C]
1	52426.7		0.0							
2	48924.2	80.1	70.122	87.5%	6089.3	6065.8	5719.4	-5.77	-5.68	-4.29
3	45808.8	163.5	141.635	86.6%	6373.0	6336.5	5944.5	17.44	17.70	20.63
4	43856.6	240.9	207.915	86.3%	6414.1	6375.8	5991.0	39.41	39.79	43.96
5	42174.4	320.6	277.370	86.5%	6744.6	6698.8	6269.0	58.53	59.08	64.73
6	40815.8	403.7	351.245	87.0%	7189.0	7143.4	6713.3	75.62	76.23	82.50
7	40784.4	480.5	423.480	88.1%	8231.7	8190.0	7812.8	82.68	83.20	88.17
8	41038.9	566.7	505.880	89.3%	9538.1	9499.8	9167.9	87.59	88.02	91.85
9	41397.1	638.3	575.385	90.1%	10838.4	10784.3	10365.4	89.42	89.95	94.25
10	41421.7	718.2	652.580	90.9%	12231.5	12170.2	11739.1	91.97	92.50	96.43
11	42059.2	808.4	740.080	91.6%	13867.2	13796.4	13340.4	94.05	94.59	98.25